Fall 2013

Propagation Of Sound In The Vicinity Of Rigid Porous Interfaces

Hongdan Tao
Purdue University

Graduate School ETD Form 9
(Revised 12/07)

PURDUE UNIVERSITY
GRADUATE SCHOOL
Thesis/Dissertation Acceptance

This is to certify that the thesis/dissertation prepared

By HONGDAN TAO

Entitled PROPAGATION OF SOUND IN THE VICINITY OF RIGID POROUS INTERFACES

For the degree of Doctor of Philosophy

Is approved by the final examining committee:

KAI MING LI
Chair

J. STUART BOLTON

JUN CHEN

GREGERY T.BUZZARD

To the best of my knowledge and as understood by the student in the *Research Integrity and Copyright Disclaimer (Graduate School Form 20)*, this thesis/dissertation adheres to the provisions of Purdue University's "Policy on Integrity in Research" and the use of copyrighted material.

Approved by Major Professor(s): KAI MING LI

Approved by: DAVID C. ANDERSON 10/02/2013
Head of the Graduate Program Date

PROPAGATION OF SOUND IN THE VICINITY OF RIGID POROUS INTERFACES

A Dissertation

Submitted to the Faculty

of

Purdue University

by

Hongdan Tao

In Partial Fulfillment of the

Requirements for the Degree

of

Doctor of Philosophy

December 2013

Purdue University

West Lafayette, Indiana

I dedicate this dissertation to my family, especially...

to my mom and dad for endless encouragement and patience;

to my brother and sister for instilling the importance of hard work and higher education;

to my husband Sheng Yuan for endless support and understanding;

and to my little loving and caring girl Vivian Yuan.

ACKNOWLEDGMENTS

I would like to give my sincerest thanks and appreciation to Professor Kai Ming Li for his guidance, support, and insight as an advisor throughout my time at Purdue. I am very grateful for his encouragement and patience whenever I come across difficulties. He has been a great source of inspiration for me over the past four years.

I would also like to thank the members of my dissertation committee: Professor J. Stuart Bolton, Professor Douglas E. Adams, Professor Jun Chen, and Professor Gregery T. Buzzard. They have generously given their time and expertise in support of my work. The knowledge and insights I have received from their courses makes my research possible. I would like to acknowledge Professor Patricia Davies, who has not only taught me a lot through her DSP course, but also in taking her time in reviewing my Inter-noise conference presentation. I would also like to acknowledge Dr. Donald G. Albert for his experimental data on sound fields over snow covered ground and for our correspondences via email which helped me validate the model developed in this dissertation.

I gratefully acknowledge China Scholarship Council (CSC) from the National Science Foundation for their four years of financial support.

I am genuinely grateful for my many friends at Herrick Lab who have assisted, advised, and supported me over the years. Especially, I need to express my gratitude and deep appreciation to Yangfan Liu and Bao Tong. They have been supporting and enlightening me through these years with their friendship, knowledge and kindness.

Lastly, I would express my best gratitude to my husband Sheng Yuan, my little daughter Vivian Yuan, and to my parents along with my brother and sister for their compassionate support and care.

TABLE OF CONTENTS

Page

Page

Page

LIST OF TABLES

LIST OF FIGURES

Figure Page

Figure Page

Figure Page

Figure Page

Figure Page

Figure Page

ABSTRACT

Tao, Hongdan Ph.D., Purdue University, December 2013. Propagation of Sound in the Vicinity of Rigid Porous Interfaces. Major Professor: Kai Ming Li, School of Mechanical Engineering.

Propagation of sound in the vicinity of rigid porous interfaces is investigated systematically to facilitate the acoustical characterization of sound absorption materials for noise reduction applications. Various rigid porous interfaces are considered: (1) a semi-infinite porous layer; (2) a porous hard-backed surface; and (3) a porous impedance-backed layer. A closed-form solution and numerical methods are derived with respect to each rigid porous interface condition.

A modified saddle-point method is exploited to investigate the sound field emanating from a monopole source above and below a rigid porous interface. The solutions can be expressed in a form that resembles the classical Weyl-Van der Pol formula. A heuristic method is then proposed to remove the singularity within the asymptotic solution via application of the double saddle-point method. Its relative simplicity and accuracy demonstrates the advantage of the double saddle-point method whenever the approximation is valid. Following this, the sound field within a hard-backed rigid porous medium due to an airborne source is examined. The accuracy of the proposed asymptotic solutions has been confirmed by comparison with benchmark numerical solutions and through indoor sound propagation experiments. Measurement

data and theoretical predictions suggest that when the receiver is positioned near the top surface of the hard-backed layer, the ground reflection of the refracted wave contributes greatly to the total sound field.

Taking into account source characteristics, an asymptotic formula is derived for predicting the sound field from a dipole source above and below an extended reaction ground. The directional effect of the dipole source on each term within the asymptotic solutions is interpreted. Further analysis shows that an accurate asymptotic solution can provide a good starter field for the Parabolic Equation--Finite Element Method (PE/FEM). The PE/FEM marching schemes are derived based on linear and cubic finite element discretization along both the vertical and horizontal directions. The Perfectly Matched Layer (PML) technique is applied to the PE/FEM, resulting in a substantial reduction in computational time. Comparison with experimental data for snow covered grounds is made and good agreement was demonstrated, which validates the accuracy of the proposed PE/FEM approach.

CHAPTER 1: INTRODUCTION

1.1 Motivation and Objective

Noise propagation from airports, roads, railways, and industrial has been of considerable interest to the environmental acoustics community. During the early days, simple models involving a homogenous and isotropic propagation medium with a perfectly reflecting ground surface were considered. More complexity was later introduced to model realistic propagation conditions. Effects such as ground properties, interference phenomena, mixed terrain topography, and atmospheric variations became increasingly important in the accurate prediction of noise over long distances.

In most of the earliest studies, the ground is typically considered as being locally reacting for ease of mathematical analysis. However, it was found that the locally reacting ground assumption is not accurate in certain practical applications. For example, rigid porous materials such as fiberglass or glass wool (modeled by a homogeneous dissipative fluid medium) do not exhibit locally reacting characteristics. These mediums are referred to as extended reaction or non-locally reacting. It is typically assumed that the layer thickness is infinite to simplify the initial analysis. More recently, multi-layered models with a rigid surface have been examined.

There are several publications in the literature concerning the application of asymptotic solutions for sound field predictions near an extended reaction ground [1],

above a layered ground [2], and above an impedance-backed porous layer [3]. To the best of our knowledge, there is no study to derive an analytical formula for the sound field below a hard-backed porous layer and also an impedance-backed ground. This motivates our development of general and complete analytical solutions for the sound field near porous interfaces of various types.

Much of the earlier asymptotic analyses [1-3] were based on a double saddle-point method supplemented by the method of pole subtraction for the sound fields above a locally reacting or a non-locally reacting plane boundary. This asymptotic solution obtained is singular when the source lies directly above (or below) the receiver, or when the specific acoustic impedance of the boundary is equal to unity. Due to this singularity, the derived asymptotic formula cannot be used conveniently in more general applications. Hence, this dissertation aims to develop a more robust asymptotic formula for predicting sound field over a rigid porous medium.

A physically meaningful solution where each term can be associated with a wave pheonomenon is desired. In situations where an analytical solution cannot be obtained, development of an accurate and efficient numerical approach becomes relavant. For example, a closed form solution cannot be obtained when atmospheric effects (*e.g.*, refraction, turbulence, wind, *etc.*) and realistic boundary conditions (*e.g.*, mixed impedance, irregular ground interfaces, *etc.*) are appreciable.

The goal of this dissertation is to accurately predict the sound propagation over rigid porous interfaces subject to various boundary conditions. Emphasis is given to both asymptotic solutions for simple cases and numerical solutions for more generalized environments. The asymptotic solutions proposed are capable of predicting the sound

field for a flat, layered porous ground with constant impedance. It is also suitable for applications as an accurate starting field for the Parabolic Equation (PE) model. The PE method is implemented to incorporate atmospheric effects and range-dependent propagation effects such as mixed-impedance ground surfaces and/or terrain variations. In addition, the Finite Element Model (FEM) techniques are applied in the discretization of the parabolic equation using either linear or cubic finite elements. Asymptotic solutions for the dipole source are also investigated. The analysis proves useful in the formulation of the starting field for higher ordered PE models.

1.2 Background

Sound propagation outdoors near a ground surface has been studied extensively. Early work dates back to 1950s. Neglecting atmospheric effects involving wind, turbulence, attenuation, and scattering due to air as well as temperature gradients, the propagation phenomena can be simplified into three categories: ground effects, characterization of ground properties, and source characteristics. With respect to more complicated propagation environments, the study of the atmospheric effects becomes important.

1.2.1 Ground Effects

The most general parameter of the ground is the complex impedance. It is defined as the ratio of the complex pressure amplitude to the normal component of complex velocity amplitude evaluated at the surface of the ground [4]. Note that there is an alternative definition for ground impedance called the characteristic impedance. The characteristic impedance of a ground surface is the ratio of the complex pressure

amplitude to the complex velocity amplitude for a sound wave traveling through a medium. In the situation when the speed of sound in the ground is much smaller than that in the air, the sound wave will travel into the ground in a direction normal to ground surface. It is called locally reacting ground (i.e., the angle of incidence does not influence the angle of refraction). For locally reacting grounds, the characteristic impedance of the ground can be used to approximate the impedance and represent its properties [4, 5].

Prior to the mid-1960s, considerations of ground effects are quite rare. The physical interaction between the ground and the incident sound waves were not well understood. In 1965, Parkin and Scholes first published their study on jet engine noise propagation around airfields located in Radlett [6] and Hatfield [7]. Effects of vector wind speeds, ground surface interactions, as well as the influence of temperature on ground effects were considered. A semi-empirical model was developed Delaney and Bazley [8] specifically for the acoustical characterization of fibrous absorbent materials. In their model, the impedance can be obtained from curve fitting experimental data using a single parameter: the flow resistivity. Their formulation is also partially based on classical theory for the acoustical characteristics of rigid porous materials. Later Chessell [9] and Embleton, et al. [10] extended the model to use for a large variety of ground and propagation conditions. Chessell also recognized a discrepancy in the normalization used in the one-parameter model when applied to soils. The flow resistivity in Delaney and Bazley's one-parameter model can be regarded as an effective flow resistivity.

Later Piercy el al. [11] investigated the ground effects under neutral atmospheric conditions (i.e., in the absence of wind) utilizing a subset of Parkins and Scholes' data. It was concluded that at low frequencies (below 300Hz), ground and surface waves are the

major carriers of environmental noise over long distances while air turbulence needs to be considered for frequencies above 1kHz. In 1988, Attenboroug [12] published a comprehensive review of ground effect models over a wide range of frequencies. The relationship between the shape and length of the ground effect region within the attenuation spectrum along with the acoustical properties of the ground are explored. It is suggested that a multi-layered structure impedance model could explain the ground effect dips at Radlett [6] or Hatfield [7].

For a simple layer-structure model, it consists of two layers. One is a single layer of finite thickness, and the other is a semi-infinite and acoustically rigid backing layer. For example, the fallen snow on hardened soil or an asphalt pavement can be modeled as a layer of rigid porous material resting on an acoustically rigid plane. In the case of a multiple-layered medium, the real part of the surface impedance (when computed from the Delaney and Bazley's model) sometimes yield a negative number at low frequency range. However, the impedance must be a positive-real function to be physical.

Attenborough [13] developed a micro-structure based model for describing multi-layered surface. A more accurate four-parameter model, which consists of: flow resistivity, shape factor, pore shape factor ratio, and tortuosity was proposed. The four-parameter model can be reduced to Attenborough's one parameter model via simplifications for high flow resistivity (e.g., >100,000 MKS units) and low frequencies (e.g., <1 kHz). Miki [14, 15] discussed the characteristic impedance and propagation constant of porous material based on experimental data by Delaney and Bazley. Some modifications from Delaney and Bazley's model were made to satisfy the real and positive impedance restrictions. It is shown that the new model is useful for predicting

the acoustical behavior of porous materials, especially for the double-layer case. Recently, Attenborough [16] assessed seven impedance models for the purpose of ground impedance predictions. By using a fixed relationship between tortuosity and porosity, the required number of adjustable parameters can be reduced to two –parameters (flow resistivity and porosity). The accuracy of the different impedance models is validated, and the applicable porous surfaces for these impedance models aredescribed.

In fact, a homogeneous ground surface may be unrealistic. For example, aviation noise propagation may involve considering transitions between concrete runways and surrounding grassy fields. Hence, impedance discontinuities need to be addressed. There are a number of different models for studying the effect of ground impedance: the semi-empirical models from De Jong [17] and Koers [18]; the Fresnel-zone approximation from Boulanger el al. [19]; and the Boundary Element Method (BEM) arpproach [20]. Further research in the incorporation of impedance discontinuities into a Fast Field Program (FFP) formulation was performed by Taherzadeh el al. [21] for a stationary source in a variety of atmospheric configurations. The PE method enables impedance transitions to occur between rang ssteps. Hence it is the preferred method in our current investigation.

1.2.2 Source Characteristics

Most of the above studies dealt with the sound field generated by a monopole point source. However, there are many noise sources that have directional characteristics, especially at close range. For instance, a dipole source is a suitable model for a fast

moving train [22] and a helicopter rotor [23]. The prediction of the sound field due to multi-pole sources deserves some consideration.

In 1957, Ingard and Lamb [24] began their work on computing the "power amplification factor" as a function of the distance between the source and the plane for monopoles, dipoles and longitudinal quadrupoles. The effect of the reflecting plane boundary on the power out of the source was studied. Later in 1960, Yildiz and Mawardi [25] made use of a Green's function constructed by spectral representations, and derived a general close form expression for the evaluation of the pressure distribution due to a multipole point source. The explicit relations for the case of dipole and quadruple fields were also studied in detail. Following the work of Ref [24], Bies [26] generalized the expression of the power to an arbitrarily oriented multipole. The results showed that averaging over a distribution of multipoles would reduce the large variations of radiated power observed for a single multipole. Later in 1981, Meecham et al. [27] describes an experiment which directly confirms the predicted diffraction effects by Ref [25]. A dipole-baffle system was set up in an anechoic chamber and the sound intensity was measured. It showed that the baffle effectively amplified the sound radiated in all directions.

In 1993, Shen and Meecham [28] studied the aerodynamic sound generated by a subsonic jet at normal and oblique incidence, impinging on a large, rigid plate. The directivity results indicate that the correlation approach resulted in quadrupolelike directivity patterns. In 1994, Hu and Bolton [29] proposed a two-dimensional finite Hankel transform technique to predict sound propagation from arbitrarily oriented dipoles and quadrupoles. The results were found to be in excellent agreement with measurements

of sound propagation over a finite impedance surface from a small, unbaffled loudspeaker. Their results indicate that the presence of a dipole component has a significant effect on the total field which includes diffraction and ground reflection. Later in 1997, Li et al. [30] derived a close-form analytical solution for an arbitrarily oriented dipole placed above an impedance ground. The analytical solutions for horizontal and vertical dipoles agree well with FFP predictions, and the asymptotic results were also confirmed via laboratory measurements. It was shown that the analytical approximations had the combined advantages of being easier to interprete physically and greatly reduced computational time. A continuation of the work was also pursued by the same authors [31] on the sound field of an arbitrarily oriented quadrupole above an impedance ground by using the method of steepest descent path. The total sound pressure was shown to be augmented by two extra terms which were particularly important when the source and receiver was in close proximity.

1.2.3 Numerical Techniques in Sound Propagation

Modeling outdoor sound propagation requires the consideration for ground effects, source characteristics, and atmospheric conditions. Atmospheric effects consist of two main aspects: atmospheric refraction and atmospheric turbulence. Atmospheric refraction results from gradients in temperature and/or wind speeds, which can have a large impact when long-range propagation is desired. It is especially important in low source, low receiver geometries. Atmospheric turbulence results from fluctuations in the temperature and/or wind velocity around some mean values. Analytical solutions exist only for the simplest cases while numerical solutions become necessary when more realistic

conditions are of interest. Different numerical approaches such as ray tracing, BEM, FFP and PE methods are commonly applied in outdoor sound propagation depending on the problem configuration.

This section will introduce the basic concepts and recent studies of ray tracing, FFP and PE methods. The BEM is commonly used for sound propagation near sound barriers. However, noise barriers are not considered in current investigation and will not be explored further.

a) Ray Tracing

Atmospheric sound propagation can be modeled using acoustic rays. Two steps are needed in ray tracing: (1) calculation of the paths between the source and the receiver; (2) summation of the contribution from all acoustic ray paths. Ray tracing has been used extensively to predict outdoor sound levels in the presence of sound speed gradients even though the mathematical conditions for the applicability of the ray-based methods are seldom satisfied. The ray path is computed via numerical integration using small increments to ensure that the elevation angle at every point along the ray path satisfies Snell's law.

For the upward refracting atmosphere, a shadow zone exists where no sound rays can reach the receiver. Hence, the ray model predicts zero sound energy in this region [32]. In reality, due to the effect of diffraction and scattering by atmospheric turbulence, the sound energy is non-zero. Wave theory and wave extensions to ray theory (where a Gaussian beam or multiple rays is traced instead of individual ray [33]) improves the basic ray model predictions in the vicinity of the shadow zone boundary. For long ranges

or in the extreme downward refracting atmosphere, there can be multiple ground reflected paths. This makes it difficult to obtain a generalized ray-based solution.

Caustic singularies [34, 35] occur when at least two neighboring rays intersect one another (at a caustic point), resulting in an infinite sound amplitude prediction. To correct for caustics, an accurate computation of the caustic diffraction field (i.e., the difference between the actual sound field and the ray-based solution) is needed. For the special case of a height dependent sound speed profile and a homogeneous ground surface, caustic singularities can be effectively eliminated by transformation from the spatial domain to the wave-number domain along the horizontal direction [36]. In general, the complex nature of the caustic diffraction field in realistic propagation conditions makes it difficult to obtain reliable predictions using ray theory alone. Hence, the development of approximate numerical schemes such as the FFP and the PE is pursued by the acoustic community.

b) The Fast Field Program (FFP)

The FFP employs a spatial Fourier transform to the wave equation which transforms spatial domain quantities into the wave number domain. The transformed wave equation is solved numerically in the wave number domain, and then an inverse Fourier transform is applied to obtain the physical sound field. The FFP method was first introduced for applications in underwater acoustics to study the effects of sound speed variations with depth [37, 38]. In the early 1980s, it was adapted for atmospheric sound propagation. An introduction to the FFP-type formulation is given for atmospheric sound propagation in Ref. [39-41]. The geometry is limited to a horizontally stratified and

stationary medium, which an approximation for the atmosphere in the absence of wind effects.

A Hankel transform can be defined to relate the field quantities in the frequency—wavenumber domain to physical space quantities. The Hankel transform is evaluated numerically by approximating the continuous integral as a finite sum of the FFT variety, as shown by Candel [42]. To compensate for the finite truncation of the infinite series, correction factors were added to the formulation. Richards and Attenborough [39] introduced a pole in their asymptotic Bessel function expansion. The symmetry property of the Fourier coefficients allows a two-fold reduction in the FFT length compared to Candel's formulation.

For sound propagation within the stratified layer, different numerical approaches have been developed to take into account horizontal stratification. DiNapoli and Deavenport [43] applied a Thomason-Haskell matrix method in their FFP formulation. West [39] applied a transfer matrix approach to involve a two-by-two matrix multiplication for wave transmission across different layers. Tooms et al. [44] evaluated the layer reflection coefficients by a global matrix approach to distribute the pressure at each layer in the wave number domain. The results are then transformed back into the space domain to obtain the physical sound field.

The FFP method provides an accurate representation of the sound field in the situation of a range-independent propagation environment (e.g., a horizontally stratified atmosphere) for most ranges of interest. Another method is required when horizontal variations along the propagation path are modelled.

c) The Parabolic Equation (PE) method

In contrast to the FFP method, the PE method is not restricted to sound propagation in a horizontally stratified atmosphere or over a homogeneous ground surface. The PE method is based on the approximate form of the wave equation, parabolic equation. It was first introduced by Leontovich and Fock [45] for electromagnetic wave propagation. Since then, the PE method has been widely used in various fields ranging from quantum mechanics, optics, seismic wave propagation, and underwater acoustics to atmospheric sound propagation. By neglecting the back scattering of the sound waves, the basic parabolic equation can be formulated. The Green's Function Parabolic Equation (GFPE) method and the Crank-Nicholson Parabolic Equation (CNPE) method are the two main formulations. The GFPE method uses a transformed Green's function of a point source with Fourier transforms to propagate sound. It can use larger range step size, but it included the atmospheric refractive effect as a phase factor, which results in the errors if the change in sound speed with height is large. Even though it has faster computational speed, it does not allow a high degree of flexibility in modelling boundaries. For the CNPE method, a Crank-Nicholson finite difference scheme is used for numerical evaluation of each range step. The CNPE method requires much smaller steps in range, which increases the computation time. However, a more generalized terrain function, and complicated boundaries can be incorporated in CNPE. Because of its atmospheric effect, range-dependent effect modeling capabilities, and increased flexibility and ease in modeling boundaries, the CNPE formulation will be chosen as the basis of the current research.

In the 1970s, the standard narrow-angle (Tappert's) [46] and third-order wide angle (Claerbout's) [47] parabolic equations were applied successfully to underwater

acoustics. The finite difference scheme was always used for the numerical evaluation of the extrapolation step for parabolic equations applied underwater acoustics. Later Gilbert and White [48, 49] extended the wide angle PE model in predicting outdoor sound propagation in a steady atmosphere over locally reacting ground, and realistic atmospheric profiles with downward-refracting and upward-refracting cases. Good numerical agreement was achieved between the PE and FFP results, e.g. within 1 dB. Then the method, together with a two-dimensional atmospheric turbulence model, was extended to investigate the sound propagation with atmospheric turbulent effect. The method was also applied to outdoor sound propagation for the case with range-varying ground impedance. Note that the finite element techniques were applied in the vertical discretization for the parabolic equations, and an artificial attenuation layer was added to the top part of the sound speed profile to simulate a radiation boundary condition. Later, West et al. [50] used the PE model for long range sound propagation in the atmosphere with a finite difference numerical solution scheme. A second-order accurate ground boundary condition and an upper boundary condition was implemented and described to minimize reflections into the computational region. Robertson et al. [51] modeled the low-frequency sound propagation over a locally reacting boundary with parabolic approximation by an implicit finite-difference method. The continuous work was done by Robertson [52] for the sound propagation over impedance discontinuities. A nonlocal boundary condition at the upper surface to model a homogeneous, semi-infinite atmosphere was used instead of the artificial absorbing layer with artificial attenuation (which enlarges the computational domain). In Refs [53, 54], split-step Fourier discretization methods are used in the atmospheric sound propagation based on the

Green's function. The absorbing layer technique was used for the numerical treatment of the outgoing radiation condition in height. Recently, Dougalis and Kampanis [55] simulated the underwater sound propagation by applying a finite element method along with an analog transformation of coordinates to standard parabolic equation numerically. Malbequi [56] and Robertson [57] applied the parabolic equations to the numerical simulation of the propagation of sound in the atmosphere over irregular terrain. One of their difficulties is a delicate treatment of the interaction with the ground surface. Kampanis [58, 59] overcome the difficulty by using a transformation of coordinates, and discretization by a finite element method. The PE model was also used to study the sound propagation in an inhomogeneous turbulent atmosphere [60]. Coupled with a micro-meteorological model, a wide-angle parabolic equation with a finite difference discretization was used for long range sound propagation over a complex terrain with mild topographic variants [61]. The comparison between measurements and predictions is presented over a valley with mild slope [62]. Very recently, Kampanis et al. [63] first transformed the problem into an orthogonal computational domain, and a linear finite element method with the nonlocal boundary condition was then used to compute the approximate solution. The Crank-Nicholson scheme was used to march the finite element solutions. The overall method was validated by testing on benchmark cases with irregular ground surface. The PE model shows its advantages over other methods for sound propagation over irregular boundaries and complex environments.

In almost all the above references, little attention has been received on the starting field. Since PE solves an initial value problem, the initial field is needed at the starting range. In general, the Gaussian starting field has been widely used as the starting field for

PE models. The reason is that it can be derived from the exact expression for a monopole source by applying far-field and small elevation angle approximations. It satisfies the requirement of the PE, which is a smooth function, finite at all points, as well as limited in energy at large vertical wave number. However, the Gaussian starting field is not good for near field prediction due to its far field approximation. Collins [64] developed an efficient PE starter called as self-starter. It is based on high-order parabolic approximations. And examples in the paper validate its accuracy for problems including wide propagation angle, low frequencies, continuous spectrum and so on. Cederberg and Collins [65] improved the self-starter using the operator of the split-step pade solution [66]. The improved self-starter has several advantages over the original starter involving the efficiency at long-range propagation and improved accuracy at relatively short ranges of interest. However, there's no standard for the short range of interest. Even for layered ground, a self-starter satisfying all boundary conditions at interfaces is harder to find, and efficiency will decrease due to the increase amount of the iterations. Hence, an accurate, yet efficient starter is required to be used for PE model, especially at short ranges. Furthermore, most of previous researches are using the Crank-Nicholson scheme, i.e. finite difference to march the vertical solutions in the range domain. In this dissertation, a Finite Element method will be used to march the sound field in the range domain, which can incorporate the boundary condition easily.

1.3 Outline of the Dissertation

The dissertation is divided into nine chapters. The motivation and objective is explained in the first chapter. In Chapter 2, instead of using double saddle-point method

with pole subtraction method, a modified saddle-point method is exploited to study the sound field from a monopole source above a rigid porous medium. The solution is expressed in a form comparable to the classical Weyl-Van der Pol formula, which offers a physical understanding of the problem.

Following Chapter 2, in Chapter 3, the modified saddle-point method is extended to predict sound penetration into a semi-infinite rigid porous medium due to a monopole source. It is shown that the solution gives higher accuracy of the sound fields even when the pole is located in close proximity to the saddle point. Both chapter 2 and chapter 3 report an endeavor to apply the modified saddle-point method for studying the propagation of sound in the vicinity of the non-locally reacting porous medium.

Chapter 4 explores a heuristic method based on asymptotic solutions by double saddle point to remove this singularity and suggests a comparable analytical form as the Weyl-Van der Pol formula. The improved formula offers a physically interpretable solution and allows accurate predictions of total sound fields above locally/non-locally reacting surfaces for all geometrical configurations.

Chapter 5 examines the sound fields within a hard-backed rigid porous medium due to an airborne monopole source. The accuracy of the asymptotic solutions has further been confirmed by comparing with indoor experimental results. Measurement data and theoretical predictions have suggested that when the receiver is located near the bottom of the hard-backed layer, the reflection of the refracted wave gives rise to a significant contribution to the total sound fields.

In Chapter 6, an asymptotic formula is derived for predicting the sound field from a dipole source above and below an extended reaction ground. A double saddle-point

method supplemented by pole subtraction is used to evaluate the diffraction integral along the steepest descent path. The accuracy of the asymptotic solutions is confirmed by comparing them with computationally intensive, but more accurate, numerical schemes. Furthermore, the directional effect of the dipole source on each term of the asymptotic solutions is interpreted. The asymptotic solutions here are also a good starting field for the PE model in the next two chapters.

Chapter 7 continues the study of sound propagation over rigid porous interfaces using the PE method combined with finite element discretization vertically. We define the method as the hybrid Parabolic Equation/Finite Element Method (PE/FEM). Linear interpolation and cubic interpolation are used for finite element discretization. The PE/FEM model is validated by comparing with already published results for benchmark cases. It also indicates that the analytical asymptotic solutions derived previously, as a starting field in PE/FEM model, give a better prediction than standard Gaussian starter. Finally, the PE/FEM model is applied to predict sound propagation over snow cover, and good agreements are obtained with experimental data.

In Chapter 8, the PE/FEM model is extended to cubic PE/FEM model with cubic FEM basis function interpolation horizontally as well. Comparison with results for benchmark cases validated the derived solutions. It is also shown that the cubic PE/FEM model costs more computation time but gives good results of sound prediction not only from monopole, but also dipole sources.

In the last chapter of the dissertation, a summary of the current research is given. Comments and future work is suggested. In summary, the dissertation is composed of two parts. The first part (chapter 2 to 6), is the study on the analytical solutions for sound

propagation over different types of rigid porous interfaces, and the second part (chapter 7 and 8) is on the numerical solutions. The types of rigid porous interfaces cover semi-infinite porous layer, hard-backed, and impedance-backed rigid porous layer. The analytical asymptotic solutions are not only able to predict the sound field near the different types of rigid porous interfaces in homogenous atmosphere accurately, but alsoo proved to be an accurate starting field for the numerical PE/FEM. For the numerical PE/FEM model, it is shown to be capable to take account of the atmospheric effects in its FEM discretization process, which makes it applicable for predicting sound propagation in complex atmosphere. Finally, based on the analytical and numerical solutions obtained in the dissertation, future work is suggested.

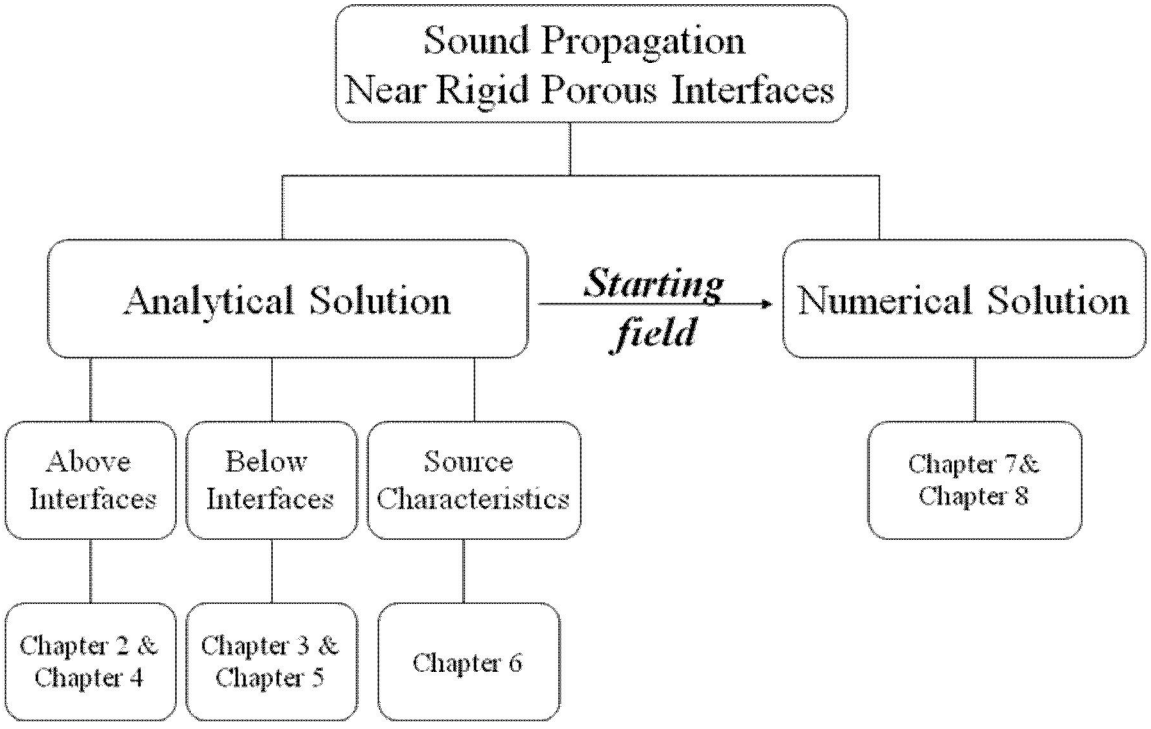

Figure 1.1: Flow chart of the dissertation.

CHAPTER 2: A MODIFIED SADDLE POINT METHOD FOR PREDICTING SOUND FIELDS ABOVE A NON-LOCALLY REACTING POROUS MEDIUM

2.1 Introduction

The study of sound propagation above a non-locally reacting plane boundary has been conducted for many decades. An exact formulation [88], precise asymptotic formulas [72, 1] and accurate numerical solutions were developed for the porous half-space. A more difficult problem involves the presence of a porous layer where the porous frame is motionless. The porous layer is often set on a rigid backing that has an application for acoustical characterization of the non-locally reacting sound absorbing materials from the measured sound fields [89–91]. This technique depends critically on the availability of an accurate numerical solution that can be used in the inversion process. Allard et al. [92] derived an asymptotic formula for the sound field above a hard-backed porous layer. More recently, Li and Liu [3] extended their formula to include the prediction of sound fields above an impedance-backed porous layer.

Most of the earlier asymptotic analyses were based on a double saddle-point method [93] supplemented by the method of pole subtraction [71] for the sound fields above a locally reacting or a non-locally reacting plane boundary. This asymptotic

solution is apparently singular when the source lies directly above (or below) the receiver or when the specific acoustic impedance of the boundary is equal 1. Because of this singularity, the derived asymptotic formula cannot be used conveniently in a more general application. Hence, one of the motivations of the present study is to develop a more robust asymptotic formula for predicting sound fields above a non-locally reacting porous medium.

There is a less popular asymptotic approach, known as a modified saddle-point method developed by, Ott [82], Pauli [83] and Clemow [84]. This asymptotic method was subsequently used by Kawai et al. [85] who derived the monopole sound-field propagation above a locally reacting plane. Chandler-Wilde and Hothersall [86] generalized the procedure to give the solution for the cylindrical-wave reflection in the form of an asymptotic series with an accurate estimation of the error bound.

The present chapter aimed to use the modified saddle-point method for developing an asymptotic series to predict the sound fields above three types of non-locally reacting porous media: half-space, hard-backed and impedance-backed rigid porous layers. In section 2.2, the derivation of the asymptotic solution is presented, and it is shown that the solution is expressed in a form comparable to the classical Weyl-Van der Pol formula, which offers a physical understanding of the problem.

In section 2.3, the asymptotic solutions are validated by comparing with those obtained by other computationally intensive, but more accurate, schemes for different source/receiver configuration. Finally, a summary is given in section 2.4.

2.2 Theoretical Formulation

2.2.1 An Integral Formulation

Figure 2.1 shows the geometrical configuration of the problem for determining the sound fields due to a monopole source above a flat porous medium with a layered structure. The time dependent factor, $e^{-i\omega t}$, is assumed and suppressed throughout the analysis. The wave number k, the density ρ, and, the speed of sound c in the upper medium will be used in the following analysis. An axi-symmetric solution is sought where the sound fields can be conveniently split into three terms as follows [3]:

$$p = \frac{e^{ikR_1}}{4\pi R_1} + \frac{e^{ikR_2}}{4\pi R_2} + p_D \,. \tag{2.1}$$

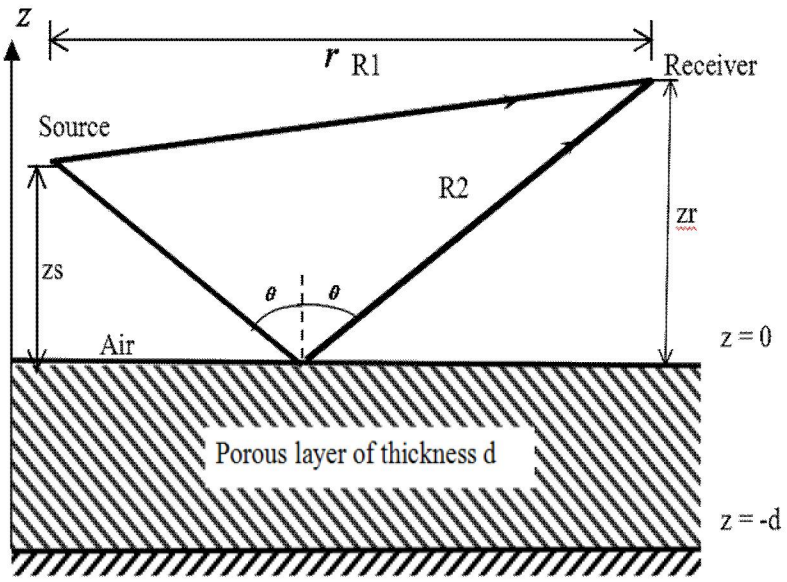

Figure 2.1: Illustration of a monopole source/receiver system above a layer of a porous medium.

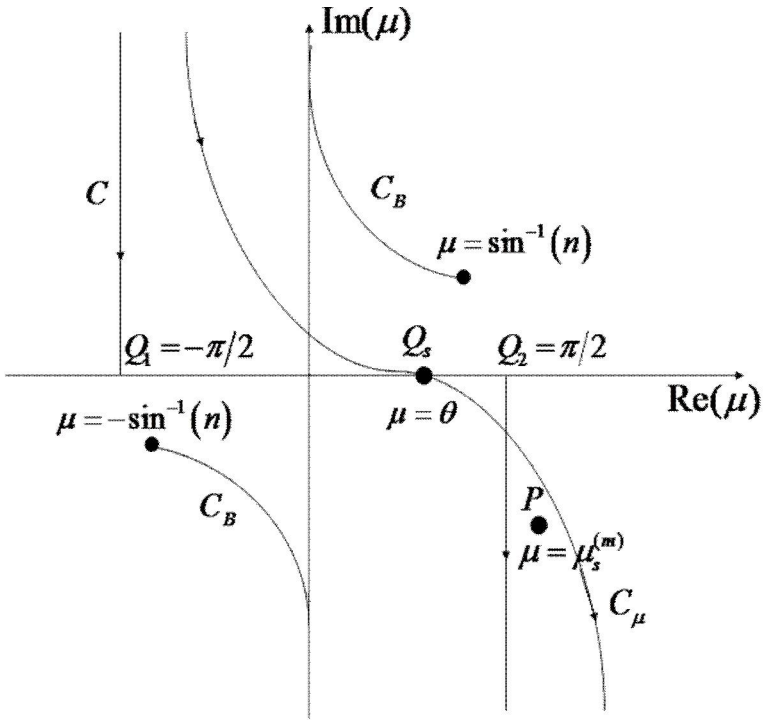

Figure 2.2: Illustration of the original integration path C and the steepest descent path Cμ.

The first and second terms of Eq. (2.1) are the sound fields due to the source and its image above a rigid ground with the respective distances of R_1 and R_2. The third term p_D is the diffraction of sound by the flat porous surface. It is dependent on the acoustical properties and the thickness of each layer of the porous medium. The diffraction term can be represented in an integral form as

$$p_D = \frac{-ik}{4\pi}\int_C \frac{\sin\mu G(\mu)\chi^{(m)}(\mu)}{\cos\mu+\chi^{(m)}(\mu)} e^{\Phi_a(\mu)} d\mu, \tag{2.2}$$

where the function $\chi^{(m)}(\mu)$ is referred as the total admittance of the flat interface where the superscript (m) is used to denote the type of media. The integration variable μ can be interpreted as a polar angle representing the incident angle of the reflected wave (measured from the vertical z-axis). The integration path C, shown in Figure 2.2, varies

from $-\pi/2+i\infty$ to $\pi/2-i\infty$ and passes through $-\pi/2$, the origin, the saddle point at θ and $\pi/2$ in the complex μ-plane. The saddle point is denoted as Q_s and the pertinent points at $-\pi/2$ and $\pi/2$, along C are marked, respectively as Q_1 and Q_2, see Figure. 2.2.

The oscillatory function, $\Phi_a(\mu)$, is given by

$$\Phi_a(\mu) = ikR_2\cos(\mu-\theta), \tag{2.3a}$$

and the variable $G(\mu)$ is a non-oscillatory term given by

$$G(\mu) = H_0^{(1)}\left(kr\sin\mu\right)e^{-ikr\sin\mu}. \tag{2.3b}$$

where $H_0^{(1)}$ is the zeroth order Hankel function of the first kind, r is the horizontal range between the source and receiver, and θ is the polar angle of the reflected wave given by

$$\theta = \tan^{-1}\left(\frac{z_s+z_r}{r}\right), \tag{2.4}$$

with z_s and z_r as the source and receiver heights. For a 'ground' with a layered structure, m = –2 is taken as a perfectly rigid surface, m = –1 as a locally reacting surface of specific normalized admittance β_1, m = 0 as a semi-infinite extended reaction porous medium. The extended reaction (either semi-infinite or layered) medium has complex density of ρ_1, complex sound speed of c_1 and complex propagation constant of k_1. With these notations for m, it is clear that the lower medium is non-locally reacting when $m \geq 0$.

Table 2.1: The total admittance and pole locations for different porous media.

m	Type of medium	Total Admittance, χ(m)(μ)	Pole location, $\cos\mu_p^{(m)}$
-2	Rigid	0	No pole
-1	Locally reacting	β1	– β1
0	Extended reaction	$\varsigma N = \varsigma\sqrt{n^2 - \sin^2\mu}$	$-\zeta\sqrt{\left(n^2-1\right)/\left(1-\zeta^2\right)}$
1	Hard-backed	$-i\zeta N\tan\left(kNd\right)$	No closed form solution
2	Impedance-backed	$\dfrac{\beta_2 - i\zeta N\tan\left(kNd\right)}{1 - i\beta_2\tan\left(kNd\right)/\zeta N}$	No closed form solution

Table 2.1 lists other types of non-locally reacting porous media and their respective total admittances that will be addressed in the analyses. In Table 2.1, the density ratio $\zeta\left(\equiv\rho/\rho_1\right)$, the index of refraction $n\left(\equiv c/c_1\right)$ and the specific normalized admittance β_2 for the second layer are used to characterize its acoustical properties. The variable N is used to denote the following function:

$$N\left(\mu\right) = \sqrt{n^2 - \sin^2\mu}\ , \tag{2.5}$$

which has been used in Table 2.1 for calculating the total admittance, $\chi^{(m)}\left(\mu\right)$. We also define the specific normalized characteristic admittance of the first layer by β_1 (= $n\zeta$).

Brekhovskikh [34] explained that there were two branch points for $N(\mu)$ denoted by $\pm\mu_B$ marked in Fig. 2.2. They are determined from Eq. (2.5) to give

$$\sin\mu_B = \pm n\ . \tag{2.6}$$

For the non-locally reacting ground ($m \geq 0$), the kernel function of Eq. (2.2) can have two values for each μ. As a result, a two-sheeted Riemann surface can be constructed where the upper sheet is defined as $\mathrm{Im}\{N(\mu)\} > 0$ and the lower sheet is identified by $\mathrm{Im}\{N(\mu)\} < 0$. The integration path for Eq. (2.2) resides in the upper sheet of this Riemann surface which implies that the positive root of $N(\mu)$, i.e. $N(\mu) = +\sqrt{n^2 - \sin^2\mu}$, is selected in computing $\chi^{(m)}(\mu)$ for the non-locally reacting medium. The contour around this branch cut is represented by C_B shown in Figure. 2.2.

The next step involves indenting the integration path from C to the steepest descent path C_μ which is defined in the complex μ-plane by

$$\cos(u-\theta)\cosh(v) = 1 \quad , \tag{2.7a}$$

where u and v are real numbers which represent the real and imaginary part of μ, i.e.

$$\mu = u + iv \, . \tag{2.7b}$$

The steepest descent path C_μ passes through the saddle point Q_s at $\mu = \theta$ as shown in Figure. 2.2. Attenborough et al [72] showed that C_B will not contribute to the closure between C and C_μ for all source/receiver geometries provided that Re(n) > 1. The known properties of outdoor ground surfaces and most sound absorption materials can readily meet this condition, i.e. Re(n) > 1. With this closure,

$$\int_C = \int_{C_\mu} + 2\pi i \, \mathrm{res}(K_P) \quad , \tag{2.8}$$

where $\mathrm{res}(K_P)$ is the residue from any poles within the closed contours, C and C_μ. Hence, the diffraction term given in Eq. (2.2) can be recast as,

$$p_D = \Psi + 2\pi i \,\mathrm{res}\left(K_P\right) \quad , \tag{2.9}$$

where the integral $\Psi(\mu)$ is defined by

$$\Psi = \frac{-ik}{4\pi} \int_{C_\mu} \frac{\sin\mu G(\mu)\chi^{(m)}(\mu)}{\cos\mu + \chi^{(m)}(\mu)} e^{\Phi_a(\mu)} d\mu \,, \tag{2.10}$$

and, $\mathrm{res}\left(K_P\right)$ in Eq. (2.9) can be determined straightforwardly by the calculus of residues if the pole locations, μ_p say, are known. The pole locations can be found by setting the denominator of the kernel function in Eq. (2.2) to zero, i.e.

$$\cos\mu + \chi^{(m)}(\mu) = 0 \quad . \tag{2.11}$$

Suppose $\mu_p^{(m)}$ is the solution of the above transcendental function which gives the information of the pole location in the complex μ-plane. The subscript p is used to denote the corresponding parameters at the pole location.

For the semi-infinite extended reaction ground, the pole locations can be determined by substituting $\chi^{(0)}(\mu) = \zeta N$ (see Table 2.1) in Eq. (2.11). Its solution can be expressed as a pair of trigonometric functions [72, 3]:

$$\cos\mu_p^{(m)} = \mp\chi^{(m)}\left(\mu_p\right) := \mp\chi_p^{(m)}, \tag{2.12a}$$

and

$$\sin\mu_p^{(m)} = \pm\sqrt{1-\left[\beta_p^{(m)}\right]^2} \,, \tag{2.12b}$$

where m = 0 and $\chi_p^{(m)}$ is known as the apparent admittance for the semi-infinite porous medium.

There is a total of 4 poles in the complex μ-plane because there are two branch points for N which appears in Eq. (2.11). Only two of these four poles are of interest in

the present study because they reside in the upper sheet of the Riemann surface. For the known properties of most outdoor ground surfaces and sound absorption materials, experimental data [94-96] suggest, firstly that the magnitude of the density ratio is small, i.e., $|\zeta| << 1$. Secondly, the sound speed in the porous media is faster than that in air and the porous media are dissipative, i.e. Re (n) > 1 and Im (n) > 0. Thirdly, the ground surfaces/porous media have a stiffness-type reactance, i.e. Im (β_1) < 0, Im (β_2), Im [$\chi_p^{(m)}$] < 0, where the parameter $\chi_p^{(m)}$ can be interpreted as the apparent admittance of the non-locally reacting porous medium. Consequently, these properties place a further restriction on the solution for Eq. (2.11) such that a finite number of poles are located near the integration paths C and C_μ for the non-locally porous medium.

In the case of the semi-infinite extended reaction medium, Attenborough et al [72] showed that there is only one pole which can be given in terms of the apparent admittance by

$$\chi_p^{(m)} = \zeta \sqrt{\left(n^2 - 1\right) \Big/ \left(1 - \zeta^2\right)} \quad . \tag{2.12c}$$

For hard-backed (m = 1) and impedance-backed (m = 2) porous media, Eq. (2.11) becomes

$$\cos\mu - i\zeta N \tan\left(kNd\right) = 0 \,, \tag{2.13a}$$

and

$$\cos\mu + \frac{\beta_2 - i\zeta N \tan\left(kNd\right)}{1 - i\beta_2 \tan\left(kNd\right)/\zeta N} = 0 \,, \tag{2.13b}$$

respectively. A careful assessment of these two equations indicates that the number of zeros is infinite because of the presence of the trigonometric term. Each of these poles is

associated with the free mode of a layered structure for m = 1 and 2. These extra modal contributions have led to a nonspecular reflection effect caused by the interaction of a light beam with an interface between two transparent media. This is often referred as a beam displacement phenomenon which was proved theoretically and verified experimentally by Goos and Hanchen [97] in the late 1940s. The analogous beam displacement effect can be observed in the propagation of acoustic waves: it was confirmed theoretically [98] and experimentally [99] in the 1950s for an ultrasonic ray incident on a liquid/solid interface.

In both situations mentioned above, the denominators of the respective kernel functions appeared in the diffraction integral [*cf* Eq. (2.2)] are more complicated than the equation shown in Eq. (2.11). The presence of these analogous modal poles has given rise to the extra contributions of the reflected fields due to the electromagnetic/acoustic beams. Detailed theoretical analyses of the bounded acoustic beams can be found in Sect. 14 of Ref. [34].

Here, the primary objective of the present study is to investigate the propagation of audio sound waves above a layered porous medium. A modified fluid approach with a complex sound speed and propagation constant [100] is used to model outdoor ground surfaces or a layer of sound absorption materials. Extensive experimental evidence and numerical analyses [89-92, 101, 102] have suggested that the modal poles for the layered porous medium are usually located far from the saddle point. Their contributions to the reflected sound fields are rather limited. Furthermore, Allard and his co-workers indicated that there was only one pole lying close to $\mu = \pi/2$ for a hard-backed porous layer. Experimental evidence [87] also supports the view that an impedance-backed

porous layer has the comparable property. In light of these studies, it is postulated that there is only one pole lying near the saddle that contributes significantly to the diffraction term.

One of the necessary conditions for the existence of the lateral waves is that the non-locally reacting porous medium has Re(n) < 1 [34, 103]. As a result, the lateral waves cannot be generated because Re(n) is normally greater than 1 for most outdoor ground surfaces and sound absorption materials. On the other hand, the leaky waves are difficult, if not impossible to detect in a porous medium with high damping losses [104]. In most outdoor ground surfaces and sound absorbing materials, the damping loss is indeed very high because Im(n) is generally much greater than 0. Hence, it is reasonable to further stipulate that neither lateral waves nor leaky waves will be excited for the propagation of the audio sound waves above a non-locally reacting porous medium in the present study.

With the exclusion of the poles due to (1) the free mode of a layered structure, (2) lateral waves, and (3) leaky waves, the contribution from the second term of Eq. (2.8) is therefore limited to the maximum of one pole only (marked as P shown in Figure. 2.2). It is often referred as the surface wave pole where its contribution can be determined by solving Eq. (2.11) for its root, see also Eqs. (2.13a) and (2.13b) for hard-backed and impedance-backed porous layers respectively. These transcendental equations cannot be solved analytically leading to a closed form solution but the pole location can be tracked numerically by a standard Newton-Raphson method [90, 91, 3]. The numerical details for solving Eq. (2.11) to obtain $\mu_p^{(m)}$ can be found elsewhere [3] and will not be repeated here. Substitutions of their values into Eqs. (2.12a) and (2.12b) give a unique numerical

parameter for the apparent admittance, $\chi_p^{(m)}$. It will then be used in Eqs. (2.9) and (2.10) to determine res (K_p) and Ψ respectively that furnishes a numerical solution for the diffraction wave term p_D in Eq. (2.9).

To facilitate the analysis, it is convenient to introduce a complex variable W that is related to μ by

$$W^2/2 = ikR_2 - \Phi_a(\mu)\,. \tag{2.14a}$$

Substitution of Eq. (2.3a) in Eq. (2.14a), application of differential calculus, and some algebraic manipulations furnish the following expression:

$$\frac{d\mu}{dW} = \frac{W}{ikR_2 \sin(\mu-\theta)} = \frac{1}{\sqrt{ikR_2 - W^2/4}}\,. \tag{2.14b}$$

Hence, change of the variable from μ to W in Eq. (2.10) leads to

$$\Psi = \frac{-ike^{ikR_2}}{4\pi} \int_{C_W} \Lambda^{(m)}(W) e^{-W^2/2} dW\,, \tag{2.15a}$$

where the kernel function $\Lambda^{(m)}(W)$ is given by

$$\Lambda^{(m)}(W) = \frac{\sin\mu G(\mu)\chi^{(m)}(\mu)}{\sqrt{ikR_2 - W^2/4}\left[\cos\mu + \chi^{(m)}(\mu)\right]}\quad, \tag{2.15b}$$

and μ in the above equation can be transformed to W according to Eq. (2.14a). The integration path in the complex W-plane, which is denoted as C_W, can also be determined by using Eq. (2.14a). This specific choice of W given in Eq. (2.14a) will become more apparent when the integral of Eq. (2.15a) is evaluated. It is possible to trace C_W by introducing the respective real and imaginary parts for W as follows:

$$W = X + iY\quad, \tag{2.16}$$

where X and Y are real variables. Making use of Eqs. (2.7b), (2.14a) and (2.16), we can then derive the corresponding expressions for X and Y in terms of u and v to confirm

$$XY/kR_2 = 1-\cos(u-\theta)\cosh v \quad , \tag{2.17a}$$

and

$$\frac{1}{2}\frac{Y^2-X^2}{kR_2} = \sin(u-\theta)\sinh v \, . \tag{2.17b}$$

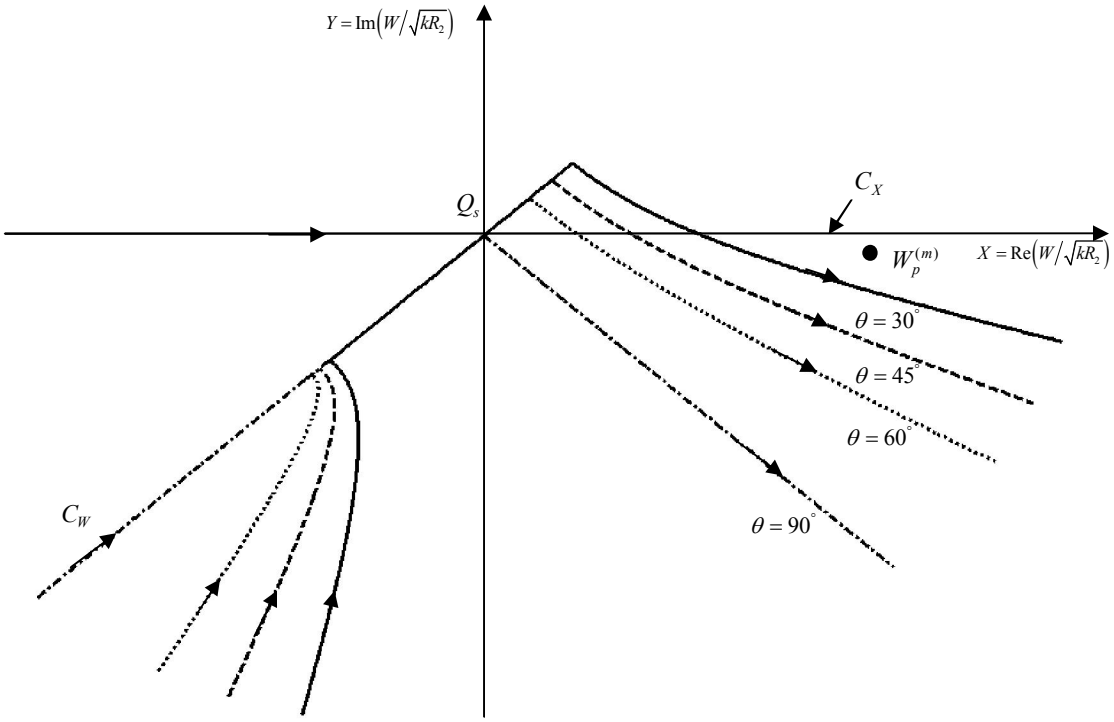

Figure 2.3: An illustration of the integration path C_W and the steepest descent path C_X in the complex W-plane for various angle of incidence, θ.

For a given path C in the μ-plane, X and Y can be determined by solving the above pair of non-linear simultaneous equations for C_W. Figure 2.3 shows the integration path for C_W in the complex W-plane for various incident angles of 30°, 45°, 60°, 90° respectively. Along the integration path C_W in the complex W-plane, the corresponding points (Q_1 and Q_2), can be determined from Eqs. (2.17a) and (2.17b) to give

$-\sqrt{kR_2(1+\sin\theta)}\,(1+i)$ and $\sqrt{kR_2(1-\sin\theta)}\,(1+i)$, respectively. The line joining Q_1 and Q_2 passes through the saddle point (Q_s) which is also the origin of the complex W-plane.

By obtaining the solution from Eq. (2.11) for the pole location in the μ-plane (i.e. $\mu_p^{(m)}$) and substituting it into Eq. (2.14a), we can readily determine the pole location in the W-plane. The pole location, which is denoted as $W_p^{(m)}$, can be expressed in terms of θ and $\chi_p^{(m)}$ as follows:

$$[W_p^{(m)}]^2/2 = ikR_2\left[1+\chi_p^{(m)}\cos\theta-\sqrt{1-[\chi_p^{(m)}]^2}\sin\theta\right] . \tag{2.18}$$

Because of the choice of W given in Eq. (2.14a), it is clear that the saddle path (marked as C_X in Fig. 2.3) that lies along the real axis of W can be identified, i.e., the exponential function exp ($-W^2$) has a constant phase along the path with $Y = 0$. This path corresponds to saddle path C_μ in the complex μ-plane shown in Figure. 2.2.

When the path is changed from C_W to W_X, the second term of Eq. (2.9) is the contribution from the pole $\mu_p^{(m)}$ if it is crossed. This term, which is known as the surface wave contribution, can be evaluated by the calculus of residues to yield

$$\mathrm{res}\left(K_P\right) = H\left\{-\mathrm{Im}\left(W_p^{(m)}\right)\right\}\frac{P^{(m)}}{2\pi i}, \tag{2.19a}$$

where H, which is the Heaviside step function with a real argument, is defined by

$$H\left(\bar{X}\right) = \begin{cases} 1 & \text{if } \bar{X} > 0 \\ 0 & \text{othereise} \end{cases}, \tag{2.19b}$$

the contribution from the pole, $P^{(m)}$, is determined by,

$$P^{(m)} = -\frac{k}{2}\frac{\chi_p^{(m)} H_0^{(1)}(kr\sin\mu_p^{(m)}) e^{ik(z_s+z_r)\cos\mu_p^{(m)}}}{E^{(m)}\left(\mu_p^{(m)}\right)}, \tag{2.19c}$$

with the denominator of the expression represented by,

$$E^{(m)}(\mu) = 1 - \frac{1}{\sin\mu}\frac{d}{d\mu}[\chi^{(m)}(\mu)]. \tag{2.19d}$$

In Eq. (2.19a), the argument of the Heaviside function is used to determine whether the pole has been crossed when the integration path has been indented. In other words, by deforming the path from C_W to C_X, the diffraction integral given in Eq. (2.11) can be recast as

$$p_D = \frac{-ike^{ikR_2}}{4\pi}\int_{-\infty}^{\infty}\Lambda^{(m)}(X)e^{-X^2/2}dX + H\left\{-\mathrm{Im}\left(W_p^{(m)}\right)\right\}P^{(m)}, \tag{2.20}$$

where W in the integrand of Eq. (15a) is set as X along the saddle path and $\Lambda^{(m)}(X)$ can be determined by Eq. (2.15b) with W replaced by X.

2.2.2 A Classical Asymptotic Solution by the Double Saddle-point Method

The double saddle-point method supplemented by the pole subtraction method is often used to approximate the integral of Eq. (2.20). This will then provide a closed form asymptotic expression for p_D. The details of the asymptotic analysis have been provided elsewhere [3]. A summary of the procedures and the final solution will be presented as follows. The first term of Eq. (2.20) may be approximated by replacing it with a reference integral in order to handle the singularity of the integrand more effectively. A correction term is then added to this approximate solution for improving its overall accuracy. This is also known as the pole subtraction method which is frequently found in numerical

quadratures for eliminating a removable singularity in an integrand [104]. In the present study, the reference integral, I_{ref}, is specified by

$$I_{ref} = -\left(\frac{ik}{4\pi}e^{ikR_2}\right)\times\left[\frac{\chi_p^{(m)}G\left(\mu_p\right)}{E^{(m)}\left(\mu_p\right)}\right]\times\int_{-\infty}^{\infty}\frac{e^{-X^2/2}}{X-W_p^{(m)}}dX\,, \tag{2.21a}$$

where $E_m \equiv E^{(m)}\left(\mu_p\right)$. Noting the integral representation of the scaled complementary error function, see Eq. (7.1.4) in Ref. [73], I_{ref} can be simplified to

$$I_{ref} = 2i\chi_p^{(m)}\sqrt{\pi}\sqrt{ikR_2/2}\,\frac{e^{-[w_p^{(m)}]^2}\operatorname{erfc}(-iw_p^{(m)})}{E_m\sqrt{\sin\theta\sin\mu_p^{(m)}}} - H\left\{-\operatorname{Im}\left(W_p^{(m)}\right)\right\}P^{(m)}, \tag{2.21b}$$

where erfc( ) is the complementary error function and $w_p^{(m)}$ is defined as

$$w_p^{(m)} = W_p^{(m)}\Big/\sqrt{2} = \sqrt{2ikR_2}\,\sin\left[(\mu_p^{(m)}-\theta)/2\right]. \tag{2.21c}$$

The term $w_p^{(m)}$ in Eq. (2.21b), which is referred as the numerical distance [3, 20, 71, 96], is customarily used to replace W_p in the complementary error function.

Together with the reference integral I_{ref} and a correction term ϕ_m, it is possible to write

$$I_{ref} + \phi_m = \frac{-ike^{ikR_2}}{4\pi}\int_{-\infty}^{\infty}\Lambda^{(m)}\left(X\right)e^{-X^2/2}dX \quad . \tag{2.22a}$$

Hence, ϕ_m can be obtained by rearranging Eq. (2.22a) and substituting Eq. (2.21a) into the resulting equation to yield

$$\phi_m = \frac{-ike^{ikR_2}}{4\pi}\int_{-\infty}^{\infty}\left[\Lambda^{(m)}\left(X\right) - \frac{\chi_p^{(m)}G\left(\mu_p\right)}{E_m[X-W_p^{(m)}]}\right]e^{-X^2/2}dX\,. \tag{2.22b}$$

Making use of Eq. (2.21b), the diffraction term in Eq. (2.20) can now be rewritten in terms of ϕ_m as

$$p_D = 2i\chi_p^{(m)}\sqrt{\pi}\sqrt{ikR_2/2}\,\frac{e^{-[w_p^{(m)}]^2}\,\mathrm{erfc}(-iw_p^{(m)})}{E_m\sqrt{\sin\theta\sin\mu_p^{(m)}}} + \phi_m \quad . \tag{2.23}$$

It is remarkable that the Heaviside step function terms shown in Eqs. (2.20) and (2.21b) have the same magnitude but of opposite signs. Their sum leads the cancellation of this term in Eq. (2.23). It is, somewhat, surprising to note that the surface wave term appear to 'vanish' in the final expression. But a close scrutiny of the first term of Eq. (2.23) indicates that the contribution from the surface wave pole is actually present implicitly in the complementary error function term. Hence, the surface wave will still be excited if $\mathrm{Im}\left(W_p^{(m)}\right) < 0$. Attenborough and his co-workers [20, 96] discussed the region in the upper medium (air) where surface wave may be observed for a given acoustical property of a locally reacting ground surface. The same analysis will not be repeated here for brevity.

The substitution of Eq. (2.23) into Eq. (2.1) and manipulation with the resulting expression provide an analytical solution for approximating the total fields above a non-locally reacting porous medium:

$$p = \frac{e^{ikR_1}}{4\pi R_1} + \frac{e^{ikR_2}}{4\pi R_2} + 2i\chi_p^{(m)}\sqrt{\pi}\sqrt{ikR_2/2}\,\frac{e^{-[w_p^{(m)}]^2}\,\mathrm{erfc}(-iw_p^{(m)})}{E_m\sqrt{\sin\theta\sin\mu_p^{(m)}}} + \phi_m\,, \tag{2.24a}$$

where ϕ_m [the integral in Eq. (22b)] can be computed numerically along the steepest descents path by using a Gaussian quadrature [35]. Alternatively, it can also be approximated asymptotically for the two terms in the square bracket. Details for the derivations of ϕ_m with different types of ground can be found in Ref. [8]. The asymptotic solution is given below:

$$\phi_m \approx \frac{e^{ikR_2}}{2\pi R_2}\left[\frac{\chi_p^{(m)}\Big/\left(E_m\sqrt{\sin\theta\sin\mu_p^{(m)}}\right)}{\sqrt{2[1-\cos(\mu_p^{(m)}-\theta)]}}-\frac{\chi_\theta^{(m)}}{\cos\theta+\chi_\theta^{(m)}}\right], \tag{2.24b}$$

where the effective admittance $\chi_\theta^{(m)}$ and the apparent admittance $\chi_p^{(m)}$ are defined, respectively, by

$$\chi_\theta^{(m)} \equiv \chi^{(m)}(\mu)\Big|_{\mu=\theta}, \tag{2.24c}$$

and

$$\chi_p^{(m)} \equiv \chi^{(m)}(\mu)\Big|_{\mu=\mu_p}, \tag{2.24d}$$

with $\chi^{(m)}(\mu)$ given in Table 2.1 for different types of ground surfaces. These two admittances can be calculated straightforwardly.

For a locally reacting ground (m = –1), it is noteworthy that three valuable approximations [71] may be made:

(i) $$\sqrt{\sin\theta\sin\mu_p^{(m)}} \approx 1, \tag{2.25a}$$

(ii) $$w_p^{(m)} \approx \sqrt{ikR_2/2}\left[\cos\theta+\beta_2\right], \tag{2.25b}$$

(iii) $$\phi_m \approx 0 \tag{2.25c}$$

where these assumptions are valid for near grazing propagation of sound waves above a relatively hard ‘ground’. With these approximations, Eq. (2.24) can be simplified to the well-known Weyl-Van der Pol formula [11] as follows:

$$p = \frac{e^{ikR_1}}{4\pi R_1}+\left[V_\theta+\left(1-V_\theta\right)F(w_p^{(m)})\right]\frac{e^{ikR_2}}{4\pi R_2}, \tag{2.26}$$

where V_θ is often referred as the plane-wave reflection coefficient specified by

$$V_\theta = \frac{\cos\theta - \beta_2}{\cos\theta + \beta_2}, \tag{2.27}$$

$w_p^{(m)}$ is the numerical distance defined by Eq. (2.24b) and $F(w_p^{(m)})$ is recognized as the boundary loss factor:

$$F(w_p^{(m)}) = 1 + i\sqrt{\pi} w_p^{(m)} e^{-[w_p^{(m)}]^2} \operatorname{erfc}\left(-i w_p^{(m)}\right) \quad . \tag{2.28}$$

This approximate expression avoids the apparent singularity when $\theta \to 0$ and/or $\beta_2 \to 0$ at the expenses that the prediction of the diffraction wave term becomes inaccurate when the source is very close to the receiver. However, it is a less important issue because the near field sound pressure is normally dominated the first two terms of Eq. (2.1). Hence, Eq. (2.26) gives accurate predictions of the total sound fields above a locally reacting ground for all ranges.

Extensive numerical and experimental analyses [3, 89-92, 87, 100-102] have revealed that the approximations suggested in Eq. (2.25a) – (2.25c) are not suitable for predicting the sound fields above a non-locally reacting medium. In this case, all terms in Eq. (2.24) are needed in order to obtain an accurate prediction of the sound fields for kR_2 greater than about 1 [3]. It is apparent from Eq. (2.24) that the formula is unbounded when $\theta \to 0$, i.e. the receiver lies directly above and below the receiver. Equation (2.24) also becomes singular when $\beta_p^{(m)} \to 0$, i.e. for a very soft 'ground'.

An in-depth analysis may be conducted to remove the above restrictions but these apparent singularities render Eq. (2.24) to be inconvenient to use for a more general application. As a result, an objective of the present study is to develop an alternative asymptotic formula that will preserve the form of the solution given in Eq. (2.26). More

importantly, the improved formulation will be applicable at all ranges for predicting the sound fields above the non-locally reacting porous medium.

2.2.3 An Improved Asymptotic Solution – a Modified Saddle-point Method

In this section, a modified saddle-point method [83, 71] is exploited for deriving a uniform asymptotic solution for the diffraction wave term that is free from singularities. This asymptotic method starts by expanding $\Lambda^{(m)}(W)$ about the saddle-point $W = 0$. A direct Taylor's expansion is not uniformly valid because the radius of convergence vanishes when $|\chi^{(m)}| \to 0$ and $\theta \to \pi/2$. It is sought to replace $\Lambda^{(m)}(W)$ by $\Gamma^{(m)}(W)$ where

$$\Gamma^{(m)}(W) = \left(W^2 - [W_p^{(m)}]^2\right)\Lambda^{(m)}(W), \tag{2.29}$$

Thus, the Taylor expansion may be applied for $\Gamma^{(m)}(W)$ around the saddle-point to confirm

$$\Gamma^{(m)}(W) = \sum_{j=0}^{\infty} \frac{\partial_j \Gamma^{(m)}}{j!} W^j \tag{2.30a}$$

where

$$\partial_j \Gamma^{(m)} = \frac{d^j}{dW^j} \Gamma^m(W)\bigg|_{W=0}. \tag{2.30b}$$

It is important to re-emphasize an important point as follows. Experimental and numerical evidence have suggested that there is only one pole located in the vicinity of the saddle point at $W = 0$. Other poles are located further away from the saddle point that causes $\Gamma^m(W)$ to be an entire function in the vicinity of the saddle-point and the pole location in the W-plane. This function, can therefore be expanded in a Taylor series given

by Eq. (2.30a) where the first few terms of the series are finite and bounded in most, if not, all situations for the non-locally medium. This is a vital assumption because only a handful of leading terms are typical needed in most asymptotic analyses. It is also notable that the choice of the form given in Eq. (2.29) enables the provision of a rigorous error bound of the asymptotic analysis [86].

The determination of $\Gamma^m(W)$, $\partial_j \Gamma^{(m)}$ and the subsequent derivation of the asymptotic formulas will be provided in Appendix A for clarity and completeness. We only provide the final solution below for succinctness. Replacing $\Lambda^{(m)}\left(W\right)$ with its Taylor series, integrating terms by terms and combining the Heaviside step function term, p_D in Eq. (2.20) can be expressed in the following form:

$$p_D = \frac{ke^{ikR_2}}{4} \sum_{j=0}^{J} \frac{\partial_{2j} \Gamma^{(m)}}{j!(-4)^j} I_j\left(-iw_p^{(m)}\right) + B_{J+1} \quad , \tag{2.31}$$

where the integral series $I_j(z)$ is given by Eqs. (A13) and (A14) and an error term, $B_{J+1,}$ has been added explicitly in Eq. (2.31). It is based on Ref. [86] where the modified saddle-point method has been used to obtain an asymptotic formula for the sound field above a locally reacting surface due to a line source. It has been shown that the magnitude of the error term, $|B_{J+1}|$, is bounded and has an order proportional to $(kR_2)^{-(J+3/2)}$. Note also that he explicit contributions from the surface wave pole have been cancelled out exactly by the second term of the square bracket of Eq. (A10). These surface wave pole contributions are absorbed implicitly in I_j given in the series of Eq. (2.31). This condition is not identified by Kawai et al [85] and Chandler-Wilde and Hothersall [86] in their discussions of the relevant problems.

Retaining the first two terms in the series, i.e., J is set to 1 in Eq. (2.31), substituting Eq. (2.15b) into Eq. (2.29), obtaining $\Gamma^{(m)}(W)$ and its second derivative at $W = 0$ from Eqs. (A2), (A3), and (A4) – (A6), replacing the Hankel function with its asymptotic approximation:

$$H_0^{(1)}(z) \approx \left(\frac{2}{i\pi z}\right)^{\frac{1}{2}} e^{iz} \quad , \tag{2.32}$$

and simplifying the resulting algebraic expression, we can confirm an asymptotic formula for p_D as

$$p_D = \frac{-\chi_\theta^{(m)}}{\cos\theta + \chi_\theta^{(m)}} \frac{e^{ikR_2}}{2\pi R_2} \left\{1 - A^{(m)} F\left(w_p^{(m)}\right)\right\} + B_2 , \tag{2.33a}$$

where $A^{(m)}$ can be treated as augmented diffraction factor

$$A^{(m)} = b^{(m)} \left[w_p^{(m)} \Big/ \sqrt{ikR_2} \right]^2 . \tag{2.33b}$$

and $b^{(m)}$ in Eq. (2.33b) is defined in Eq. (A4) in Appendix A, $F(w_p^{(m)})$ is referred as the boundary loss factor given by Eq. (2.28) and $|B_2|$ is the error bound of the approximation which has an order of $(kR_2)^{-5/2}$.

From Table 2.1, we have $\chi^{(m)} = \beta_1$ for a locally reacting surface, i.e. $m = -1$. Hence, it is possible to show that

$$b^{(m)} \approx \frac{2\left(1 + \beta_1 \cos\theta\right)}{\left(\cos\theta + \beta_1\right)^2}, \tag{2.34}$$

where the details of its derivation are given in Appendix B. Substitution of Eq. (2.34) into Eq. (2.33a) leads to an asymptotic formula for calculating the diffraction wave term

above a locally reacting surface. This expression is identical to that derived by Kawai et al. [85].

It is now possible to obtain the asymptotic formulas for computing the diffraction wave terms for different types of non-locally reacting porous media, with m = 0 for an extended reaction medium, m = 1 for a hard-backed layer and m = 2 for an impedance-backed layer. However, the expressions for $b^{(m)}$ become increasingly more complicated as m increases. The details of these expressions are demoted to Appendix B for information. The sound field above an interface, either locally reacting or non-locally reacting, can be derived by substituting Eq. (2.33a) into Eq. (2.1) to yield

$$p = \frac{e^{ikR_1}}{4\pi R_1} + Q^{(m)} \frac{e^{ikR_2}}{4\pi R_2} + B_2, \tag{2.35}$$

where the last term of Eq. (2.35), B_2, is the error bound of the asymptotic formula that has an order of $(kR_2)^{-5/2}$, see Eq. (2.31). The parameter, $Q^{(m)}$, is the spherical-wave reflection coefficient given by

$$Q^{(m)} = V_\theta^{(m)} + \left(1 - V_\theta^{(m)}\right)\left\{b^{(m)}\left[w_p^{(m)} \Big/ \sqrt{ikR_2}\right]^2\right\} F(w_p^{(m)}), \tag{2.36a}$$

$V_\theta^{(m)}$ is referred as the plane-wave reflection coefficient specified by

$$V_\theta^{(m)} = \frac{\cos\theta - \beta_\theta^{(m)}}{\cos\theta + \beta_\theta^{(m)}}, \tag{2.36b}$$

$\beta_\theta^{(m)}$, which is known as the effective admittance of the medium [30], is determined by using Eq. (2.24c), $w_\theta^{(m)}$ is the numerical distance defined by Eq. (2.18), and $F(w_p^{(m)})$ is the boundary loss factor that can be calculated by using Eq. (2.28).

Equation (2.35) supplies an asymptotic formula for predicting the sound fields above a non-locally reacting porous medium. It is expressed in a closed form that can be used to compute the sound fields readily by using standard mathematical functions available in many commercial software packages.

2.3 Comparisons and Validation of the Asymptotic Formulas

In the last section 2.2, the modified saddle-point approach has been used to derive the asymptotic formula for the sound fields above a layered porous medium. In summary, the asymptotic method leads to an analogous expression for the total sound field above a layered medium. It can be approximated asymptotically as

$$p \approx \frac{e^{ikR_1}}{4\pi R_1} + \left[V_\theta^{(m)} + \left(1 - V_\theta^{(m)}\right) A^{(m)} F\left(w_p^{(m)}\right) \right] \frac{e^{ikR_2}}{4\pi R_2} \quad , \tag{2.37}$$

where the augmented diffraction factor $A^{(m)}$ is given in Eq. (2.33b). Comparing Eq. (2.37) with Eq. (2.26), it is apparent that the expression for predicting the sound fields above a non-locally reacting porous medium can be written in the classical Weyl-Van der Pol form. Its error bound has an order of $(kR_2)^{-5/2}$. The form of the solution given in Eq. (2.37) has not been identified in previous publication [85, 83] when the modified saddle-point was applied to derive an asymptotic solution of the related problems.

An examination of Eq. (2.37) indicates that the first term is the direct wave contribution. The second term is the contribution from ground reflected waves which consists of two components as shown in the square bracket of Eq. (2.37). Its first component is the plane wave reflection term where effective admittance of the non-locally medium, $\beta_\theta^{(m)}$ is used in the plane wave reflection coefficient. The second term of

the square bracket has been referred as the *ground wave*, which is comparable to the theory of AM radio reception. Note also that the presence of the $A^{(m)}$ in the ground wave term. More interestingly, the ground wave term consists implicitly a surface wave component and its detail discussions can be found in Refs. [20, 96].

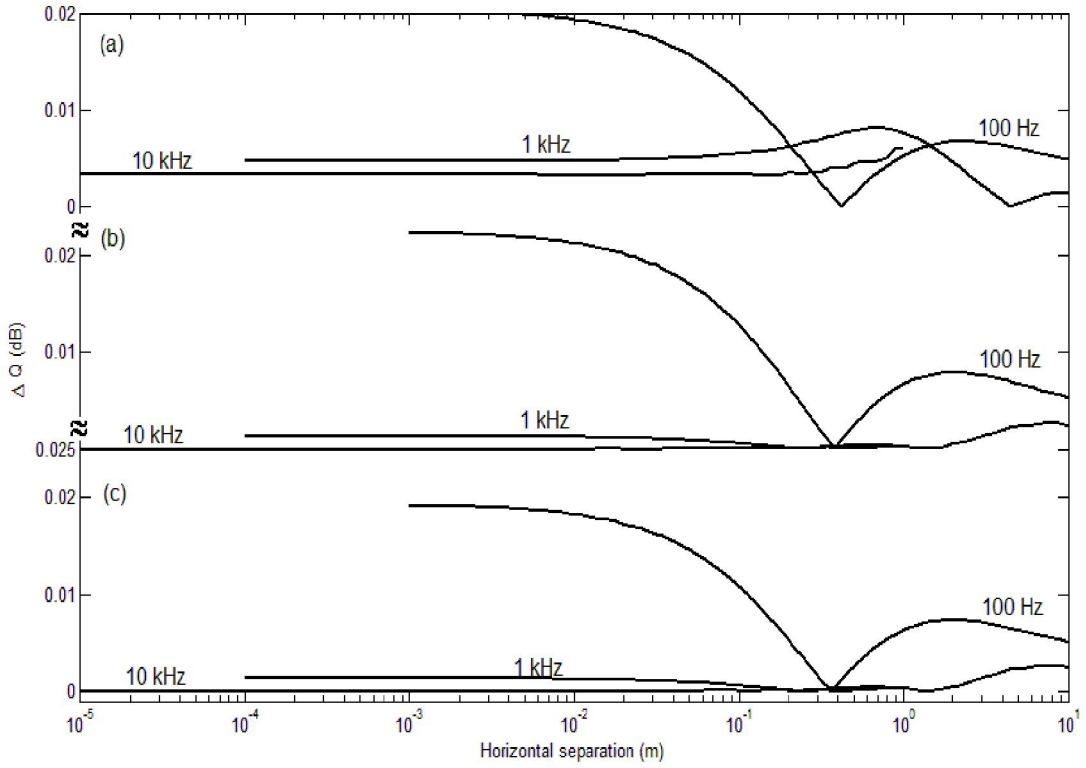

Figure 2.4: A comparison of solutions with ΔQ versus horizontal separation. (a): extended reaction porous medium, (b): hard-backed layer, (c): impedance-backed layer. The thickness of the hard and impedance layers is 0.05 m. The impedance-backed plane is with an effective flow resistivity of 300 kPa s m^{-2}. The Miki empirical model was used for the porous layer with the effective flow resistivity of 80 kPa s m^{-2}, tortuosity of 1.1, and porosity of 0.9.

For the present study, we are interested to validate the accuracy of Eq. (2.37) for different types of non-locally reacting grounds. Indeed, it is particularly convenient to show a direct comparison of the numerical results according to the asymptotic formula with those predicted by the accurate wave-based solution. The wave-based solution is developed as a combination of the fast field program (FFP) for the far-field solutions and

a direct numerical integration approach in the wavenumber domain for the near-field solutions. This hybrid approach is referred as the integrated exact solution (IES), the details of which is provided in Ref. [1] and will not be duplicated here.

To enable prediction of sound fields above a non-locally reacting porous medium, the Miki empirical model [14] is used to describe its acoustical characteristic. The index of refraction (propagation constant) and density ratio of a rigid porous medium can be determined as follows:

$$n = q\left[1 + 0.109(\sigma_e / f)^{0.618} + 0.160i(\sigma_e / f)^{0.618}\right], \tag{2.38a}$$

and

$$\zeta = \frac{\Omega\left[1 + 0.07(\sigma_e / f)^{0.632} + 0.107i(\sigma_e / f)^{0.632}\right]^{-1}}{q^2\left[1 + 0.109(\sigma_e / f)^{0.618} + 0.160i(\sigma_e / f)^{0.618}\right]}, \tag{2.38b}$$

where q is tortuosity, Ω is the porosity, and σ_e is the effective flow resistivity of the porous medium. Substituting Eqs. (2.38a) and (2.38b) into Eq. (2.12c), an analytical expression to calculate $\chi_p^{(m)}$ for the semi-infinite rigid porous medium can be obtained. On the other hand, use of them in Eqs. (2.13a) and (2.13b) can lead the numerical solutions of $\chi_p^{(m)}$ for the respective rigid porous layers.

Since the total sound field above a layered porous medium is dependent on $Q^{(m)}$, it is more illustrative to compare the asymptotic solution for $Q^{(m)}$ with the respective numerical solution obtained by the IES. Preliminary calculations indicate that the accuracy of $Q^{(m)}$ is dependent on the source and receiver heights. Its agreement with IES is excellent in all cases except when both the source and receiver are very close the interface and are separated at a small horizontal distance. To highlight the accuracy of the

modified saddle-point asymptotic solution, the source height is chosen as 0.2 m and the receiver height as 0.3 m above the layered porous medium in the following figure. Defining $\Delta Q^{(m)}$ as the logarithmic ratio of the IES and the asymptotic solution:

$$\Delta Q^{(m)} = 10\log_{10}\left[\frac{\left(Q^{(m)}\right)_{\text{IES}}}{\left(Q^{(m)}\right)_{\text{MSP}}}\right] \quad , \tag{2.39}$$

we show their comparisons in Figure 2.4 where the source is placed 0.2 m above a porous medium.

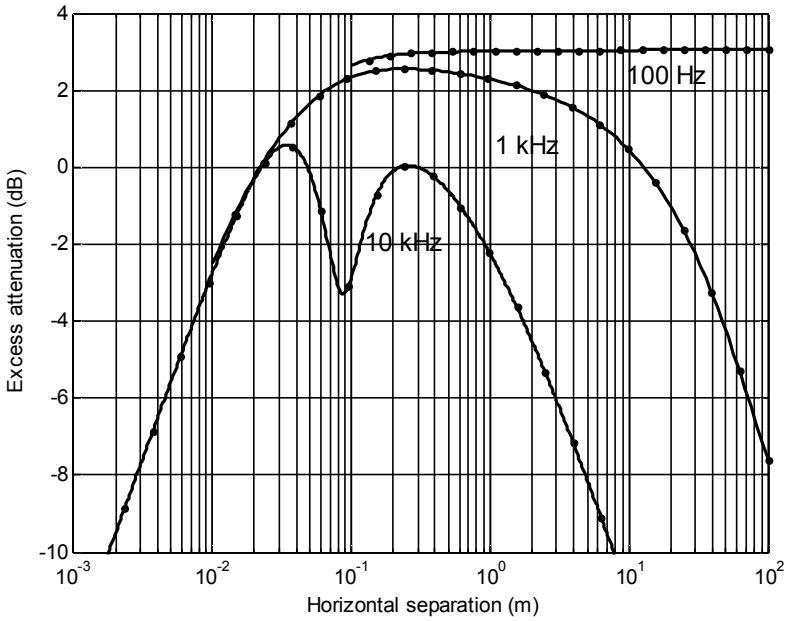

Figure 2.5: The Excess Attenuation (EA) versus horizontal separation for the receiver located at 0.02 m and source at 0.04 m above the interface. The Miki empirical model was used for the porous layer with the effective flow resistivity of 50 kPa s m^{-2}, tortuosity of 1.1, and porosity of 0.9. Solid line: modified saddle-point; circles: Integrated Exact Solution (IES).

Figure 2.4 displays three plots of $\Delta Q^{(m)}$ versus the horizontal range for low, mid, and high frequencies at 100 Hz, 1 kHz, and 10 kHz, respectively for all three different types of non-locally reacting porous media. At such low source/receiver heights (0.2 m and 0.3 m, respectively), the agreement of the modified saddle-point solutions with IES

are excellent when the horizontal range r is greater than about 0.3 m. This has been illustrated by the fact that the predicted $\Delta Q^{(m)}$ are very close to zero when $r \geq 0.3$ m. Numerical simulations (not presented here for brevity) indicate that these agreements are generally better at a shorter range when either the source or receiver is elevated from the layered medium. Nevertheless, the predictions according to the method start to deviate from that predicted by the IES if the source and receiver get closer (i.e., $\theta \to 0$). This apparent inaccuracy is reflected by the fact that when $\theta \to 0$ and at the same horizontal range, $\Delta Q^{(m)}$ is generally smaller for a higher source frequency. This is due to the fact that the error bound of the asymptotic analysis is given by B_2, which has a magnitude proportional to $(kR_2)^{-5/2}$.

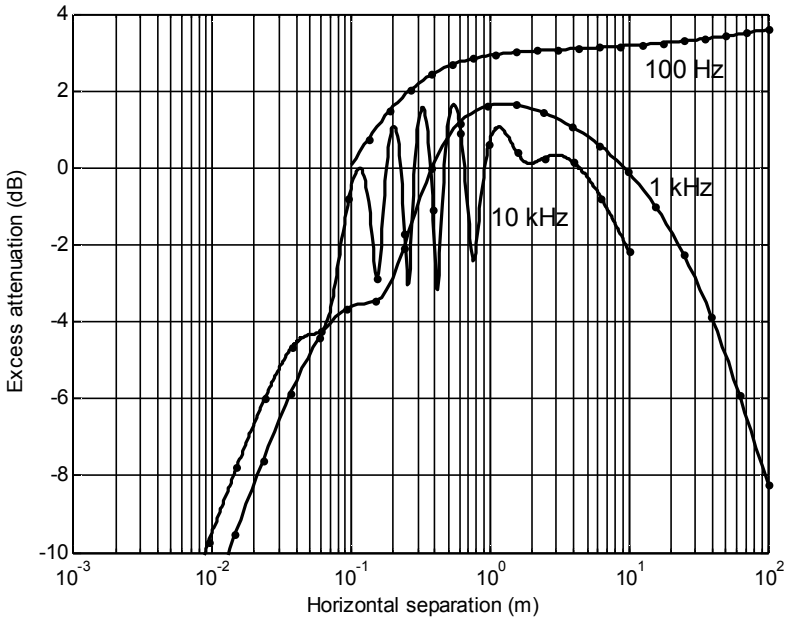

Figure 2.6: Same as Fig. 2.5 except for a hard-backed layer, which has the same properties but it has a layer thickness of 0.05 m. The receiver is located at 0.1 m, and the source is at 0.2 m above the interface.

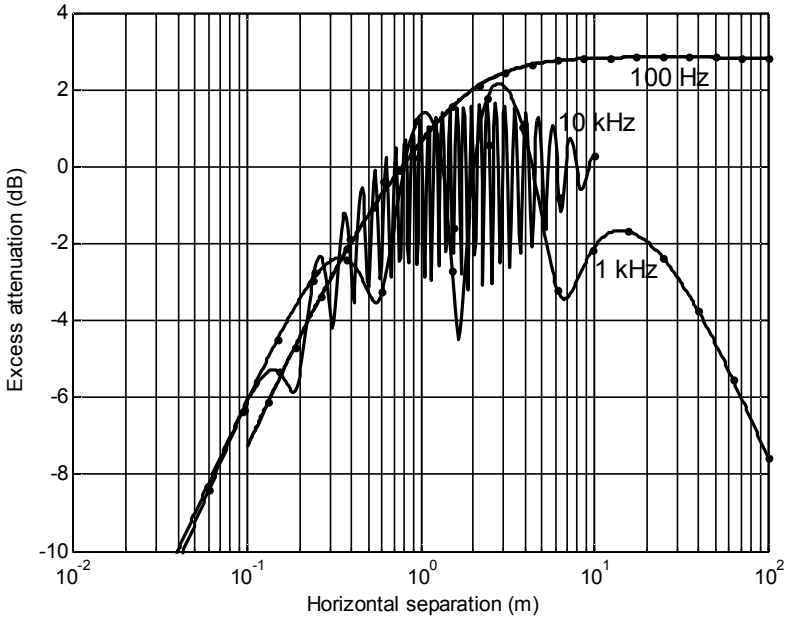

Figure 2.7: Same as Fig. 2.5 except for an impedance-backed layer, which has the same properties with a layer thickness of 0.05 m and with an effective flow resistivity of 300 kPa s m^{-2} at the impedance plane. Here, the receiver is located at 0.5 m and the source is at 1 m above the interface.

This level of accuracy for calculating $Q^{(m)}$ guarantees that the prediction of the total sound fields is excellent for all types of non-locally reacting porous media discussed in the present study. Figures 2.5 to 2.7 show the plots of an EA function against the horizontal range for an extended reaction porous medium, a hard-backed layer and an impedance-backed layer, respectively. Here, in these figures, *EA* is defined as

$$EA = 10\log_{10}\left[\frac{p}{e^{ikr}/4\pi r}\right]. \tag{2.40}$$

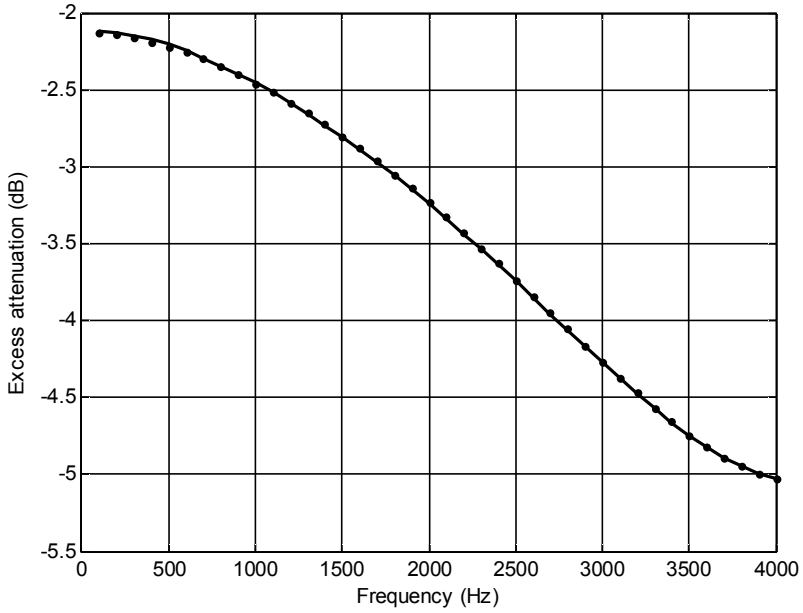

Figure 2.8: The Excess Attenuation (EA) versus the frequency for the receiver located at 0.02 m and source at 0.04 m above the interface. The Miki empirical model was used for the porous layer with the effective flow resistivity of 80 kPa s m^{-2}, tortuosity of 1.1, and porosity of 0.9. Solid line: modified saddle-point; circles: Integrated Exact Solution (IES). The horizontal separation is set to be 0.01 m.

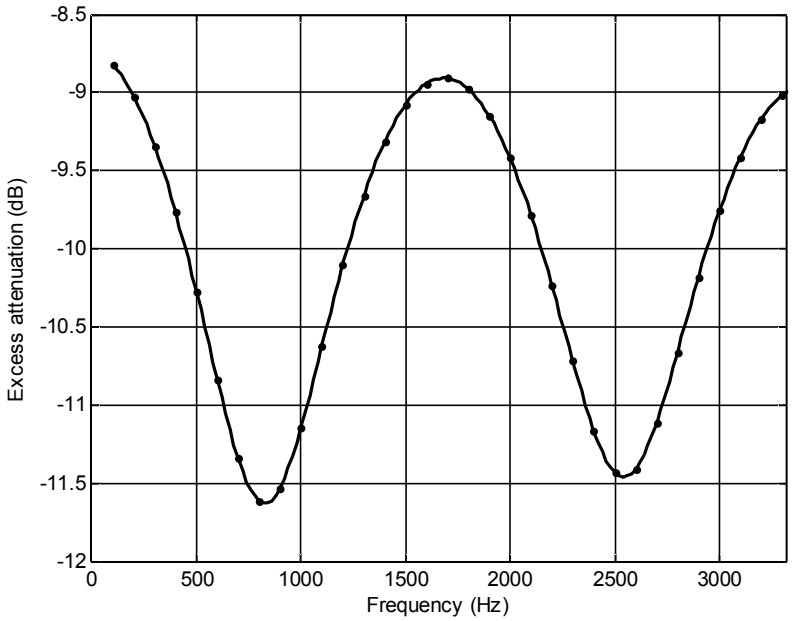

Figure 2.9: Same as Fig. 2.6 except for a hard-backed layer, which has the same properties but it has a layer thickness of 0.05 m. The receiver is located at 0.1 m and the source is at 0.2 m above the surface.

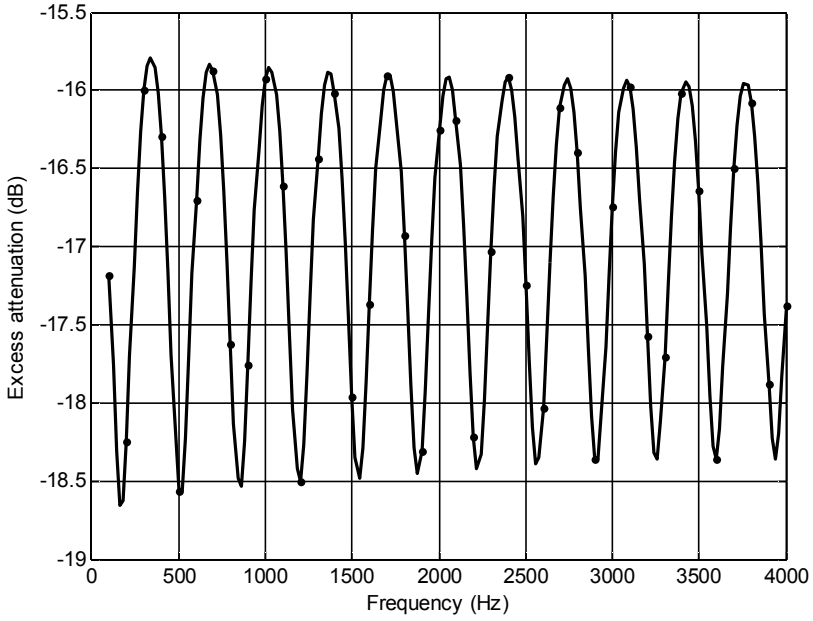

Figure 2.10: Same as Fig. 2.6 except for an impedance-backed layer, which has the same properties but it has a layer thickness of 0.05 m and with an effective flow resistivity of 300 kPa s m^{-2} at the impedance plane. Here, the source is located at 0.5 m and the receiver is at 1 m above the interface.

In addition, the same acoustic parameters as in Figure 4 are used to prepare the graphs. In Figs. 2.8 to 2.10, the *EA* spectra are presented where the same acoustic parameters as Figs. 2.5–2.7 are used. However, the source/receiver geometries are different in these figures for a wide range of conditions for small kR_2 (see captions of each figure for these geometrical configurations). All these numerical results confirm that the numerical solutions according to the method agree very well with the IES that provide validations of the asymptotic formula given in Eq. (2.37).

2.4 Summary

In this chapter, an analytical closed-form solution for the sound field above a non-locally reacting porous medium was derived. It was demonstrated that the approximate

solution could be expressed in the classical Weyl-Van der Pol form consisting of a direct wave term and a ground-reflected wave term. The second term consists of a spherical-wave reflection coefficient where it can further be represented by a plane-wave reflection and the ground wave terms. An augmented diffraction term is needed to model different types of non-locally reacting porous surfaces. An earlier study has suggested that the absolute error of the asymptotic solution is bounded by a factor proportional to kR_2 where k is the wavenumber of the incident sound wave and R_2 is the geometrical distance measured from the image source to the receiver. The modified saddle-point method provides a uniform asymptotic expression for the sound field above the non-locally reacting porous medium for all receiver locations. The formula should find its application in the acoustical characterization of sound absorption materials from the measurements of the total sound field at near-grazing propagation.

CHAPTER 3: A MODIFIED SADDLE POINT METHOD FOR SOUND PENETRATION INTO A RIGID POROUS HALF-PLANE

3.1 Introduction

In recent years, porous materials have increasingly been used in conjunction with a complex structure in support of sound absorption and sound insulation for passive noise control in enclosures. They have found applications in the automotive and aerospace industries, buildings, and many types of industrial machinery. Many numerical tools have been developed to assist the design of porous materials coupled with the strategic use of multilayer structures and cavities [106-109].

The information on the acoustical characteristics of sound absorption materials has different levels of complexity depending on the models used in the analysis [106]. It varies from the most sophisticated poroelastic model based on Biot theory [110,111] to the simplest locally reacting impedance model. A commonly used model assumes the modified fluid approach where the frame of the porous material is motionless, i.e., a rigid porous medium. This model as well as the Biot model has an advantage in that the visco-inertial and thermal dissipations can be modeled in the system. The acoustic and non-acoustic (microscopic) properties of the porous materials are needed; these may be determined by an inversion method where the properties are adjusted in the model to

match the acoustic measurement results. Most of these inverse methods [79, 80] are based on impedance tube measurements where only the macroscopic acoustic parameters at normal incidence can be determined.

It is well known that the microscopic properties of the porous materials are dependent only on the geometry in the local scale of the micro-structural parameters [112]. It will be useful to deduce these macroscopic parameters from the measurement of sound fields at the near-grazing propagation both above and within the rigid materials [81]. An accurate computation of sound fields above and below the rigid porous material is therefore needed. To this end, an accurate and efficient Green's function is frequently needed for use in many boundary element methods for calculating the sound field scattered by buried objects [76].

Li and Liu [1] obtained an asymptotic solution for the sound penetration into the rigid porous ground by a double saddle-point method. They used the pole subtraction method to improve the accuracy of the asymptotic solution when the pole lies close to the saddle point. However, their solution has an irremovable singularity when the source is directly above (or below) the observer. In chapter 2, a modified saddle-point method is applied to predict the sound field above a non-locally reacting porous medium. In this chapter, the modified saddle-point method is further exploited to study sound penetration into a rigid porous half-plane. The asymptotic solution based on the modified saddle-point method is compared with numerical solutions, and good agreement validates its accuracy, which is presented in section 3.3. A summary is given in section 3.4.

3.2 Theoretical Formulation

Suppose an airborne source is placed above a porous half-plane where the upper medium is air with density ρ and sound speed c. The lower medium is a porous half-space with complex density ρ_1 and sound speed c_1. The interface between the air and the porous half-plane is located at the $z = 0$ plane. Figure 3.1a shows a schematic diagram of the problem. It is useful to define the respective ratio of densities and sound speeds as

$$\zeta = \rho / \rho_1 \text{ and } n = c / c_1 . \tag{3.1a, b}$$

Starting from the respective Helmholtz equation for the upper and lower media, Li and Liu [1] showed that the sound penetration into the porous half-space can be written in an integral form in terms of the horizontal propagation wave vector κ where

$$\kappa = k \sin \mu , \tag{3.1c}$$

k is the wave number of the monochromatic sound and μ is the angle of angle of incidence of all possible plane waves transmitted from the air in the upper medium to the rigid porous medium in the lower medium. Using μ in favor of κ, the integral expression for sound penetration into the porous medium can be simplified as follows [15, 18]:

$$p_1 = \frac{ik}{4\pi} \int_C \frac{\cos\mu \sin\mu G(\mu)}{\cos\mu + \chi(\mu)} e^{\Phi_b(\mu)} d\mu , \tag{3.2}$$

where $\chi(\mu)$ is the apparent admittance of the porous half-space which is given by

$$\chi(\mu) = \varsigma N(\mu) , \tag{3.3}$$

the function N is defined as

$$N(\mu) = \sqrt{n^2 - \sin^2 \mu} = n \cos \mu_1 , \tag{3.4}$$

and μ_1 can be interpreted as the refracted angle of the transmitted wave. The angle of incidence μ and the angle of refraction μ_1 are measured from the positive z-axis. These two polar angles of plane waves are related according to Snell's Law, i.e., $\sin\mu = n\sin\mu_1$.

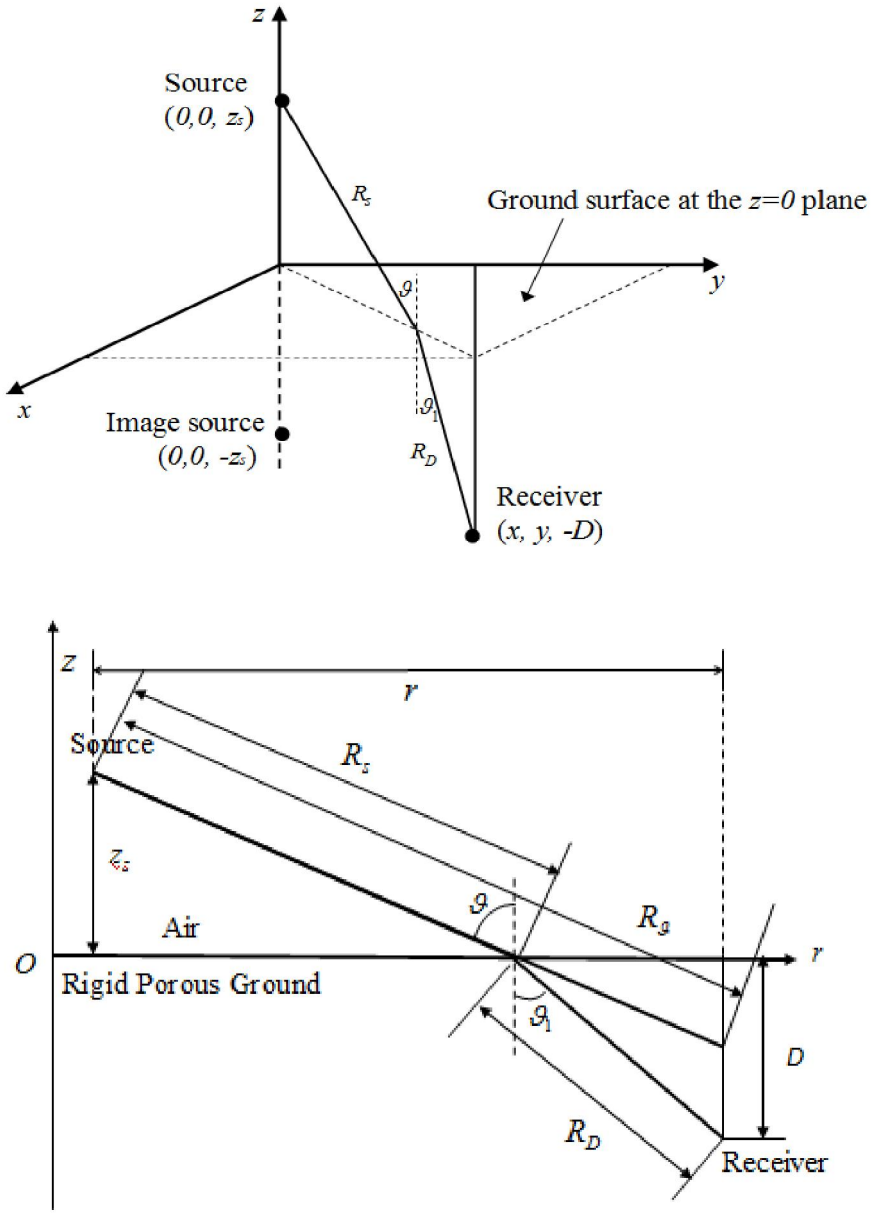

Figure 3.1: (a) A schematic diagram of the problem when the source is located above the porous medium, but the receiver is located below the rigid porous medium. (b) An illustration of different geometrical parameters used in the theoretical formulation.

The non-oscillatory term $G(\mu)$ in Eq. (3.2) is expressed in terms of the zeroth-order Hankel function of the first kind, $H_0^{(1)}$, as

$$G(\mu) = H_0^{(1)}\left(kr\sin\mu\right)e^{-ikr\sin\mu}, \tag{3.5}$$

where r is the horizontal range between the source and the receiver. The phase function $\Phi_b(\mu)$ in the exponential term of the diffraction integral is given by

$$\Phi_b(\mu) = ik\left[r\sin\mu + z_s\cos\mu + nD\cos\mu_1\right], \tag{3.6}$$

where z_s is the height of the source from the porous interface (measured positive upward), and D is the depth of the receiver measured positive downward from the porous interface.

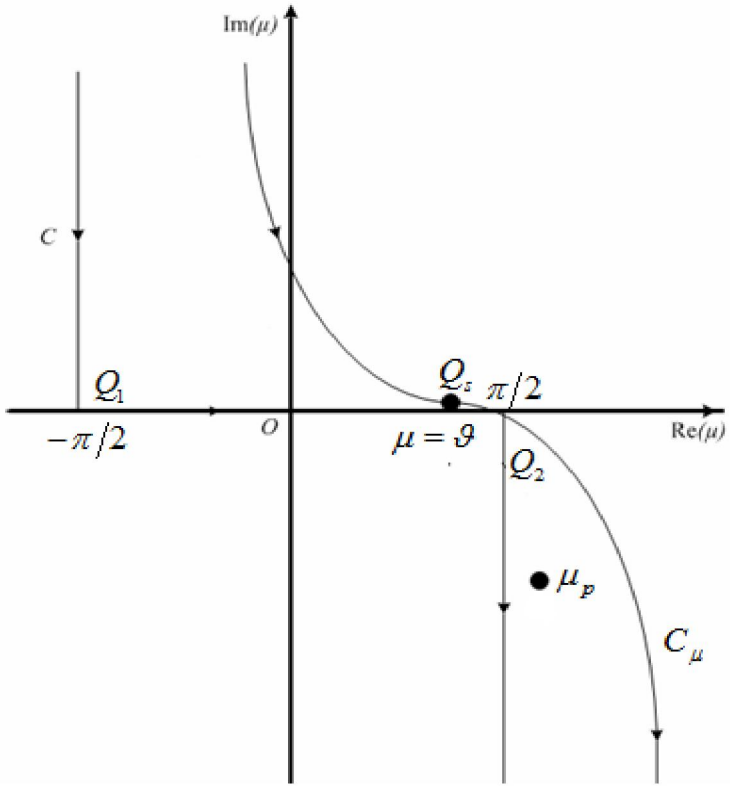

Figure 3.2: An illustration of the original integration path C and the steepest descent path C_μ in the complex μ plane.

Figure 3.2 shows the integration path C of the integral in Eq. (3.2), which starts at Q_∞ to reach the origin in the complex μ-plane en route to point Q_1 (at $-\pi/2$). It then arrives at Q_2 (at $\pi/2$) and ends at $Q_{-\infty}$. To evaluate the integral asymptotically, it is necessary to determine the steepest descent path and the saddle point. According to Li and Liu [1], the saddle point (say, $\mu = \vartheta$) is determined by setting $\partial\Phi_b/\partial\mu\big|_{\mu=\vartheta}$ to zero, which leads to a transcendental function of

$$r = z_s \tan\vartheta + D\tan\vartheta_1, \tag{3.7}$$

where ϑ and ϑ_1 can be interpreted as the incident and refracted angles measured from the vertical axis for the spherical sound wave transmitted from the upper medium to the porous half-plane lying below. Again, these two angles are associated by Snell's Law:

$$\sin\vartheta = n\sin\vartheta_1. \tag{3.8}$$

For a given source/receiver geometry and refractive index of the porous half-space, ϑ and ϑ_1 can be obtained by solving Eqs. (3.7) and (3.8) simultaneously. Li and Liu [1] outlined a simple numerical scheme to compute ϑ and ϑ_1 for a given index of refraction of the rigid porous medium. The index of refraction n is a complex variable for modeling the dissipative property of the lower medium. This renders the two angles, ϑ and ϑ_1, as complex variables. In other words, the sound waves transmitted from the upper to the lower media are both dissipative. An analysis of the numerical solution for the polar angle confirms that $\mathrm{Re}(\vartheta) \geq 0$. The horizontal ranges for the source and receiver can be expressed as

$$r_s = z_s\tan\vartheta,\ r_D = D\tan\vartheta_1,\ \text{and}\ r = r_s + r_D. \tag{3.9a-c}$$

Here, r_s and r_D are complex, but their sum gives r, which is a real variable. The total separations above (R_s) and below (R_D) the porous interface can be written in terms of ϑ and ϑ_1 as

$$R_s = z_s/\cos\vartheta \quad , \quad R_D = D/\cos\vartheta_1 \quad . \tag{3.10a,b}$$

The phase function Φ_b in the exponential term of Eq. (3.2) can then be rewritten as

$$\Phi_b(\mu) = ik\left[R_s\cos(\mu-\vartheta) + nR_D\cos(\mu_1-\vartheta_1)\right]. \tag{3.11}$$

Figure 3.1b shows a schematic diagram illustrating these geometrical parameters.

In the complex μ-plane, the steepest descent path can be found by tracing the path such that

$$\mathrm{Im}\left[ikL - \Phi_b(\mu)\right] = 0\,, \tag{3.12}$$

where L is the acoustical path length [20] defined by

$$L = \frac{\Phi_b(\vartheta)}{ik} = R_s + nR_D = \frac{z_s}{\cos\vartheta} + \frac{nD}{\cos\vartheta_1}. \tag{3.13}$$

The steepest descent path is sketched in Figure 3.2 as C_μ. The asymptotic evaluation of Eq. (3.2) can be facilitated by introducing a new complex variable, W_ϑ [1]:

$$W_\vartheta^2/2 = ikL - \Phi_b(\mu)\,. \tag{3.14}$$

Hence, the original integration path C in the complex μ-plane can be transformed to C_W in the complex W_ϑ-plane. It is possible to trace C_W by introducing the respective real and imaginary parts for W_ϑ, μ and μ_1, as follows:

$$W_\vartheta = X + iY \quad , \quad \mu = u + iv\,, \text{ and } \mu_1 = u_1 + iv_1\,, \tag{3.15a,b,c}$$

where X, Y, u, v, u_1, and v_1 are real variables.

For a given path C in the μ-plane, X and Y can be determined by solving the above pair of nonlinear simultaneous equations for C_W in the W_ϑ -plane. It follows immediately from Eq. (3.15a) that

$$W_\vartheta^2 = X^2 - Y^2 + i(2XY). \tag{3.16}$$

Making use of Eqs. (3.14) and (3.16), we can then derive the corresponding expressions for X and Y in terms of u and v to confirm that

$$\frac{XY}{k} = \mathrm{Re}(L) - \mathrm{Re}\left[\Phi_b(\mu)/(ik)\right], \tag{3.17a}$$

and

$$\frac{1}{2}\frac{Y^2 - X^2}{k} = \mathrm{Im}(L) - \mathrm{Im}\left[\Phi_b(\mu)/(ik)\right]. \tag{3.17b}$$

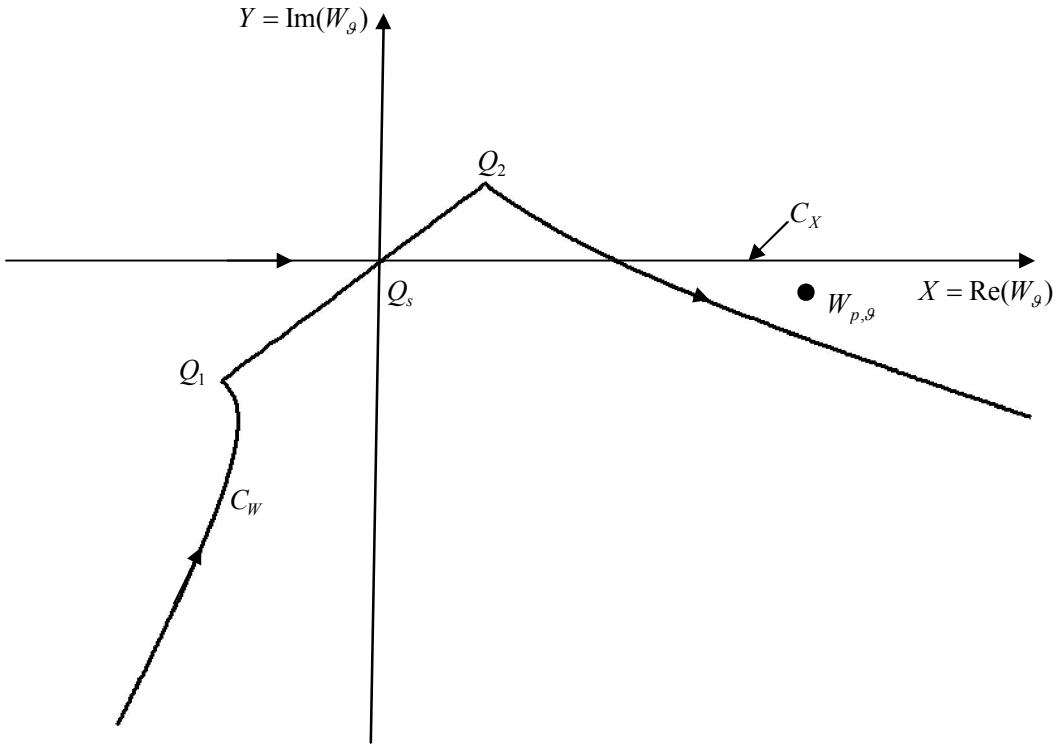

Figure 3.3: An illustration of the integration path C_W and the steepest descent path C_X in the complex W-plane.

The steepest descent path, say C_X, corresponds to the choice of an integration path along the real axis of the complex plane because $e^{-W_\vartheta^2/2}$ gives exponentially small values as $X \to \pm\infty$ and its phase term vanishes because $Y = 0$ along the path. These two paths, C_W and C_X, are sketched in the complex W_ϑ-plane as shown in Figure. 3.3.

Replacing μ with W_ϑ, changing the integration path from C to C_W, and splitting the integral into two parts, it is possible to rewrite Eq. (3.2) as [1]:

$$p_1 = p_e + p_b, \tag{3.18}$$

where

$$p_e = \frac{ike^{ikL}}{4\pi} \int_{C_W} \sin\mu G(\mu)\left(d\mu/dW_\vartheta\right)e^{-W_\vartheta^2} dW_\vartheta, \tag{3.19a}$$

$$p_b = -\frac{ike^{ikL}}{4\pi} \int_{C_W} \frac{\sin\mu G(\mu)\chi(\mu)}{\cos\mu + \chi(\mu)}\left(d\mu/dW_\vartheta\right)e^{-W_\vartheta^2} dW_\vartheta, \tag{3.19b}$$

and

$$\frac{d\mu}{dW_\vartheta} = \frac{-W_\vartheta}{\Phi_b'(\mu)} = \frac{W_\vartheta}{ik\cos\mu\left(z_s\tan\mu + D\tan\mu_1 - r\right)}. \tag{3.20}$$

Since the integrand of p_e [see Eq. (3.19a)] is an entire function, there is no pole contribution when the path is indented from C_W to the steepest descent path C_X. Hence, Eq. (3.19a) can be transformed directly to

$$p_e = \frac{ike^{ikL}}{4\pi} \int_{C_X} \cos\mu G(\mu)\left(d\mu/dW_\vartheta\right)e^{-W_\vartheta^2/2} dW_\vartheta. \tag{3.21}$$

Expanding the integrand of Eq. (3.21) about the saddle point at $W_\vartheta = 0$ and noting that $\mu = \vartheta$ at the saddle point, Li [1, 74] showed that p_e can be evaluated asymptotically to yield

$$p_e = \frac{e^{ikL}}{2\pi\Delta}\left[1 + O\left(1/kr\right) + \cdots\right], \tag{3.22}$$

where L is the acoustical path length defined in Eq. (3.13), and Δ can be interpreted as the effective physical path length determined by

$$\Delta = \sqrt{R_g R_r}\,. \tag{3.23a}$$

R_g is the apparent distance of the sound ray traveling in the absence of the lower medium

$$R_g = \frac{r}{\sin\vartheta}, \tag{3.23b}$$

and R_r is the acoustical energy path length [34]:

$$R_r = \frac{z_s}{\cos\vartheta} + \frac{D\cos^2\vartheta}{n\cos^3\vartheta_1}. \tag{3.23c}$$

Equation (3.22) implies that the present asymptotic analysis is applicable when $kr \gg 1$, i.e. a high frequency approximation when k is large or a far field approximation when r is large.

The following identities related to Φ_b have been found to be useful in the above and the subsequent formulations:

$$d\mu/dW_g\big|_{W_g=0} = \sqrt{1/\left[-\Phi_b''(\vartheta)\right]} = i\left[\Phi_b''(\vartheta)\right]^{-1/2}, \tag{3.24a}$$

$$d^2\mu/dW_g^2\big|_{W_g=0} = -\frac{1}{3}\left[\Phi_b'''(\vartheta)/\Phi_b''(\vartheta)\right]^2 \left(d\mu/dW_g\right)\big|_{W_g=0}, \tag{3.24b}$$

$$d^3\mu/dW_g^3\big|_{W_g=0} = \frac{1}{4}\left[\frac{\Phi_b'''(\vartheta)}{\Phi_b''(\vartheta)} - \frac{\Phi_b^{\mathrm{IV}}(\vartheta)}{\Phi_b''(\vartheta)}\right]^2 \left(\frac{d\mu}{dW_g}\right)^3\Bigg|_{W_g=0}, \tag{3.24c}$$

$$\Phi_b(\vartheta)/ik = L = R_s + nR_D, \tag{3.24d}$$

$$\Phi_b'(\vartheta) = 0, \tag{3.24e}$$

$$\Phi_b''(\vartheta)/ik = -R_r = -\left(\frac{z_s}{\cos\vartheta} + \frac{D\cos^2\vartheta}{n\cos^3\vartheta_1}\right), \tag{3.24f}$$

$$\Phi_b'''(\vartheta)/ik = -3(1-n^2)D\cos\vartheta\sin\vartheta/\left(n^3\cos^5\vartheta_1\right), \tag{3.24g}$$

and

$$\Phi_b^{\mathrm{IV}}(\vartheta)/ik = \frac{z_s}{\cos\vartheta} + \frac{nD}{\cos\vartheta_1}\left[\left(\frac{\cos\vartheta}{n\cos\vartheta_1}\right)^4 - \frac{(1-n^2)(4-7\sin^2\vartheta+11\sin^2\vartheta_1)}{n^4\cos^6\vartheta_1}\right], \tag{3.24h}$$

where the primes denote the derivatives with respect to their argument, and IV is the fourth-order derivative.

Applying the same transformation [*cf* Eq. (3.14)] from μ to W_ϑ, the integral Eq. (3.19b) can be expressed as

$$p_b = \frac{-ike^{ikL}}{4\pi}\int_{C_W}\Lambda_\vartheta(W_\vartheta)e^{-W_\vartheta^2/2}dW_\vartheta, \tag{3.25}$$

where the kernel function $\Lambda(W_\vartheta)$ is given by

$$\Lambda_\vartheta(W_\vartheta) = \frac{\chi\sin\mu G(\mu)}{(\cos\mu+\chi)}\frac{d\mu}{dW_\vartheta}. \tag{3.26}$$

The integration path for the integral of Eq. (3.25) may now be indented from C_W to C_X. However, there is a complication in the process because $\Lambda(W_\vartheta)$ has a singularity, i.e., a pole, when $\cos\mu+\chi=0$. Noting Eqs. (3.3) and (3.4), the pole location can be determined analytically in the μ-plane as

$$\mu_p = \pi/2 + \cos^{-1}(\chi_p), \tag{3.27}$$

where the subscript p denotes the parameter at the pole location, and χ_p [$\equiv \chi(\mu_p)$] can be treated as the apparent admittance of the porous layer. The pole can be determined

analytically to yield

$$\beta_p := \chi_p = \varsigma\sqrt{\left(n^2-1\right)/\left(1-\varsigma^2\right)}\,. \tag{3.28a}$$

The pole location in the W_ϑ-plane can then be determined by substituting Eq. (3.27) into Eq. (3.12) to give, say, $W_{p,\vartheta}$. The pole location is marked schematically in Fig. 3.3, and its analytical expression can be derived from Eqs. (3.11) and (3.14) to give

$$W_{p,\vartheta} = \sqrt{2ik}\left\{L-\left[R_s\cos(\mu_p-\vartheta)+nR_r\cos(\mu_{p_1}-\vartheta_1)\right]\right\}^{1/2}, \tag{3.28b}$$

where μ_p is given by Eq. (3.27), and μ_{p_1} is related to μ_p by Snell's Law, i.e., $\sin\mu_p = n\sin\mu_{p1}$.

There is a saddle point at $W_\vartheta = 0$ in the integral of Eq. (3.25). The use of the standard steepest descent method to evaluate the integral becomes inapplicable if the pole $W_{p,\vartheta}\to 0$. This is because a direct Taylor expansion of $\Lambda\left(W_\vartheta\right)$ becomes increasingly inadequate when $|\chi_p| \to 0$ and $\theta \to \pi/2$. In this paper, a modified saddle-point method [16-18] will be used to evaluate the integral asymptotically. The method starts by replacing $\Lambda\left(W_\vartheta\right)$ with

$$\Lambda_\vartheta\left(W_\vartheta\right) = \Gamma_\vartheta\left(W_\vartheta\right)/\left(W_\vartheta^2 - W_{p,\vartheta}^2\right), \tag{3.29}$$

where $\Gamma_\vartheta\left(W_\vartheta\right)$ is an entire function that is analytic near the saddle point and the pole location in the W_ϑ-plane.

The Taylor expansion of $\Gamma_\vartheta\left(W_\vartheta\right)$ about the saddle point, $W_\vartheta = 0$, can be written as

$$\Gamma_{\vartheta}\left(W_{\vartheta}\right)=\sum_{j=0}^{\infty}\frac{W_{\vartheta}^{j}}{j!}\left[\frac{d^{j}}{dW_{\vartheta}^{j}}\Gamma_{\vartheta}(W_{\vartheta})\right]_{W_{\vartheta}=0}. \tag{3.30}$$

Thus, the substitution of Eqs. (3.29) and (3.30) into Eq. (3.25) and the retention of the first four terms in the series give a uniformly valid asymptotic expansion for p_b:

$$p_b \approx \frac{-ike^{ikL}}{4\pi}\left\{\Gamma_{\vartheta}(0)I_0+\frac{1}{2}\Gamma''_{\vartheta}(0)I_1+\ldots\right\}, \tag{3.31}$$

where the integral I_i can be written in a more general form as

$$I_i=\int_{C_W}\frac{W_{\vartheta}^{2i}e^{-W_{\vartheta}^2/2}dW_{\vartheta}}{W_{\vartheta}^2-W_{p,\vartheta}^2}\ , i=0,\ 1,\ \ldots\ , \tag{3.32a}$$

and the double primes are the second derivatives with respect to its argument. Here, there are only two terms left in the asymptotic expression given in Eq. (3.31) because all odd terms of j in the series of Eq. (3.30) vanish.

The two integrals, I_0 and I_1, can be expressed in terms of the complimentary error function and its related function as follows:

$$I_0=-\frac{1}{2w_b^2}\sqrt{2\pi}\left\{1-F(w_b)\right\}, \tag{3.33a}$$

and

$$I_1=\sqrt{2\pi}F(w_b), \tag{3.33b}$$

where w_b is the effective numerical distance,

$$w_b=W_{p,\vartheta}\Big/\sqrt{2}=\sqrt{ik}\left\{L-\left[R_s\cos(\mu_p-\vartheta)+nR_r\cos(\mu_{p_1}-\vartheta_1)\right]\right\}^{1/2}, \tag{3.34}$$

and $F(w_b)$ is the boundary loss factor related to the complementary function,

$$F(w_b)=1+i\sqrt{\pi}w_b e^{-w_b^2}\operatorname{erfc}\left(-iw_b\right). \tag{3.35}$$

The details of the derivation of Eqs. (3.33a) and (3.33b) are provided in the Appendix C.

To calculate p_b in Eq. (3.31), analytical expressions for $\Gamma_\vartheta(0)$ and $\Gamma''_\vartheta(0)$ are needed in addition to I_0 and I_1. Noting Eqs. (3.29) and (3.24a-c), it is possible to verify that

$$\Gamma_\vartheta(0) = -2iw_b^2 \Lambda_\vartheta(0)\left[\Phi''_b(\vartheta)\right]^{-1/2}, \tag{3.36a}$$

and

$$\Gamma''_\vartheta(0) = \frac{2\Lambda_\vartheta(0)}{w_b^2}\left(\frac{bw_b^2}{ikR_r} - 1\right), \tag{3.36b}$$

where b is the modification factor given by

$$b = \frac{\Lambda''_\vartheta(0)}{\Lambda_\vartheta(0)} - \frac{\Lambda'_\vartheta(0)}{\Lambda_\vartheta(0)}\frac{\Phi'''_b(\vartheta)}{\Phi''_b(\vartheta)} + \frac{1}{4}\left\{\left[\Phi'''_b(\vartheta)/\Phi''_b(\vartheta)\right]^2 - \frac{\Phi_b^{IV}(\vartheta)}{\Phi''_b(\vartheta)}\right\}, \tag{3.37}$$

and the effective numerical distance w_b is given by Eq. (3.34).

Now, the use of Eqs. (3.24a-h) and (3.26) leads to the corresponding expressions for $\Gamma_\vartheta(0)$ and $\Gamma''_\vartheta(0)$ yielding

$$\Gamma_\vartheta(0) = \frac{-2w_b^2 G(\vartheta)}{\sqrt{ikR_r}}\frac{\beta_\vartheta \sin\vartheta}{\cos\vartheta + \beta_\vartheta}, \tag{3.38a}$$

and

$$\Gamma''_\vartheta(0) = \frac{G(\vartheta)}{\sqrt{ikR_r}}\frac{\beta_\vartheta \sin\vartheta}{\cos\vartheta + \beta_\vartheta}\left(\frac{bw_b^2}{ikR_r} - 1\right), \tag{3.38b}$$

where $G(\vartheta)$ is determined by Eq. (3.5), and β_ϑ is defined as

$$\beta_\vartheta := \chi(\vartheta) = \zeta\sqrt{n^2 - \cos^2\vartheta}, \tag{3.38c}$$

which can be interpreted as the effective admittance of the rigid porous medium.

Replacing $G(\vartheta)$ with its asymptotic expansion [22], Eqs. (3.38a, b) can be approximated further by

$$\Gamma_\vartheta(0)=\frac{-2\sqrt{2/\pi}w_b^2}{ik\Delta}\frac{\beta_\vartheta}{\cos\vartheta+\beta_\vartheta}, \tag{3.39a}$$

and

$$\Gamma''_\vartheta(0)=\frac{-\sqrt{2/\pi}}{ik\Delta}\frac{\beta_\vartheta}{\cos\vartheta+\beta_\vartheta}\left(\frac{bw_b^2}{ikR_r}-1\right). \tag{3.39b}$$

On the other hand, $\Lambda''_\vartheta(0)/\Lambda_\vartheta(0)$ and $\Lambda'_\vartheta(0)/\Lambda_\vartheta(0)$ in Eq. (3.37) can be expressed in terms of ϑ by deriving from Eq. (3.26) to obtain

$$\frac{\Lambda''_\vartheta(0)}{\Lambda_\vartheta(0)}=\frac{2\left[\chi'^2-2\chi'\sin\vartheta+1+\beta_\vartheta\cos\vartheta-\left(\chi'/\sin\vartheta\right)(1+\beta_\vartheta\cos\vartheta)\right]}{(\cos\vartheta+\beta_\vartheta)^2}$$

$$+\left[\frac{2\chi'(\sin\vartheta-\chi')}{(\cos\vartheta+\beta_\vartheta)}+\frac{1}{2}(\chi'/\sin\vartheta)\cos\vartheta\right]\frac{1}{\beta_\vartheta}+\frac{\chi''}{\beta_\vartheta}-\frac{1}{4}\cot^2\vartheta\,, \tag{3.40a}$$

and

$$\frac{\Lambda'_\vartheta(0)}{\Lambda_\vartheta(0)}=\frac{\chi'}{\beta_\vartheta}+\frac{\sin\vartheta-\chi'}{\cos\vartheta+\beta_\vartheta}+\frac{1}{2}\cot\vartheta\,, \tag{3.40b}$$

where the first and second derivatives of χ can be determined analytically from Eq. (3.38c) to verify that

$$\chi'=d\chi/d\vartheta=-\varsigma\sin\vartheta\cos\vartheta\Big/\sqrt{n^2-\sin^2\vartheta}\,, \tag{3.41a}$$

and

$$\chi''=d^2\chi/d\vartheta^2=-\left(\varsigma/\beta_\vartheta\right)^2\left[\beta_\vartheta\cos2\vartheta-\tfrac{1}{2}\chi'\sin2\vartheta\right]. \tag{3.41b}$$

There are apparent singularities in Eqs. (3.40a) and (3.40b) when $r\to 0$ (i.e., $\vartheta\to 0$) because of the presence of the $\cot\vartheta$ term. This term is calculated by simply setting ϑ at

$\pi/4$ (i.e., cot ϑ is set at 1) in the following numerical analyses. This assumption is consistent with an earlier study by Kawai et al. [23], who used the modified saddle point method to derive an asymptotic expression for the sound field above an impedance ground. With this approximation, Eqs. (3.40a) and (3.40b) become

$$\frac{\Lambda_\vartheta''(0)}{\Lambda_\vartheta(0)} = \frac{2\left[\chi'^2 - 2\chi'\sin\vartheta + (1-\chi'/\sin\vartheta)(1+\beta_\vartheta\cos\vartheta)\right]}{(\cos\vartheta+\beta_\vartheta)^2} + \frac{2(\sin\vartheta-\chi')}{(\cos\vartheta+\beta_\vartheta)}\frac{\chi'}{\beta_\vartheta}$$

$$+\frac{1}{2\beta_\vartheta}(\chi'/\sin\vartheta)\cos\vartheta + \frac{\chi''}{\beta_\vartheta} - \frac{1}{4}, \tag{3.42a}$$

and

$$\frac{\Lambda_\vartheta'(0)}{\Lambda_\vartheta(0)} = \frac{\chi'}{\beta_\vartheta} + \frac{\sin\vartheta-\chi'}{\cos\vartheta+\beta_\vartheta} + \frac{1}{2}. \tag{3.42b}$$

Substituting Eqs. (3.33a, 3.33b), (3.37), and (3.39a, 3.39b) and simplifying the resulting expressions, we obtain an asymptotic approximation for p_b as follows:

$$p_b \cong -\frac{2\beta_\vartheta}{\cos\vartheta+\beta_\vartheta}\frac{e^{ikL}}{4\pi\Delta}\left[1 - \frac{bw_b^2}{ikR_r}F(w_b)\right], \tag{3.43}$$

where the modification factor b can be obtained by using Eqs. (3.24 e-g), (3.40a, b), and (3.41a-c) in Eq. (3.37).

The application of Eqs. (3.22) and (3.43) in Eq. (3.18) yields an asymptotic expression for the total sound penetration into the porous medium by a monopole source as follows:

$$p_1 = \left[T_\vartheta + A(1-V_\vartheta)F(w_b)\right]\frac{e^{ikL}}{4\pi\Delta} \tag{3.44}$$

where T_ϑ is the effective plane wave transmission coefficient,

$$T_\vartheta = \frac{\beta_\vartheta}{\cos\vartheta + \beta_\vartheta}, \tag{3.45}$$

V_ϑ is the effective plane wave reflection coefficient,

$$V_\vartheta = \frac{\cos\vartheta - \beta_\vartheta}{\cos\vartheta + \beta_\vartheta}, \tag{3.46}$$

and A is the augmented diffraction factor,

$$A = \frac{bw_b^2}{ikR_r}, \tag{3.47}$$

and w_b is defined in Eq. (3.34). Equation (3.44) is the main result of the present study. It represents a uniform asymptotic expression for predicting the sound field below the porous medium by a monopole source. We can also see the linkage of T_ϑ and V_ϑ, and the presence of the transmitted wave term T_ϑ and the boundary wave term that is used to model the diffracted waves. In the next section, we shall validate the asymptotic formula by comparing the predictions with other solutions obtained by the more accurate wave-based numerical scheme.

3.3 Validation of the Asymptotic Formula

In this section, the asymptotic solution derived above will be compared with the numerical results obtained by a more accurate wave-based numerical method. The integrated exact solution (IES) [15] is a hybrid numerical method based on a direct integration method and the fast field program (FFP) formulation. It has been shown to be able to provide accurate numerical results for sound fields above and below the porous

medium. In the following analysis, a series of comparisons is made between the computed results by the modified saddle point method and those by the IES method.

To facilitate the presentation of numerical results for comparison, an excess attenuation (*EA*) function is defined as

$$EA = 10\log_{10}\left[\frac{p_1}{e^{ikr}/4\pi r}\right], \tag{3.48}$$

where r is the horizontal distance between the source and the receiver. For the porous interface, the model by Johnson et al. [113] is used to approximate the complex density ρ_1. Here, the density ratio ζ is given by

$$\zeta = \frac{\rho}{\rho_1} = \alpha_\infty^{-1}\left[1 + \frac{i\eta\phi}{\rho_0\alpha_\infty\tau_0\omega}\left(1 - \frac{4\alpha_\infty^2\tau_0^2 i\omega\rho_0}{\Lambda^2\phi^2\eta}\right)^{\frac{1}{2}}\right]^{-1}, \tag{3.49}$$

where α_∞ is the tortuosity; γ, the ratio of the specific heats; τ_0, the viscous permeability; Λ, the viscous thermal characteristic length; ϕ, the porosity of the porous medium and η the viscosity of air. The model according to Lafarge et al. [114] is used to calculate the dynamic compressibility C_1 of the rigid porous medium:

$$C_1 = \gamma - (\gamma - 1)\left[1 + \frac{i\eta\phi}{\rho_0\tau_0'\omega\,\mathrm{Pr}}\left(1 - \frac{4\tau_0'^2 i\omega\rho_0\,\mathrm{Pr}}{\Lambda'^2\phi^2\eta}\right)^{\frac{1}{2}}\right]^{-1}, \tag{3.50}$$

where τ_0' is the thermal permeability, Λ' is the thermal characteristic length and Pr is and Prandtl number of air. Consequently, the index of refraction n can be calculated by

$$n = \frac{c}{c_1} = \sqrt{\frac{C_1}{\zeta\left(\gamma P_0/K_0\right)}}, \tag{3.51}$$

where P_0 is the atmospheric pressure and $K_0(\equiv \rho c^2)$ is the bulk modulus of air. In addition, the viscous permeability τ_0 is related to the flow resistivity σ of the porous material by

$$\tau_0 = \eta/\sigma . \tag{3.52}$$

The specific impedance of the porous ground is customarily calculated by including the porosity in the porous ground [91]. We therefore need to replace χ_m with $\phi\chi_m$ in the following computation of the sound fields below a rigid porous ground.

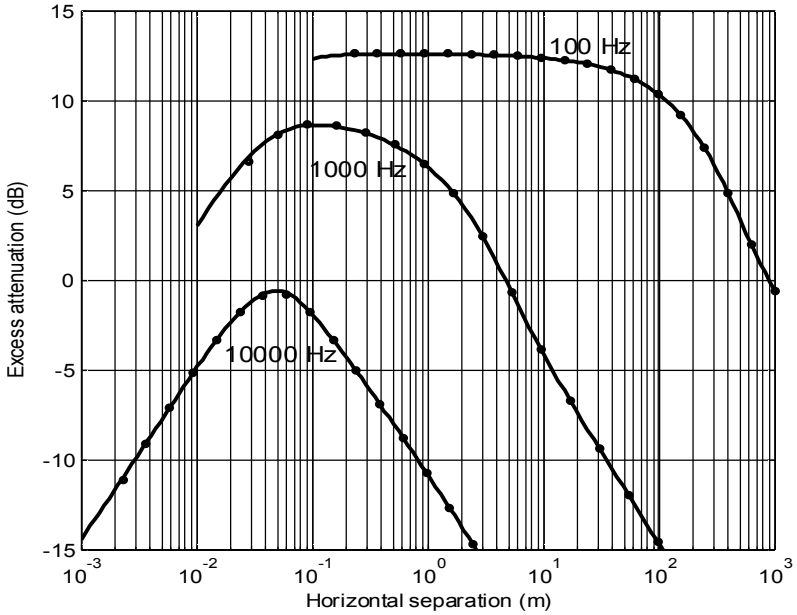

Figure 3.4: The Excess Attenuation (EA) versus horizontal separation. Solid line: modified saddle-point; circles: Integrated Exact Solution (IES).

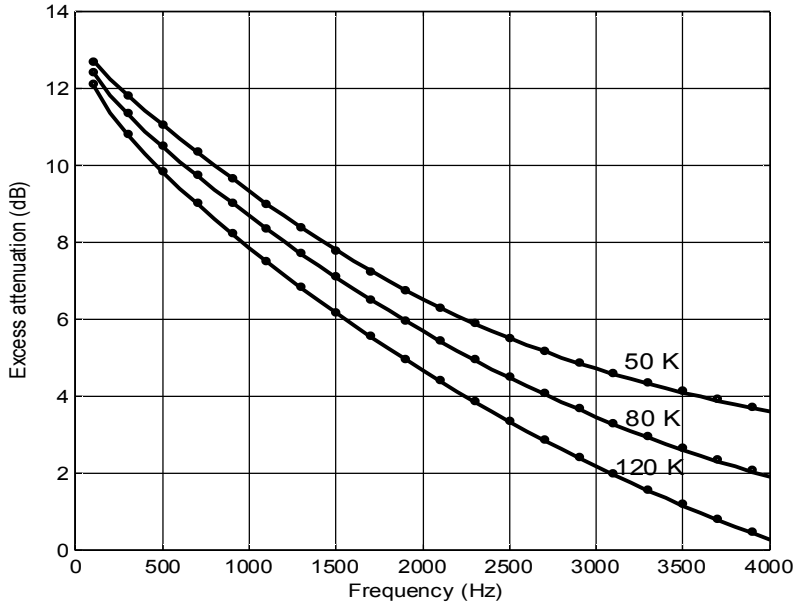

Figure 3.5: The Excess Attenuation (EA) spectra. The horizontal range is 0.1m. The same acoustic parameters as Fig. 4 are used but the numerical results with the effective flow resistivity of 50 kPa m s^{-2}, 80 kPa m s^{-2}, 120 kPa m s^{-2} are shown. Solid line: modified saddle-point; circles: Integrated Exact Solution (IES).

Figure 3.4 displays the typical results of the predicted *EA* as a function of the horizontal separation at various frequencies in the modified saddle method and the IES method. Particularly, the source is chosen at 0.04 m and the receiver at 0.02 m below the rigid porous medium. The abscissa of the plots, which is the horizontal separation, varies from 0.0001 m to 1000 m in a logarithm scale. The rigid porous medium was characterized by Johnson's model as having $\phi = 0.98$, $\alpha_\infty = 1.1$, $\Lambda = 70$ μm, $\Lambda' = 210$ μm, $\tau_0' = 6.1\times10^{-10}$ m^2 and $\sigma = 10$ kPa m s^{-2} at frequencies of 100 Hz, 1 kHz, and 10 kHz. The numerical results calculated by the modified saddle-point method are in excellent agreement with those computed by the IES method, and they are indistinguishable from each other in these plots. More noticeably, the results agree with each other very well even when the horizontal range is reduced to 0.001 m. The modified saddle method

shows an advantage in predicting the sound field at a very short range. More computations were conducted with different flow resistivities, as shown in Figure 3.5. The *EA* spectrum is presented, with the source frequency varying from 100 Hz to 4000 Hz and different flow resistivities of 50 kPa s m^{-2}, 80 kPa s m^{-2}, and 120 kPa s m^{-2}. The respective parametric values for ϕ, α_∞, Λ, Λ' and τ_0' were kept unchanged in this set of numerical simulations. Again, the agreements are very good for all these cases.

Figures 3.6 and 3.7 further show comparisons for different cases when the source is located at 0.4 m and the receiver is set at 0.02 m below the porous medium. The excellent agreement of the *EA* in both the horizontal range and the frequency domain proves the accuracy of the solutions by the modified saddle-point method.

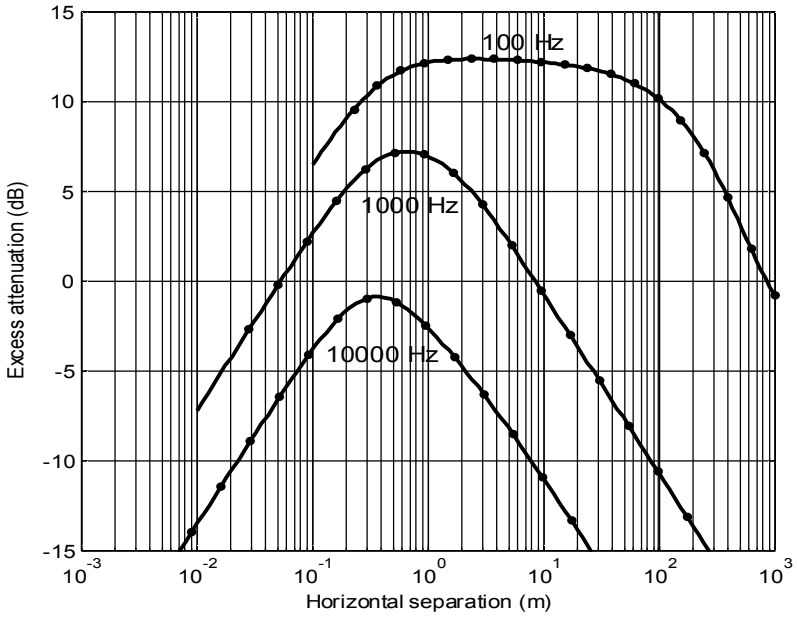

Figure 3.6: Caption is same as Figure 3.4 except that the receiver is located at 0.02 m below the porous medium and source at 0.4 m above the porous medium.

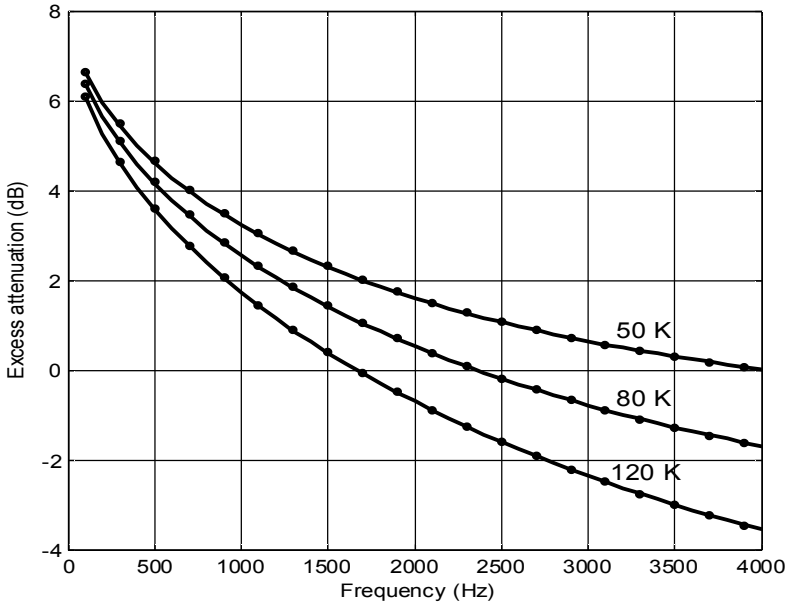

Figure 3.7: Caption is same as Figure. 3.5 except that the receiver is located at 0.02 m below the porous medium and source at 0.4 m above the porous medium.

All the above comparisons show the validity of the asymptotic solution based on the modified saddle-point method. These comparisons also confirm the validity of the assumption for setting $\cot \vartheta$ to 1 in Eqs. (3.40a) and (3.40b). These approximations work well even, for example, when the horizontal separation is of the order of 10^{-2} m at 1 kHz, which corresponds to $kr < 0.1$.

3.4 Summary

In this chapter, a modified saddle-point method was applied to derive an asymptotic solution for the propagation of sound from an airborne source penetrating into a rigid porous medium. The study demonstrated that the solution is composed of two terms: a plane wave transmitted term and a diffraction wave term. Comparisons of the numerical solutions with those computed by the more accurate wave-based solution

suggest that the asymptotic formula can give sufficiently accurate results for most practical calculations when $kr > 0.1$.

CHAPTER 4: HEURISTIC SOLUTIONS FOR SOUND FIELDS ON RIGID POROUS INTERFACES

4.1 Introduction

Many studies (e.g. Refs. [3, 71, 72, 92]) have been devoted to derive different but compatible asymptotic formulas for predicting the sound fields above various types of plane interfaces. Applying the pole subtraction technique in the double saddle-point method, it is possible to obtain asymptotic solutions for the sound fields above an impedance-backed rigid porous layer [3], a hard-backed rigid porous layer [92], a semi-infinite rigid porous medium [72] and a locally reacting impedance surface [71]. Li and Liu [3] showed that the asymptotic formula for the impedance-backed rigid porous layer was the most general one. It can be used as the basis to confirm appropriate solutions for other three types of interfaces mentioned above.

Using appropriate approximations, Chien and Soroka [71] indicated that the asymptotic formula for the monopole sound field above an impedance ground can be expressed as a sum of two terms comprising a direct wave and a reflected wave contributions. The latter contribution can be split further into two parts: a plane wave contribution supplemented by a ground wave component. This asymptotic solution is

frequently referred as the Weyl-Van der Pol formula. However, Attenborough et al [72], Allard and co-workers [92] and Li [3] were unable to provide analogous formulas for semi-infinite porous medium, a hard-backed rigid porous layer and an impedance backed rigid porous layer. More importantly, all of these asymptotic formulas have a singularity in their respective solutions. The prediction of the reflected wave fields is unbounded when the horizontal separation between the source and receiver vanishes. In this case, the method of a direct numerical integration is needed to compute the reflected sound fields in order to resolve this problem of apparent singularity at short ranges.

This chapter is a continuation of the study in the paper [3]. Two intriguing issues are addressed here. Is it possible to obtain an analogous WVPD formula for predicting the sound fields above a non-locally reacting interface? Can the analytical formula be modified to allow for accurate predictions of the total sound field even when the horizontal range is close to zero? A satisfactory resolution of these two issues enables one to develop an efficient, convenient and accurate Green's function for predicting the spherical waves reflected from a non-locally reacting medium. Indeed, the accurate and rapid computation of the Green's function should find its applications in the boundary element formulation near non-locally reacting media [89] and the acoustical characterization of sound absorbing materials [69].

This chapter is arranged as follows. Section 4.2 describes a brief formulation of the problem providing necessary information to make this paper self-contained. In section 4.3, the asymptotic solution in the classical Weyl-Van der Pol form is then developed offering physical interpretable terms. Next, a heuristic approach is initiated in section 4.4 aiming to provide accurate near-field and far-field numerical solutions. They are then

compared with the accurate wave-based numerical solutions to validate this modified Weyl-Van der Pol formula. Finally, concluding remarks are presented in section 4.5.

4.2 Theoretical Formulation

In a recent study [3], Li and Liu generalized the theory for predicting the monopole sound field above a plane interface that can either be a locally reacting ground or a non-locally reacting porous medium. The total sound field due to a monopole source can be expressed as a sum of three terms:

$$p = \frac{e^{ikR_1}}{4\pi R_1} + \frac{e^{ikR_2}}{4\pi R_2} + p_D, \tag{4.1}$$

where R_1 and R_2 are the respective distances from the source and its image to the receiver, k is the wavenumber of the source. The third term of the right side of Eq. (4.1) is known as the diffraction wave term that can be expressed in an integral form as

$$p_D = \frac{-ik}{4\pi}\int_C \frac{\sin\mu\chi^{(m)}(\mu)}{\cos\mu+\chi^{(m)}(\mu)}\left[H_0^{(1)}\left(kr\sin\mu\right)e^{-ikr\sin\mu}\right]e^{ikR_2\cos(\mu-\theta)}d\mu, \tag{4.2}$$

where $\chi^{(m)}(\mu)$ is referred as the total admittance of the ground surface with the superscript (m) representing the different types of ground surfaces. The incident angle of the reflected wave and the horizontal separation between the source and receiver are denoted by θ and r, respectively. The square bracket term in the integrand is a non-oscillatory function due to the fact that the zeroth order Hankel function of the first kind $H_0^{(1)}$ is normalized with its associated exponential function. The integration variable μ can be treated as the polar angle which is used to characterize the propagation vector of

the plane wave reflected from the boundary surface. Both θ and μ are angles measured from the vertical axis aligned along the *z*-direction.

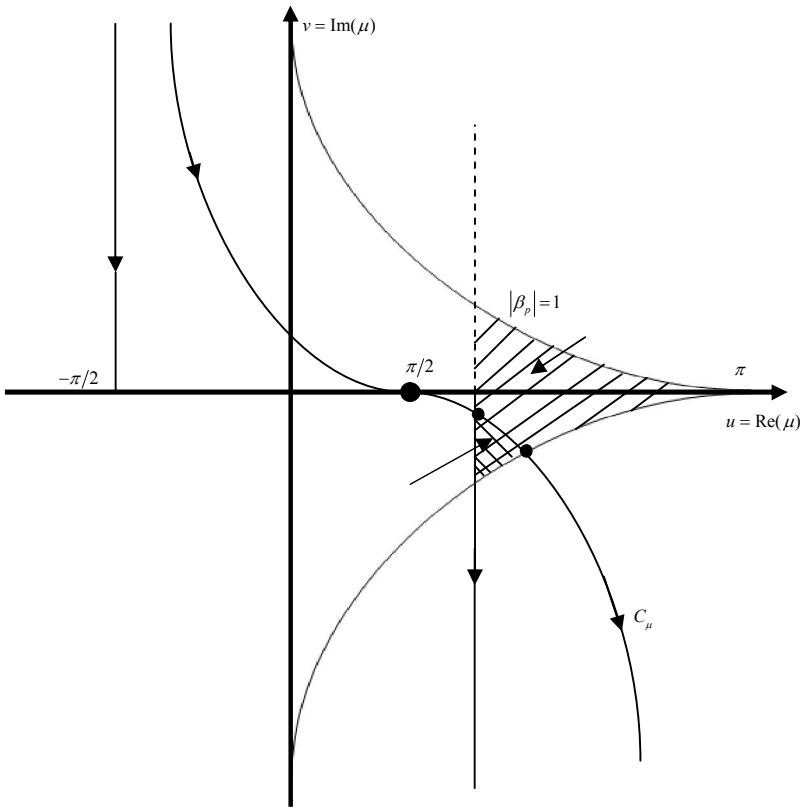

Figure 4.1: A sketch of the steepest descent path C_μ and the pole location.

Table 2.1 in Chapter 2 lists different types of ground surfaces and their respective $\chi^{(m)}(\mu)$ where the density and the speed of sound in the upper medium (air) are denoted by ρ and c, respectively. They are, respectively, signified by ρ_1 and c_1 in the lower medium (ground/sound absorbing materials). The density ratio of the two media $\zeta\left(\equiv \rho / \rho_1\right)$, the index of refraction $n\left(\equiv c / c\right)$ and the specific normalized admittance β_1 are used to characterize the acoustical properties of the air/ground interface. The depth for a layer rigid porous medium is specified by *d*. The specific normalized admittance of the bottom layer for the impedance-backed porous layer is denoted by β_2. The variable *N*

for the porous layer is defined by

$$N(\mu) = \sqrt{n^2 - \sin^2 \mu} \ , \tag{4.3}$$

which has also been used in Table 2.1.

The path C for the complex integral in Eq. (4.2) begins at μ = -π/2+i∞ moving through the points, -π/2, 0, π/2 before reaching the end points at π/2-i∞, see Fig. 4.1. In the passage, the exponential term traverses through a stationary point at $\mu = \theta$. Generally speaking, the complex integral cannot be evaluated exactly but it can readily be handled by an asymptotic analysis known as the double saddle-point method [1]. It starts by indenting the path from C to the steepest descent path C_μ that is specified by

$$\mathrm{Im}\left(W^2\right) = 0 \ , \tag{4.4a}$$

where the complex variable, W, is defined as

$$W^2(\mu)/2 = ikR_2\left[1 - \cos(\mu - \theta)\right]. \tag{4.4b}$$

The steepest descent path C_μ is also shown in Figure. 4.1 for information. The method leads to an approximate solution for large kR_2.

There is a pole (at the location of $\mu_p^{(m)}$, say) in the integrand of Eq. (4.2) which can be determined by solving the transcendental function of

$$\cos \mu_p^{(m)} + \chi^{(m)}\left(\mu_p^{(m)}\right) = 0 \, . \tag{4.5a}$$

The subscript p denotes the corresponding parameter for the pole location. It should be stated that the presence of poles in the integrand has limited the applicability of the double saddle-point method. However, this deficiency can be removed by using the method of pole subtraction [9].

Since the type of ground surface is known in the context of most discussions, the superscript (m) can conveniently be suppressed in the following presentation of results unless there is a conflict for its use. Let the apparent admittance of the air/ground interface be β_p such that

$$\beta_p := \chi\left(\mu_p\right) \; ; \; \mathrm{Re}\left(\sqrt{1-\beta_p^2}\right) > 0 \; . \tag{4.5b,c}$$

The pole location μ_p can be defined uniquely in terms of β_p by the following pair of trigonometrical functions:

$$\cos\mu_p = -\beta_p \text{ and } \sin\mu_p = +\sqrt{1-\beta_p^2} \quad , \tag{4.6a,b}$$

which implies that $\pi \geq \mathrm{Re}\left[\mu_p\right] \geq \pi/2$. By noting $\left|\beta_p\right| \leq 1$ and writing

$$\mu_p = \pi/2 + u_p + iv_p \, , \tag{4.7}$$

where $0 \leq u_p \leq \pi/2$, the range for v_p can then be determined as a function of u_p as follows:

$$-\cos\left[u_p\right] \leq \sinh\left[v_p\right] \leq \cos\left[u_p\right] . \tag{4.8a}$$

The assumption of $\left|\beta_p\right| \leq 1$ is valid for most outdoor ground surfaces and sound absorbing materials.

By considering Eqs. (4.6), (4.7) and (4.8a), a region of all admissible values of μ_p can be mapped out in the complex μ plane:

$$\pm\cos\left[u_p\right] - \sinh\left[v_p\right] = 0 \, , \tag{4.8b}$$

where ± represents the corresponding equations for the upper and lower bounds of the region. For instance, v_p is bounded between $-\ln\left(1+\sqrt{2}\right)$ and $\ln\left(1+\sqrt{2}\right)$ when u_p = 0. On the other hand, the lower and upper bounds of v_p are identical at zero when $u_p = \pi/2$. This enclosed area is marked as Region *I* in Figure. 4.1.

Analytical solutions for $\beta_p = \beta_p^{(m)}$ are available for the locally reacting (m = -1) and the extended reaction (m = 0) grounds. In the contrary, numerical solutions are only available for hard-backed (m = 1) and impedance-backed (m = 2) porous layers. Table 2.1 summarizes the results of the pole locations for different types of ground surfaces.

The pole described in the integrand of Eq. (4.2) is often referred as the surface wave pole. It leads to the generation of surface waves from the ground surface due to an airborne source. In addition to the acoustical characteristics, its existence and detection are also dependent on the angle of incidence of the reflected wave, θ. According to the analysis, the surface wave is excited when $\mathrm{Im}\left[W^2(\mu_p)\right] \le 0$. Consequently, a combination of Eq. (4.4a) with Eq. (4.8a) classifies a region of μ_p in the complex μ-plane (marked as Region II in Figure. 4.1).

Upon using the double saddle-point nethod together with the pole subtraction method, the diffraction wave term [see Eq. (4.2)] can be evaluated asymptotically. The analytical solution [1] can be summarized as follows,

$$p_D = P_{\mathrm{erfc}} + \phi_s \,. \tag{4.9a}$$

where

$$P_{\text{erfc}} = 2i\sqrt{\pi}\left(ikR_2/2\right)^{1/2} \frac{\beta_p e^{-w_p^2}\text{erfc}(-iw_a)}{E_p\sqrt{\sin\theta\sin\mu_p}} \cdot \frac{e^{ikR_2}}{4\pi R_2}, \tag{4.9b}$$

and erfc( ) is the complementary error function term with a complex argument and w_a is identified as the apparent numerical distance. According to Eq. (4.4b), the apparent numerical distance is related to $W(\mu)$ by

$$w_a = W\left(\mu_p\right)\Big/\sqrt{2} \quad , \tag{4.10a}$$

which can be written in terms of μ_p and θ as

$$\frac{w_a^2}{ikR_2} = 1-\cos\left(\mu_p-\theta\right) = 1+\beta_p\cos\theta-\sqrt{1-\beta_p^2}\sin\theta \ . \tag{4.10b}$$

The definitions for E_p and ϕ_s in Eq. (4.9b) will be explained in the following paragraphs. The first term of Eq. (4.9a), P_{erfc}, is referred as the complementary error function term and the second term, ϕ_s is called the correction term.

It is remarkable that the surface wave component does not appear explicitly as a separate term in expression for p_D and P_{erfc}. Rather, its contribution has been absorbed into the complementary error function shown in Eq. (4.9b). Additionally, E_p in Eq. (4.9b) can be determined for different types of ground surfaces as follows:

(i) a locally reacting surface, m = -1

$$E_p = E_p^{(-1)} = 1, \tag{4.11a}$$

(ii) an extended reaction surface, m = 0

$$E_p = E_p^{(0)} = 1-\zeta^2 \quad , \tag{4.11b}$$

(iii) a hard-backed porous layer, m = 1

$$E_p = E_p^{(1)} = 1 + i\left(\zeta\beta_p^{(1)}/N_p\right)\left[\tan\left(kN_p d\right) + \left(kN_p d\right)\sec^2\left(kN_p d\right)\right] \quad , \tag{4.11c}$$

(iv) an impedance-backed porous layer, $m = 2$

$$E_p = E_p^{(2)} = 1 + \frac{i[\beta_p^{(2)}]^2}{N_p^2}\left\{\frac{\tan\left(kN_p d\right) + kN_p d\sec^2\left(kN_p d\right)}{\left(\beta_2/\zeta N_p\right) - i\tan\left(kN_p d\right)} - \right.$$

$$\left.\left(\beta_2/\zeta N_p\right)\times\frac{\tan\left(kN_p d\right) - kN_p d\sec^2\left(kN_p d\right)}{1 - i\left(\beta_2/\zeta N_p\right)\tan\left(kN_p d\right)}\right\}, \tag{4.11d}$$

where $N_p \equiv N(\mu_p)$ with $N(\mu)$ defined in Eq. (4.3).

The correction term in Eq. (4.9a) can be estimated asymptotically to yield

$$\phi_s \approx \overline{P}_{\text{erfc}} - \left(1 - V_\theta\right)\frac{e^{ikR_2}}{4\pi R_2} \quad , \tag{4.12a}$$

where $\overline{P}_{\text{erfc}}$ can be considered as an asymptotic approximation of the complementary error function term [see Eq. (4.9b)], V_θ is often treated as the plane wave reflection coefficient:

$$V_\theta = \frac{\cos\theta - \beta_\theta}{\cos\theta + \beta_\theta}, \tag{4.12b}$$

and β_θ is recognized as the effective admittance of the flat ground [10]:

$$\beta_\theta := \chi(\theta) \ ; \ \text{Re}\left(\sqrt{1 - \beta_\theta^2}\right) > 0 \ , \tag{4.13a,b}$$

which is a different parameter in contrast with the apparent admittance, β_p given in Eq. (4.3). The asymptotic approximation of P_{erfc} can be determined by

$$\overline{P}_{\text{erfc}} = \left[\frac{2\beta_p/\sqrt{\sin\theta\sin\mu_p}}{E_p\sqrt{2[1 - \cos(\mu_p - \theta)]}}\right]\frac{e^{ikR_2}}{4\pi R_2}. \tag{4.14}$$

It is noteworthy that the second term of ϕ_s is written conveniently in terms of V_θ. It should be straightforward to show that ϕ_s is identical to that shown in Ref. [3].

Substitution of Eqs. (4.9a) and (4.9b) into Eq. (4.1) verifies an asymptotic expression for the sound fields above a plane interface:

$$p = \frac{e^{ikR_1}}{4\pi R_1} + \frac{e^{ikR_2}}{4\pi R_2} + P_{\text{erfc}} + \phi_s \,, \tag{4.15}$$

where P_{erfc} is given by Eq. (4.9b) and ϕ_s is approximated asymptotically by Eq. (4.12a). An approximation may be applied for near-grazing propagation about a ground surface of small β_p. The correction factor, $\phi_s \approx 0$ and the factor, $E_p = \sqrt{\sin\theta \sin\mu_p} \approx 1$. Hence, the sound field can be simplified by substituting Eq. (4.9b) into Eq. (4.15) to yield

$$p \approx \frac{e^{ikR_1}}{4\pi R_1} + \left[V_p + \left(1 - V_p\right) F\left(w_a\right)\right] \frac{e^{ikR_2}}{4\pi R_2} \,, \tag{4.16}$$

where V_p is sometimes termed as the poles of reflection coefficient [13]:

$$V_p = \frac{\cos\theta - \beta_p}{\cos\theta + \beta_p} \,, \tag{4.17}$$

and the boundary loss factor F is defined by

$$F\left(w_a\right) = 1 + i\sqrt{\pi} w_a e^{-w_a^2} \operatorname{erfc}\left(-i w_a\right) \quad . \tag{4.18}$$

The poles of reflection coefficient resemble a similar form as the plane wave reflection coefficient except that β_θ and β_p are used in the respective expressions, *cf* Eqs. (4.12b) and (4.17).

The approximations used for deriving Eq. (4.16) are only applicable for a ground type with high flow resistivity. A locally reacting ground can naturally meet all of these

conditions [71], but they become too stringent for some extended reaction ground surfaces and most layered grounds [3]. It is generally not possible to lay down a set of simple criteria for the geometrical locations, the acoustical characteristics of the ground, and the thickness of the layer such that Eq. (4.16) is sufficiently accurate to predict the total sound fields. As a result, the two terms in Eq. (4.12a) for ϕ_s are needed in order to give an accurate and uniform asymptotic expression for predicting the sound fields above a layered ground. This allows the second order terms to be included in the asymptotic series giving a more accurate numerical solution.

A closer examination of ϕ_s in Eq. (4.12a) and P_{erfc} in Eq. (4.9b) indicates the asymptotic solution can be reorganized in the classical form as

$$p \approx \frac{e^{ikR_1}}{4\pi R_1} + Q\frac{e^{ikR_2}}{4\pi R_2} \quad , \tag{4.19a}$$

where Q can be regarded as spherical reflection coefficient for different types of ground surfaces:

$$Q = V_\theta + g_w \, . \tag{4.19b}$$

where V_θ is furnished by Eq. (4.12b) and the ground wave term g_w is given by

$$g_w = P_{\text{erfc}} - \overline{P}_{\text{erfc}} \quad . \tag{4.19c}$$

The two terms, P_{erfc} and $\overline{P}_{\text{erfc}}$, in Eq. (4.19c) are respectively defined by Eqs. (4.9b) and (4.14). Mathematically speaking, the difference between the complementary error function term and its asymptotic expression give rise to the ground wave term. Substitution of Eqs. (4.9b) and (4.9c) into Eq. (4.19c) leads to

$$g_w = \frac{2\beta_p}{E_p\sqrt{\sin\theta\sin\mu_p}}\left\{\left(2\left[1-\cos(\mu_p-\theta)\right]\right)^{-1/2} + i\sqrt{\pi}\left(ikR_2/2\right)^{1/2} e^{-w_a^2}\operatorname{erfc}(-iw_a)\right\}. \quad (4.20a)$$

Replacing the first term of the curly bracket with the apparent numerical distance [see Eq. (4.10b)], g_w can be expressed in terms of the boundary loss factor $F(w_a)$ as:

$$g_w = \frac{\beta_p}{E_p\sqrt{\sin\theta\sin\mu_p}}\frac{F\left(w_a\right)}{\sqrt{1-\cos(\mu_p-\theta)}} = \frac{\sqrt{2ikR_2}\beta_p F\left(w_a\right)}{E_p w_a\sqrt{\sin\theta\sin\mu_p}} \ , \quad (4.20b)$$

where $F(w_a)$ is the boundary loss factor given in Eq. (4.18).

Three new terms, the approximate numerical distance w_θ, the admittance ratio r_β and the ratio of numerical distances, r_w are introduced. They are defined as follows:

$$w_\theta = \sqrt{ikR_2/2}\left(\cos\theta+\beta_\theta\right) \quad , \quad (4.21a)$$

$$r_\beta = \beta_p/\beta_\theta \ , \quad (4.21b)$$

and

$$r_w = w_a/w_\theta \ . \quad (4.21c)$$

It becomes clear that there is a need to define w_a [see Eq. (4.10)] separately in order to differentiate it from w_θ given in Eq. (4.21a). They are, respectively, named as the apparent and approximate numerical distances which are not identified explicitly in the earlier publications [1-4, 11]. The two dimensionless ratios, r_β and r_w, are also found useful to simplify the resulting expression for the ground wave term. Making use of these three new terms, g_w can be condensed further to a more recognizable form as,

$$g_w = A\left(1-V_\theta\right)F\left(w_a\right), \quad (4.22a)$$

where

$$A = \frac{\left(r_\beta / r_w\right)}{E_p \sqrt{\sin\theta \sin\mu_p}}, \tag{4.22b}$$

which is known as the augmented diffraction factor.

To summarize the mathematical analysis, the total sound fields above a plane interface (either locally reacting or non-locally reacting) can be obtained by substituting Eqs. (4.22a) and (4.22b) into Eq. (4.19b) which, in turn, into Eq. (4.19a) to yield

$$p \approx \frac{e^{ikR_1}}{4\pi R_1} + \left[V_\theta + A\left(1 - V_\theta\right) F(w_a)\right] \frac{e^{ikR_2}}{4\pi R_2} \quad . \tag{4.23}$$

It is enlightening to show that the monopole sound field above the plane interface can be cast in the classical form of Eq. (4.19a). The solution consists of a direct wave term plus the ground reflected wave term multiplied by the spherical wave reflection coefficient. Furthermore, the spherical wave reflection coefficient can be split to a plane wave reflection coefficient term plus a ground wave component. The spherical wave reflection coefficient is different for various types of ground surface owing to their differences in the apparent admittance β_p and the augmented diffraction factor A.

In the earlier study [3], Li and Liu correctly derived the formula shown in Eq. (4.15) but they were unable to reduce it to the form given in Eq. (4.23). Nevertheless, their numerical analyses indicated that the asymptotic formula is very accurate even for a relatively short horizontal separation. The close similarity between V_p and V_θ [see Eqs. (4.17) and (4.12b)] is notable. Their only difference lies on their use of either the apparent admittance, β_p or the effective admittance, β_θ. Use of V_p in Eq. (4.16) is accurate only for a limited class of ground surfaces [9]. On the other hand, use of V_θ in

Eq. (19b) for Q permits a more accurate computation of the total monopole sound fields in Eq. (4.23). The improved formulation offers better physical interpretations for each term. With limited comparisons, its use as the numerical solutions has been demonstrated to be accurate for $kR_2 >> 0.5$, and, for most outdoor ground surfaces and sound absorbing materials [1].

4.3 A Heuristic Approximation of the Ground Wave Term at Short Ranges with $kR_2 < 0.5$

For the near grazing propagation above a locally reacting ground, Chien and Soroka [4] suggested that $w_\theta \approx w_a$, i.e. $r_w \approx 1$. In addition, $E_p = 1$, $r_\beta = 1$ and $\sqrt{\sin\theta \sin\mu_p} \approx 1$. Consequently, $A \approx 1$ that leads to an approximate expression for g_w as

$$g_w = \left(1 - V_\theta\right) F\left(w_\theta\right) \quad , \tag{4.24a}$$

Substitution Eq. (4.24a) into (4.20) and its subsequent employment in Eq. (4.19a) give the sound field in the classical form of the Weyl-Van der Pol formula:

$$p \approx \frac{e^{ikR_1}}{4\pi R_1} + \left[V_\theta + \left(1 - V_\theta\right) F(w_\theta)\right] \frac{e^{ikR_2}}{4\pi R_2} \quad , \tag{4.24b}$$

It should be emphasized that the term in Eq. (4.24a) is different from the 'exact' formula for g_w, see Eq. (4.20b), on two aspects. First, A is approximately set at 1. Secondly, the approximate numerical distance w_θ is used instead of the apparent numerical distance w_a in the calculation of the boundary loss term. The approximate numerical distance was simply identified as the numerical distance in all previous publications, [e.g. 4-6]. Despite these two approximations, the Weyl-Van der Pol formula has proved to be accurate for

predicting the sound fields above an impedance ground for all source/receiver geometries [5].

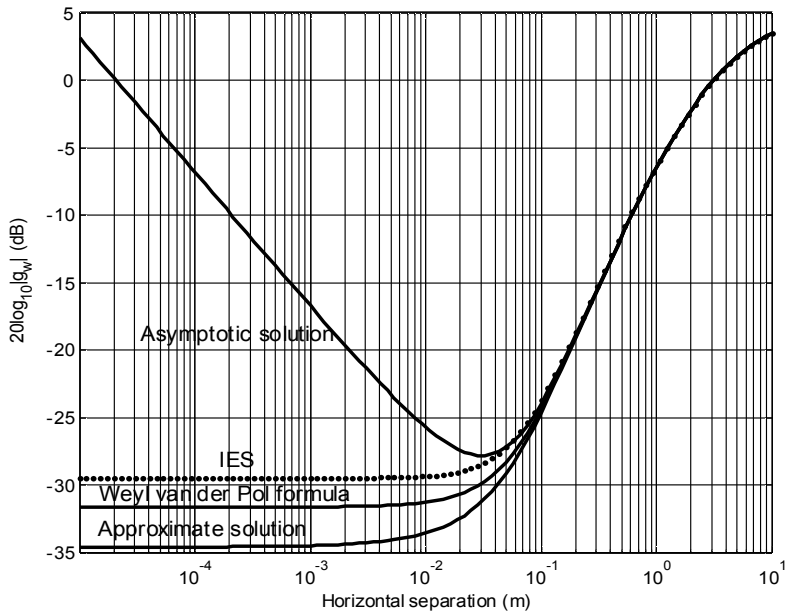

Figure 4.2: The prediction of ground wave term versus the horizontal separation above a locally reacting ground. Solid line: Weyl-Van der Pol formula; circles: Integrated Exact Solution (IES); dotted line: full asymptotic solution; dashed line: approximate solution with the $1/\sqrt{\sin\theta}$ term removed.

To examine the validity of the classical Weyl-Van der Pol formula, we compare in Figs. 4.2 and 4.3 the predictions of g_w and p above a typical locally reacting ground. Prior numerical simulations, have suggested that the effect of the ground wave term is more pronounced if the source and receiver are both close to the air/ground interface. Consequently, the source and receiver are chosen at 0.02 m and 0.04 m above the ground in all numerical simulations presented below unless stated otherwise.

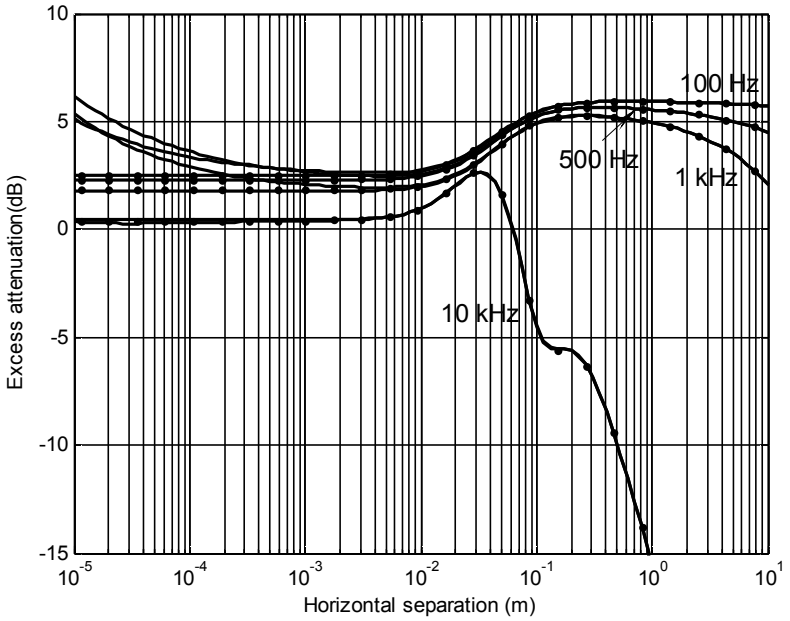

Figure 4.3: The prediction of Excess Attenuation (EA) versus horizontal separation above a locally reacting ground. The same geometrical configuration as Figure 4.2 is used. The captions are the same as Figure 4.2.

For convenience, a 2-parameter model [14] is used to calculate the specific normalized impedance of a locally reacting ground as follows:

$$Z_c / \rho c = 0.436(1+i)\sqrt{\sigma_e / f} + 19.74i(\alpha_e / f), \tag{4.25}$$

where σ_e is the effective flow resistivity given in Pa m s^{-2} and α_e is the effective rate of change of porosity in depth given in m^{-1}. The respective parametric value of 300 kPa m s^{-1} and 100 m^{-1} for σ_e and α_e, which are representative of a typical ground surface, are chosen in the numerical simulations shown in Figs. 4.2 and 4.3. For different horizontal ranges, the magnitude of g_w is plotted and shown in Fig. 4.2. Comparisons are made for g_w calculated by the wave-based numerical solutions, the Weyl-Van der Pol formula [see Eq. (24b)] and the full asymptotic solution given in Eq. (4.20b). The numerical solutions according to wave-based method are referred as the integrated exact solutions (IES)

where the details of its implementation is provided in Ref. [1]. The simulation results for other different frequencies have comparable forms. Hence, selected results for the source frequency at 1 kHz are only shown in Fig. 4.2 and simulations for other frequencies are not displayed in this paper for succinctness. The numerical solutions computed by the Weyl-Van der Pol formula for different ranges are displayed in solid line. The accurate solutions computed by the IES scheme are shown in black circles. The numerical results according to the full asymptotic solution are plotted in dotted line.

For this particular ground surface, the specific normalized admittance, β_θ, has an approximate magnitude of 0.082 and a lagging phase angle of 0.9 radian at the source frequency of 1 kHz. Hence, the assumption of $\sqrt{\sin \mu_p} \approx 1$ is valid for all source/receiver geometrical configurations. Furthermore, the presence of surface wave component is evinced with this choice of ground parameters and source frequency. It is because, as shown in Fig. 4.2, the ground wave term g_w is greater than 0 dB for a horizontal range between 1.2 m and 12 m. This 'positive' excess attenuation indicates an enhancement of the total sound fields which is largely due to the presence of the surface wave component [5]. The prediction of g_w according to the Weyl-Van der Pol formula agrees very well with IES at ranges greater than about 0.3 m ($\theta \sim 78°$). Extending beyond this range ($r \geq$ 0.3 m and $\theta \geq 78°$), the assumptions of $\sqrt{\sin\theta} \approx 1$, $w_a \approx w_\theta$ and $kR_2 \to \infty$ are all valid. Thus, Weyl-Van der Pol formula can give an accurate calculation of g_w that leads to an excellent agreement with IES for the prediction of the total sound fields at long ranges.

The numerical error becomes more noticeable for the horizontal range $r < 0.1$ ($\theta \leq 60°$). In the intermediate range where the horizontal range lies between 0.1 and 0.3 m

($60° \le \theta \le 78°$), the presence of the $1/\sqrt{\sin\theta}$ term is essential in the prediction of g_w but the assumption of $\sqrt{\sin\theta} \approx 1$ is not sufficiently accurate to give precise predictions (to within 0.2 dB) in this range. In contrast, the assumption of $w_a \approx w_\theta$ still holds in this intermediate range. As a result, the prediction according to the Weyl-Van der Pol formula agrees reasonably well with the IES predictions in the intermediate range.

For the near field when $r < 0.1$ m ($\theta \le 60°$), the assumption of near-grazing propagation and large kR_2 are not strictly valid. Hence, the numerical error gradually increases as the horizontal range reduces. According to the IES predictions, the horizontal range can be treated effectively as zero when r is less than 1×10^{-3} (or θ is less than 1°). This limiting value of $20\log_{10}|g_w|$ is predicted to be constant at about – 23 dB when $r <$ 0.1 mm. On the other hand, the Weyl-Van der Pol formula underpredicts it by about 3 dB because of the assumptions of near-grazing propagation and large kR_2 cannot be met. In this situation, the asymptotic method fails. A numerical evaluation of the integral is needed in order to calculate g_w precisely. Although there is a significant error in the prediction of g_w in the near field, the Weyl-Van der Pol formula can still give accurate predictions of the total sound fields at short ranges. It should be noted at the near field that $w_\theta \to 0$, $F(w_\theta) \to 1$ and, hence, $g_w \approx \beta_\theta << 0$ for a locally reacting ground surface. As a result, the contribution from the ground wave term is much smaller than the contributions from the direct sound field. Hence, the error in predicting g_w does not have any significant impacts on the prediction of the total sound fields. Figure 4.3 presents the comparison of the predicted results according to different numerical schemes. Here, the excess attenuation (*EA*), which is defined as the ratio of total field to the free field, is

presented for four frequencies at 100 Hz, 500 Hz, 1 kHz and 10 kHz. The agreement between IES and Weyl-Van der Pol formula are excellent in all predictions for all frequencies at all ranges.

Based on the Weyl-Van der Pol formula, it is apparent that it is advantageous to remove the $1/\sqrt{\sin\theta}$ term in the asymptotic solution because its inclusion causes a non-removable singularity when $\theta \to 0$. In fact, the presence of the $1/\sqrt{\sin\theta}$ term in A [see Eq. (4.22b)] somewhat limits the general applicability of Eq. (4.23) for computing the total fields above a locally and non-locally reacting grounds. As shown in Fig. 4.2, the predictions of g_w according to Eq. (4.22a) are also presented for comparison with the IES and the Weyl-Van der Pol scheme. It becomes clear of the superiority for using Eq. (4.22a) to calculate the sound fields in the intermediate and long ranges when $r > 0.02$ m ($\theta > 18°$). However the numerical solution becomes divergence at the near field. This error becomes too excessive in the near field that can affect the accuracy when Eq. (4.23) is applied to predict the total sound fields, see the dotted line in Figure. 4.4.

For the near grazing propagation, a simple approximation may be suggested that the $1/\sqrt{\sin\theta}$ term can be set to 1 in Eq. (4.22b). Again, Figure. 4.2 shows a comparison of this simple approximate scheme (shown in dashed line) with other methods. It has been demonstrated that the 'removal' of the $1/\sqrt{\sin\theta}$ term is only satisfactory for long ranges. Noticeable discrepancies in the predictions are observed for the intermediate range and the near field. The numerical results computed by this simple approximate scheme are even inferior to that according to the Weyl-Van der Pol scheme for this set of the source/receiver geometry and the acoustical characteristic of the ground. On the other

hand, the replacement of w_a with w_θ as per the Weyl-Van der Pol formula has led to a better numerical agreement with the IES method by comparing the numerical results shown in solid and dashed lines in Figure 4.2.

To devise a better and uniform scheme at all ranges, it is important to examine the characteristic of the ground wave term g_w. An assessment of Eq. (4.20b) indicates that g_w can be more conveniently be expressed in a logarithm form as

$$B = 20\log_{10}\left|g_w\right|$$

$$= 20\log_{10}\left[\frac{\beta_p F\left(w_a\right)}{E_p\sqrt{\sin\mu_p}}\right] - 4.343\times\left[\ln\left(\sin\theta\right) + \ln\left|1-\cos(\mu_p-\theta)\right|\right]. \tag{4.26}$$

At the near field ($\theta \to 0$), $w_a \to 0$ and $F(w_a) \to 1$. Hence the first term of Eq. (4.26) is independent of θ at the close range. It is then straightforward to determine the stationary point of B by setting $\partial B/\partial\theta = 0$ to yield the following transcendental function:

$$\cosh\left(v_p\right)\cos\theta + \sin\left(u_p - 2\theta\right) = 0 \tag{4.27}$$

where Eq. (4.7) is used to replace μ_p in Eq. (4.26) in order to obtain the above equation. The solution of Eq. (4.27) leads to the stationary point $\theta_{\min}$.

No closed form solution is available for $\theta_{\min}$ but it can be determined by rearranging Eq. (4.27) as

$$\theta_{\min} = \cos^{-1}\left[\cos\left(u_p + \pi/2 - 2\theta_{\min}\right)\Big/\cosh\left(v_p\right)\right]. \tag{4.28}$$

The first approximation may be obtained by assuming v_p = 0 to give $\theta_{\min} = u_p/3$. The second approximation can be obtained by substituting the first approximation into Eq. (4.28) to give an improved approximation as

$$\theta_{\min} = \cos^{-1}\left[\cos\left(\pi/2 + u_p/3\right)\Big/\cosh\left(v_p\right)\right]. \tag{4.29}$$

This iteration process can be repeated recursively to give a converged solution for $\theta_{\min}$ that satisfies Eq. (4.28). A second derivative of B with respect to θ may be applied straightforwardly to confirm that $\theta_{\min}$ represents a local minimum value. These details are not shown for brevity.

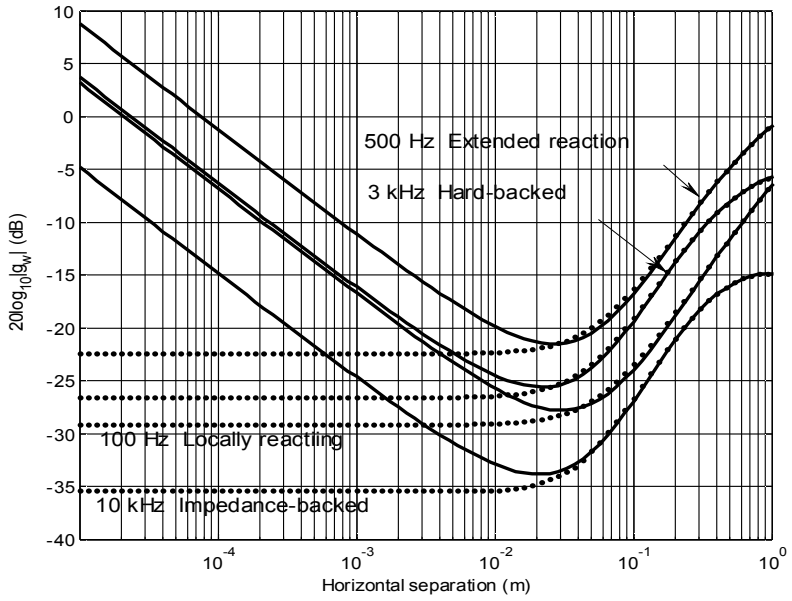

Figure 4.4: The comparison of ground wave terms computed by the asymptotic solution (shown in solid lines) and the Integrated Exact Solution (IES shown in circles).

To see the characteristic of B at the stationary point $\theta_{\min}$, it is instructive to plot B versus the horizontal range for different types of ground surfaces. For the locally reacting ground, the two-parameter impedance model [see Eq. (4.25)] is used. An empirical model [13] is employed to model the acoustical characteristics of the non-locally reacting interface such that the index of refraction (propagation constant), and density ratio are given respectively by Eqs.(2.38a) and (2.38b). Again, the parametric values of σ_e = 300

kPa m s^{-1} and α_e = 100 m^{-1} are used to model the normalized characteristic impedance of the locally reacting interface. On the other hand, the parametric values of σ_e = 50 kPa m s^{-2}, q = 1.39, and Ω = 0.269 are selected for the extended reaction interface. For a rigid porous layer, its thickness is set at 0.05 m. These parametric values are used in the numerical simulations of the following graphs with the source and receiver heights fixed respectively at 0.04 m and 0.02 m above the air/ground interface. In the numerical simulations shown in Fig. 4.4, an individual frequency is used for each ground type because the results can be generalized as follows: the value of B decreases as r reduces, i.e. θ, increases. Regardless of the ground type, a local minimum point $\theta_{\min}$ can therefore be identified such that the solution for g_w starts to diverge when $\theta < \theta_{\min}$. It is known that approximate solution for g_w by the asymptotic method is invalid at the short range but the contribution of g_w to the total sound field is negligibly small in comparison with the direct wave term. It may be concluded as follows. So long as the error is not more than a few dB in g_w, it will not affect the accuracy for the prediction of the total sound fields. Hence, an acceptable solution may be simply recast from Eq. (4.23) to give

$$p \approx \frac{e^{ikR_1}}{4\pi R_1} + \left[V_\theta + G_w(\theta)\right]\frac{e^{ikR_2}}{4\pi R_2} \quad , \tag{4.30a}$$

where

$$G_w(\theta) = \begin{cases} g_w(\theta) & \text{if } \theta > \theta_{\min} \\ g_w(\theta_{\min}) & \text{if } \theta \le \theta_{\min} \end{cases} \quad , \tag{4.30b}$$

and $g_w(\theta)$ is given by Eq. (4.22a). Equation (4.30a) represents a uniformly valid solution that can be used to calculate the total sound field above a locally and non-locally reacting ground. Figure 4.5 presents the comparison of simulation results according to IES and

those calculated by Eq. (4.30a). In these graphs, typical results are shown for different types of ground surfaces where *EA* is plotted against the horizontal range. The agreement between the modified Weyl-Van der Pol formula and IES is excellent for all situations.

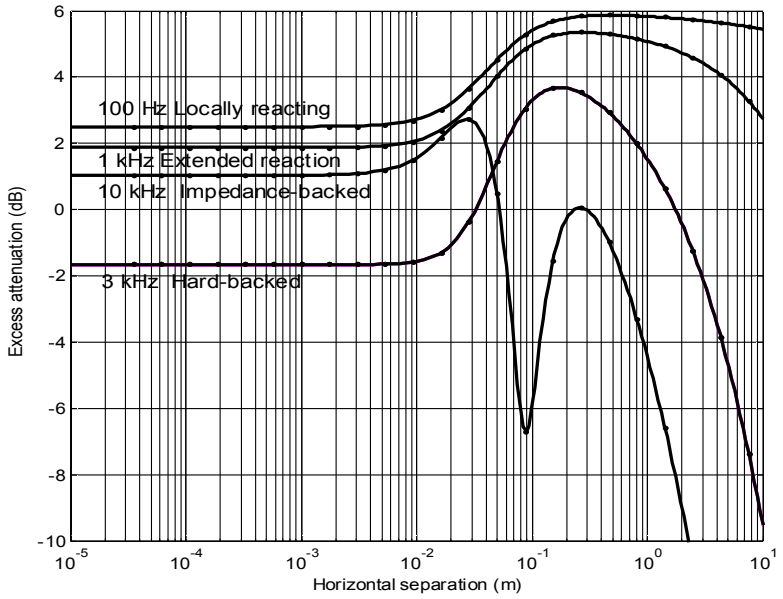

Figure 4.5: Same as Figure. 4.4 except the excess attenuation function is used to plot against the horizontal separation.

4.4 Summary

In this chapter, a modified Weyl-Van der Pol formula, see Eq. (4.30), has been presented for predicting the sound fields reflected from a plane interface. The interface can be a locally reacting ground or a non-locally rigid porous medium including a semi-infinite extended reaction ground, a hard-backed rigid porous layer and an impedance-backed rigid porous layer. The solution is based on an asymptotic analysis although a simple approximate scheme has been applied that allows an accurate prediction of the total sound fields at short ranges. Numerical comparisons have been conducted to confirm the validity of the formula. The modified Weyl-Van der Pol formula is valid for

all frequencies and all geometrical configurations. Unlike other computationally intensive schemes, the implementation of the modified Weyl-Van der Pol should allow real-time computations of the total sound fields even at high frequencies for all ranges.

CHAPTER 5: SOUND PENETRATION INTO A HARD-BACKED RIGID POROUS LAYER: THEORY AND EXPERIMENT

5.1 Introduction

Numerous studies have been conducted on sound propagation above a flat ground. There were also related studies for sound penetration into the porous half-space with an application for acoustic detection of buried objects [70, 76-78]. The acoustical properties of sound absorption materials, such as fiberglass and glass wool, are conveniently modeled as a rigid porous medium [89, 90] with a semi-infinite extent [1]. However, a model using multiple layers with finite thicknesses backed by a rigid plane is found necessary in many practical situations. Indeed, the acoustical properties of these layered structures were closer in modeling many realistic outdoor grounds. This type of ground surfaces is often referred as a hard-backed layer ground.

The sound propagation above a hard-backed porous ground was studied by Thomasson in mid 70s [95]. He found that the problem was analogous to the study of the propagation of sound above a locally reacting ground if the refractive index of the layer was sufficiently large. Allard and his coworks [89, 90] conducted a series studies exploring the phenomenon for the propagation of sound above a hard-backed porous layer in which they referred it as a non-locally reacting gound. More recently, Li and

Liu [2, 3] developed accurate asymptotic formulas for predicting the sound fields above a hard-backed and impedance-backed porous layer. They showed that the proposed formulas are numerically more efficient than other exact wave-based computational schemes, especially at long ranges and at high source frequencies. However, to the best of our knowledge, there are no related studies devoted to consider the sound fields within a hard-backed rigid porous medium. Indeed, a better understanding of this type of problems is one of the pre-requisites for an improved formulation to model the sound absorption characteristics of a multi-layer porous material placed above a perfectly-reflecting plane. This information will be particularly useful for the design of sound absorption materials by noise control engineers. We therefore see that there is a need to develop an accurate asymptotic formula for calculating the sound field within a hard-backed rigid porous medium.

In the chapter, the sound penetration into the hard-backed rigid porous medium due to a point monopole source will be investigated by means of a standard asymptotic method. A double saddle-point asymptotic method and the pole subtraction scheme will again be used in the present study. The asymptotic formula will be presented in section 5.2 with the detail mathematical analysis provided in the Appendix D. Numerical comparisons between the asymptotic solutions and the accurate wave-based numerical solutions will be provided for several cases in section 5.3. A set of precise laboratory measurements have been conducted to offer experimental data for validating the asymptotic formula. These details can be found in section 5.3. Finally, conclusions are provided in Section 5.4.

5.2 Theory

A rectangular co-ordinate system O-*x*-*y*-*z* is used in the following analysis where a layer of rigid porous medium is placed on a perfectly-reflecting ground. The thickness of the rigid porous medium is *d*. Its upper surface is set to coincide with the $z = 0$ plane and the hard ground is located at the plane of $z = -d$.

Suppose a monopole source with the angular frequency of ω is placed at $(0, 0, z_s)$ above the layered porous medium. The upper medium $z > 0$, is filled with air with density ρ and the speed of sound, *c*. The lower layer, $-d < z < 0$, is occupied by a homogeneous, rigid-frame porous material with the complex density, ρ_1 and the complex sound speed, c_1. The subscript 1 denotes the respective properties of the rigid porous medium.

The characteristic impedance of the rigid porous medium can be expressed in terms of the complex density ratio, ζ, and the index of refraction, *n*, as

$$Z_1 = \rho_1 c_1 / \rho c = 1/\zeta n, \tag{5.1a}$$

where

$$\zeta = \rho / \rho_1, \tag{5.1b}$$

and

$$n = c / c_1 \ . \tag{5.1c}$$

In an earlier study,[18] Li and Liu investigated the propagation of sound above an impedance-backed layered ground from a monopole source in the air. In the present study, we are interested in predicting the sound fields within the rigid porous medium. The time

dependent factor $e^{-i\omega t}$ is understood and omitted throughout the analysis. Figure 5.1(a) shows the rectangular coordinate system used in the analysis and the geometrical configuration of the problem.

The sound fields above a hard-backed layered medium can be modeled by the Helmholtz equation:

$$\nabla^2 p + k^2 p = -\delta(x)\delta(y)\delta(z - z_s) \tag{5.2}$$

where p is the sound pressure, $k(=\omega/c)$ is the wave number and delta function at the right side of Eq. (5.1) represents a monopole source locating at (0, 0, z_s). The sound pressure p_1 within the rigid porous medium is given by

$$\nabla^2 p_1 + k_1^2 p_1 = 0 \quad , \tag{5.3}$$

where k (= ω/c_1) is also known as the propagation constant of lower medium. The boundary conditions at the two interfaces require that (i) the acoustic pressure and normal particle velocity are continuous at $z = 0$, and, (ii) the normal particle velocity goes to zero due to the presence of the hard ground at $z = -d$. It is considered that the receiver is situated at $(x, y, -D)$ in the porous medium where $d \geq D \geq 0$ and r $(=\sqrt{x^2 + y^2})$ is the horizontal separation between the source and receiver, see Figure. 5.1(b).

By using the method of Fourier transformation in Eqs. (5.2) and (5.3) and imposing the required boundary conditions at the two interfaces, p and p_1 can be solved that can subsequently be expressed in terms of their respective inverse Fourier integrals. In particular, the sound fields within the rigid porous medium can be written as the sum of a pair of inverse Fourier integrals as,

$$p_1(0, z_s \mid r, -D) = I_C(D) + I_C(2d - D)\,, \tag{5.4a}$$

where I_C, which is a canonical integral, is given by

$$I_C(Z) = \frac{i}{4\pi}\int_0^{\infty} \frac{\kappa(1 - i\tan K_1 d)}{K - i\zeta K_1 \tan K_1 d} J_0(\kappa r) e^{iKz_s} e^{iK_1 Z} d\kappa\,, \tag{5.4b}$$

in which the dummy argument Z is the depth specifying the location of an arbitrary receiver with the same range r. In Eq. (5.4b), J_0 as the zero-order Bessel function and the integral variable κ taken as the horizontal components of the wave vectors for the upper and lower media. The parameters, K and K_1, are defined by

$$K = +\sqrt{k^2 - \kappa^2}\quad, \tag{5.5a}$$

and

$$K_1 = +\sqrt{k_1^2 - \kappa^2}\,. \tag{5.5b}$$

They can be interpreted as the vertical components of the propagation wave vectors in the upper and the lower media, respectively. The choice of positive roots for K and K_1 guarantees that both Im(K) and Im(K_1) are greater than zero. These two conditions permit bounded and finite solutions for the inverse Fourier integrals as $z \to -\infty$ for all K and K_1.[5]

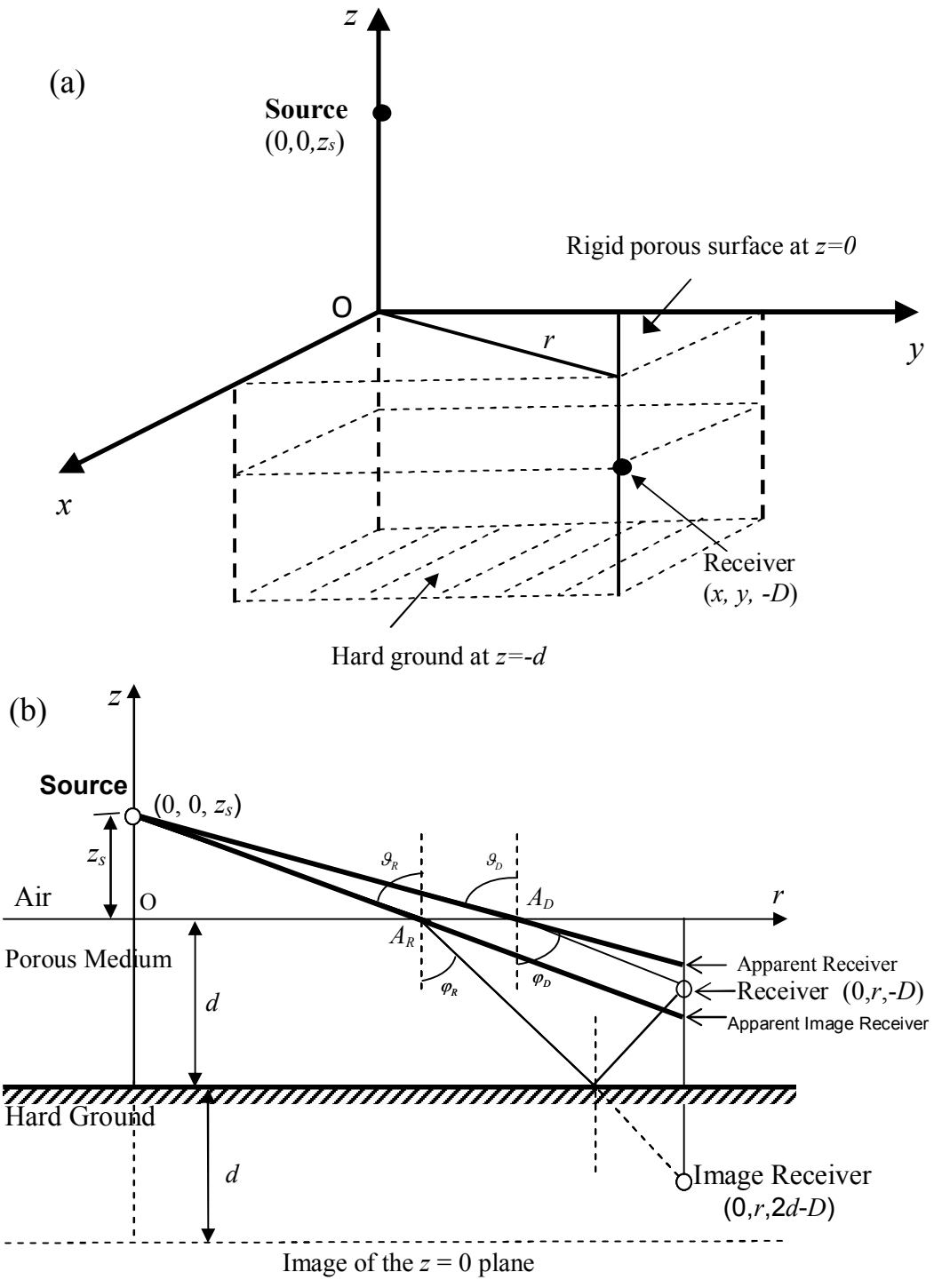

Figure 5.1: The schematic diagram of the problem. (a) The co-ordinate system used in the study; (b) A two-dimensional view of the source/receiver configuration.

The reason for this specific choice of branch cuts can be illustrated further by considering a limiting case when $d \to \infty$, i.e. an extended reaction ground. In this situation, the integrand of the second integral vanishes because the term $e^{iK_1(2d-D)}$ becomes exponentially small. Hence, p_1 can then be reduced from Eq. (5.4) to an identical expression given for the penetration of sound into a semi-infinite extended reaction ground [1] in this limiting case. However, it is important to note that the canonical integral [see Eq. (5.4b)] is different from the corresponding expression for the penetration of sound into a semi-infinite extended reaction ground even when all other parameters are identical in these two different types of rigid porous media. It is because the term $\left(1-i\tan K_1 d\right)/\left(K-i\zeta K_1 \tan K_1 d\right)$ in Eq. (5.4b) is replaced by $1/\left(K+\zeta K_1\right)$ for the latter case. Hence, the refracted sound fields are fundamentally different in these two cases.

In the current study, we are primarily interested in the sound fields within the hard-backed rigid porous layer. According to Eq. (5.4), p_1 consists of two terms due to the source and its image. As shown in Fig. 5.1b, the hard ground creates an image receiver. It is possible to trace the sound rays emanating from the source to the receiver and its image. The first integral can therefore be identified as the contribution from the transmitted wave travels from air to the receiver directly. The second integral is then recognized as the refracted wave broadcasts through the rigid porous medium that hits the hard ground before it reaches the receiver. It is then possible to interpret this refracted wave reaches the image receiver as shown in Fig. 1b. For ease of reference, the first integral is referred as the D-refracted wave term while the second is named as the R-

refracted wave term. Hence, the pair of inverse Fourier integrals can be represented suitably by the canonical integral shown in Eq. (5.4b).

Exact analytical solutions for the D-refracted and R-refracted wave terms are difficult, if not impossible, to obtain. However, the integral of Eq. (5.4b) can be evaluated quite conveniently by a standard asymptotic technique using the saddle path method [1]. To assist subsequent presentation, it is convenient to introduce a pair of complex polar angles μ and μ_1 in the upper and lower medium respectively. They are measured from the vertical z-axis which are used to characterize the directions of the incident waves propagated in the upper medium and the refracted wave transmitted into the lower medium. These two angles are related according to Snell's law by

$$\sin\mu = n\sin\mu_1 . \tag{5.6a}$$

They can also be written in terms of the horizontal propagation vector, κ, as

$$\kappa = k\sin\mu = k_1\sin\mu_1 \quad . \tag{5.6b}$$

It follows immediately from Eqs. (5.5a) and (5.5b) that the vertical components of the propagation wave vectors can be shown to give,

$$K = k\cos\mu \quad , \tag{5.7a}$$

and

$$K_1 = kN(\mu) \ , \tag{5.7b}$$

where

$$N(\mu) = +\sqrt{n^2 - \sin^2\mu} \ , \tag{5.7c}$$

and the positive root of the branch point is chosen for N.

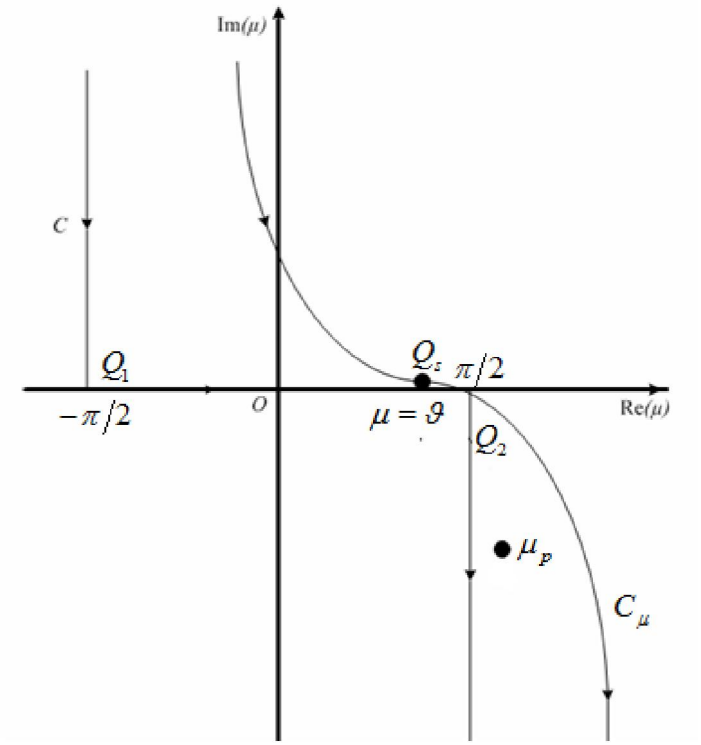

Figure 5.2: The integration paths in the complex μ plane. The label C is the original path, C_μ is the steepest descent path and Q_s is the saddle point.

Substitution of Eqs. (5.6) and (5.7) into Eq. (5.4b) gives

$$I_C(Z) = \frac{ik}{4\pi}\int_C \frac{\gamma(\mu)\sin\mu\cos\mu G_0^{(1)}(\mu)}{\cos\mu+\chi(\mu)} e^{ikf_b(\mu,Z)} d\mu \ , \tag{5.8}$$

where $\gamma(\mu)$ is specified by

$$\gamma(\mu) = \left[1 - i\tan(kNd)\right]/2 \ , \tag{5.9a}$$

which is introduced to facilitate the presentation of the analytical formulas. The "non-oscillatory" Hankel function of the first kind $G_0^{(1)}(\mu)$ is defined as

$$G_0^{(1)}(\mu) = H_0^{(1)}(kr\sin\mu)e^{-ikr\sin\mu} \ , \tag{5.9b}$$

$f_b(\mu)$ is the oscillatory part of the integral in Eq. (5.8) :

$$f_b(\mu, Z) = r\sin\mu + z_s\cos\mu + Z\cos\mu_1 \quad , \tag{5.9c}$$

and $\chi(\mu)$ is the total admittance of the hard-backed layered medium:

$$\chi(\mu) = -i\zeta N\tan(kNd) \tag{5.9d}$$

where $N(\mu)$ is given in Eq. (5.7c).

The integration path C can be stipulated by starting μ at $-\pi/2 + i\infty$ moving parallel to the imaginary axis to the point $-\pi/2$. It is then traversed along the real axis to $\pi/2$ before following the path parallel to the imaginary axis again to arrive at $\pi/2 - i\infty$. Figure 5.2 shows the schematic diagram of the integration path C in the complex μ plane. The ray path linking the source and receiver can be determined by using Snell's Law. Alternatively, it can also be found by locating the stationary point of the oscillatory function, f_b, given in Eq. (5.9b). This involves solving the following function,

$$\frac{\partial f_b(\mu, Z)}{\partial\mu} = 0 \tag{5.10a}$$

for the stationary point at the complex angle, $\mu = \vartheta$ and $\mu_1 = \varphi$. Substituting Eq. (5.9c) into Eq. (5.10a), it is possible to set up a trigonometric function

$$r = z_s\tan\vartheta + Z\sin\varphi, \tag{5.10b}$$

for determining the ray path. Li and Liu [1] outlined a straightforward method to determine ϑ and φ numerically where these two complex angles are related according to the Snell's law, see Eq. (5.6a). They can be interpreted as the polar angles of the sound ray in the upper (air) and lower (rigid porous) media, respectively. It is handy to introduce the following distances to aid physical interpretation of the ray paths at different segments in the upper and lower media. Figure 5.3 shows a schematic diagram

for these geometrical configurations. The separations above (R_s) and below (R_Z) the porous interface can be written in terms of ϑ and φ as

$$R_s = z_s/\cos\vartheta \text{ and } R_Z = Z/\cos\varphi . \quad (5.11a,b)$$

The apparent distance of the sound ray traveling in the absence of the lower medium is denoted by

$$R_\vartheta = \frac{r}{\sin\vartheta} . \quad (5.11c)$$

With these physical parameters, the acoustical path length (L), the energy path length (R_r) and the physical path length (Δ) can be written as,[20]

$$L(Z) = f_b(\vartheta) = R_s + nR_Z , \quad (5.12a)$$

$$R_r = \frac{z_s}{\cos\vartheta} + \frac{Z\cos^2\vartheta}{n\cos^3\varphi} \quad (5.12b)$$

and

$$\Delta(Z) = \sqrt{R_\vartheta R_r} . \quad (5.12c)$$

The acoustical and physical path lengths are found to be useful to construct an asymptotic solution for the total sound fields within the porous medium.

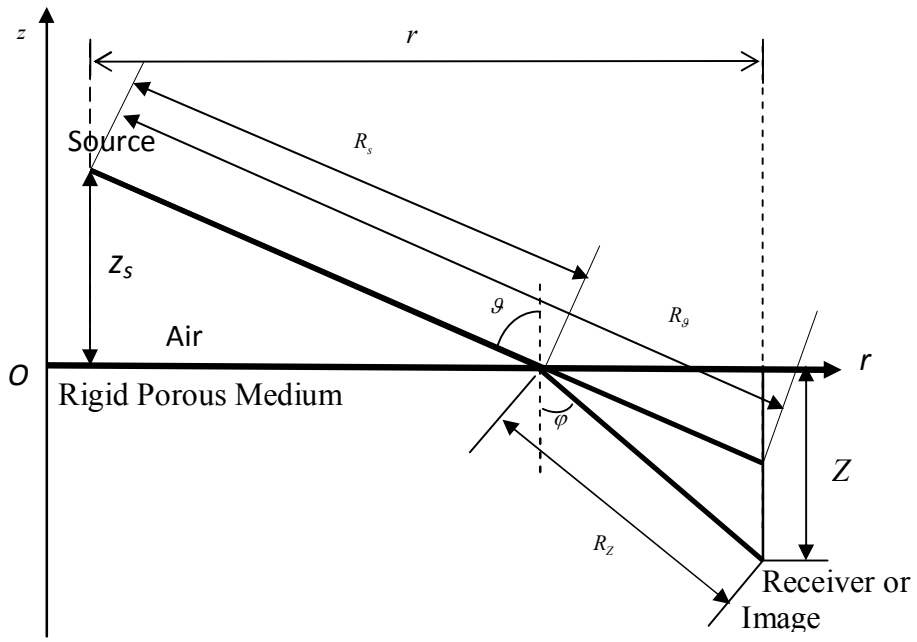

Figure 5.3: A schematic diagram show different geometrical terms used in the analytical solution.

The asymptotic solution for I_C can be derived in a straightforward manner and its details are provided in Appendix D for completeness. Indeed, I_C can be stated in a rather compact form by introducing the plane wave reflection coefficient $V(\vartheta)$, the plane wave transmission coefficient $T(\vartheta)$, and, the spherical wave refraction coefficient $q(\vartheta)$:

$$V\left(\vartheta\right)=\frac{\cos\vartheta-\beta_\vartheta}{\cos\vartheta+\beta_\vartheta}, \tag{5.13a}$$

$$T\left(\vartheta\right)=1+V\left(\vartheta\right)=\frac{2\cos\vartheta_\vartheta}{\cos\vartheta+\beta_\vartheta} \quad , \tag{5.13b}$$

and

$$q(Z)=\gamma(\vartheta)T\left(\vartheta\right)+A\left(\mu_p\right)\gamma(\mu_p)\left[1-V\left(\vartheta\right)\right]F\left(\overline{w}\right) \quad , \tag{5.13c}$$

where β_ϑ is the effective admittance given by

$$\beta_\vartheta=\chi\left(\vartheta\right)=-i\zeta\sqrt{n^2-\sin^2\vartheta}\tan\left(kd\sqrt{n^2-\sin^2\vartheta}\right) \quad , \tag{5.14a}$$

μ_p is the zero for the denominator in the integrand of Eq. (5.8), i.e.

$$\cos\mu_p + \chi\left(\mu_p\right) = 0\,. \tag{5.14b}$$

which can be solved numerically by a standard Newton Rasphson method.[18] Once μ_p is determined, the apparent admittance of the hard-backed rigid porous medium χ_p can be established as,

$$\beta_p = \chi\left(\mu_p\right) = -\cos\mu_p\,. \tag{5.14c}$$

In Eq. (5.12c), the function F is known as the boundary loss factor:

$$F\left(\overline{w}\right) = 1 + i\sqrt{\pi}\,\overline{w}e^{-w^2}\operatorname{erfc}\left(-i\overline{w}\right)\quad, \tag{5.15a}$$

where $\overline{w}$ is the apparent numerical distance below the air/ground interface:

$$\overline{w} = \sqrt{ik}\left\{L - \left[R_s\cos\left(\mu_p - \vartheta\right) + nR_r\cos\left(\mu_p - \varphi\right)\right]\right\}^{\frac{1}{2}}, \tag{5.15b}$$

and the approximate numerical distance $\overline{w}_g$ is defined by

$$\overline{w}_g = \sqrt{\frac{1}{2}ikR_r}\left(\cos\vartheta + \beta_g\right). \tag{5.15c}$$

The augmented diffraction factor A is defined as

$$A(\vartheta) = \frac{\left(r_p / r_w\right)}{E_p\sqrt{\sin\vartheta\sin\mu_p}}, \tag{5.16a}$$

where r_p is the admittance ratio and r_w is ratio of the numerical distances:

$$r_p\left(\vartheta\right) = \beta_p / \beta_g\quad, \tag{5.16b}$$

and

$$r_w\left(\vartheta\right) = \overline{w}/\overline{w}_g\ . \tag{5.16c}$$

The parameter E_p in Eq. (5.18a) is given by

$$E_p = 1 - \frac{i\zeta \cos \mu_p}{N(\mu_p)} \left\{ \tan\left[kN(\mu_p)d \right] + \left[kN(\mu_p)d \right] \sec^2\left[kN(\mu_p)d \right] \right\}. \tag{5.16d}$$

With all necessary terms defined in Eqs. (5.11) – (5.16), the canonical integral for the sound transmitted between a hard-backed rigid porous medium can be calculated by

$$I_C(Z) = q(Z) \frac{e^{ikL(Z)}}{4\pi\Delta(Z)} \ . \tag{5.17}$$

Making use of Eq. (5.17) to calculate the sound fields at the receiver and image receiver locations respectively, it is possible to calculate the total field between within the hard-backed rigid porous medium as

$$p_1(0, z_s \mid r, -D) = q_D \frac{e^{ikL_D}}{4\pi\Delta_D} + q_R \frac{e^{ikL_R}}{4\pi\Delta_R} \ . \tag{5.18}$$

where subscripts D and R denote the corresponding terms for D-refracted and R-refracted waves. They are calculated by setting the depth parameter Z in Eqs. (5.11) – (5.16) to D and $2d - D$ respectively.

Furthermore, a similar procedure can be used to derive the sound fields within an impedance-backed porous interface. which is

$$p_1(0, z_s \mid r, -D) = I_C\left(D\right) + I_C\left(2d - D\right) - 2\beta_2 I_\beta\left(2d - D\right) \tag{5.19}$$

where I_C, which is a canonical integral, is given by

$$I_C(Z) = \frac{ik}{8\pi} \int_C \frac{\sin\mu \cos\mu G_0^{(1)}(\mu)}{\cos\mu + \chi\left(\mu\right)} \left[\frac{\zeta N + \chi}{\zeta N} \right] e^{ikf_b(\mu, Z)} d\mu \tag{5.20a}$$

and

$$I_\beta(Z) = \frac{ik}{8\pi} \int_C \frac{\sin\mu \cos\mu G_0^{(1)}(\mu)}{\left(\cos\mu + \chi\right)\left(\zeta N + \beta_2\right)} \left[\frac{\zeta N + \chi}{\zeta N} \right] e^{ikf_b(\mu, Z)} d\mu \tag{5.20b}$$

and β_2 is the specific normalized admittance of the backing layer. As seen in Eq.(5.20b), there's another pole basides the pole calculated by Eq.(5.14b), which satisfied

$$\zeta\sqrt{n^2-\left(\sin\mu_{p,2}\right)^2}+\beta_2=0 \tag{5.21}$$

i.e.

$$\mu_{p,2}=\frac{\pi}{2}+\cos^{-1}\left[\left(\beta_2/\zeta\right)^2-n^2+1\right] \ . \tag{5.22}$$

The asymptotic solution for the sound fields below the impedance-backed interface is derived as

$$p_1(0,z_s\mid r,-D)=q_D\frac{e^{ikL_D}}{4\pi\Delta_D}+q_R\frac{e^{ikL_R}}{4\pi\Delta_R} \tag{5.23}$$

where

$$q_D=\gamma(\vartheta_D)T\left(\vartheta_D\right)+\gamma(\mu_p)\left[1-V\left(\vartheta_D\right)\right]A\left(\mu_p\right)F\left(w\right) \tag{5.24a}$$

$$q_R=\gamma(\vartheta_R)V_2\left(\vartheta_R\right)T\left(\vartheta_R\right)+\gamma(\mu_p)V_2\left(\mu_p\right)\left[1-V\left(\vartheta_R\right)\right]A\left(\mu_p\right)F\left(\overline{w}\right)$$

$$+\gamma(\mu_{p,2})T\left(\mu_{p,2}\right)\left[1-V_2\left(\vartheta_R\right)\right]A\left(\mu_{p,2}\right)F\left(\overline{w}_2\right) \tag{5.24b}$$

$$V_2=\frac{\zeta\sqrt{n^2-\cos^2\varphi_R}-\beta_2}{\zeta\sqrt{n^2-\cos^2\varphi_R}+\beta_2} \ . \tag{5.24c}$$

Note that Eq. (5.23) can be simplified to Eq.(5.18) when the specific normalized admittance of the backing layer goes to zero, which is the case of hard-backed porous interfac.

5.3 Numerical Comparisons and Experimental Validation

The direct numerical integration scheme and the fast field formulation [39] are well known for yielding accurate numerical results in many situations. We shall combine these two accurate numerical approaches leading to a hybrid scheme known as the integrated exact solution (IES). It will be used to validate the asymptotic formula derived in the present study. To facilitate the comparison, an excess attenuation (EA) function is defined as

$$EA = 20\log_{10}\left[\frac{p_1}{e^{ikr}/4\pi r}\right] \tag{5.25}$$

where r is the horizontal separation between the source and receiver. The Miki model [14] is used to characterize the acoustical property of the ground surface. It is chosen for its simplicity but yet it reveals sufficient details for accurate modeling of ground surfaces.

Figure 5.4 displays the comparisons between the asymptotic solution and IES for the EA versus the horizontal range at various frequencies. The source and receiver are respectively chosen at 0.04 m above and 0.02 m below the porous interface. An effective flow resistivity (σ_e) of 50 kPa s m^{-2}, tortuosity (q) of 1.1 and the porosity (Ω) of 0.9 are selected to represent the rigid porous medium with a layer thickness of 0.03 m. Four different frequencies of 100 Hz, 1 kHz, 5 kHz and 10 kHz are used in the numerical simulations to produce four EA spectra. The predictions according to the asymptotic formulas agree very well with those predicted by the IES. We can see in Figure. 5.4 that both predictions agree to within the thickness of the lines. Other computations have been

conducted with different ground parameters and they all show good agreement between IES and the asymptotic solutions. These comparisons are not shown here for brevity.

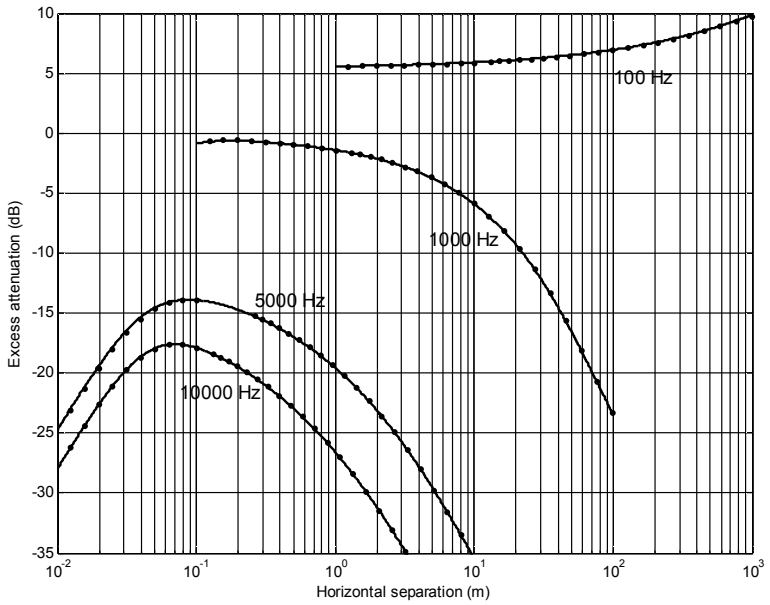

Figure 5.4: Predicted excess attenuation of the sound field versus the frequency. Solid line: asymptotic solution; circles: Integrated Exact Solution (IES).

Next, Figure. 5.5 shows plots of the EA spectra for the monopole source placed at 0.04 m above the hard-backed porous layer of thickness 0.03 m. The receiver is also chosen to be 0.02 m below the porous interface and the horizontal range is set at 1 m. The predicted results are for different values of σ_e at 50, 100, and 150 kPa s m^{-2} but q and Ω are set constant at 1.1 and 0.9 respectively. The EA spectra predicted by asymptotic formulas are in excellent agreement with the numerical results calculated by IES. These two typical sets of comparisons serve to highlight the validity of the derived asymptotic formulas for computing the sound penetration into the hard-backed rigid porous medium.

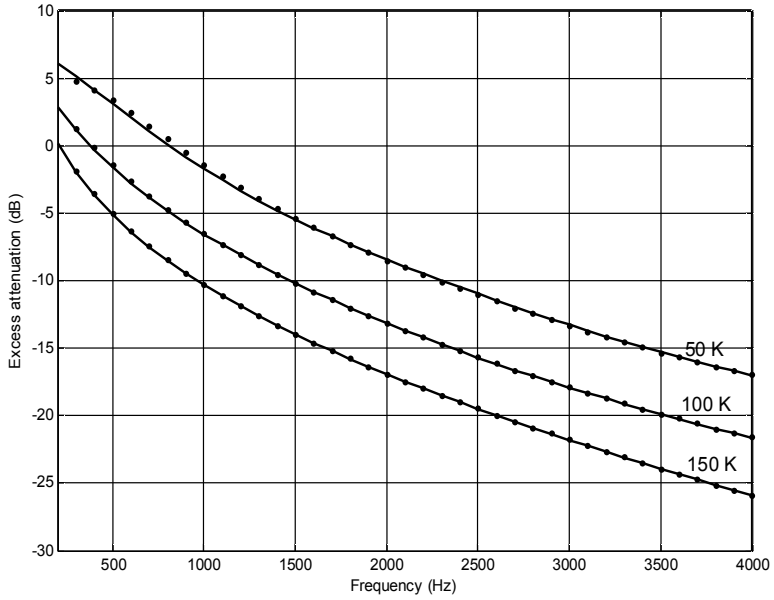

Figure 5.5: Predicted excess attenuation of the sound field versus the frequency. Solid line: asymptotic solution; circles: Integrated Exact Solution (IES).

A set of laboratory measurements was conducted in an anechoic chamber (about 3.5 m × 3.5 m × 3.5 m) for validating the proposed asymptotic formulas of sound penetration into a hard-backed layer ground. A CIE 30 w Tap Loudspeaker, connected to a brass tube with a length of 1 m and an internal diameter of 0.03 m, was used to simulate a point monopole source. The receiver used in the measurement was a Bruel & Kjaer type 4189 pre-polarized free field 1/2-inch microphone. A pool of uniform spherical glass beads with average diameters varying from 0.3 mm to 0.4 mm was used to model a rigid porous medium. They are placed in a wooden container of size 2 m × 2 m × 0.2 m (depth) which provided a rigid backing for the porous materials. The upper surface of the pool of glass beads was located at a nominal height of 0.038m from the bottom of the wooden container. Figure 5.6 shows a photograph for the experimental setup of the present study

in an anechoic chamber. As a precaution, some sound absorption materials were used to cover the edges of the wooden box to minimize unwanted reflections from its edges.

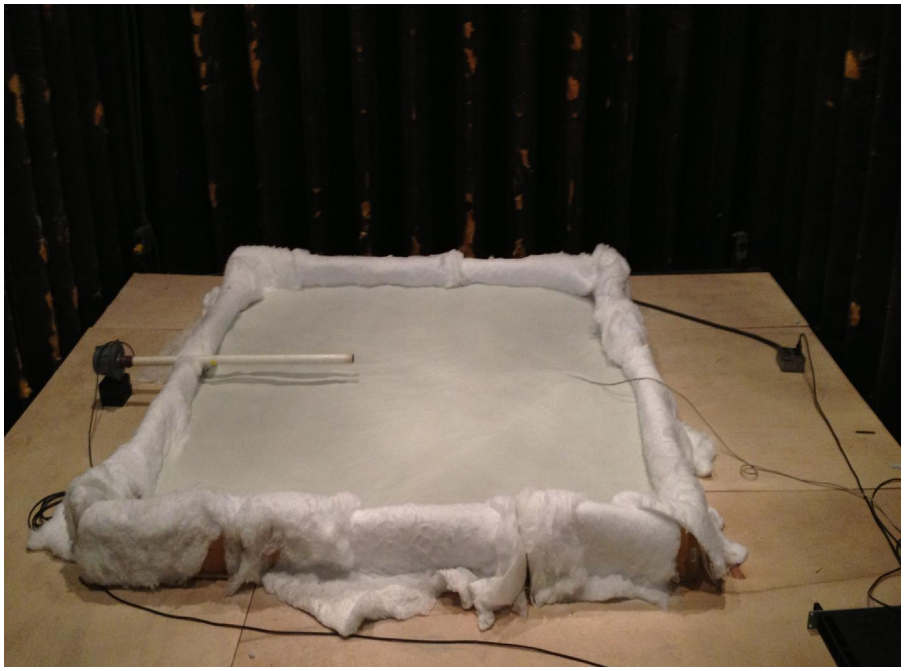

Figure 5.6: Photograph of the measurement setup when the microphone is buried inside the glass bead in an anechoic chamber.

A PC based Maximum-Length Sequence System Analyzer (MLSSA)[23] was used as a signal generator for the source to generate a pseudorandom sequence of pulses as the source output which allows measurements of wideband long duration impulse response. The MLSSA has the advantage that no correction of background noise is necessary for a signal-to-noise ratio of 0 dB. After the impulse response was measured in the time domain, it was then exported to MatLab program for the subsequent processing. The signal was processed with a right sized Hamming window and the Fast Fourier Transform (FFT) technique. Each spectral level was normalized by the prerecorded direct field measurement signals taken without the impedance floor. The final output was then the excess attenuation spectrum.

Several measurements were conducted at various source and receiver heights. The speaker driver was supported by a tripod with the center of the brass tube located at a height of 0.09m above the surface of the porous ground. Two microphones were used in order to reduce any disturbances on the surface of glass beads for each set of measurements. One microphone was supported by a tripod at 0.09m above the surface and the second microphone was buried with its center at a depth of 0.0075 m below the surface of the glass beads. The second microphone was then moved to a deeper depth of 0.014 m, 0.0175 m, and 0.0225 m below the surface. The surface roughness of the rigid porous ground was identical for the measured sound field above and below ground for a fixed source/receiver location. A set of measurements was conducted when the source and receiver were separated by a horizontal distance of 0.6 m. Care was taken to avoid contacts with the surface of the glass beads when the source was positioned for the next set of measurements.

To characterize the impedance of the ground, data from the measurement above the porous surface were used. In the measurements, the source and receiver were suspended at the height of 0.09 m above the rigid porous surface with a horizontal separation of 0.6 and 1.0 m respectively. The two measurements were subsequently fitted by means of Attenborough's four parameters impedance model. There are four resulting microscopic parameters which describe the acoustical properties of a homogeneous porous material: flow resistivity σ, porosity Ω, tortuosity q^2 and pore shape factor s_f. The expression for the index of refraction and the density ratio are given by

$$n^2 = q^2\left[1-2\left(\lambda_p\sqrt{i}\right)^{-1}T\left(\lambda_p\sqrt{i}\right)\right]^{-1}\left\{1+2(\gamma-1)\left(\sqrt{N_{pr}}\lambda_p\sqrt{i}\right)^{-1}T\left(\sqrt{N_{pr}}\lambda_p\sqrt{i}\right)\right\}, \qquad (5.26)$$

$$\zeta = \frac{q^2}{\Omega}\left[1 - 2\left(\lambda_p\sqrt{i}\right)^{-1} T\left(\lambda_p\sqrt{i}\right)\right]^{-1}, \tag{5.27}$$

where

$$\lambda_p = \left(1/s_f\right)\sqrt{8\rho q^2\omega/(\Omega\sigma)}, \tag{5.28a}$$

and

$$T(x) = J_1(x)/J_0(x), \tag{5.28b}$$

ρ is the density of air, γ is the ratio of specific heats, N_{pr} is Prandtl's number.

For the glass beads with the size of 0.3 mm to 0.4 mm used in the measurement, we started from these trial values shown in these previous studies. The aim is to search for a set of parametric values that best fit the agreement between the experimental data and the analytical predictions for sound fields above a hard-backed impedance ground with the properties of the glass beads calculated by Eqs. (5.26) and (5.27). Best fit parameters were found to be as follows: flow resistivity σ = 140 kPa s m^{-2}, porosity Ω = 0.4, tortuosity q^2 = 1.6 and pore shape factor s_f = 0.8. Typical examples of the measured and fitted excess attenuation measurements are shown in Figures. 5.7 and 5.8. These parameters have been used in the following part together with the measurement geometries to obtain the predictions of sound propagation from a monopole into an impedance plane backed by a hard ground with the measured data.

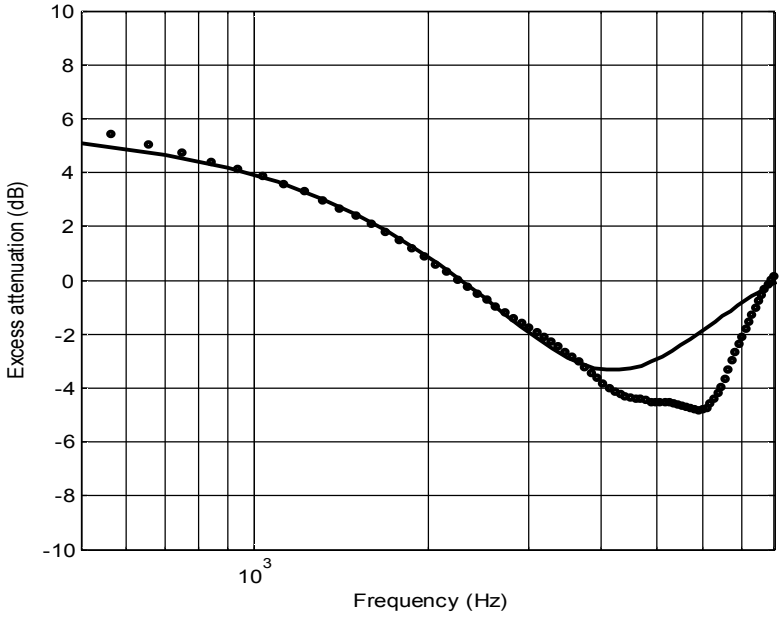

Figure 5.7: Measured(circle) and fitted(solid line) excess attenuation spectrum due to a monopole source above a hard-backed 0.038 m glass bead. $z_s = z_r = 0.09$ m, range $r = 0.6$ m. The ground parameters are flow resistivity $\sigma = 140$ kPa s m^{-2}, porosity $\Omega = 0.4$, tortuosity $q^2 = 1.6$ and pore shape factor $s_f = 0.8$.

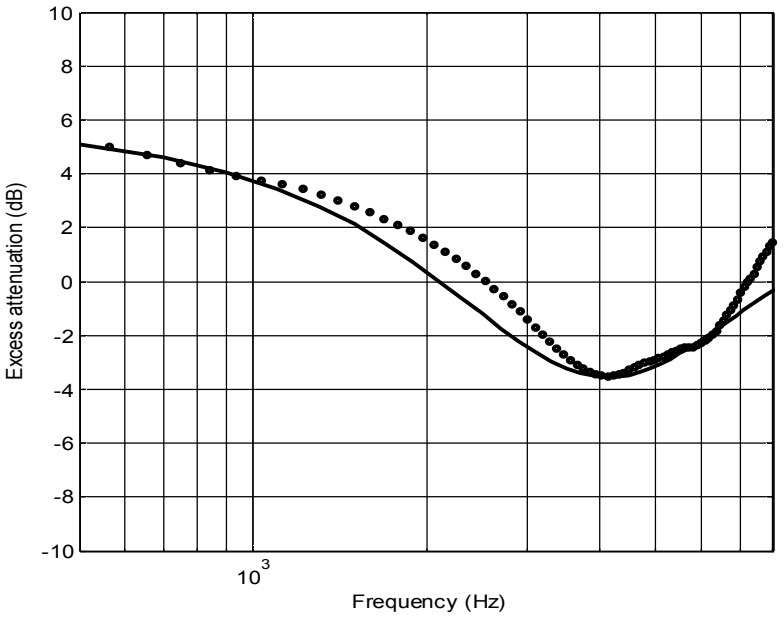

Figure 5.8: Caption same as Figure 5.7 except that the range was chosen as 1.0 m.

Figure 5.9 shows the measured and predicted total sound fields at the horizontal separation of 0.6 m as a function of frequency with the source at a height of 0.09 m above the porous surface and the receiver located at various locations of 0.75 cm, 1.4 cm, 1.75 cm and 2.25 cm below the surface. The agreement between measured data and predictions according to Eq. (5.18) is good. Also shown is the prediction for the sound field due to a monopole source inside a semi-infinite extended reaction ground for source and receiver location at 0.09 m above and 2.25 cm below the surface respectively with the same horizontal separation. There are significant differences between the sound fields below the hard-backed impedance ground and the semi-infinite extended reaction ground especially . The compared results indicate that the existence of the hard-backed ground have a significant effect on the total sound fields inside the porous layer. When the receiver is located near the bottom of the hard-backed layer, the reflection of the refracted wave gives rise to a significant contribution to the total sound fields.

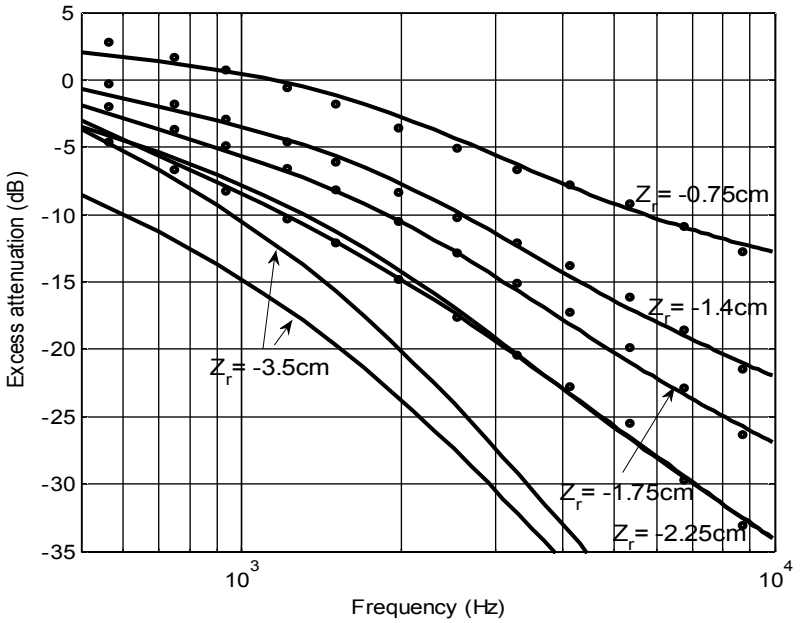

Figure 5.9: Measured (circle) and predicted (solid line) excess attenuation spectrum due to a monopole source below a hard-backed 0.038 m glass bead, range $r = 0.6$ m. Predicted (dashed line) excess attenuation spectrum below a semi-finite extended reaction ground when receiver height was chosen to be 2.25cm and 3.5cm below the surface.

5.4 Summary

In this chapter, the study of sound transmission and reflection from a layer of sound absorption materials placed on a hard plane has been investigated. A uniform asymptotic solution has been derived for the penetration of sound into the hard-backed layer porous materials. The numerical results obtained by the asymptotic formula agree very well with those calculated by the more exact wave-based numerical solutions. It has also been shown that the asymptotic solution provides a convenient means for rapid and accurate computations of sound fields in the hard-backed rigid porous layer. A set of precise laboratory measurements was conducted for validating the asymptotic formulas experimentally. It has been shown that the effect of the reflecting backing is particularly important for the total sound fields when the receiver is located near the rigid backing.

The R-refracted wave term, i.e., the second term of Eq. (5.18) provides a significant contribution to the sound field that cannot be ignored in the calculations of the sound penetration into the rigid porous medium.

CHAPTER 6: REFLECTION AND TRANSMISSION OF SOUND FROM A DIPOLE NEAR A RIGID POROUS MEDIUM

6.1 Introduction

The reflection of sound from a porous half-space has been the subject of interest for many decades [1, 72]. There have also been related studies on the transmission of sound through an interface into a porous half-space. An application of these studies is the acoustic detection of buried objects [70, 76-78]. Most of these studies were based on the sound fields generated by a point monopole source. Other studies considered a directional noise source but these were mainly restricted to the analysis of sound fields above a locally reacting ground [29, 30, 67].

The purpose of this study is to develop accurate numerical solutions for predicting the sound fields above and below a porous half-space due to a dipole source placed above the interface since many noise sources have directional characteristics. For instance, a fast moving train [22] and a helicopter rotor [23] can be modeled as dipole noise sources. The analytical and numerical solutions developed in this paper will be beneficial in the accurate assessment of the noise impacts from directional sources. It should be pointed out that there were comparable studies on the propagation of electromagnetic waves over a conducting half-plane due to an electric dipole in recent decades [93]. However,

these analytical results cannot be applied directly without further adaptations to most acoustic problems.

Indeed, the problem of predicting the sound fields due to a point monopole source above a plane interface, and also the related problem for a dipole source, is of great theoretical interest. It is because they can be posed as an exactly solvable canonical problem with a rich structure. Their analytical solutions are also of considerable practical importance in, for instance, the implementation of noise mapping software. There are many exact computational schemes, such as the fast field program [39], finite element method [75], offering accurate numerical solutions for predicting sound fields for the canonical problems. However, the computational costs of these numerical schemes are prohibitively expensive for high source frequencies. These numerical solutions do not yield physically interpretable terms to enhance a better understanding of the problem. An alternative route is pursued in the present study where an asymptotic method is applied to derive an approximate solution for the dipole sound fields of the classical two-medium problem. Previous studies [34, 71, 72, 74] have shown that the method of steepest descent is a versatile mathematical technique that offers accurate and fast asymptotic solutions for computation of sound fields above a flat interface. The present study generalizes this mathematical technique to tackle the problem of the sound field due to a dipole source placed above a rigid porous medium.

Another application of the present study is its provision of an accurate Green's function that can be used to calculate the pressure gradient at any arbitrary field point above a rigid porous ground. Accurate Green's functions for calculating the pressure and the pressure gradients are normally required in the boundary integral equation (BIE)

formulation for predicting the combined effects of a porous road surface and the application of sound absorbing materials on a barrier's surface. In the absence of appropriate Green's functions, Anfosso-Ledee et al. [69] used a two-domain BIE approach to impose the continuity of pressure and velocity at the porous interface. Their BIE approach invariably increases the number of elements needed in the formulations, which limits its suitability as a three-dimensional boundary element model. On the other hand, an analytical solution below ground facilitates the acoustical characterization of sound absorbing materials and has an application in the acoustic detection of buried objects by means of a BIE formulation [76].

It is well known that the sound field above a rigid porous medium consists of three terms: a direct wave, a reflected wave, and a component due to sound diffracted at the interface. In a recent study, Li and Liu [1] showed that the sound field below the porous interface consists of two terms: a sound transmission component and a diffracted wave term. This paper reports a continuation of these efforts to develop asymptotic formulas for predicting the sound field above and below a rigid porous medium. A double saddle-point method [71] will be used to evaluate the diffraction integral along the steepest descent path. The method of pole subtraction is then applied to provide a uniform asymptotic solution for the sound fields above and below the porous interface. In this paper, we shall interpret the directional effect of the dipole source on each term of the asymptotic solutions. The accuracy of the asymptotic solutions will be confirmed by comparing them with computationally intensive, but more accurate, numerical schemes.

6.2 Review of the Diffraction Integrals from a Monopole Above a Rigid Porous Medium

A rectangular coordinate system is used with the vertical z-axis passing through the source, i.e., the coordinate of the source is (0, 0, z_s). The frequency of the dipole source is f, the corresponding wave number is k, and the speed of sound in air (upper medium) is c. A receiver is placed at z above the porous interface where the height z is measured positive upward. Alternatively, the receiver may be placed at a depth $-D$ below the interface where $D > 0$. A horizontal coordinate of $\boldsymbol{r} = (x, y)$ is used where its scalar horizontal distance from the source is $r = \sqrt{x^2 + y^2}$ and the corresponding azimuthal angle is $\psi = \tan^{-1}(y/x)$. The parameters, R_1 and R_2, are defined as the respective distances from the source and its image to the receiver, i.e., the distances of the direct and reflected waves. The ground is assumed to have a complex sound speed and complex density of c_1 and ρ_1, respectively. Figure 6.1a shows the geometrical configuration.

According to a recent study, Li and Liu [1] showed that the sound fields above (at height of $z > 0$) and below (at depth of $D > 0$) the porous interface can be expressed as

$$p^{(m)}(r, z_s, z) = \frac{e^{ikR_1}}{4\pi R_1} + \frac{e^{ikR_2}}{4\pi R_2} + p_a^{(m)}, \tag{6.1a}$$

and

$$p^{(m)}(r, z_s, -D) = p_b^{(m)} \tag{6.1b}$$

where $p_a^{(m)}\left[\equiv p_a^{(m)}(r, z_s, z)\right]$ and $p_b^{(m)}\left[\equiv p_b^{(m)}(r, z_s, D)\right]$ are the respective integrals to calculate the contribution of the diffracted wave terms above and below the porous interface. The superscript (m) represents the sound field due to a monopole source i.e., a

zeroth order multipole.

(a)

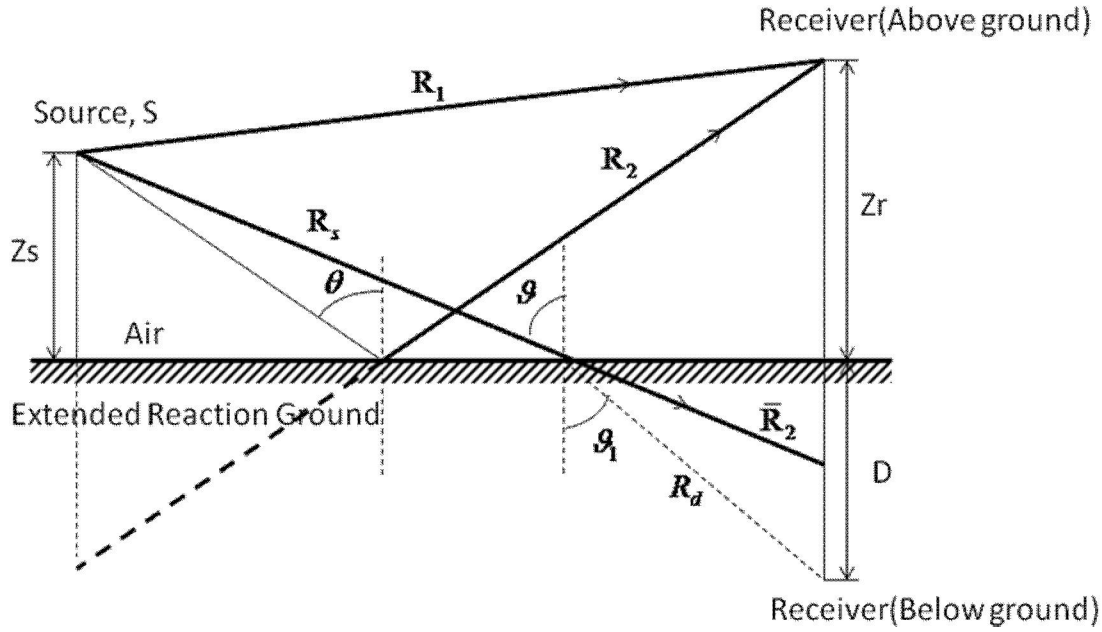

(b)

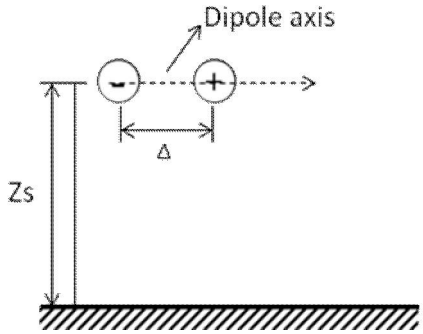

(c)

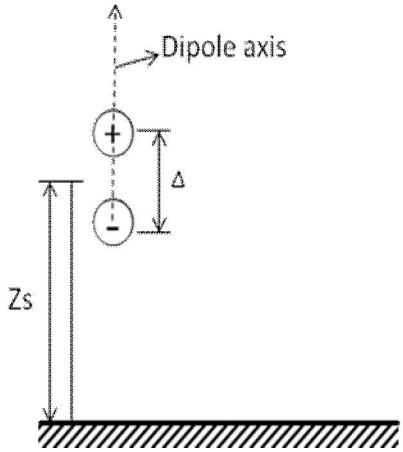

Figure 6.1: (a) Schematic diagram showing a source located in the air in the upper medium, a receiver situated at height z_r above the interface, and another receiver located at depth D below the incident angle for the refracted ray, and ϑ_1 is the refracted angle. The distance R_s is measured from the source to the ground and $\bar{R}_2$ is measured from the source to the apparent receiver below the ground. The schematic diagrams of dipole sources are shown in (b) a horizontal dipole, and (c) a vertical dipole. A pair of monopole sources of opposite signs are aligned accordingly and placed at a height of z_s above the rigid porous medium.

Li and Liu showed that the diffraction integrals due to a monopole source can be written as

$$p_a^{(m)}(r, z_s, z) = \frac{-ik}{4\pi} \int_C \frac{\zeta \sqrt{n^2 - \sin^2 \mu} \sin \mu G_0(\mu) \exp[ikf_a(\mu)]}{\cos \mu + \zeta \sqrt{n^2 - \sin^2 \mu}} d\mu , \tag{6.2a}$$

and

$$p_b^{(m)}(r, z_s, D) = \frac{ik}{4\pi} \int_C \frac{\cos \mu \sin \mu G_0(\mu) \exp[ikf_b(\mu)]}{\cos \mu + \zeta \sqrt{n^2 - \sin^2 \mu}} d\mu , \tag{6.2b}$$

where $\zeta = \rho / \rho_1$ is the complex density ratio, $n = c/c_1$ is the index of refraction from the upper medium to the lower medium, and $G_j(\mu)$ [where j = 0, 1, …], is the corresponding jth order Hankel function $H_j^{(1)}$ normalized with the exponential factor, $e^{-ikr\sin\mu}$:

$$G_j(\mu) = H_j^{(1)}(kr \sin \mu) e^{-ikr \sin \mu} . \tag{6.3a}$$

The asymptotic form for $G_j(\mu)$ can be expressed as [73]

$$G_j(\mu) \approx (-i)^j \left(\frac{2}{i\pi kr \sin \mu} \right)^{\frac{1}{2}} \left\{ 1 - \frac{4j^2 - 1}{8ikr \sin \mu} + \ldots \right\} . \tag{6.3b}$$

Here, j is set at zero for a monopole source. The variable μ in the diffraction integrals can be interpreted as the angle of incidence of the reflected plane wave [34] in the upper medium. The exponential factor $f_a(\mu)$ in Eq. (6.2a) and $f_b(\mu)$ in Eq. (6.2b) are defined, respectively, by

$$f_a(\mu) = r \sin \mu + (z_s + z) \cos \mu = R_2 \cos(\mu - \theta) , \tag{6.4a}$$

and

$$f_b(\mu) = r \sin \mu + z_s \cos \mu + D\sqrt{n^2 - \sin^2 \mu} , \tag{6.4b}$$

where z_s, z, $D \geq 0$.

The integration path for the two diffraction integrals is shown as C in Fig. 6.2. The integration path for μ varies from $-\pi/2+i\infty$ to $-\pi/2$ to $\pi/2$ to $\pi/2-i\infty$. It is remarkable that the pole μ_p is the same for both integrands shown in Eqs. (6.2a) and (6.2b). It can be determined by setting the denominators of the respective integrands to zero, i.e. $\cos\mu+\zeta\sqrt{n^2-\sin^2\mu}=0$. Its solution gives a pair of trigonometrical functions defining its location at the complex μ-plane as follows:

$$\cos\mu_p=-\zeta\sqrt{\left(n^2-1\right)/\left(1-\zeta^2\right)}=-\beta_p, \tag{6.5a}$$

and

$$\sin\mu_p=\sqrt{\left(1-\zeta^2n^2\right)/\left(1-\zeta^2\right)}=+\sqrt{1-\beta_p^2}, \tag{6.5b}$$

where the subscript p stands for the parameter at the pole. Figure 6.2 also shows the schematic location of the pole in the complex μ-plane. The term β_p, which is introduced in Eqs. (6.5a) and (6.5b), can be treated as the apparent admittance of the rigid porous medium.

It should be pointed out that accurate asymptotic solutions [1] were available to compute the diffraction integrals, $p_a^{(m)}$ and $p_b^{(m)}$. In principle, the dipole sound fields could be obtained directly by taking directional derivatives of these asymptotic solutions. However, the spatial derivatives of the diffraction integral lead to more complex expressions [93]. A preliminary analysis suggests that this direct approach leads to a set of complicated asymptotic solutions which is tedious to apply for computing the dipole sound fields. We are therefore refrained from providing the approximate solutions due to

a monopole source in this section. The diffraction integrals described above will be used instead as a basis for the derivation of the dipole sound fields in the following sections.

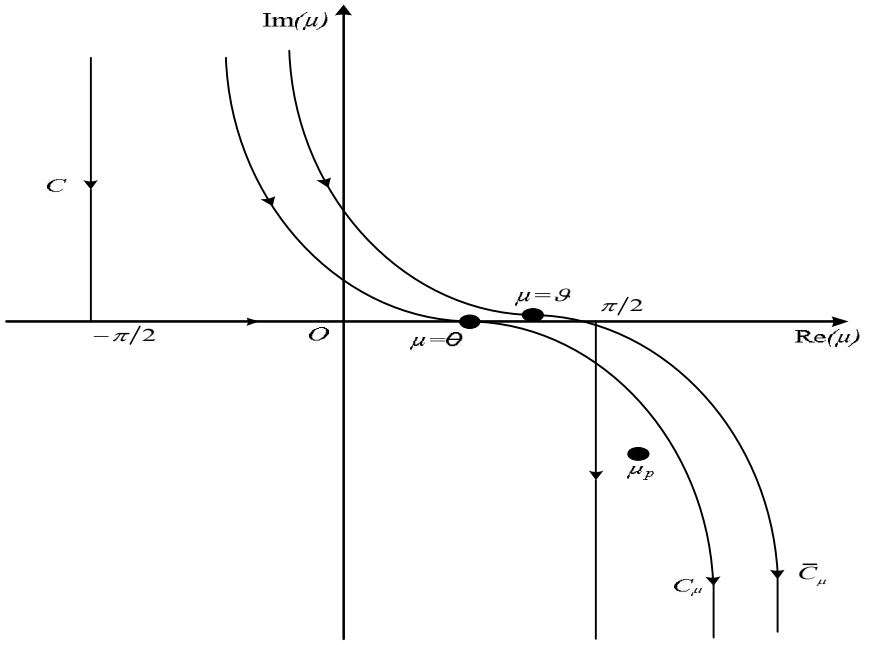

Figure 6.2: Sketch of the integration paths. The original integration path is denoted by *C*, whereas C_μ and $\overline{C}_\mu$ are the steepest descent paths for the sound fields above and below the rigid porous ground, respectively.

6.3 Dipole Sound Fields above a Rigid Porous Medium

6.3.1 Integral Expressions for the Diffracted Wave Term

Suppose a dipole is placed at a height of z_s above a semi-infinite plane interface. Figures 1b and 1c show schematic diagrams for a horizontal dipole and a vertical dipole. The dipole sources may be considered as a pair of opposite monopole sources separated by a small distance Δ (where $\Delta \rightarrow 0$) along the dipole axis.

The dipole axis is specified by the polar and azimuthal angles (γ_L and ψ_L). The direction cosines $\mathbf{l} = (l_x, l_y, l_z)$ of the dipole axis can be specified by

$$l_x = \sin\gamma_L \cos\psi_L \,;\; l_y = \sin\gamma_L \sin\psi_L \,;\; l_z = \cos\gamma_L \,. \tag{6.6}$$

The horizontal and vertical components for the dipole orientation are introduced such that $\mathbf{l} = (\mathbf{l_h}, \mathbf{l_v})$, where $\mathbf{l_h}$ = (l_x, l_y) and $\mathbf{l_v}$ = (l_z). The use of these two components can simplify the expression given in our analytical solution. It is because the two planar direction cosines, l_x and l_y, can be grouped together as a single term for the sound field due to the horizontal dipoles. On the other hand, the polar direction cosine l_z gives rise to the contribution due to the vertical dipole. Unless stated otherwise, the subscripts *h* and *v* are used to denote the horizontal and vertical components of the variable.

Taking directional derivatives [72], the sound fields due to an arbitrarily oriented dipole source can be written in terms of $p^{(m)}$ as

$$p^{(d)}(r, z_s, z) = -\left[\sin\gamma_L \cos(\psi - \psi_L)\partial_r + \cos\gamma_L \partial_z\right] p^{(m)}(r, z_s, z), \tag{6.7}$$

where r and ψ are the magnitude and direction of the receiver in the azimuthal plane. The superscripts (*d*) and (*m*) represent the parameters for a dipole source (i.e., the first order multi-pole) and a monopole source (i.e., the zero order multi-pole) respectively. The subscripts *r* and *z* in ∂ represent the spatial derivatives $\partial/\partial r$ and $\partial/\partial z$, respectively. Differentiation the first two terms of Eq. (6.1a) with respect to *r* and *z*, substitution of the resulting expressions into Eq. (6.7) and manipulation of the algebraic terms lead to

$$p^{(d)}(r, z_s, z) = (\mathbf{l} \cdot \mathbf{u_1}) \left[\frac{1 - ikR_1}{4\pi R_1^2}\right] e^{ikR_1} + (\mathbf{l} \cdot \mathbf{u_2}) \left[\frac{1 - ikR_2}{4\pi R_2^2}\right] e^{ikR_2} + p_a^{(d)}, \tag{6.8a}$$

where the diffracted wave term $p_a^{(d)}$ is given by

$$p_a^{(d)} = -\left[\sin\gamma_L \cos(\psi - \psi_L)\partial_r + \cos\gamma_L \partial_z\right] p_a^{(m)}, \tag{6.8b}$$

and the unit vectors $\mathbf{u}_1$ and $\mathbf{u}_2$ are the respective directions pointing from the source and its image to the receiver. Centering at the source and image source, $\mathbf{u}_1$ and $\mathbf{u}_2$ can be written in terms of the polar and azimuthal angles as

$$\mathbf{u}_1 = \left(\sin\phi\cos\psi, \sin\phi\sin\psi, \cos\phi\right) \tag{6.9a}$$

and

$$\mathbf{u}_2 = \left(\sin\theta\cos\psi, \sin\theta\sin\psi, \cos\theta\right) \tag{6.9b}$$

where ϕ and θ are the respective polar angles of the direct and reflected waves, and ψ is the azimuthal angle for both the direct and reflected wave.

We can see that the diffracted wave term for the dipole $p_a^{(d)}$ can also be split into its horizontal and vertical components. Straightforward directional derivatives of the asymptotic solution for $p_a^{(m)}$ in Eq. (6.8b) will result in a more complicated asymptotic solution [29]. Here, we shall take an alternative approach by reversing the order of differentiation and integration for $\partial_r p_a^{(m)}$ and $\partial_z p_a^{(m)}$ to yield,

$$\partial_r p_a^{(m)} = \frac{\partial p_a^{(m)}}{\partial r} = \frac{ik^2}{4\pi}\int_C \frac{\zeta \sin^2\mu\sqrt{n^2-\sin^2\mu}\,G_1(\mu)e^{ikf_a(\mu)}}{\cos\mu+\zeta\sqrt{n^2-\sin^2\mu}}d\mu, \tag{6.10a}$$

and

$$\partial_z p_a^{(m)} = \frac{\partial p_a^{(m)}}{\partial z} = \frac{k^2}{4\pi}\int_C \frac{\zeta \cos\mu\sin\mu\sqrt{n^2-\sin^2\mu}\,G_0(\mu)e^{ikf_a(\mu)}}{\cos\mu+\zeta\sqrt{n^2-\sin^2\mu}}d\mu, \tag{6.10b}$$

where $G_j(\mu)$ [where j = 0, 1, …] is defined by Eqs. (6.3a,b) and the exponential function f_a above the rigid porous medium is given by Eq. (6.4a).

It is important to mention that the diffracted sound fields above a rigid porous

medium due to the horizontal and vertical dipoles can be obtained from Eqs. (6.10a) and (6.10b). In the special case where $n \to \infty$, i.e., a locally reacting ground, these integral expressions can be reduced to the analogous forms given by Li et al. [29] which can be evaluated asymptotically leading to a closed form solution. However, to the best of our knowledge, the corresponding asymptotic solutions are not available for the arbitrarily oriented dipole. One of the objectives of the present study is to derive such asymptotic formulas for providing fast and accurate numerical solutions to predict the dipole sound fields above a rigid porous medium. The details of the derivation will be given in the following sections.

6.3.2 Diffracted Wave Fields due to a Horizontal Dipole

In this section, an analytical method [1] will be used to derive an asymptotic solution for the horizontal dipole $\partial_r p_a^{(m)}$. The corresponding solution for the vertical dipole $\partial_z p_a^{(m)}$ will be discussed in the next section. The sum of these two solutions, $\partial_r p_a^{(m)}$ and $\partial_z p_a^{(m)}$, leads to an analytical formula for the diffracted wave term due to an arbitrarily oriented dipole.

The main steps for evaluating the integrals asymptotically are described for the sake of completeness. First, the integration path C is deformed to the steepest descent path C_μ (see Figure. 6.2) that passes through the saddle point at $\mu = \theta$. The steepest descent path can then be determined by setting

$$\mathrm{Im}\left\{i\left[1-\cos(\mu-\theta)\right]\right\} = 0\,. \tag{6.11}$$

Figure 6.2 shows both integration paths in the complex μ plane.

By indenting the path from C to C_μ, the contribution from the pole is included, which yields an expression for $\partial_r p_a^{(m)}$ as

$$\partial_r p_a^{(m)} = \frac{ik^2}{4\pi}\int_{C_\mu} \frac{\zeta N(\mu)\sin^2\mu G_1(\mu) e^{ikR_2\cos(\mu-\theta)}}{\cos\mu+\zeta N(\mu)} d\mu + H\left[-\mathrm{Im}\left\{i\left[1-\cos(\mu_p-\theta)\right]\right\}\right] P_h^{(d)} \tag{6.12a}$$

where H is the Heaviside step function and $P_h^{(d)}$ is the pole contribution that can be determined by the calculus of residue to confirm

$$P_h^{(d)} = \frac{k^2\zeta N(\mu_P)\sin\mu_p H_1^{(1)}(kr\sin\mu_p) e^{ik(z_s+z)\cos\mu_p}}{2\left(1-\zeta^2\right)} \tag{6.12b}$$

The evaluation of the integral in Eq. (6.12a) is facilitated by introducing a complex variable W to replace μ by

$$\frac{1}{2}W^2 = ikR_2\left[1-\cos\left(\mu-\theta\right)\right]. \tag{6.13a}$$

The pole location W_p in the W-plane can then be determined, but it is usually written in terms of the numerical distance w as follows:

$$w = W_p\big/\sqrt{2} = \sqrt{2ikR_2}\sin\left[(\mu_p-\theta)/2\right]. \tag{6.13b}$$

Because the steepest descent path in the W-plane corresponds to the integration path along its real axis, Eq. (6.12a) can therefore be transformed to

$$\partial_r p_a^{(m)} = I_1 + H\left[-\mathrm{Im}\left(W_p\right)\right] P_h^{(d)} \tag{6.14a}$$

where

$$I_1 = \frac{ik^2}{4\pi} e^{ikR_2}\int_{-\infty}^{\infty} \varpi_h^{(1)} e^{-X^2/2} dX\,, \tag{6.14b}$$

$$\varpi_h^{(d)}(X) = \frac{\zeta N(\mu)\sin^2\mu G_1(\mu)}{\left[\cos\mu + \zeta N(\mu)\right]\sqrt{ikR_2 - X^2/4}}, \tag{6.14c}$$

$X = \mathrm{Re}(W)$, and μ can be converted to W according to Eq. (6.13a).

Essentially, the method of pole subtraction is needed when the pole μ_p is positioned very close to the saddle point θ, i.e., when W_p is very close to 0. In this case, the apparent singularity of the integrand in Eq. (6.12a) can be removed by the method of pole subtraction [71]. Specifically, Eq. (6.12a) can be rewritten as

$$\partial_r p_a^{(m)} = I_2 + H\left[-\mathrm{Im}\left(W_p\right)\right]P_h^{(d)} + \phi_h^{(d)} \quad , \tag{6.15a}$$

where

$$I_2 = \frac{ik^2}{4\pi}e^{ikR_2}\int_{-\infty}^{\infty}\left[\Theta_h^{(1)}(X)\right]e^{-X^2/2}dX, \tag{6.15b}$$

$$\Theta_h^{(d)}(X) = -\frac{\zeta N(\mu_p)\sin\mu_p G_1\left(\mu_p\right)}{\left(1-\zeta^2\right)\left(X - W_p\right)}, \tag{6.15c}$$

and

$$\phi_h^{(d)} = I_1 - I_2 = \frac{ik^2}{4\pi}e^{ikR_2}\int_{-\infty}^{\infty}\left[\varpi_h^{(d)}(X) - \Theta_h^{(d)}(X)\right]e^{-X^2/2}dX\,. \tag{6.15d}$$

By noting $P_h^{(d)}$ in Eq. (6.12b), an asymptotic expression for G_1 [see Eq. (6.3b)] in Eq. (6.15c), and, an integral expression for the complementary error function [73],

$$\int_{-\infty}^{\infty}\frac{e^{-X^2/2}}{X - \sqrt{2}w}dX = -\frac{\pi}{i}e^{-w^2}\left\{\mathrm{erfc}(-iw) - 2H[-\mathrm{Im}(w)]\right\}, \tag{6.16}$$

the integral I_2 can be simplified to confirm

$$I_2 = \left(ik\Xi\sin\mu_p\right)\frac{e^{ikR_2}}{4\pi R_2} - H\left[-\mathrm{Im}\left(W_p\right)\right]P_h^{(d)} \quad , \tag{6.17}$$

where Ξ is defined in terms of the complimentary error function as

$$\Xi = 2i\sqrt{\pi}\left(ikR_2/2\right)^{1/2}\frac{\beta_p e^{-w^2}\,\mathrm{erfc}(-iw)}{(1-\zeta^2)\sqrt{\sin\theta\sin\mu_p}}. \tag{6.18}$$

The application of the Taylor's series expansion to the integrand of Eq. (6.14b), retention of the first term in the series, and, evaluation of the resulting integral yield a closed form asymptotic solution for I_1 as follows:

$$I_1 = \left(ik\phi_A \sin\theta\right)\frac{e^{ikR_2}}{4\pi R_2} \quad , \tag{6.19}$$

where ϕ_A is given by

$$\phi_A \approx \frac{-2\beta_e}{\cos\theta + \beta_e} \, , \tag{6.20a}$$

and

$$\beta_e = \zeta\sqrt{n^2 - \sin^2\theta} \, . \tag{6.20b}$$

The asymptotic representation for I_2 can be derived using the following asymptotic formula for the complimentary error function:

$$e^{-W_p^{\,2}/2}\left\{\mathrm{erfc}(-iW_p/\sqrt{2}) - 2H[-\mathrm{Im}(W_p)]\right\} \approx \frac{1}{-iW_p\sqrt{\pi/2}}\left\{1 + \frac{1}{W_p^{\,2}} + \cdots\right\} \, . \tag{6.21}$$

The substitution of Eq. (6.21) into Eq. (6.17) yields

$$I_2 = \left(ik\phi_B \sin\mu_p\right)\frac{e^{ikR_2}}{4\pi R_2}, \tag{6.22a}$$

where ϕ_B is given by

$$\phi_B \approx \frac{-2\beta_p \Big/ \sqrt{2\sin\theta\sin\mu_p}}{\left(1-\zeta^2\right)\sqrt{1-\cos\left(\mu_p-\theta\right)}}, \tag{6.22b}$$

The subtraction of I_2 from I_1 leads to an asymptotic expression for the correction term $\phi_h^{(d)}$ as follows:

$$\phi_h^{(d)} = \left[\left(ik\sin\theta\right)\phi_A - \left(ik\sin\mu_p\right)\phi_B\right]\frac{e^{ikR_2}}{4\pi R_2}. \tag{6.23}$$

This is the correction term that has been modified to take into account a spatial derivative with respect to *r* for the horizontal dipole. Namely, the multiplication factors of (ik sin θ) and (ik sin μ_p) appear in the first and the second term of the square bracket of Eq. (6.23), respectively. Substituting Eqs. (6.17) and (6.23) into Eq. (6.15a), an asymptotic expression to calculate $\partial_r p_a^{(m)}$ can be obtained to confirm

$$\partial_r p_a^{(m)} = ik\left[\phi_A\sin\theta + \Upsilon_a\sin\mu_p\right]\frac{e^{ikR_2}}{4\pi R_2}, \tag{6.24a}$$

where the correction term, Υ_a, is referred as the diffraction factor:

$$\begin{aligned}\Upsilon_a &= \Xi - \phi_B \\ &= \frac{2\beta_p}{(1-\zeta^2)\sqrt{\sin\theta\sin\mu_p}}\left\{\left[2\left(1-\cos\left(\mu_p-\theta\right)\right)\right]^{-1/2} + i\sqrt{\pi}\left(ikR_2/2\right)^{1/2}e^{-w^2}\,\mathrm{erfc}(-iw)\right\}.\end{aligned} \tag{6.24b}$$

6.3.3 Diffracted Wave Fields due to a Vertical Dipole

In this section, the derivation of an asymptotic solution for the diffracted wave term due to a vertical dipole, $\partial_z p_a^{(m)}$, will be shown. Its exact solution can be specified in an integral form, as shown in Eq. (6.10b). By indenting the integration path from *C* to C_μ

(see Fig. 6.2), splitting the integral into two parts, replacing μ with W according to Eq. (6.13a), and evaluating the integral along the steepest descent path (i.e., along the real axis of W), the integral solution for $\partial_z p_a^{(m)}$ can be transformed into

$$\partial_z p_a^{(m)} = I_A + I_B \ , \tag{6.25a}$$

where

$$I_A = \frac{k^2}{4\pi} e^{ikR_2} \int_{-\infty}^{\infty} \frac{\zeta N(\mu) \sin \mu G_0(\mu) e^{-X^2/2}}{\sqrt{ikR_2 - X^2/4}} dX \ , \tag{6.25b}$$

$$I_B = I_3 + H\left[-\mathrm{Im}\left(W_p\right)\right] P_v^{(d)} , \tag{6.25c}$$

$$I_3 = -\frac{k^2}{4\pi} e^{ikR_2} \int_{-\infty}^{\infty} \varpi_v^{(d)} e^{-X^2/2} dX \ , \tag{6.26a}$$

$$\varpi_v^{(d)}(X) = \frac{\zeta^2 N^2(\mu) \sin \mu G_0(\mu)}{\left[\cos \mu + \zeta N(\mu)\right] \sqrt{ikR_2 - X^2/4}} , \tag{6.26b}$$

and

$$P_v^{(d)} = ik\beta_p \frac{k}{2} \frac{\beta_p G_0(\mu_p)}{\left(1-\varsigma^2\right)} e^{ikR_2} e^{-W_p^2/2} . \tag{6.26c}$$

When deforming the integration path from C to C_μ, the contributions from the poles are required. Because the integrand of the first term in Eq. (6.25a) is an entire function [see also Eq. (6.25b)], there is no pole contribution from this term. The integral I_A can therefore be evaluated asymptotically to yield,

$$I_A = -ik\beta_e \frac{e^{ikR_2}}{2\pi R_2} \ . \tag{6.27}$$

However, there is a pole in the second term of Eq. (6.25a), see also Eqs. (6.25c), (6.26a)

and $\varpi_v^{(1)}(X)$ in Eq. (6.26b). Hence, the pole contribution is calculated by the second term of Eq. (6.25c). It can be determined by using the same method as described in the last section to give an analytical expression for $P_v^{(1)}$ shown in Eq. (6.26c).

Using the same procedure as detailed in the last section, I_3 can be evaluated by the pole subtraction method to verify

$$I_B = I_4 + H\left[-\mathrm{Im}\left(W_p\right)\right]P_v^{(d)} + \phi_v^{(d)}, \tag{6.28}$$

where

$$I_4 = -\frac{k^2}{4\pi}e^{ikR_2}\int_{-\infty}^{\infty}\left[\Theta_v^{(d)}(X)\right]e^{-X^2/2}dX, \tag{6.29a}$$

$$\Theta_v^{(d)}(X) = -\frac{\zeta^2 N^2(\mu)G_0\left(\mu_p\right)}{\left(1-\zeta^2\right)\left(X-W_p\right)}, \tag{6.29b}$$

and

$$\phi_v^{(d)} = I_3 - I_4 = -\frac{k^2}{4\pi}e^{ikR_2}\int_{-\infty}^{\infty}\left[\varpi_v^{(d)}(X) - \Theta_v^{(d)}(X)\right]e^{-X^2/2}dX. \tag{6.29c}$$

Using Eq. (6.17), the integral I_4 can be represented exactly in terms of Ξ, *cf* Eq. (6.18), to give

$$I_4 = (ik\Xi\cos\mu_p)\frac{e^{ikR_2}}{4\pi R_2} - H\left[-\mathrm{Im}\left(W_p\right)\right]P_v^{(d)}\ . \tag{6.30a}$$

The asymptotic solution for I_3 can be derived by a straightforward application of asymptotic analysis to give

$$I_3 = \left(ik\phi_A\cos\theta_e\right)\frac{e^{ikR_2}}{4\pi R_2}, \tag{6.30b}$$

where θ_e is defined in an analogous form as the pole location θ_p as

$$\cos\theta_e + \beta_e = 0 \ , \tag{6.30c}$$

with β_e defined in Eq. (6.20b)). The asymptotic representation of I_4 can be obtained readily by using Eq. (6.21) to yield,

$$I_4 = (ik\phi_B \cos\mu_p)\frac{e^{ikR_2}}{4\pi R_2}, \tag{6.31}$$

where ϕ_B is defined in Eq. (6.22b). Hence, the substitution of Eqs. (6.30b) and (6.31) into Eq. (6.29c) yields an asymptotic expression for the correction term as

$$\phi_v^{(d)} = \left[\left(ik\cos\theta_e\right)\phi_A - (ik\cos\mu_p)\phi_B\right]\frac{e^{ikR_2}}{4\pi R_2}. \tag{6.32}$$

Finally, the diffracted wave term above a rigid porous medium, due to a vertical dipole can be derived by first substituting Eq. (6.32) into Eq. (6.28). Then, the resulting asymptotic expressions for I_A and I_B [*cf* Eqs. (6.27) and (6.28)] are used in Eq. (6.25a) to obtain

$$\partial_z p_a^{(m)} = ik\left[(2+\phi_A)\cos\theta_e + \Upsilon_a \cos\mu_p\right]\frac{e^{ikR_2}}{4\pi R_2}, \tag{6.33}$$

where ϕ_A and Υ_a are given respectively by Eq. (6.20a) and Eq. (6.24b).

6.3.4 Sound Fields due to an Arbitrarily Oriented Dipole

For an arbitrarily oriented dipole with its dipole axis aligned according to Eq. (6.6), the diffracted wave term can be obtained by substituting Eqs. (6.24a) and (6.33) into Eq. (6.8b) to verify

$$p_a^{(d)} = -ik\left\{\left[\phi_A \sin\theta \sin\gamma_L \cos\left(\psi - \psi_L\right) + (2+\phi_A)\cos\theta_e \cos\gamma_L\right]\right.$$

$$+\Upsilon_a\left[\sin\gamma_L\cos\left(\psi-\psi_L\right)+\cos\gamma_L\right]\Big\}\frac{e^{ikR_2}}{4\pi R_2}. \tag{6.34}$$

Using the spatial unit vectors **l** and $\mathbf{u_2}$ [see Eqs. (6.6) and (6.9b)] and introducing a unit vector $\mathbf{u_s}$ that characterizes the propagation direction of the boundary wave, Eq. (6.34) can be written in a more compact form as

$$p_a^{(d)} \approx \left(\mathbf{l}\cdot\mathbf{u_2}\right)\phi_A\left[\frac{1-ikR_2}{4\pi R_2^2}\right]e^{ikR_2}+\left(\mathbf{l}\cdot\mathbf{u}_s\right)\Upsilon_a\left[\frac{1-ikR_2}{4\pi R_2^2}\right]e^{ikR_2}, \tag{6.35}$$

where

$$\mathbf{u_s}=\left(\sin\mu_p\cos\psi,\sin\mu_p\sin\psi,\cos\mu_p\right). \tag{6.36}$$

In Eq. (6.35), an assumption of $kR_2 >> 1$ is used such that the parameter ikR_2 is approximated by $(1 - ikR_2)$ in each of the two square bracket terms of the asymptotic formula. These modifications will not cause significant errors in the asymptotic expressions at the far-field, and its introduction can provide a more convenient solution for the total near-field sound pressure given above.

The substitution of Eq. (6.35) into Eq. (6.8a) leads to a uniform asymptotic solution for the total sound field of

$$p^{(d)}\left(r,z_s,z\right)=\left(\mathbf{l}\cdot\mathbf{u_1}\right)\left[\frac{1-ikR_1}{4\pi R_1^2}\right]e^{ikR_1}+\left[\left(\mathbf{l}\cdot\mathbf{u_2}\right)V_\theta+\left(\mathbf{l}\cdot\mathbf{u}_s\right)\Upsilon_a\right]\left[\frac{1-ikR_2}{4\pi R_2^2}\right]e^{ikR_2}, \tag{6.37a}$$

where V_θ can be identified readily as the plane wave reflection coefficient, which is given by

$$V_\theta=\frac{\cos\theta-\beta_e}{\cos\theta+\beta_e}. \tag{6.37b}$$

Equation (6.37a) is the main result of section 6.2. It offers a closed form analytical formula for rapid computation of sound fields due to an arbitrarily oriented dipole placed above a rigid porous medium. This asymptotic solution will be implemented numerically and compared with other more accurate wave-based numerical solutions. Their validations will be offered in section 6.5 but the simplified expressions for two special cases will be presented as follows.

An interesting situation arises when the rigid porous medium has a relatively high flow resistivity. In this case, Allard et al. [92] suggested that the factor $E\sqrt{\sin\theta \sin\mu_p} \approx 1$ if both θ and μ_p are close to π/2. Then, the total sound field can be reduced to

$$p^{(d)}(r, z_s, z) \approx (\mathbf{l}\cdot\mathbf{u}_1)\left[\frac{1-ikR_1}{4\pi R_1^2}\right]e^{ikR_1} + \left[(\mathbf{l}\cdot\mathbf{u}_2)V_p + (\mathbf{l}\cdot\mathbf{u}_s)(1-V_p)F(w)\right]\left[\frac{1-ikR_2}{4\pi R_2^2}\right]e^{ikR_2}, \tag{6.38a}$$

where V_p is referred to as the poles of reflection coefficient,

$$V_p = \frac{\cos\theta - \beta_p}{\cos\theta + \beta_p}, \tag{6.38b}$$

and $F(w)$ is the boundary loss factor calculated by

$$F(w) = 1 + i\sqrt{\pi}we^{-w^2}\,\mathrm{erfc}(-iw), \tag{6.38c}$$

with the numerical distance w approximated by

$$w \approx \sqrt{ik_0R_2/2}(\cos\theta + \beta_p). \tag{6.38d}$$

In the next special case, we have $n >> 1$ for a locally reacting ground. Hence, $\beta_e \approx \beta = \zeta n$, which can be interpreted as the specific normalized admittance of the ground surface. Then, it is possible to show that

$$\phi_A \approx \frac{-2\beta}{\cos\theta + \beta}, \tag{6.39a}$$

$$\phi_B \approx \frac{-2\beta \Big/ \sqrt{2\sin\theta \sin\mu_p}}{\sqrt{1-\cos\left(\mu_p - \theta\right)}}, \tag{6.39b}$$

$$\Xi = 2i\sqrt{\pi}\left(ikR_2/2\right)^{1/2} \beta e^{-w^2} \operatorname{erfc}(-iw) \Big/ \sqrt{\sin\theta \sin\mu_p}, \tag{6.40}$$

$$w = \sqrt{2ikR_2}\,\sin\left[(\mu_p - \theta)/2\right] \approx \sqrt{ikR_2/2}\left(\cos\theta + \beta\right), \tag{6.41a}$$

$$\mu_p = \pi/2 + \cos^{-1}(\beta), \tag{6.41b}$$

and

$$V_p \approx V_\theta. \tag{6.42}$$

Using Eqs. (6.39)–(6.42), assuming θ and μ_p are close to π/2, and taking $\phi_A - \phi_B \approx 0$, we can transform Eq. (6.38a) into the same equation derived by Li et al. [30], who studied the sound field due to an arbitrarily oriented dipole located above an impedance ground.

6.4 Sound Penetration into a Rigid Porous Medium

In an earlier study, Li and Liu showed that the penetration of sound due to an airborne monopole source can be written in terms of the boundary wave term given earlier in Eq. (6.1b). The diffracted wave term below the ground can be written in an integral form given in Eq. (6.2b). In their analysis for a monopole source, Li and Liu evaluated the integral of Eq. (6.2b) asymptotically along the steepest descent path $\bar{C}_\mu$ (see Fig. 6.2). Their solution can be written in an analogous form to yield [*cf* Eq. (61) of Ref. (1)],

$$p_b^{(m)}\left(r,z_s,-D\right)=\frac{e^{ikL}}{4\pi\Delta}\left[2+2i\sqrt{\pi}\left(ikR_r/2\right)^{\frac{1}{2}}\frac{\beta_p e^{-\bar{w}^2}\operatorname{erfc}\left(-i\bar{w}\right)}{\left(1-\zeta^2\right)\sqrt{\sin\vartheta\sin\mu_p}}+\bar{\phi}^{(m)}\right], \tag{6.43}$$

where $D > 0$ is the depth below the interface, the overbar represents the corresponding parameters in the rigid porous medium, L is the acoustical path length and Δ is the physical path length where

$$L=f_b\left(\vartheta\right)=R_s+nR_D, \tag{6.44a}$$

and

$$\Delta=\sqrt{\bar{R}_2R_r}\ . \tag{6.44b}$$

The separations between the source and the receiver, R_s and R_D, are respectively given by

$$R_s=z_s/\cos\vartheta\ , \tag{6.45a}$$

and

$$R_D=D/\cos\vartheta_1\ . \tag{6.45b}$$

In Eqs. (6.43) and (6.44b), the apparent distance of the sound ray traveling in the absence of the lower medium, which is denoted by $\bar{R}_2$, is defined as

$$\bar{R}_2=r/\sin\vartheta, \tag{6.46a}$$

and the acoustical energy path length [34] R_r is calculated by

$$R_r=R_s+\left(R_D/n\right)\left(\cos\vartheta/\cos\vartheta_1\right)^2 \tag{6.46b}$$

where ϑ is the incident angle and ϑ_1 is the refracted angle. These two angles are related according to Snell's Law, i.e. $\sin\vartheta = n \sin\vartheta_1$. The representations of these physically interpretable parameters are shown in Fig. 6.1. Li and Liu [1] outlined a simple numerical scheme to determine ϑ and ϑ_1 numerically for a given source/receiver configuration and

the acoustical characteristic of the ground surface.

In Eq. (6.43), the numerical distance of the refracted wave $\overline{w}$ is given by,

$$\overline{w} = \sqrt{ik}\left\{L - \left[R_s \cos\left(\mu_p - \vartheta\right) + nR_D \cos\left(\mu_{p1} - \vartheta_1\right)\right]\right\}^{\frac{1}{2}} \tag{6.47}$$

where μ_p and μ_{p1} is the pole in the respective complex μ-plane and μ_1-plane. Again, these two angles are related according to the Snell Law, i.e., $\sin\mu_p = n\sin\mu_{p1}$. Furthermore, the correction factor $\overline{\phi}^{(m)}$ in Eq. (6.43) can be written in a familiar form as

$$\overline{\phi}^{(m)} = \overline{\phi}_A - \overline{\phi}_B . \tag{6.48a}$$

where

$$\overline{\phi}_A \approx \frac{-2\beta_\vartheta}{\cos\theta + \beta_\vartheta} , \tag{6.48b}$$

$$\overline{\phi}_B \approx \frac{-2\beta_p \Big/ \sqrt{2\sin\vartheta\sin\mu_p}}{\left(1-\zeta^2\right)\sqrt{1-\cos\left(\mu_p - \vartheta\right)}} , \tag{6.48c}$$

and the effective admittance β_ϑ of the rigid porous medium is given by

$$\beta_\vartheta = \zeta\sqrt{n^2 - \sin^2\vartheta} . \tag{6.48d}$$

In light of the analysis shown in the Appendix E, it is possible to rewrite the diffracted wave term below the rigid porous medium, i.e., Eq. (6.43), in a comparable form as follows:

$$p_b^{(m)} = \frac{e^{ikL}}{4\pi\Delta}\left[T_\vartheta + \Upsilon_b\right] \tag{6.49a}$$

where the plane wave transmission coefficient can be defined as

$$T_\vartheta = 2 + \overline{\phi}_A = 2\cos\vartheta \Big/ \left(\cos\vartheta + \beta_\vartheta\right), \tag{6.49b}$$

the diffraction factor below the ground is given by

$$\Upsilon_b = \bar{\bar{\Xi}} - \bar{\phi}_B , \tag{6.49c}$$

and the variable $\bar{\bar{\Xi}}$, *cf* Eq. (6.18), can be calculated by

$$\bar{\bar{\Xi}} = 2i\sqrt{\pi}\left(ikR_r/2\right)^{\frac{1}{2}} \frac{\beta_p e^{-\bar{w}^2}\operatorname{erfc}\left(-i\bar{w}\right)}{\left(1-\zeta^2\right)\sqrt{\sin\vartheta \sin\mu_p}} . \tag{6.49d}$$

By noting Eq. (6.4), it is possible to write the dipole sound field below the porous ground in terms of $p_b^{(m)}$ as follows:

$$p_b^{(d)} = \sin\gamma_L \cos\left(\psi - \psi_L\right)\frac{\partial p_b^{(m)}}{\partial r_s} + \cos\gamma_L \frac{\partial p_b^{(m)}}{\partial z_s} , \tag{6.50}$$

where the first term is the sound field due to the horizontal dipole and the second term is that due to the vertical dipole. Using the expression in Eq. (6.2b) for $p_b^{(m)}$, we can write the horizontal and vertical dipole terms in the respective integral forms as

$$\partial_r p_b^{(m)} = \frac{\partial p_b^{(m)}}{\partial r} = \frac{ik^2}{4\pi}\int_C \frac{\cos\mu \sin\mu G_1\left(\mu\right)\exp\left[ikf_b(\mu)\right]}{\cos\mu + \zeta N(\mu)} d\mu , \tag{6.51a}$$

and

$$\partial_z p_b^{(m)} = \frac{\partial p_b^{(m)}}{\partial z} = \frac{k^2}{4\pi}\int_C \frac{\cos^2\mu G_0\left(\mu\right)\exp\left[ikf_b\left(\mu\right)\right]}{\cos\mu + \zeta N(\mu)} d\mu . \tag{6.51b}$$

Using the same procedures as described in Sec 6.3, Eqs. (6.51a) and (6.51b) can be evaluated asymptotically to yield

$$\partial_r p_b^{(m)} = ik\left[2\sin\vartheta + \bar{\bar{\Xi}}\sin\mu_p + \bar{\phi}_A \sin\vartheta - \bar{\phi}_B \sin\mu_p\right]\frac{e^{ikL}}{4\pi\Delta} \tag{6.52a}$$

and

$$\partial_z p_b^{(m)} = ik\left[2\cos\vartheta + \bar{\Xi}\cos\mu_p + \bar{\phi}_A\cos\vartheta - \bar{\phi}_B\cos\mu_p\right]\frac{e^{ikL}}{4\pi\Delta}. \tag{6.52b}$$

Noting Eq. (6.37a), it is useful to derive a comparable expression for the sound field below the ground. The dipole sound pressure can be obtained by an alternative approach

$$\partial_r p_b^{(m)} = \frac{\partial}{\partial r}\left[p_b^{(m)}\right], \qquad \partial_z p_b^{(m)} = \frac{\partial}{\partial z}\left[p_b^{(m)}\right]. \tag{6.53a,b}$$

The respective near-field components can then be derived to yield

$$\partial_r p_b^{(m)} \approx -\frac{\left[T_\vartheta + \Upsilon_b\right]e^{ikL}}{4\pi\Delta^2}\frac{\partial\Delta}{\partial r}, \tag{6.54a}$$

and

$$\partial_z p_b^{(m)} \approx -\frac{\left[T_\vartheta + \Upsilon_b\right]e^{ikL}}{4\pi\Delta^2}\frac{\partial\Delta}{\partial z}, \tag{6.54b}$$

where only the $(1/\Delta^2)$ term remains in the above equations when r $\to$ 0, i.e., $\vartheta \approx \vartheta_1 \approx 0$. It then follows from Eq. (6.44a) that the acoustical energy path length can be approximated by $R_r \approx r/\sin\vartheta = \bar{R}_2$. Thus, the physical length [see Eq. (6.44b)] can be reduced to $\Delta \approx r/\sin\vartheta = \bar{R}_2$. Consequently, it can be easily shown that

$$\partial\Delta/\partial r \approx \sin\vartheta\,,\ \partial\Delta/\partial z \approx \cos\vartheta \tag{6.55a,b}$$

at the near-field.

By matching Eqs. (6.54a) and (6.54b) with the corresponding asymptotic solution given in Eqs. (6.52a) and (6.52b), we can establish a generalized solution that is both accurate at the near-field and far-field as follows. For the sound field due to a horizontal dipole, the asymptotic solution is given by

$$\partial_r p_b^{(m)} = -T_\vartheta\sin\vartheta\left[\frac{1-ik\Delta}{4\pi\Delta^2}\right]e^{ikL} - \Upsilon_b\left[\frac{\sin\vartheta - ik\Delta\sin\mu_p}{4\pi\Delta^2}\right]e^{ikL}. \tag{6.56a}$$

For a vertical dipole, the sound field is expressed as

$$\partial_z p_b^{(m)} = -T_\vartheta \cos\vartheta \left[\frac{1-ik\Delta}{4\pi\Delta^2}\right] e^{ikL} - \Upsilon_b \left[\frac{\cos\vartheta - ik\Delta\cos\mu_p}{4\pi\Delta^2}\right] e^{ikL}. \tag{6.56b}$$

Substituting Eqs. (6.56a) and (6.56b) into Eq. (6.50) and assuming $k\Delta >> 1$, we can obtain an asymptotic expression for the dipole sound field below the ground as

$$p_b^{(d)}\left(r, z_s, -D\right) = \left(\mathbf{l}\cdot\bar{\mathbf{u}}_\mathbf{2}\right) T_\vartheta \left[\frac{1-ik\Delta}{4\pi\Delta^2}\right] e^{ikL} + \Upsilon_b \left[\frac{\left(\mathbf{l}\cdot\bar{\mathbf{u}}_\mathbf{2}\right) - ik\left(\mathbf{l}\cdot\mathbf{u}_s\right)\Delta}{4\pi\Delta^2}\right] e^{ikL} \tag{6.57}$$

where $\bar{\mathbf{u}}_\mathbf{2}$ and $\mathbf{u}_\mathbf{s}$ are the unit vectors that characterize the direction of the transmitted wave and the boundary wave propagation, respectively. The unit vector $\bar{\mathbf{u}}_\mathbf{2}$ is given by

$$\bar{\mathbf{u}}_\mathbf{2} = \left(\sin\vartheta\cos\psi, \sin\vartheta\sin\psi, \cos\vartheta\right) \tag{6.58}$$

and $\mathbf{u}_\mathbf{s}$ defined in Eq. (6.36).

Equation (6.57) presents an analytical solution for predicting sound penetration into porous ground due to an arbitrarily oriented dipole source. This asymptotic formula, which has not been published elsewhere, is the main result of this section. The validity of Eq. (6.57) will be confirmed in Section 6.5.

6.5 Validation of Asymptotic Formulas

The asymptotic formulas derived in the last section can be used to efficiently calculate the sound fields due to an arbitrarily oriented dipole. For the present study, it is sufficient to use a simple empirical Miki model [14] for modeling the acoustical characteristics of the ground surfaces. The numerical solutions computed by the asymptotic formulas are compared with the exact numerical solutions calculated by a

combination of the fast field program (FFP) and the direct numerical integration method in the wave number space. This exact computation scheme is referred to as the integrated exact solution (IES) in the following paragraphs. To present the numerical results, an excess attenuation function is used, which is defined as

$$EA\left(G_\beta\right) = 20\log_{10}\left[\frac{G_\beta}{e^{ikr}/4\pi r}\right], \tag{6.59}$$

and G_β is the function of interest that can be the diffracted wave terms for the horizontal dipole placed above and below the rigid porous medium, i.e., $\partial_r p_a^{(m)}$ and $\partial_r p_b^{(m)}$. It can also be used to represent the respective diffracted wave terms (above and below the ground) due to the vertical dipole, which are $\partial_z p_a^{(d)}$ and $\partial_z p_b^{(d)}$, respectively.

Extensive computations have been conducted for a series of source/receiver geometries and for a wide range of ground surfaces. It is found that all the numerical results based on the asymptotic formulas agree well (to within about 0.5 dB) with the IES when $kr \sim 1$. The agreements are generally even better for large values of kr (to within 0.1 dB). Unless stated otherwise, the parametric values of 50 kPa s m^{-2}, 1.1, and 0.9 were selected for the effective flow resistivity (σ_e), tortuosity (q) and porosity (Ω), respectively, in all the numerical simulations. They represent typical values for a rigid porous interface. It is possible to use the asymptotic formula due to an arbitrarily oriented dipole for comparison with the IES. However, it is more convenient to separately validate each of the asymptotic formulas for the horizontal and vertical dipoles.

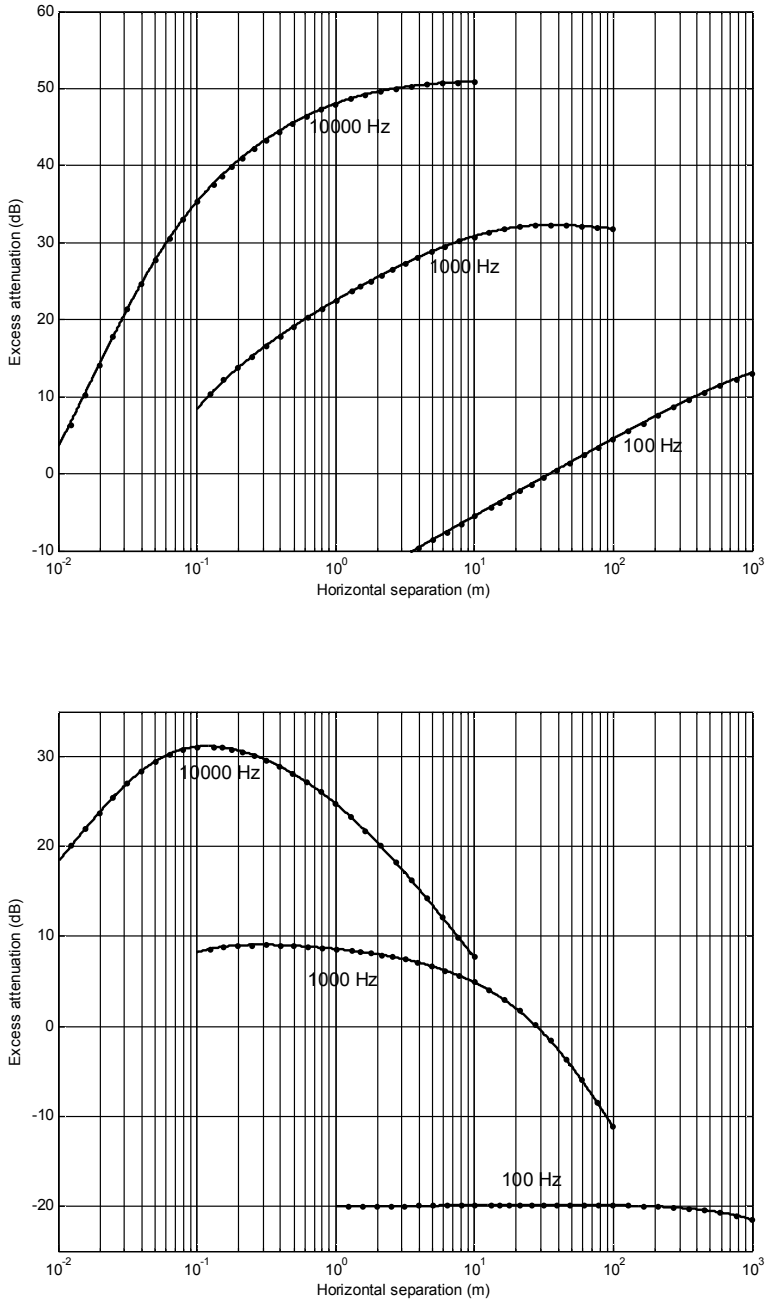

Figure 6.3: Predicted excess attenuation of the diffracted wave term against horizontal separation. The Miki empirical model was used for the porous layer with the effective flow resistivity of 50 kPa s m^{-2}, tortuosity of 1.1, and porosity of 0.9. (a) a horizontal dipole; (b) a vertical dipole. Solid line: asymptotic formulas; circles: Integrated exact solution (IES).

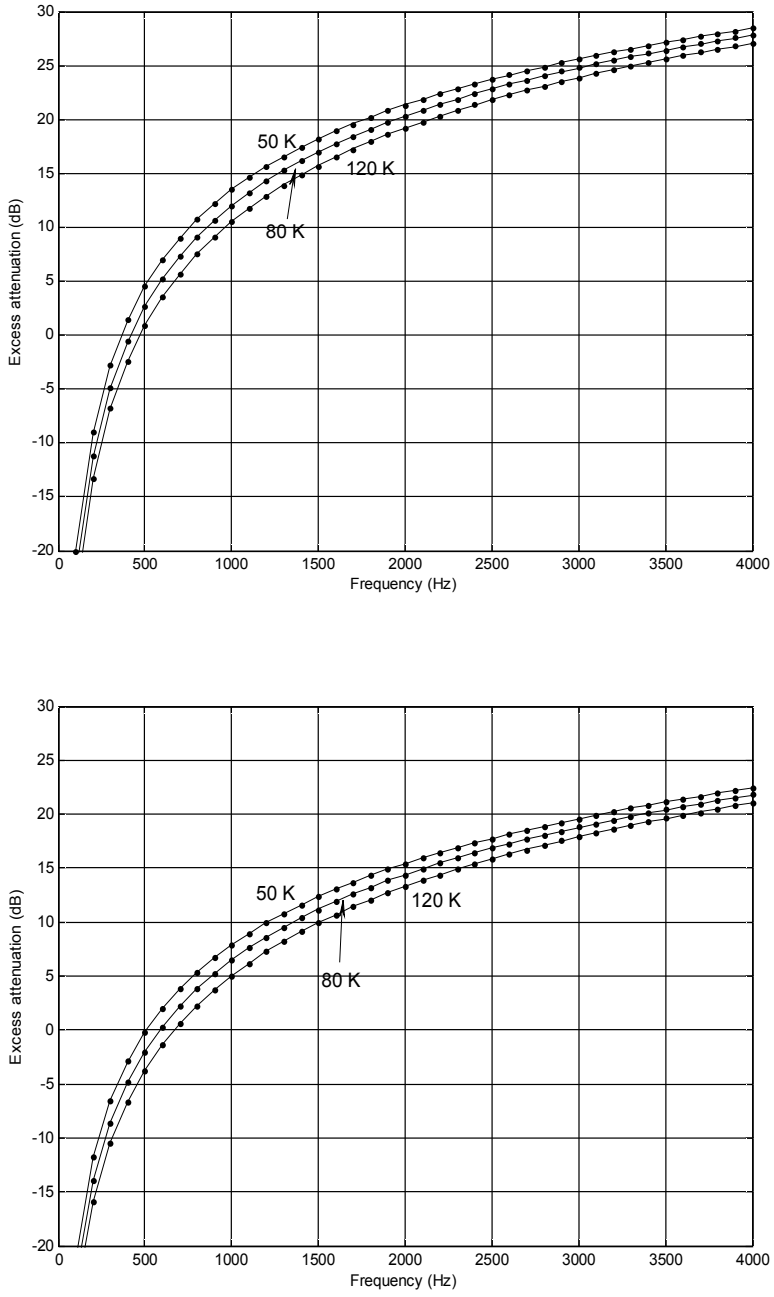

Figure 6.4: Predicted excess attenuation spectrum of the diffracted wave term. (a) a horizontal dipole; (b) a vertical dipole. Solid line: the asymptotic formulas. Circles: Integrated exact solution (IES).

First, we present the numerical results for the dipole sound fields above a rigid porous medium. Figures 6.3a and 6.3b show the comparisons of the diffracted wave

terms due to a horizontal dipole and a vertical dipole, respectively. The corresponding excess attenuation functions, see Eq. (6.61), are plotted against the horizontal separation r. The numerical results for frequencies at 100 Hz (low), 1 kHz (mid), and 10 kHz (high) are shown in these two plots. We found that the diffracted wave terms became more critical when the source and receiver was close to the ground surface. Hence, the source and receiver were respectively chosen at 0.04 m and 0.02 m above the ground surface to highlight the accuracy of the asymptotic formulas in these presentations. Generally, the predictions according to the asymptotic formulas agreed very well with those predicted by the IES, provided that kR_2 is greater than approximately 1, which may be treated as a heuristic condition for the asymptotic formulas.

Figures 6.4a and 6.4b display the corresponding EA spectra for the horizontal dipole and vertical dipole. In these two plots, the source and receiver remained at 0.04 m and 0.02 m above the ground but the horizontal range was set at 1 m. In addition, we also show the predicted results for different values of σ_e at 50, 80, and 120 kPa s m^{-2}; however, q and Ω were set constant at 1.1 and 0.9, respectively. Excellent agreements are shown in these two EA spectra for the respective diffracted wave terms above the rigid porous medium due to the horizontal and vertical dipoles.

In the next two sets of figures, we show the validation of the asymptotic formulas for the prediction of the dipole sound fields below the air/ground interface. Because there was no direct wave term as the interface shielded the direct line of sight between the source and receiver, the diffracted wave term represented the total sound field in each of the respective situations for the horizontal and vertical dipoles.

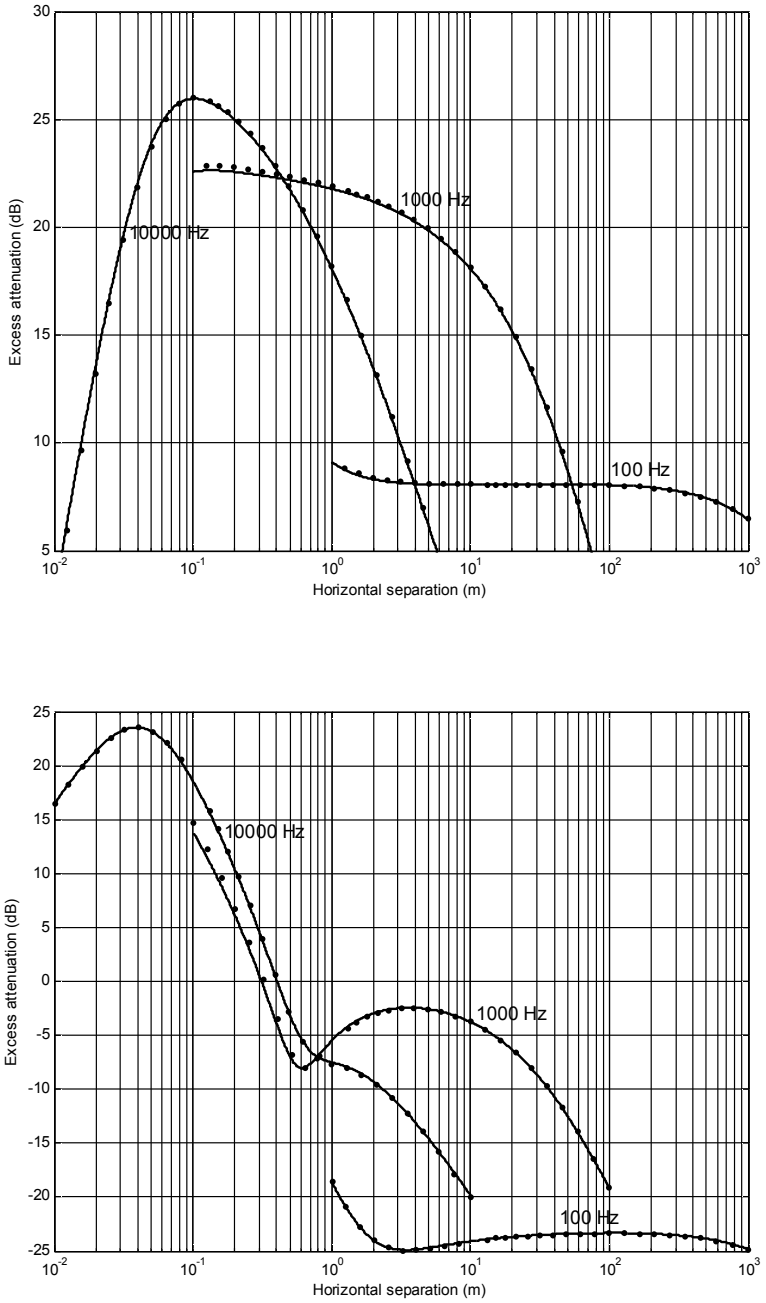

Figure 6.5: Predicted excess attenuation of the diffracted wave terms is plotted against the horizontal separation: (a) a horizontal dipole; (b) a vertical dipole. The ground parameters and other captions are the same as for Fig. 6.3 except that the receiver is located 0.02 m below the ground.

Figures 6.5a and 6.5b are the numerical results for the diffracted wave terms plotted against the horizontal range. The same type of ground surfaces were used in the simulations, which were identical to those used in Figs. 6.3a and 6.3b. However, in Figures. 6.5a and 6.5b, the source was located at the same height of 0.04 m above the air/ground interface but the receiver was located 0.02 m below the interface. The acoustical characteristics of the ground surface used were the same as those used for the simulations for Figs. 6.4a and 6.4b. With the matched asymptotic solutions, we can see that both formulas agreed very well with the predictions according to the IES, provided that kR_2 was greater than approximately 1.

Figures 6.6a and 6.6b are the corresponding EA spectra for the sound fields due to the horizontal dipole and the vertical dipole, respectively. In this set of simulations, the source was located 0.2 m above ground but the receiver was situated 0.03 m below the interface. The horizontal separation between the source and receiver was 1 m. As shown in this set of figures, the agreements between the asymptotic solutions and the IES were reasonably good.

It is of interest to point out that the IES method is based on the summation of the contributions from a large number of sampling points in order to achieve the required accuracy in the calculation of the sound fields. For instance, a total of about 400,000 sampling points is typically needed for a source frequency of 10 kHz and a source/receiver separation of 100 m. On the other hand, the calculations of the asymptotic sound fields can usually be achieved in real time at all frequencies.

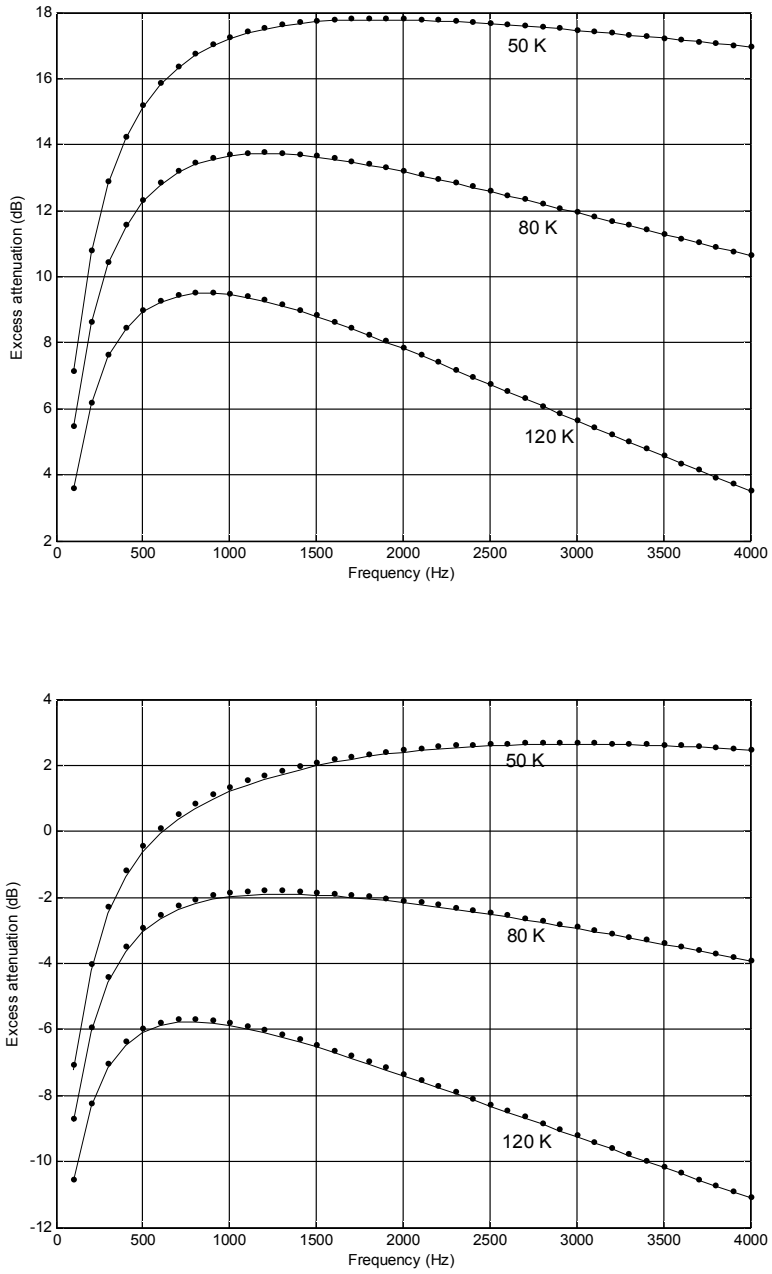

Figure 6.6: Predicted excess attenuation spectrum for (a) a horizontal dipole; (b) a vertical dipole. The parameters and other captions are the same as for Fig. 6.4 except that the receiver is located 0.03 m below the ground.

6.6 Summary

The asymptotic formulas developed in this chapter provide an efficient means for calculating the sound fields due to an arbitrarily oriented dipole placed above a rigid porous medium. There are separate analytic formulas to predict the contributions from the diffracted wave terms accounting for the sound reflected from and transmitted through a fluid-fluid interface. The validity of these asymptotic formulas has been confirmed by comparison with an accurate, but computational intensive wave-based numerical scheme. The asymptotic solutions can be applied in the boundary element formulation by providing an appropriate Green's function for modeling a more complex environment with the presence of non-locally reacting sound absorbing materials.

CHAPTER 7: A PARABOLIC EQUATION/FINITE ELEMENT METHOD FOR PREDICTING SOUND PROPAGATION NEAR RIGID POROUS INTERFACES

7.1 Introduction

In the previous chapters, sound propagation above and below a porous interface has been investigated via asymptotic analysis. Accurate closed-form solutions are derived for various rigid porous interfaces. These interfaces are restricted to be planar, homogeneous ground surfaces. The atmosphere is assumed to be homogeneous as well. In reality, typical ground interfaces are non-planar and may exhibit mixed impedances. The above ground environment can be further complicated by atmospheric effects such as turbulence, boundary layer effects, and wind velocities. An accurate and robust numerical approach is needed to address these complexities and to model more realistic propagation conditions.

The Parabolic Equation (PE) method can be implemented to address some of these complex propagation conditions. In the PE method, backscattered waves are neglected, thus information propagates only in one direction. A marching algorithm can be implemented to propagate wavefronts away from the source. Using an initial starting field, the PE method advances the wavefront in the horizontal direction. Horizontal changes in environmental conditions are permissible in between steps.

Application of the PE methods for atmospheric acoustics [48-66] has been investigated by many researchers since the late 80's. Much of the research applied a linear finite element or finite difference approximation along the vertical direction to solve the parabolic equation. These approaches tend to ignore the continuity of slope in the pressure field. Typically, a physical absorbing layer is used to absorb sound energy reaching the top of the numerical grid in order to reduce undesired reflections when modeling a semi-infinite atmosphere. Unfortunately, this approach requires a large number of grid points which makes the computation highly inefficient for long-range computations.

The intent of this chapter is to extend the work of Gilbert *et al.* [48] to more general cases. In section 7.2, the linear and cubic finite element discretization process is reviewed. An arbitrary function can be written as the sum of the finite element basis functions, which is the basis for solving the parabolic equation in the subsequent sections. Section 7.3 outlines the derivation of the range dependent parabolic equation with either narrow-angle or wide-angle propagation. Following that, the numerical implementation of solving the parabolic equation is detailed in section 7.4. The finite element discretization, boundary conditions, and the starting fields are discussed in this section to complete the Parabolic Equation (PE) and/or Finite Element Method (FEM) formulation. The numerical results using PE/FEM are displayed in section 7.5, which including predictions for the sound field above an impedance ground, an extended reaction ground, and a hard-backed porous layer. The numerical accuracy of the proposed method is validated against classical asymptotic solutions using benchmark cases found in the

literature and through experimental investigation. A brief summary is provided in section 7.6.

7.2 Review of Finite Element Discretization

In this section, the steps for applying the finite element method to discretize a function are outlined. Both linear and cubic finite element shape functions will be reviewed.

a) Linear finite element shape functions

To begin, the finite element mesh on $\Omega = (x_b, x_t)$ is defined

$$X_h := \{x_i : x_b = x_1 < x_2 < \cdots < x_N = x_t\}. \tag{7.1}$$

The interval $e_j = [x_j, x_{j+1}]$ for $j = 1, 2, \cdots N-1$ is called the finite elements, and we say that the mesh is uniform if all the elements have the same size $h = 1/N$. For each element, we will use the notation $\varphi_{j,i}$, $i = 1, 2$ to denote the linear local node basis functions defined over the element $[x_j, x_{j+1}]$.

First, we consider the following local nodal basis functions in each element e_j,

$$\varphi_{j,1}(x) = 1 - \varsigma \text{ and } \varphi_{j,2}(x) = \varsigma, \tag{7.2a,b}$$

where

$$\varsigma = \frac{x - x_j}{h_j}, h_j = x_{j+1} - x_j. \tag{7.3a,b}$$

Then a set of hat functions defined for $j = 1$ by

$$\tau_1(x) = \begin{cases} \varphi_{1,1}, & x \in [x_1, x_2] \\ 0. & elsewhere \end{cases} \tag{7.4}$$

for $j = 2,\ldots N-1$ by

$$\tau_j(x) = \begin{cases} \varphi_{j-1,2}, & x \in [x_{j-1}, x_j] \\ \varphi_{j,1}, & x \in [x_j, x_{j+1}] \\ 0. & elsewhere \end{cases} \tag{7.5}$$

and for $j = N$ by

$$\tau_N(x) = \begin{cases} \varphi_{N,2}, & x \in [x_{N-1}, x_N] \\ 0. & elsewhere \end{cases}. \tag{7.6}$$

These basis functions on $\Omega = (0,1)$ are illustrated in Figure 7.1.

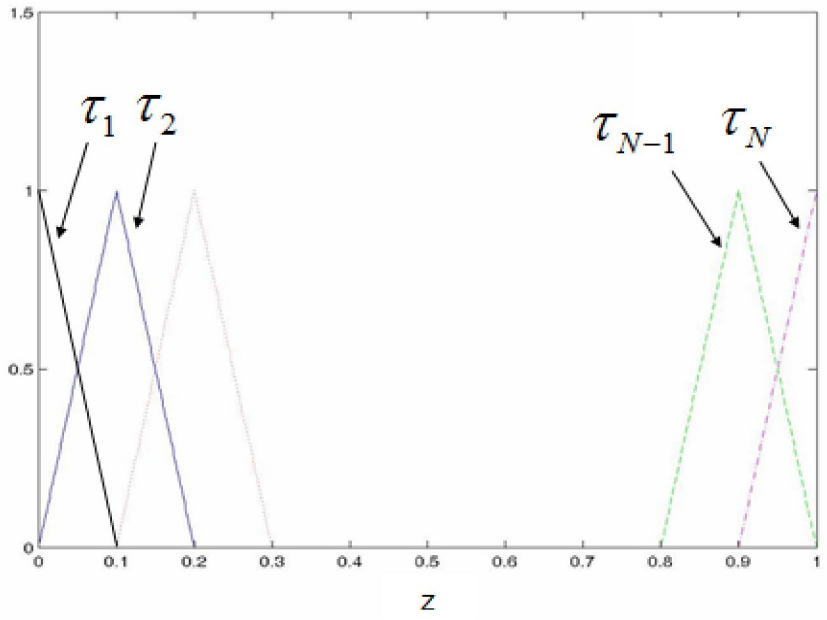

Figure 7.1: The hat functions for linear finite element basis function.

Hence, we can expand an arbitrary function ϕ in terms of linear finite element basis functions,

$$W(z) = \sum_{j=1}^{N} W(z_j)\tau_j(z) \tag{7.7}$$

where $W(z_j)$ are the expansion coefficients, which are unknown.

b) Cubic Hermite finite elements

As we can see in the last part of the linear finite element basis function, such an interpolation preserves continuity between the elements but fails to preserve continuity in the slope. Alternatively, we can apply the Hermite cubic finite element functions to solve the problem. The procedures are similar to those found for the linear finite element functions, but with additional complications. Instead of defining two local nodal basis functions in each element, we define four local node basis functions

$$\psi_{j,1}(z) = (1-\xi)^2(2\xi+1)\,;\ \psi_{j,2}(z) = h_j\xi(\xi-1)^2\,, \tag{7.8a,b}$$

$$\psi_{j,3}(z) = \xi^2(3-2\xi)\,;\ \psi_{j,4}(z) = h_j\xi^2(\xi-1)\,. \tag{7.8c,d}$$

These are plotted in Figure 7.2.

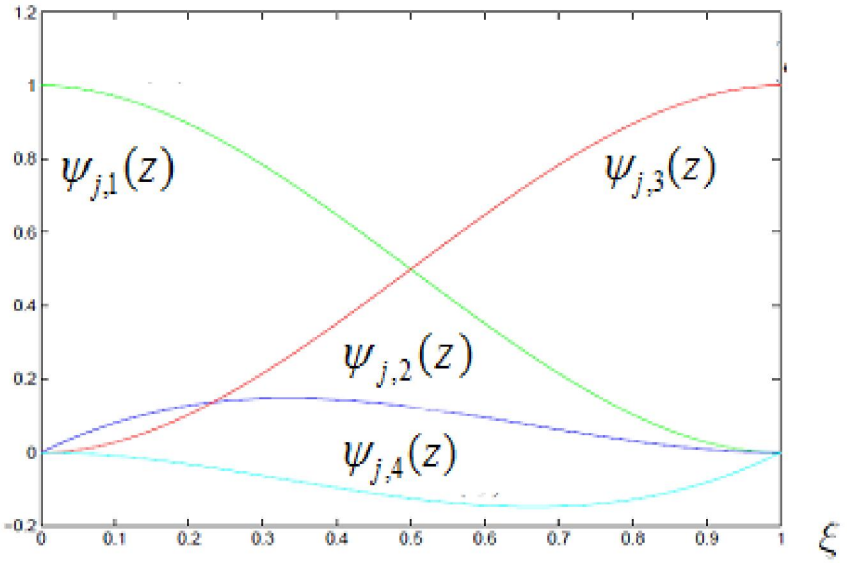

Figure 7.2: Four nodal basis functions for cubic finite elements.

Then, a set of functions defined for $j = 1$ by

$$\eta_1(z)=\begin{cases}\psi_{1,1}(z), & z\in[z_1,z_2],\\ 0 & elsewhere\end{cases} \quad \text{and} \tag{7.9a}$$

$$\eta_2(z)=\begin{cases}\psi_{1,2}(z), & z\in[z_1,z_2],\\ 0 & elsewhere\end{cases}. \tag{7.9b}$$

For $j=2,\ldots N-1$ by

$$\eta_{2j-1}(z)=\begin{cases}\psi_{j-1,3}(z), & z\in[z_{j-1},z_j],\\ \psi_{j,1}(z), & z\in[z_j,z_{j+1}],\\ 0 & elsewhere.\end{cases} \quad \text{and} \tag{7.10a}$$

$$\eta_{2j}(z)=\begin{cases}\psi_{j-1,4}(z), & z\in[z_{j-1},z_j],\\ \psi_{j,2}(z), & z\in[z_j,z_{j+1}]\\ 0 & elsewhere\end{cases}. \tag{7.10b}$$

For $j=N$ by

$$\eta_{2N-1}(z)=\begin{cases}\psi_{N,3}(z), & z\in[z_{N-1},z_N],\\ 0 & elsewhere\end{cases} \tag{7.11a}$$

$$\eta_{2N}(z)=\begin{cases}\psi_{N,4}(z), & z\in[z_N,z_{N-1}],\\ 0 & elsewhere\end{cases} \tag{7.11b}$$

The nodal value for $\phi_k(z_j)$, $k=1,2,\cdots 2N-1,2N$ and $j=1,2,\cdots,N$ is given by

$$\phi_{2i-1}(z)=\begin{cases}1, & z_j=z_i,\\ 0. & elsewhere\end{cases} \tag{7.12a}$$

for $i=1,2,\cdots,N$, and

$$\frac{\partial\phi_{2i}(z)}{\partial z}=\begin{cases}1, & z_j=z_i,\\ 0. & elsewhere\end{cases} \tag{7.12b}$$

for $i=1,2,\cdots,N$.

Notice that the properties of the Hermite cubic local nodal functions $\psi_{k,i}(z)$, $i=1,2,3,4$ determine the nodal values for ϕ_k, $k=1,2,\cdots 2N-1,2N$. Here, we plot the standard Hermite cubic basis functions with several nodes on the interval [0, 1] to help visualize these global basis functions (shown in Figure 7.3).

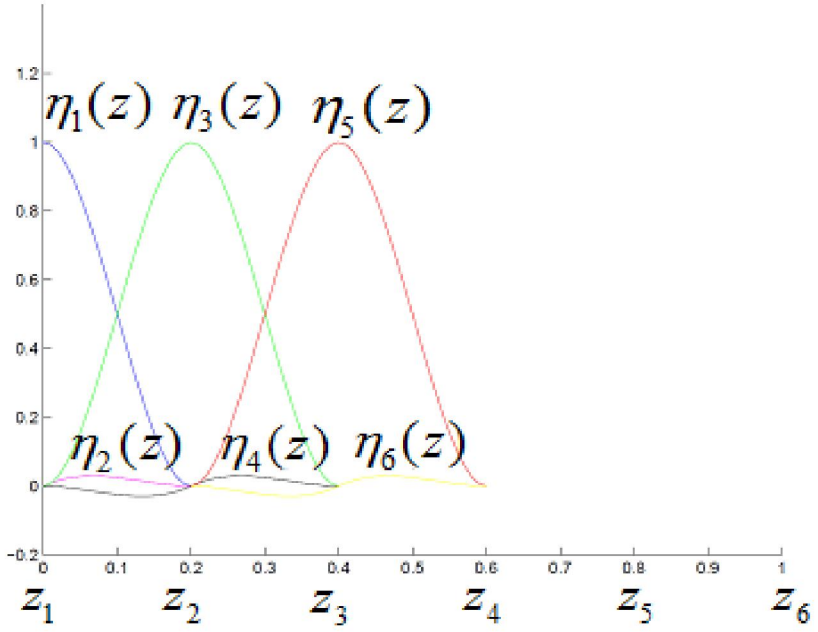

Figure 7.3: Global basis functions on the interval [0, 1].

In this case, we can expand an arbitrary function ϕ in terms of Hermite cubic linear finite element basis functions,

$$W(z)=\sum_{j=1}^{N} W(z_j)\eta_{2j-1}(z)+\frac{\partial W(z_j)}{\partial z}\eta_{2j}(z) \tag{7.13}$$

where $W(z_j)$, $\dfrac{\partial W(z_j)}{\partial z}$ are the expansion coefficients, which are unknown.

In summary, based on finite element discretization, an arbitrary function can be expanded as the sum of linear basis functions as seen in Eq.(7.7). It can also be expanded

as the sum of cubic basis functions as seen in Eq.(7.13). In the following sections, the linear and cubic finite element basis functions are used to discretize the field quantities.

7.3 Theoretical Formulation

Consider the 3-D Helmholtz equation for a constant-density medium in cylindrical coordinates (r, φ, z) in terms of the acoustic pressure P:

$$\frac{1}{r}\frac{\partial}{\partial r}\left(r\frac{\partial P}{\partial r}\right)+\frac{1}{r^2}\frac{\partial^2 P}{\partial \varphi^2}+\frac{\partial^2 P}{\partial z^2}+\frac{\omega^2}{c^2(r,\varphi,z)}P=0. \tag{7.14}$$

Assuming azimuthal symmetry and hence no dependence on the φ coordinate, this reduces to the standard 2-D Helmholtz equation:

$$\frac{\partial^2 P}{\partial r^2}+\frac{1}{r^2}\frac{\partial^2 P}{\partial r^2}+\frac{\partial^2 P}{\partial z^2}+k_0^2 n^2 P=0 \tag{7.15}$$

where $k_0=\omega_0/c_0$ is a reference wavenumber, where ω_0 is the angular frequency and c_0 is the sound speed in air; and $n(r,z)=c_0/c(r,z)$ is the index of refraction, where $c(r,z)$ is the sound speed. By making far-field approximation of $k_0 r >> 1$, the associated far-field equation for the variable $u=\sqrt{r}P$ (a form of the acoustic pressure that excludes attenuation from cylindrical spreading) is given by

$$\left(\frac{\partial^2}{\partial r^2}+Q\right)u=0 \tag{7.16}$$

and $Q=\partial^2/\partial z^2+k_0^2 n^2$. Eq.(7.16) can be interpreted as the product of incoming and outgoing wave operators, $\partial/\partial r \mp i\sqrt{Q}$. The (+) and (-) presents the wave propagating in the forward or backward direction. If only the outgoing component is considered (i.e.,

little back scattering), the one-way wave equation exclusively for a forward-going wave is obtained: $\frac{\partial u}{\partial r} = i\sqrt{Q}$.

For the purpose of numerical implementation, it is convenient to remove a "carrier wave" by defining a new, more slowly varying wave ϕ, where $\phi = q\exp(-ik_0 r)$, and where k_0 is set to be equal to the wave number in the air above the surface. Hence,

$$\partial\phi/\partial r = i(\sqrt{Q} - k_0)\phi. \tag{7.17}$$

Let $q = \frac{1}{k_o^2}\frac{\partial^2}{\partial z^2} + n^2 - 1$, then Eq.(7.4) becomes

$$\partial\phi/\partial r = ik_0(\sqrt{1+q} - 1)\phi. \tag{7.18}$$

Eq.(7.18) is the parabolic equation of interest. The finite element method is used to solve this problem.

For simplicity in continued analysis, the sound field ϕ is normalized using non-dimensional parameters such as $\overline{r} = k_0 r$, $\Delta\overline{r} = k_0\Delta r$, $\overline{z} = k_0 z$, and $\overline{c} = c/c_0$. In this case, Eq.(7.18) can be written as

$$\partial\phi/\partial\overline{r} = i(\sqrt{1+q} - 1)\phi. \tag{7.19}$$

The over-bar is implied in subsequent discussions.

To set up the finite element method to solve the problem, our first step is to rewrite Eq.(7.19) in its weak form. We begin by multiply Eq.(7.19) by a test function υ, and integrating to obtain:

$$\int_{r_1}^{r_2} \partial\phi/\partial r \cdot \upsilon(r)dr = \int_{r_1}^{r_2} (\sqrt{1+q} - 1)\phi \cdot \upsilon(r)dr \tag{7.20}$$

where $r \in (r_1, r_2)$, r_1 and r_2 is starting point and the end point for each marching step respectively. In addition, any arbitrary function can be represented as the sum of linear or cubic basis functions based on the finite element discretization in Section 7.1. Here, we start with a range-dependent function $W(r)$ in $r \in (r_1, r_2)$. For a small enough range step, $W(r)$ can be discretized into

$$W(r) = (1-\xi)W_1 + \xi W_2 \quad . \tag{7.21}$$

where

$$\xi = \frac{r - r_1}{\Delta r}, \Delta r = r_2 - r_1, \tag{7.22a,b}$$

$$W_1 = W(r_1), \; W_2 = W(r_2). \tag{7.22c,d}$$

Hence, the function $W(r)$ can be used as the test function to solve our problem:

$$\int_0^1 \frac{\partial \phi}{\partial r} \cdot W(r) d\xi = \int_0^1 i(\sqrt{1+q} - 1)\phi \cdot W(r) d\xi. \tag{7.23}$$

Integrating by part, the left-hand side and right-hand side of Eq. (7.23) can be written as:

$$\int_0^1 \frac{\partial \phi}{\partial r} \cdot W d\xi = \phi_2 \left(W_2 - \Delta r \cdot \Delta W/2\right) - \phi_1 \left(W_1 + \Delta r \cdot \Delta W/2\right), \tag{7.24a}$$

$$\int_0^1 \phi \cdot W d\xi = \frac{\Delta r}{2}\left(\phi_1 \cdot W_a + \phi_2 \cdot W_b\right) \tag{7.24b}$$

where $\Delta W = W_2 - W_1$, $W_a = \left(2W_1 + W_2\right)/3$ and $W_b = \left(2W_2 + W_1\right)/3$. It is interesting to note that when W is in the same direction as r, ΔW goes to zero while both W_a and W_b tends towards unity.

By substituting Eqs. (7.24a) and (7.24b), it can be shown that

$$\phi_2\left(W_2-\frac{\Delta r}{2}\Delta W\right)-\phi_1\left(W_1+\frac{\Delta r}{2}\Delta W\right)=\frac{i\Delta r(\sqrt{1+q}-1)}{2}\left(\phi_1\cdot W_a+\phi_2\cdot W_b\right). \tag{7.25}$$

For the special case when the function W is range-independent in the horizontal direction, Eq.(7.25) can be simplified:

$$\phi_2-\phi_1=\frac{i\Delta r}{2}(\sqrt{1+q}-1)\left(\phi_1+\phi_2\right). \tag{7.26}$$

That is,

$$\left(1-\frac{i\Delta r}{2}(\sqrt{1+q}-1)\right)\phi_2=\left(1+\frac{i\Delta r}{2}(\sqrt{1+q}-1)\right)\phi_1\ , \tag{7.27}$$

which is exactly the same as the expression for the split-step finite-element based parabolic-equation propagation[66].

Expanding the square root while neglecting higher ordered q terms (i.e., linearization), Eq.(7.27) can be rewritten as:

$$\left(1-\frac{i\Delta r}{4}q\right)\phi_2=\left(1+\frac{i\Delta r}{4}q\right)\phi_1, \tag{7.28}$$

which is the narrow-angle approximation for the PE marching scheme. The marching scheme is proven to be accurate when the propagation angle is up to 10^o [4]. A more accurate expansion for $\sqrt{1+q}$ is given by Claerbout's method [47], which is

$$\sqrt{1+q}\approx\frac{A+Bq}{C+Dq}, \tag{7.29}$$

where A, B, C and D are real constants, and $1/\left(C+Dq\right)$ means the inverse of $\left(C+Dq\right)$. By choosing A=1, B=3/4, C=1, D=1/4, the wide-angle PE propagation can be obtained:

$$\left(1+\frac{1}{4}q-\frac{i\Delta r}{4}q\right)\phi_2=\left(1+\frac{1}{4}q+\frac{i\Delta r}{4}q\right)\phi_1. \tag{7.30}$$

This approximation has quadratic accuracy in q and represents a considerable improvement over the narrow-angle PE propagation, which has a high accuracy with propagation angle up to 35^{o}. The narrow-angle PE propagation scheme can be recovered by selecting A=1, B=1/2, C=1, D=0. In the following analysis, we use A, B, C, D to derive the final formulation for ease of distinguishing the narrow-angle from the wide-angle PE propagation schemes. Hence, substitution of Eq.(7.29) into Eq.(7.27) gives the following operator equation for advancing ϕ from r to $r+\Delta r$:

$$M_b\phi(r+\Delta r) = M_a\phi(r)\,, \tag{7.31}$$

where

$$M_b = \left(W_2 - \frac{\Delta r \Delta W}{2}\right)\left(C + Dq\right) - \frac{i\Delta r W_b}{2}\left[\left(A-C\right)+\left(B-D\right)q\right], \tag{7.32a}$$

$$M_a = \left(W_1 + \frac{\Delta r \Delta W}{2}\right)\left(C + Dq\right) + \frac{i\Delta r W_a}{2}\left[\left(A-C\right)+\left(B-D\right)q\right]. \tag{7.32b}$$

Using $q = \left(\partial^2/\partial z^2 + k^2\right)\big/ k_0^2 - 1$ gives

$$M_b = \left(W_2 - \frac{\Delta r \Delta W}{2}\right)A_1 - \frac{i\Delta r W_b}{2}A_2 + \left[\left(W_2 - \frac{\Delta r \Delta W}{2}\right)A_3 - \frac{i\Delta r W_b}{2}A_4\right]\left(\frac{\partial^2}{\partial z^2} + n^2\right),$$

$$M_a = \left(W_1 + \frac{\Delta r \Delta W}{2}\right)A_1 + \frac{i\Delta r W_b}{2}A_2 + \left[\left(W_1 + \frac{\Delta r \Delta W}{2}\right)A_3 + \frac{i\Delta r W_a}{2}A_4\right]\left(\frac{\partial^2}{\partial z^2} + n^2\right),$$

(7.33a,b)

where $A_1 = C - D$, $A_2 = (A - C) - (B - D)$, $A_3 = D$ and $A_4 = B - D$. Since $\Delta W = W_2 - W_1$, Eqs.(7.33a) and (7.33b) can be reorganized:

$$M_b = B_1^* W_1 + B_2^* W_2 + \left(E_1^* W_1 + E_2^* W_2\right)\left(\frac{\partial^2}{\partial z^2} + n^2\right), \tag{7.34a}$$

$$M_a = B_2 W_1 + B_1 W_2 + \left(E_2 W_1 + E_1 W_2\right)\left(\frac{\partial^2}{\partial z^2} + n^2\right), \tag{7.34b}$$

where

$$B_1 = A_1 \frac{\Delta r}{2} + A_2 \frac{i\Delta r}{6},\ B_2 = A_1\left(1 - \frac{\Delta r}{2}\right) + A_2 \frac{i\Delta r}{3}, \tag{7.35a,b}$$

$$E_1 = A_3 \frac{\Delta r}{2} + A_4 \frac{i\Delta r}{6},\ E_2 = A_3\left(1 - \frac{\Delta r}{2}\right) + A_4 \frac{i\Delta r}{3}, \tag{7.36a,b}$$

and "*" denotes the complex conjugate of a complex number. If the horizontal density variation is taken into consideration, W_1 and W_2 represents the respective density at the range location r and $r + \Delta r$. If there's also density variations in the vertical direction, the operator $\partial^2/\partial z^2$ will be replaced with $\rho\,\partial/\partial z\left(1/\rho\right) \times (\partial/\partial z)$. By making this replacement and dividing by ρ, slightly modified forms for M_b and M_a can be obtained.

$$M_b = B_1^* \frac{1}{\rho_1} + B_2^* \frac{1}{\rho_2} + E_1^*\left(\frac{\partial}{\partial z}\left(\frac{1}{\rho_1}\right)\frac{\partial}{\partial z} + \frac{n^2}{\rho_1}\right) + E_2^*\left(\frac{\partial}{\partial z}\left(\frac{1}{\rho_2}\right)\frac{\partial}{\partial z} + \frac{n^2}{\rho_2}\right), \tag{7.37a}$$

$$M_a = B_2 \frac{1}{\rho_1} + B_1 \frac{1}{\rho_2} + E_2\left(\frac{\partial}{\partial z}\left(\frac{1}{\rho_1}\right)\frac{\partial}{\partial z} + \frac{n^2}{\rho_1}\right) + E_1\left(\frac{\partial}{\partial z}\left(\frac{1}{\rho_2}\right)\frac{\partial}{\partial z} + \frac{n^2}{\rho_2}\right). \tag{7.37b}$$

Here ρ_1 and ρ_2 represents the density at the location of r and $r + \Delta r$ respectively. They can be expressed as

$$\rho_1 = \rho(r, z),\ \rho_2 = \rho(r + \Delta r, z). \tag{7.38}$$

7.4 Numerical Implementation

A numerical approach for solving Eq. (7.31) is outlined in this section. By discretizing the vertical dependence of the acoustic field, the operator-function equations

become matrix-vector equations. Instead of using finite difference approximations, we employ finite elements. This approach enables small-scale vertical variations in both density and speed of sound to be present during the propagation steps. Furthermore, non-uniform vertical point spacing in the numerical grid can be treated more effectively. First, consider the linear finite element discretization as an example.

7.4.1 Finite Elements

As stated in section 7.2, $\phi(r+\Delta r)$ and $\phi(r)$ can be expanded in terms of linear finite element basis functions, $\tau_j(z)$ as below

$$\phi(r+\Delta r,z)=\sum_{j=1}^{N}\phi(r+\Delta r,z_j)\tau_j(z)\,, \tag{7.39a}$$

and

$$\phi(r,z)=\sum_{j=1}^{N}\phi(r,z_j)\tau_j(z)\,, \tag{7.39b}$$

where $\phi(r+\Delta r,z_j)$ and $\phi(r,z_j)$ are the expansion coefficients. Note that expanding $\phi(r+\Delta r,z)$ and $\phi(r,z)$ in terms of the linear basis function is equivalent to linear interpolation of the function between the grid points z_j, which is defined as

$$Z_h := \left\{ z_j : z_b = z_1 < z_2 < \cdots < z_N = z_t \right\} \tag{7.40}$$

where z_b and z_t represents the value of z at the bottom layer and top layer. To obtain the matrix expression for the marching scheme, the hat function expansion for ϕ is sustitutited into Eq. (7.31):

$$M_b\sum_{j=1}^{N}\phi(r+\Delta r,z_j)\tau_j(z)=M_a\sum_{j=1}^{N}\phi(r,z_j)\tau_j(z)\,. \tag{7.41}$$

To solve the above equation, we multiply by $\tau_i(z)$ and integrate over z. For convenience, at the range location *r*, we define $\left(\rho(r,z)\right)^{-1}$ as $f_a(z)$ and $n^2(r,z)\left(\rho(r,z)\right)^{-1}$ as $g_a(z)$. At the range location $r+\Delta r$, we define $\left(\rho(r+\Delta r,z)\right)^{-1}$ as $f_b(z)$ and $n^2(r+\Delta r,z)\left(\rho(r+\Delta r,z)\right)^{-1}$ as $g_b(z)$. The following matrix elements are obtained:

$$F_{ij}(f)=\int_{z_b}^{z_t}\tau_i(z)f(z)\tau_j(z)dz\,, \tag{7.42a}$$

$$G_{ij}(g)=\int_{z_b}^{z_t}\tau_i(z)g(z)\tau_j(z)dz\,, \tag{7.42b}$$

$$J_{ij}(f)=-\int_{z_b}^{z_t}\frac{\partial\tau_i(z)}{\partial z}f(z)\frac{\partial\tau_j(z)}{\partial z}dz\,, \tag{7.42c}$$

to allow a more convenient expression for M_a and M_b. Note that the basis function $\tau_i(z)$ overlaps only with its nearest neighbor, the matrix elements $F_{ij}(f)$, $G_{ij}(g)$ and $J_{ij}(f)$ are tridiagonal, symmetric matrices. To obtain simple analytical expressions for these matrices, we take *f* and *g* to be linear function of *z* between the grid points, and assume to be continuous at the grid points. Hence, for the element $[z_j,z_{j+1}]$, we approximate $f(z)$ as

$$f(z)=f(z_j)+(z-z_j)\left(\frac{f(z_{j+1})-f(z_j)}{z_{j+1}-z_j}\right). \tag{7.43}$$

Inserting the linear approximation for $f(z)$ into Eq. (7.42a) yields

$$F_{i,i}(f)=\frac{1}{6}\left\{\Delta z_{i-1}\left(\overline{f}_{i-1}+f_i\right)+\Delta z_i\left(\overline{f}_i+f_i\right)\right\}\qquad \text{for } 2\le i\le N\,, \tag{7.44a}$$

$$F_{i,i+1}(f)=\frac{1}{6}\Delta z_i\overline{f}_i\,, \tag{7.44b}$$

$$F_{i,i-1}(f)=\frac{1}{6}\Delta z_{i-1}\overline{f}_{i-1}\ . \tag{7.44c}$$

where f_i is defined as the value of f at the location $z=z_i$ for $i=1,2,\cdots N$. And we introduce the mean value $\overline{f}_i$ as the average value of f_i and f_{i+1} .When $i=1$ and $i=N$, the respective expression for $F_{1,1}(f)$ and $F_{N,N}(f)$ needs to be calculated separately. That is,

$$F_{1,1}(f)=\frac{1}{6}\Delta z_1\left(\overline{f}_1+f_1\right), \tag{7.45a}$$

and

$$F_{N,N}(f)=\frac{1}{6}\Delta z_N\left(\overline{f}_{N-1}+f_N\right). \tag{7.45b}$$

Similarly, the expression for $G_{ij}(g)$ is the same as $F_{ij}(f)$ except that replacing f with g. Furthermore, substitution of the linear approximation for $f(z)$ into Eq. (7.42c) yields,

$$J_{i,i}(f)=-\left\{\frac{\overline{f}_i}{\Delta z_i}+\frac{\overline{f}_{i-1}}{\Delta z_{i-1}}\right\} \quad \text{for } 2\le i\le N, \tag{7.46a}$$

$$J_{i,i+1}(f)=\frac{\overline{f}_i}{\Delta z_i}, \tag{7.46b}$$

$$J_{i,i-1}(f)=\frac{\overline{f}_{i-1}}{\Delta z_{i-1}}\ , \tag{7.46c}$$

$$J_{1,1}(f)=-\frac{\overline{f}_1}{\Delta z_1}, \tag{7.46d}$$

$$J_{N,N}(f)=-\frac{\overline{f}_N}{\Delta z_N}\ , \tag{7.46e}$$

Hence, the respective structure of M_b and M_a is shown to be

$$M_b = \begin{bmatrix} K_{1,1}^b & K_{1,2}^b & 0 & 0 & \cdots \\ K_{2,1}^b & K_{2,2}^b & K_{2,3}^b & 0 & \cdots \\ 0 & K_{3,2}^b & K_{3,3}^b & K_{3,4}^b & \cdots \\ 0 & 0 & \ddots & \ddots & \ddots \end{bmatrix}_{N\times N}, \tag{7.47a}$$

and

$$M_a = \begin{bmatrix} K_{1,1}^a & K_{1,2}^a & 0 & 0 & \cdots \\ K_{2,1}^a & K_{2,2}^a & K_{2,3}^a & 0 & \cdots \\ 0 & K_{3,2}^a & K_{3,3}^a & K_{3,4}^a & \cdots \\ 0 & 0 & \ddots & \ddots & \ddots \end{bmatrix}_{N\times N}. \tag{7.47b}$$

Here,

$$K_{i,j}^b = B_1^* F_{ij}(f_a) + B_2^* F_{ij}(f_b) + E_1^* \left(G_{ij}(g_a) + J_{ij}(f_a)\right) + E_2^* \left(G_{ij}(g_b) + J_{ij}(f_b)\right), \tag{7.48a}$$

$$K_{i,j}^a = B_2 F_{ij}(f_a) + B_1 F_{ij}(f_b) + E_2 \left(G_{ij}(g_a) + J_{ij}(f_a)\right) + E_1 \left(G_{ij}(g_b) + J_{ij}(f_b)\right), \tag{7.48b}$$

where the subscript *a* and *b* denotes the position *r* and $r + \Delta r$. For range-independent case, where *f* and *g* are constant at position *r* and $r + \Delta r$, the expression for $K_{i,j}^b$ and $K_{i,j}^a$ can be simplified to be

$$K_{i,j}^b = \left(B_1^* + B_2^*\right) F_{ij}(f) + \left(E_1^* + E_2^*\right)\left(G_{ij}(g) + J_{ij}(f)\right), \tag{7.49a}$$

$$K_{i,j}^a = \left(B_1 + B_2\right) F_{ij}(f) + \left(E_1 + E_2\right)\left(G_{ij}(g) + J_{ij}(f)\right), \tag{7.49b}$$

where $B_1 + B_2 = A_1 + A_2 \frac{i\Delta r}{2}$, and $E_1 + E_2 = A_3 + A_4 \frac{i\Delta r}{2}$.

The above derivations are based on the linear FEM discretization of the function in the vertical direction. However, when a cubic FEM discretization is used, the forms are

similar except the matrix elements for $F_{ij}(f)$, $G_{ij}(f)$, $J_{ij}(f)$ are no longer constants—they each become a 2×2 matrices. Appendix F gives the expression for these matrices.

Note that the matrix form of M_b and M_a are tri-diagnoal with *N* diagonal elements and *N-1* off-diagonal elements and symmetric, the formation of the matrices can be done by vectorization of the diagonal and off-diagonal matrices. Hence, Eq. (7.31) can be solved by

$$\phi(r+\Delta r)=\left\{\left[M_b\right]^{-1}M_a\right\}\phi(r), \tag{7.50}$$

where $\left[M_b\right]^{-1}M_a$ can be obtained by Gauss elimination. Further investigation of the above expressions indicates that boundary conditions have yet to be incorporated.

7.4.2 Boundary Conditions

We start by considering part of boundary conditions at the horizontal position *r*, as seen in Eq.(7.37b):

$$\int_{z_b}^{z_t}\left[E_2\frac{\partial}{\partial z}\left(\frac{1}{\rho_1}\right)\frac{\partial}{\partial z}\right]\phi(r,z)\tau_i(z)dz=E_2\left\{\tau_i(z)\left(\frac{1}{\rho_1(z)}\right)\frac{\partial\phi(r,z)}{\partial z}\bigg|_{z_b}^{z_t}-\int_{z_b}^{z_t}\frac{\partial\tau_i(z)}{\partial z}\left(\frac{1}{\rho_1(z)}\right)\frac{\partial\phi(r,z)}{\partial z}dz\right\}. \tag{7.51}$$

After a series of simplifications, Eq.(7.51) is shown to be

$$\int_{z_b}^{z_t}\left[E_2\frac{\partial}{\partial z}\left(\frac{1}{\rho_1}\right)\frac{\partial}{\partial z}\right]\phi(r,z)\tau_i(z)dz=E_2\left\{f_N\partial_z\phi_N-f_1\partial_z\phi_1\right\}+E_2J_{ij}(f). \tag{7.52a}$$

Here, f represents $1/\rho_1$, and f_N =f(z_t), f_1 =f(z_b), ∂_z is the abbreviated representation of $\partial/\partial z$. In a similar way, all other boundary conditions can be incorporated into the equations:

$$\int_{z_b}^{z_t}\left[E_1\frac{\partial}{\partial z}\left(\frac{1}{\rho_2}\right)\frac{\partial}{\partial z}\right]\phi(r,z)\tau_i(z)dz = E_1\left\{f_N\partial_z\phi_N - f_1\partial_z\phi_1\right\} + E_1J_{ij}(f)\,. \tag{7.52b}$$

Here, f represents $1/\rho_2$, and f_N=f(z_t), f_1=f(z_b).

(a) Impedance boundary condition

For the impedance ground, the relationship between the pressure and velocity is

$$\frac{p}{u} = Z\rho c\,, \tag{7.53}$$

where Z is the normalized impedance of the locally ground surface, ρc is the impedance of the air, p is the complex pressure, and u is the complex velocity. According to Euler's Equation, the velocity and pressure have the relationship like

$$u = \frac{1}{j\omega\rho}\frac{dp}{dz}\,. \tag{7.54}$$

By substituting Eq.(7.54) into Eq.(7.53), we obtain

$$\frac{dp}{dz} + ik_0\beta p = 0\,, \tag{7.55}$$

at the impedance surface. The admittance β is the normalized admittance and it is equal to $1/Z$. If the bottom layer is impedance ground, by relating p with ϕ, the bottom boundary conditions can be written as

$$\partial_z\phi(r,z_b) + ik_0\beta\phi(r,z_b) = 0\,, \tag{7.56a}$$

$$\partial_z\phi(r+\Delta r,z_b) + ik_0\beta\phi(r+\Delta r,z_b) = 0\,. \tag{7.56b}$$

Eqs.(7.56a) and (7.56b), as the boundary conditions, can be incorporated directly into Eqs.(7.52a) and (7.52b).

(b) Radiation boundary condition

Near the top of the vertical grid, we essentially wish to terminate the solution domain in $z = z_t$ by a radiation boundary condition. The usual approach is to use an absorbing layer of approximately *50* wavelengths at the top of the vertical grid to ensure that no significant energy is reflected from the top boundary which can interfere with our solution. Let's define the height of where the absorbing layer begins as z_a. The absorbing layer is implemented by adding an imaginary term to the wave number for $z_a \le z \le z_t$ to provide a gradual attenuation. The imaginary term used in this paper is selected as [4]

$$iA_t (z - z_a)^2 / (z_t - z_a)^2 , \tag{7.57}$$

where A_t is a constant. The optimum choice of A_t varies with frequency, which is set to be 1, 0.5, 0.4 and 0.2 for frequencies of 1000, 500, 125, 30Hz respectively. Values of A_t are linearly interpolated between these frequencies for other intermediate frequencies.

For the very top boundary $z = z_t$, unity impedance is used since it corresponds to the normalized impedance of air:

$$\frac{dp}{dz} - ik_0 p = 0 , \tag{7.58}$$

at the top boundary $z = z_t$. Similar to the bottom boundary condition, we can rewrite the top boundary condition as

$$\partial_z \phi(r, z_t) - ik_0 \phi(r, z_t) = 0 , \tag{7.59a}$$

$$\partial_z \phi(r + \Delta r, z_t) - ik_0 \phi(r + \Delta r, z_t) = 0 , \tag{7.59b}$$

which can be directly used in Eq.(7.52). This completes the requirement for the boundary conditions in PE marching algorithm.

(c) Intermediate boundary condition

In the case of non-locally reacting porous ground interfaces, the sound fields above and below the interface needs to be solved simultaneously. Since the properties of the medium above and below the ground are different, not only the continuity of the pressure, but also the continuity of the particle velocity needs to be accounted. In the linear finite elements approach, the pressure continuity is already present in the construction of the matrices. That is,

$$(M_b)_{above}\phi_{above}(r+\Delta r,z)=(M_a)_{above}\phi_{above}(r,z), \tag{7.60a}$$

$$(M_b)_{below}\phi_{below}(r+\Delta r,z)=(M_a)_{below}\phi_{below}(r,z), \tag{7.60b}$$

where $\phi_{above}(r+\Delta r,z)$, $\phi_{below}(r+\Delta r,z)$, $\phi_{above}(r,z)$ and $\phi_{below}(r,z)$ are vectors depending on the number of grids discretized in the z direction. For instance, if we defines the number of grids as N_1 for the vertical grids of nodes below ground, and the number of grids for nodes above ground as N_2 , $\phi_{above}(r+\Delta r,z)$ and $\phi_{above}(r,z)$ become a $N_1\times 1$ vector, while $\phi_{below}(r+\Delta r,z)$ and $\phi_{below}(r,z)$ become a $N_2\times 1$ vector. Since they have the common node at the ground interface, the two set of grids for above and below grounds can be added directly, which makes the total number of the grids be $N=N_1+N_2-1$. However, the linear finite element fails to consider the continuity of velocity. At the interface, it also satisfies velocity continuity besides pressure continuity, which is

$$\phi(z_{0^+})=\phi(z_{0^-}), \tag{7.61a}$$

$$\frac{1}{\rho(z_{0^+})}\frac{\partial\phi(z_{0^+})}{\partial z}=\frac{1}{\rho(z_{0^-})}\frac{\partial\phi(z_{0^-})}{\partial z}. \tag{7.61b}$$

By using cubic finite elements, the pressure and velocity continuity can be guaranteed at the same time since the velocity is related to the slope of pressure based on Euler's equation in Eq.(7.54).

Applying the cubic finite element discretization discussed in Section 7.2, $\phi(r,z)$ and $\phi(r+\Delta r,z)$ can be written as

$$\phi(r,z)=\sum_{j=1}^{N}\phi(r,z_j)\eta_{2j-1}(z)+\frac{1}{\rho(z_j)}\partial_z\phi(r,z_j)\eta_{2j}(z), \tag{7.62}$$

and

$$\phi(r+\Delta r,z)=\sum_{j=1}^{N}\phi(r+\Delta r,z_j)\eta_{2j-1}(z)+\frac{1}{\rho(z_j)}\partial_z\phi(r+\Delta r,z_j)\eta_{2j}(z). \tag{7.63}$$

At each node z_j, there are two properties: $\phi(r,z_j)$ and $\frac{1}{\rho(z_j)}\partial_z\phi(r,z_j)$. The column vector related to the three nodes near the ground surface is:

$$\left[\phi(r,z_{-1}),\frac{1}{\rho(z_{-1})}\partial_z\phi(r,z_{-1}),\phi(r,z_0),\frac{1}{\rho(z_0)}\partial_z\phi(r,z_0),\phi(r,z_1),\frac{1}{\rho(z_1)}\partial_z\phi(r,z_1)\right]^T, \tag{7.64}$$

since Eq.(7.61a) and (7.61b) are satisfied at the interface.

The matrices $(M_b)_{above}$ and $(M_a)_{above}$ are expanded into $2N_2\times 2N_2$ matrices, and $(M_b)_{below}$ and $(M_a)_{below}$ are expanded into $2N_1\times 2N_1$ matrices. To form the global matrix, we need to first expand the matrices $(M_b)_{above}$, $(M_a)_{above}$ from a $2N_2\times 2N_2$ matrix to a $2N\times 2N$ by simply adding zeros at the nodes related to those of below ground with the exception of the node at the ground surface. Second, the same operations are applied to $(M_b)_{below}$, $(M_a)_{below}$, where zeros are added to the nodes related to those above the ground surface. Then the two matrices can be added up to form the new matrices:

$$\left[(M_b)_{below} + (M_b)_{above}\right]\phi(r+\Delta r, z) = \left[(M_a)_{below} + (M_a)_{above}\right]\phi(r, z). \tag{7.65}$$

Figure 7.4 shows the combination of the nodes for above ground and below ground. The interface is the ground surface where node z_0 is located.

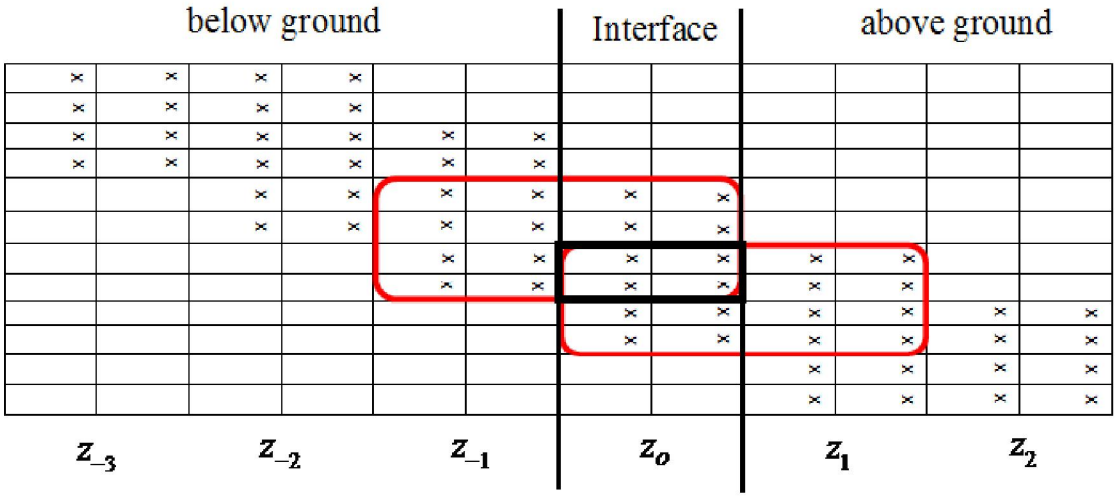

Figure 7.4: The combination process of the finite elements at the node of the porous interfaces.

From Eq. (7.52a), the two extra terms from the nodes are from the sound field above ground

$$E_2\left\{\frac{1}{\rho(z_t)}\partial_z\phi(r, z_t) - \frac{1}{\rho(z_{0^+})}\partial_z\phi(r, z_{0^+})\right\}, \tag{7.66a}$$

and the two extra terms from the nodes below ground due to the finite element discretilization

$$E_2\left\{\frac{1}{\rho(z_{0^-})}\partial_z\phi(r, z_{0^-}) - \frac{1}{\rho(z_b)}\partial_z\phi(r, z_b)\right\}. \tag{7.66b}$$

Adding Eqs.(7.66a) and (7.66b) together and using the relationship in Eq.(7.61), the four terms become

$$E_2\left[\frac{1}{\rho(z_t)}\partial_z\phi(r,z_t)-\frac{1}{\rho(z_b)}\partial_z(r,z_b)\right], \tag{7.67}$$

which represents the top and below boundaries of the vertical grid. The boundary conditions in Eqs.(7.56a), (7.56b) and Eqs.(7.59a), (7.59b) are substituted into Eq.(6.67) directly. Figure 7.5 shows the geometry of the vertical grids in more detail.

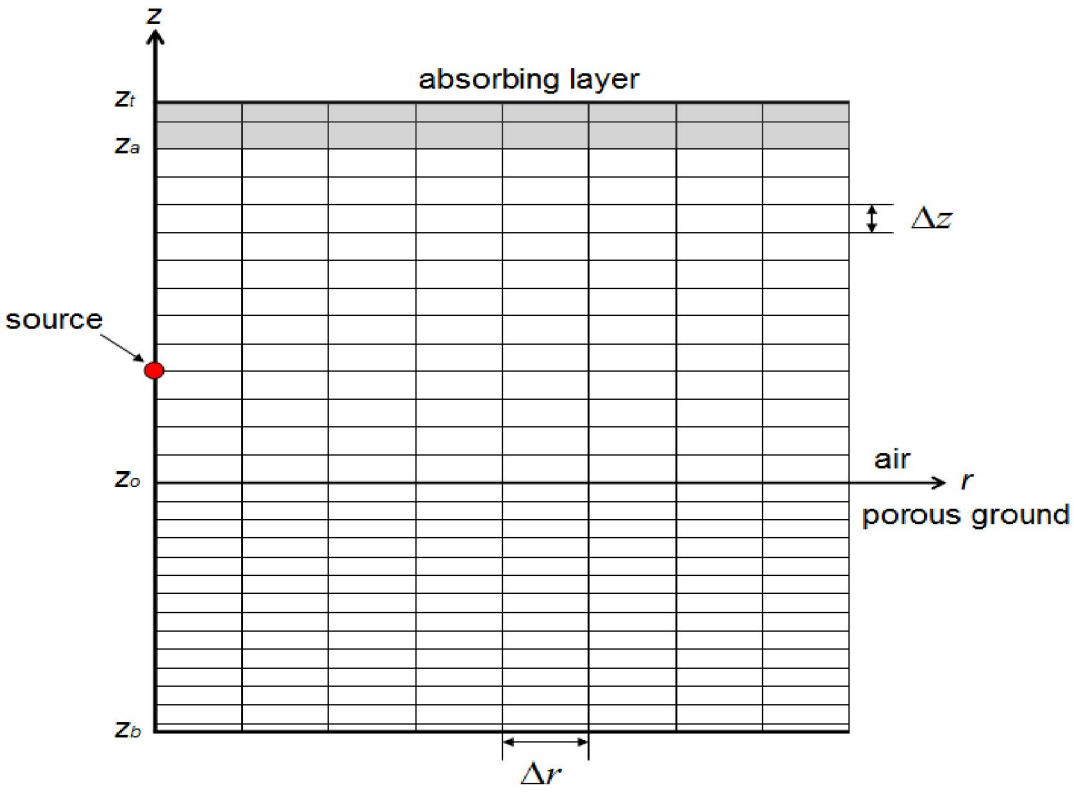

Figure 7.5: The geometry of the vertical grids.

7.4.3 Perfectly Matched Layer (PML)

The absorbing layer methods in section 7.3.2 to model radiation boundary condition requires the length of approximately 50 wavelengths, which makes the computation time consuming. Herein, the perfectly matched layer (PML) technique [115] is adopted for use with parabolic equation propagation. It incorporates an imaginary

component into the transverse coordinate that mimics the introduction of a fictitious absorber on the edge of the computational domain. For the parabolic equation of interest, the PML corresponds to changing the depth z to the complex variable $\hat{z}$:

$$\hat{z} = z + i\int_0^z \sigma(\tau)d\tau\,, \tag{7.68}$$

where $\sigma(z) = 0$ for $0 \le z \le H$, and $\sigma(z) > 0$ for $z > H$. From Eq.(7.68), it's shown that

$$\partial\hat{z} = \left[1 + i\sigma(z)\right]\partial z\,. \tag{7.69}$$

By replacing ∂z in Eqs.(7.37a) and (7.37b) by Eq.(7.69), we obtain the following modified expression for M_b and M_a :

$$M_b = B_1^*\frac{1}{\rho_1} + B_2^*\frac{1}{\rho_2} + E_1^*\left(\frac{\partial}{\eta\partial z}\left(\frac{1}{\rho_1\eta}\right)\frac{\partial}{\partial z} + \frac{n^2}{\rho_1}\right) + E_2^*\left(\frac{\partial}{\eta\partial z}\left(\frac{1}{\rho_2\eta}\right)\frac{\partial}{\partial z} + \frac{n^2}{\rho_2}\right), \tag{7.70a}$$

$$M_a = B_2\frac{1}{\rho_1} + B_1\frac{1}{\rho_2} + E_2\left(\frac{\partial}{\eta\partial z}\left(\frac{1}{\rho_1\eta}\right)\frac{\partial}{\partial z} + \frac{n^2}{\rho_1}\right) + E_1\left(\frac{\partial}{\eta\partial z}\left(\frac{1}{\rho_2\eta}\right)\frac{\partial}{\partial z} + \frac{n^2}{\rho_2}\right), \tag{7.70b}$$

where $\eta = 1 + i\sigma(z)$. By multiplying both sides of Eq.(7.37) by η , the new expression for the wide-angle parabolic equation is changed by new M_b and M_a , i.e.,

$$M_b = B_1^*\frac{\eta}{\rho_1} + B_2^*\frac{\eta}{\rho_2} + E_1^*\left(\frac{\partial}{\partial z}\left(\frac{1}{\rho_1\eta}\right)\frac{\partial}{\partial z} + \frac{\eta n^2}{\rho_1}\right) + E_2^*\left(\frac{\partial}{\partial z}\left(\frac{1}{\rho_2\eta}\right)\frac{\partial}{\partial z} + \frac{\eta n^2}{\rho_2}\right), \tag{7.71a}$$

$$M_a = B_2\frac{\eta}{\rho_1} + B_1\frac{\eta}{\rho_2} + E_2\left(\frac{\partial}{\partial z}\left(\frac{1}{\rho_1\eta}\right)\frac{\partial}{\partial z} + \frac{\eta n^2}{\rho_1}\right) + E_1\left(\frac{\partial}{\partial z}\left(\frac{1}{\rho_2\eta}\right)\frac{\partial}{\partial z} + \frac{\eta n^2}{\rho_2}\right). \tag{7.71b}$$

After reorganizing the matrix representation, Eq.(7.48a) and (7.48b) become

$$K_{i,j}^b = B_1^*F_{ij}(f_a\eta) + B_2^*F_{ij}(f_b\eta) + E_1^*\left(G_{ij}(g_a\eta) + J_{ij}(f_a/\eta)\right) + E_2^*\left(G_{ij}(g_b\eta) + J_{ij}(f_b/\eta)\right),$$

$$K_{i,j}^a = B_2F_{ij}(f_a\eta) + B_1F_{ij}(f_b\eta) + E_2\left(G_{ij}(g_a\eta) + J_{ij}(f_a/\eta)\right) + E_1\left(G_{ij}(g_b\eta) + J_{ij}(f_b/\eta)\right).$$

(7.72a, b)

For numerical computations, it is necessary to truncate the variable z to a finite interval, say $z_b < z < z_t$, where $z_t > H$. The interval (H, z_t) is then the actual PML layer. By reference to PML used in the paper [115], we define $\eta = 1 + \gamma(z) + i\sigma(z)$, and have

$$\sigma(z) = \frac{200\tau^3}{1+\tau^2}, \gamma(z) = \frac{100\tau^3}{1+\tau^2}, \tau = \frac{z-H}{z_t - H}. \quad (7.73a,b,c)$$

7.4.4 Starting Field

As shown in Eq. (7.31), the value of ϕ at range $(r + \Delta r)$ is computed from the value at range r. The PE algorithm marches results forward in range by extrapolating from vertical vectors of results from previous range steps. Therefore, an initial sound field ϕ_0 is required at the starting range r_0 for all elevations. (Typically, $r_0 = 0$ is used.) Ideally, we would like to specify a spatial δ function $\delta(z - z_s)$ for the source at height z_s. This would have a constant vertical k_z space transform with all k components of equal modulus. As the delta function cannot be accommodated in the process of solving Eq. (7.31) at each range step, a spatial Gauss function centered on $z = z_s$ will be used. The sharper the function is in the z domain, the more broadly spread is the transform in the k_z domain. A Gaussian starter field, originally proposed by Tappert [46] is given as:

$$\phi(0, z) = Ae^{-\frac{(z-z_s)^2}{W^2}}. \quad (7.74)$$

By using appropriate numerical techniques such as complex Fourier transform, integration by parts, expansion of the exponential function, and/or normalized point-

source field in a homogeneous medium, it is easily verified that a field matching is achieved by using the following values for A and W:

$$A = \sqrt{k_0}, W = \frac{\sqrt{2}}{k_0}. \tag{7.75}$$

Figure 7.6 shows that starting field corresponding to an arbitrary starting at origin.

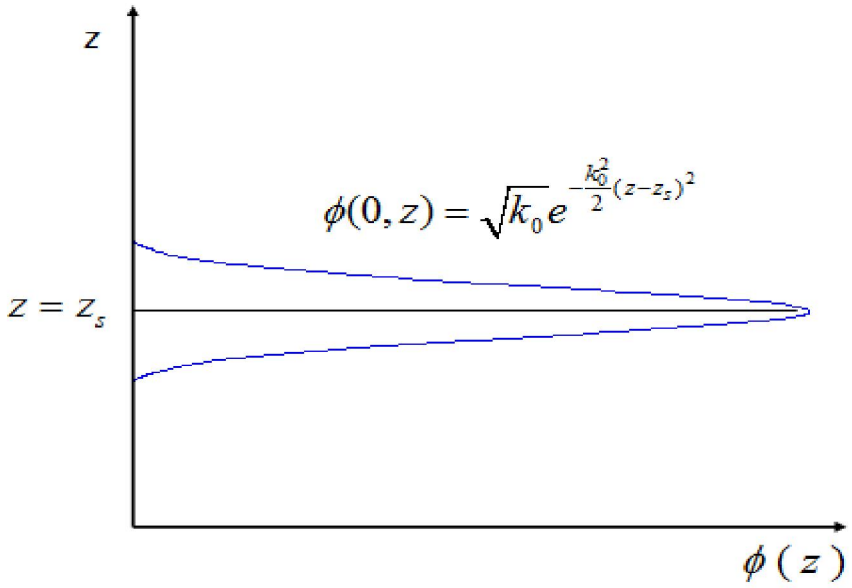

Figure 7.6: The standard Gaussian Starter.

The starting field given in Eq. (7.74) can now be written as

$$\phi(0,z) = \sqrt{k_0} e^{-\frac{k_0^2 (z-z_s)^2}{2}}, \tag{7.76}$$

which is known as the standard Gaussian source.

The Gaussian source has been used extensively as a starter field for the numerical implementation of the standard PE method since it can be generated with minimal computational effort. However, a more wide-angled starter field is required for the wide-angle propagation problems. For this, a Green's source [4] can be implemented:

$$\phi(0,z) = \sqrt{k_0}\left[1.4467 - 0.4201k_0^2(z-z_s)^2\right]e^{-\frac{k_0^2(z-z_s)^2}{3.0512}}. \tag{7.77}$$

The main advantages of the Gaussian starter includes: (i) it is a good approximation for a cylindrical or spherical source within the constraints of the small angle approximation used in PE; (ii) it has minimal side lobes in z and none in k-space; (iii) its phase and its depth dependence to second order in $|z-z_s|/x$ are close to that of a point source in a homogeneous medium. Its main disadvantage are its omission of boundary effects in the starting plane and its slow roll-off in wavenumber space which allows energy at high angles to propagate, which does not occur with a true point source.

If the source is located at position $(r,z) = (0,z_s)$ above a finite-impedance ground surface at $z = 0$, the following starting field can be used:

$$\phi(0,z) = \phi_0(z-z_s) + C\phi_0(z+z_s), \tag{7.78}$$

where the function $\phi_0(z)$ is defined as the starting field for a source at position $(r,z) = (0,0)$ in an unbounded atmosphere, and C is a reflection coefficient. For narrow angle parabolic equation, Eq. (7.61) can be used for the function $\phi_0(z)$. For the wide-angle parabolic equation, Eq. (7.62) can be used.

The first term on the right-hand side of Eq.(7.78) represents the direct field of the source; the second term represents the field reflected by the ground surface or, equivalently, the field of the image source at position (0,-z_s). Since the Gaussian starting field assumes we are interested in the far field solution, it is not suitable for near field sound predictions. In this disertation, we apply the analytical asymptotic solutions

obtained in previous chapters as the starting field. The starting field is chosen to start at a certain separation distance from the origin. The pressure is related to the starting field by

$$\phi(r,z) = \sqrt{r}\, p(r,z) e^{-ik_0 r}. \tag{7.79}$$

For linear finite elements method, the pressure field is only required at the location of the starting field. However, for the cubic finite elements method, the pressure and the slope of pressure along the *z*-direction are both required. Because the definition for the pressure field from a dipole source is equal to the slope of the pressure along the *z*-direction, the asymptotic solutions we obtained in Chapter 6 can be reused. This provides an approach for implementing a cubic finite element interpolation to solve the parabolic equation. In summary, the starting fields based on the asymptotic solutions for different rigid porous interfaces are listed as follows.

For sound fields above the ground, the relevant ground types consists of: impedance ground, extended reaction ground, hard-backed ground, and impedance-backed ground, whose sound fields are expressed as

$$p = \frac{e^{ikR_1}}{4\pi R_1} + \left[V_\theta + A(1-V_\theta)F(w)\right]\frac{e^{ikR_2}}{4\pi R_2}, \tag{7.65}$$

where $F(w)$ is the boundary loss factor, is given by

$$F(w) = 1 + i\sqrt{\pi}\, w \exp(-w^2) erfc(-iw), \tag{7.66a}$$

and V_θ is the plane wave reflection coefficient,

$$V_\theta = \frac{\cos\theta - \beta}{\cos\theta + \beta}. \tag{7.66b}$$

And A is known as the augmented diffraction factor.

$$A = \frac{\left(r_\beta / r_w\right)}{E_p \sqrt{\sin\theta \sin\mu_p}}, \tag{7.67a}$$

For impedance ground,

$$A = 1; \tag{7.67b}$$

For extended-reaction ground,

$$E_p = 1 - \xi^2; \tag{7.67c}$$

For hard-backed ground,

$$E_p = 1 + i\left(\zeta\chi_p / N_p\right)\left[\tan\left(k_0 N_p d\right) + \left(k_0 N_p d\right)\sec^2\left(k_0 N_p d\right)\right]; \tag{7.67d}$$

For impedance-backed ground,

$$E_p = 1 + \frac{i\chi_p^2}{N_p^2}\left\{\frac{\tan\left(k_0 N_p d\right) + k_0 N_p d\sec^2\left(k_0 N_p d\right)}{\left(\beta_2/\zeta N_p\right) - i\tan\left(k_0 N_p d\right)} - \right.$$

$$\left.\left(\beta_2/\zeta N_p\right) \times \frac{\tan\left(k_0 N_p d\right) - k_0 N_p d\sec^2\left(k_0 N_p d\right)}{1 - i\left(\beta_2/\zeta N_p\right)\tan\left(k_0 N_p d\right)}\right\}. \tag{7.67e}$$

The sound fields below the ground can be expressed as

$$p_1(0, z_s \mid r, -D) = q_D \frac{e^{ikL_D}}{4\pi\Delta_D} + q_R \frac{e^{ikL_R}}{4\pi\Delta_R}; \tag{7.68}$$

For extended-reaction ground, $q_R = 0$ and

$$q(Z) = T\left(\vartheta\right) + A\left(\mu_p\right)\left[1 - V\left(\vartheta\right)\right]F\left(\overline{w}\right); \tag{7.69a}$$

For hard-backed ground,

$$q(Z) = \gamma(\vartheta)T\left(\vartheta\right) + A\left(\mu_p\right)\gamma(\mu_p)\left[1 - V\left(\vartheta\right)\right]F\left(\overline{w}\right); \tag{7.69b}$$

For impedance-backed ground,

$$q_D = \gamma(\vartheta_D)T(\vartheta_D) + \gamma(\mu_p)\left[1 - V(\vartheta_D)\right]A(\mu_p)F(w), \tag{7.70a}$$

$$q_R = \gamma(\vartheta_R)V_2(\vartheta_R)T(\vartheta_R) + \gamma(\mu_p)V_2(\mu_p)\left[1 - V(\vartheta_R)\right]A(\mu_p)F(\bar{w}) + \gamma(\mu_{p,2})T(\mu_{p,2})\left[1 - V_2(\vartheta_R)\right]A(\mu_{p,2})F(\bar{w}_2), \tag{7.70b}$$

$$V_2 = \frac{\zeta\sqrt{n^2 - \cos^2\varphi_R} - \beta_2}{\zeta\sqrt{n^2 - \cos^2\varphi_R} + \beta_2}\ . \tag{7.70c}$$

7.5 Numerical Results

7.5.1 Sound Propagation for Benchmark Cases

The PE methods have been used extensively in the computation of sound fields. There are several established benchmark results [32] available for verification of the models. Comparisons were made between model-produced and published results for various PE methods. In this section, we are interested in comparing the results for frequencies of 10Hz and 100 Hz with source and receiver height at 5*m* and 1*m* respectively. Test case 1 is a homogeneous medium with a constant speed of sound c_0. Test case 2 models sound propagation in a downward refracting situation with positive sound speed gradient. The sound speed gradient is held constant at 0.1 s^{-1}. Test case 3 represents the upwind propagation condition where the sound speed gradient changes its sign from case 2 (i.e., -0.1 s^{-1}). The Transmission Loss (TL) function is defined as the following to facilitate the comparisons:

$$TL = 20\log_{10}\left[\frac{p_1}{e^{ikr}/4\pi r}\right], \tag{7.71}$$

where *r=1 m* is chosen as the free-field reference.

As shown in Figure 7.7, Figure 7.8 and Figure 7.9, the results using the PE/FEM method agree well with those found in the benchmark cases in Ref. [32].

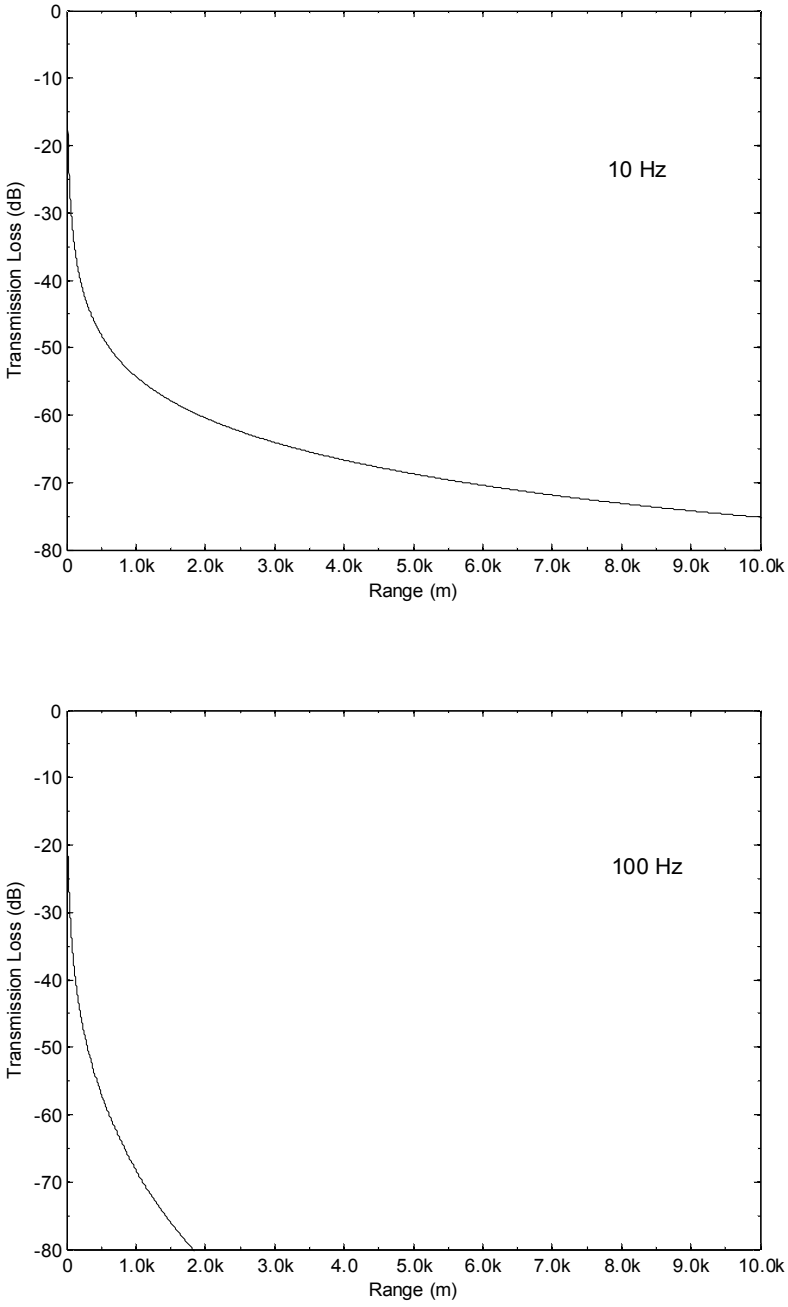

Figure 7.7: Transmission loss for benchmark case 1 using PE/FEM.

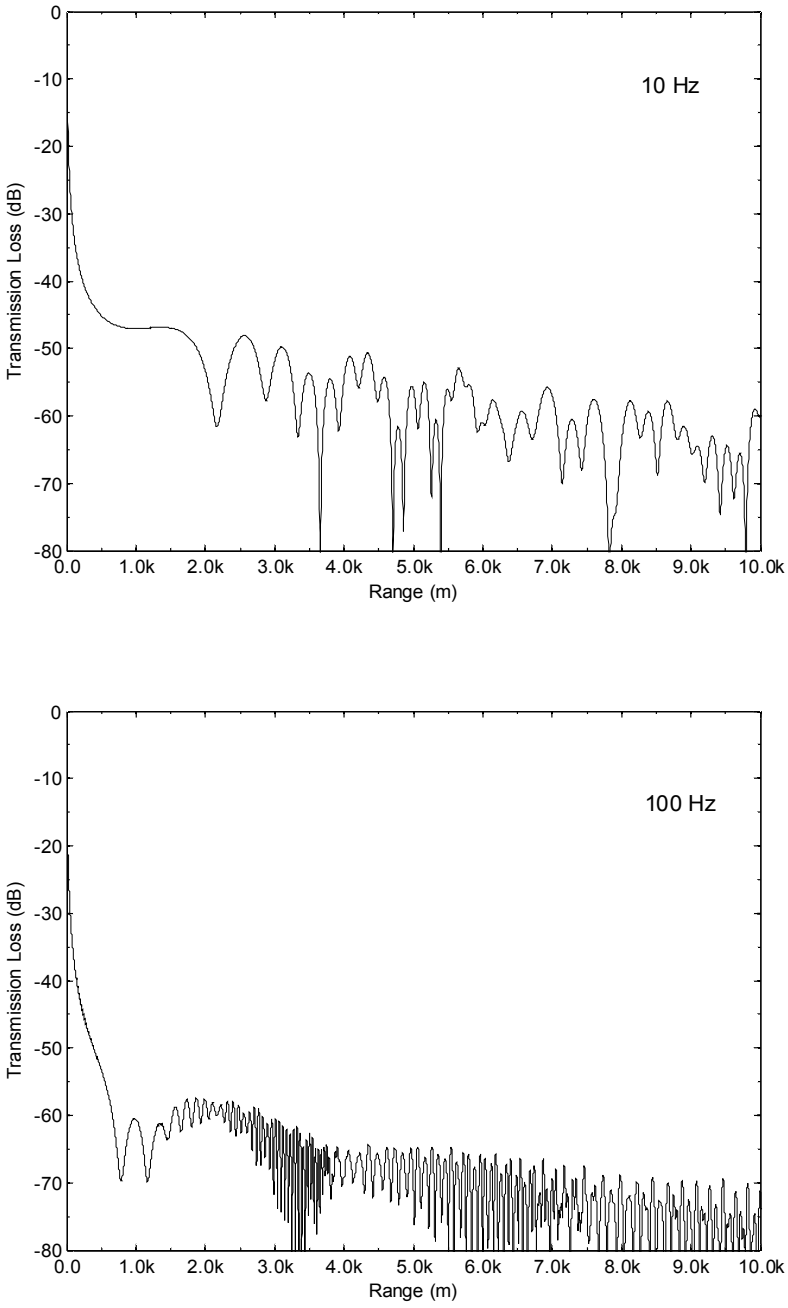

Figure 7.8: Transmission loss for benchmark case 2 using PE/FEM.

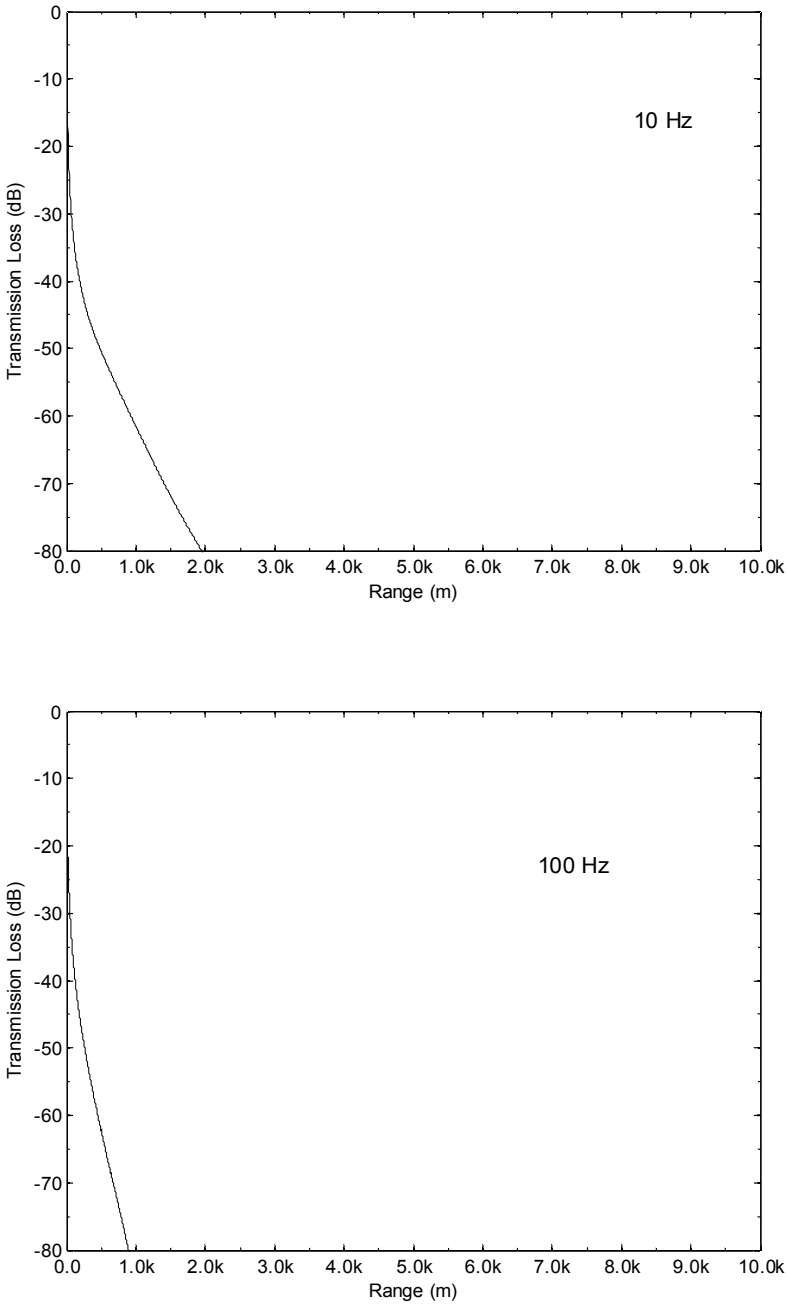

Figure 7.9: Transmission loss for benchmark case 3 using PE/FEM.

7.5.2 Sound Fields Above an Impedance Ground

In this section, we will apply the PE/FEM method to predict the sound fields above an impedance ground for homogeneous atmosphere. First, the contour plot for the sound fields above an impedance ground will be shown by using PE/FEM method based on both narrow-angle and wide-angle propagation. Since the impedance of the ground depends on the frequency, we selected a hard ground as a special case for illustrative purposes to identify the differences between the narrow-angle and wide-angle propagation. Figure 7.10 displays the contour plot of the sound field above a hard ground for a monopole source. The source height was set at a normalized height of $kz = 5$, or $2\pi z/\lambda = 5$, where λ is the wavelength. The results are also compared with that by using the classical Weyl-Van der Pol formulation. In figure 7.10, the propagation angle ranges are marked seperately to show its respective accuracy by comparison with the accurate asymptotic solution provided by the WVP formulation. It is apparent that the propagation angle for the narrow-angle PE/FEM propagation is accurate up to 10^{o} while the wide-angle PE/FEM method extends up to 35^{o}.

Furthermore, the computation time for the numerical PE/FEM method and the WVP formulation are compared. For the computation domain, where $kr \in [0,100]$ and $kz \in [0,35]$, the PE/FEM computation time is 10 seconds while WVP computational time goes to 47.5 seconds. Next, the comparison of the computation time is performed in terms of the area of the computational domain.

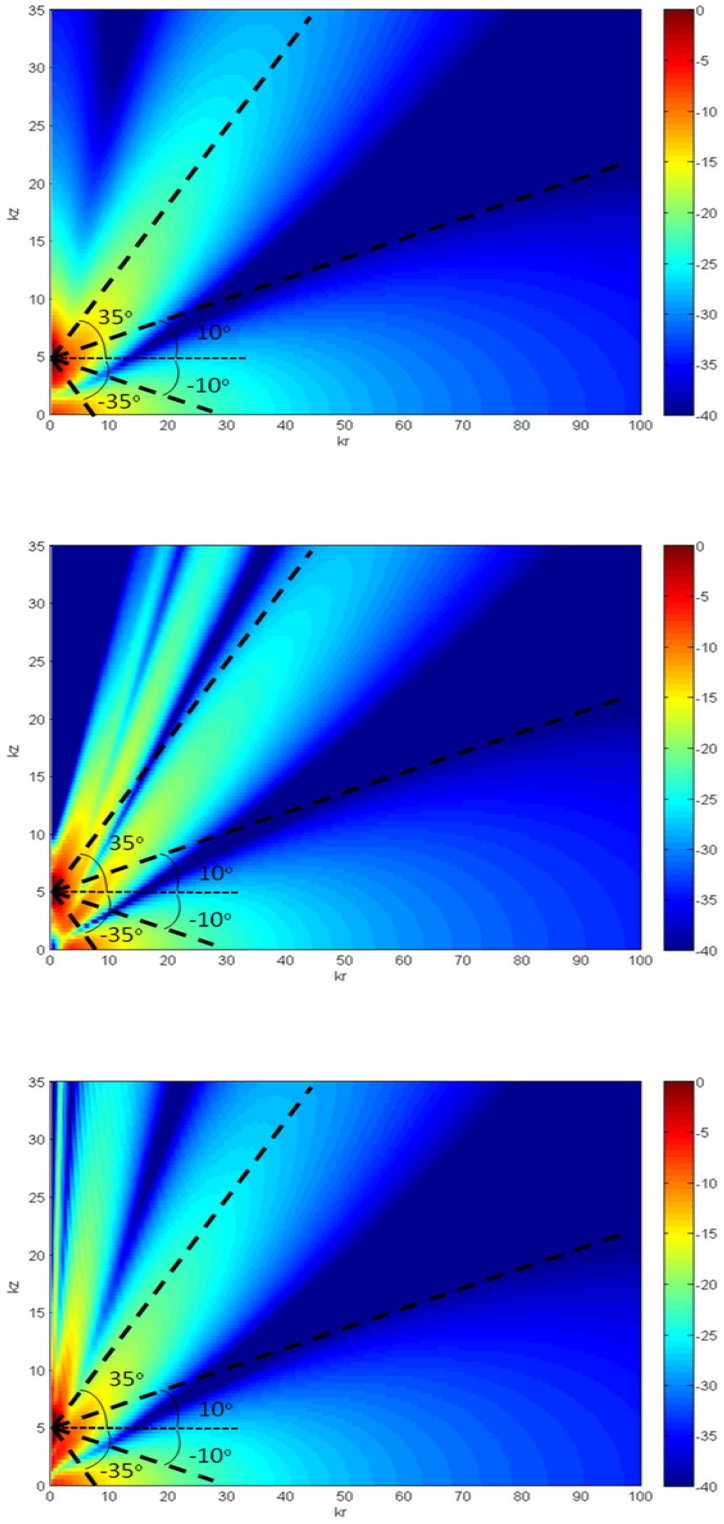

Figure 7.10: The contour plot for Transmission Loss (dB) at a normalized source height kz of 5. (a) Weyl-Van der Pol formula; (b) Narrow-angle parabolic equation; (c) Wide-angle parabolic equation.

For the narrow-angle propagation, the accurate computation domain is calculated as the shade area of plot (a) in Figure 7.11. Based on the total area and the propagation angle, the shaded area of plot is calculated as *1,310.9* with respect to the total area *3500* of the computation domain, which corresponds to 37.35% of the total computation domain. In the same way, for the wide-angle propagation, the shade area of plot (b) in Figure 7.11 is calculated to be *2,838.8*, which is 81.11% of the total computation domain. With the accurate WVP formulation, it takes 47.5s to compute the sound field for the entire computation domain. In contrast, the PE/FEM method with either narrow-angle or wide-angle propagation will predict the sound fields faster than the classical WVP formulation since the PE/FEM method is capable of calculating the sound field for different receiver heights at a fixed horizontal separation distance simultaneously.

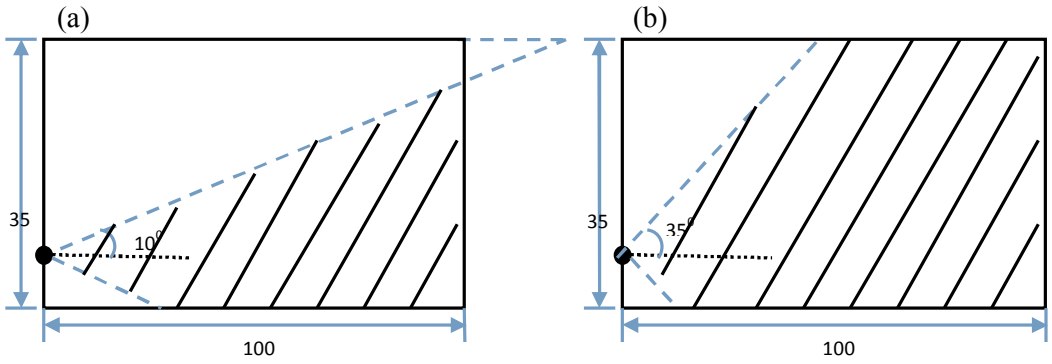

Figure 7.11: An illustration of the computation domain by PE/FEM method (a) Narrow-angle Parabolic equation; (b) Wide-angle Parabolic equation.

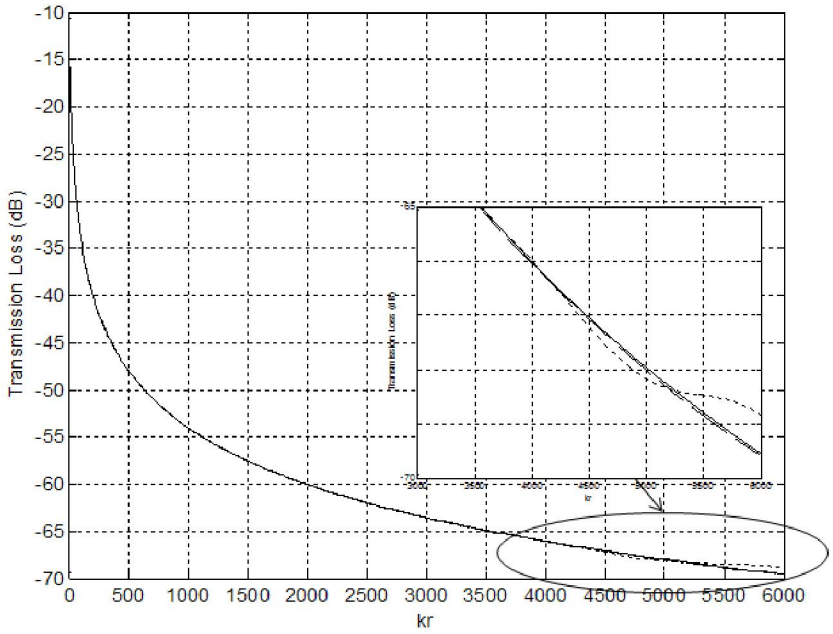

Figure 7.12: Transmission Loss (TL) versus normalized horizontal separation. Solid line: Weyl-Van der Pol formulation; dashed line: PE/FEM with PML; dot line: PE/FEM with absorbing boundry layer.

Next, we will discuss the advantage of using the PML technique. The comparison is made between using the classical absorbing boundary condition and PML boundary conditions. The same normalized source height of *5* as Fig 7.10 is used. With the absorbing boundary layer, a length of 50 wavelengths is required to model the radiation boundary condition, which could absorbs sound reaching the top of the numerical grids, and reduces the reflection off the top end. However, with the PML, the length of the layer can be reduced to be a quarter wavelengths. Note that the number of points per wavelength is set to be *20* except the one for PML is *200* points per wavelength. Based on the same geometry as Figure 7.10, the transsmission loss is plotted against the normalized horizontal separation in Figure 7.12. The results by using absorbing boundary layer and PML layer are compared with classical WVP formulation. Good agreement is achieved when the normalized horizontal separation goes up to *6,000*. However, after

zooming out, we could tell that the sound field with PML is much more accurate than the one with the absorbing boundary layer when the normalized horizontal separation gets closer to 6,000. Furthermore, the computation time when using PML is 15.9s while the time with absorbing boundary layer is 4,912 s. The computation time is reduced significantly when the PML is implemented. Hence, it is concluded that the application of the PML in the PE/FEM formulation not only increases accuracy at a long range, but also reduces the computation time significantly.

Another advantage of the PE/FEM method in this chapter is in the selection of the starting field. As discussed in section 7.3.4, the PE/FEM method is a marching scheme which relies on information from previous range steps. The starting field plays a crucial role in the accuracy of predicting the sound fields. Figure 7.13 displays the transmission loss above a hard ground at *5* different source heights when using Gaussian starter and the asymptotic solution as the starting field. Different normalized source heights are used from 2 to 10, with a step of 2, for comparison. By comparison with the Weyl-Van der Pol formula, the two starter fields are both good for far field sound predictions. However, for near field sound prediction, it is apparent that the asymptotic solution starter is better than the Gaussian starter based on the results in Figure 7.13. Because the wide-angle PE/FEM propagation is used, the accuracy starts at a different normalized horizontal separation *kr* with a normalized source height. Detailed study shows the results are accurate within its wide-angle propagation angle, which is 35^{o}.

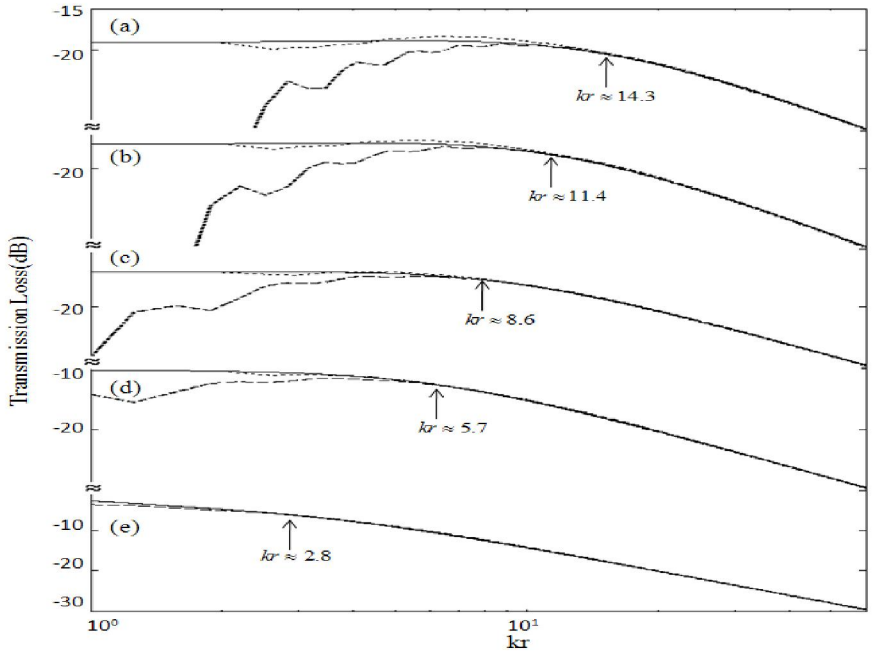

Figure 7.13: Transmission Loss (TL) versus the normalized horizontal separatin kr for different normalized source height kz_s. (a) kz_s=10; (b) kz_s=8; (c) kz_s=6; (d) kz_s=4; (e) kz_s=2; Solid line: Weyl-Van der Pol formula; dashed line: Gauss starter; dot line: Asymptotic solution starting field.

7.5.3 Sound Propagation Above and Below Extended Reaction Ground

In this section, we extend the PE/FEM method to the sound propagation above and below an extended reaction groun. The Miki empirical model [14] is used to describe the acoustic characteristics of the ground surface. A flow resistivity (σ_e) of 100 kPa s m^{-2}, tortuosity (q) of 1.1 and the porosity (Ω) of 0.9 are selected to calculate the acoustical characteristics of the porous layer. The excess attenuation (EA) function is defined to facilitate the comparison,

$$EA = 20\log_{10}\left[\frac{p_1}{e^{ikr}/4\pi r}\right], \tag{7.72}$$

where r is the horizontal separation between the source and receiver.

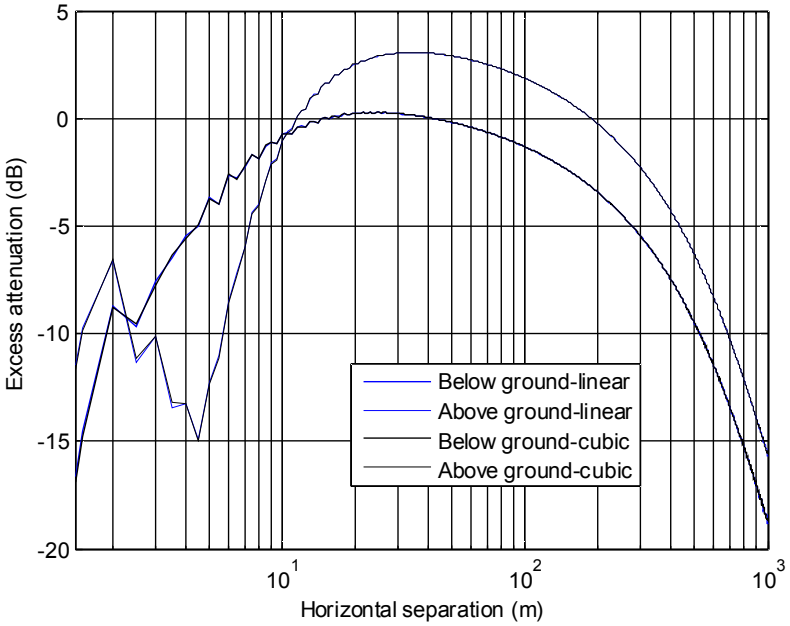

Figure 7.14: EA versus the horizontal separation using Gaussian Starter with the source height of 5m above ground. The receiver height is choosen to be 1m above ground, and 0.02m below the ground.

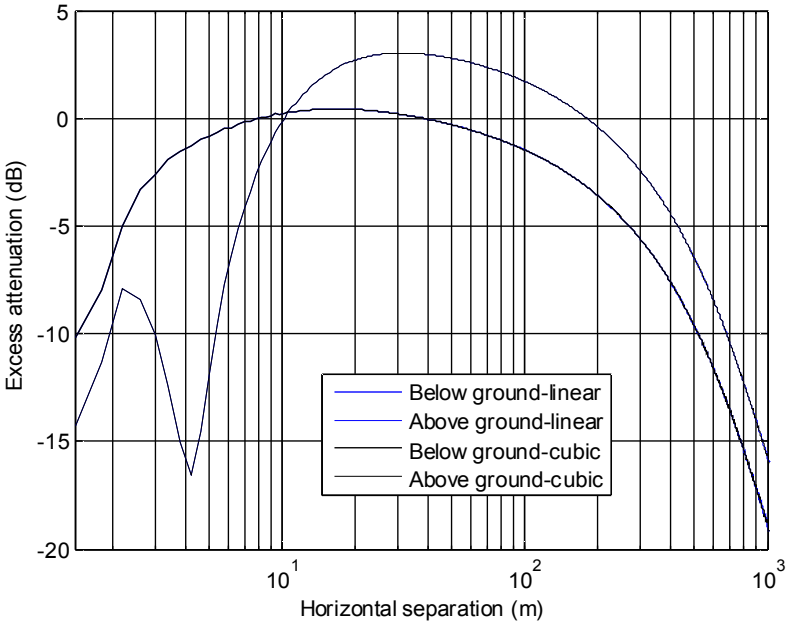

Figure 7.15: EA versus the horizontal separation using the asymptotic solution starter with the source height of 5 m above ground. The receiver height is choosen to be 1 m above ground, and 0.02 m below the ground.

Figure 7.14 and Figure 7.15 displays the EA versus the horizontal range in the homogeneous atmosphere for linear and cubic finite element discretization using the Gaussian starter and the asymptotic solution starter respectively. First we choose the source height to be $5m$, and the receiver height above the ground to be $1.0m$ while the receiver height below ground is set to be $0.02m$ from the interface. The results using either linear finite elements or cubic finite elements agree well with one another. Further comparison indicates that the results from the asymptotic solution starter at the range of less than 10m are much smoother than those obtained from a Gaussian starter.

Next, we choose the source height to be 0.05m and the receiver height above the ground to be 1m while the receiver below the ground is set to be 0.02m away from the interface. The results are shown in Fig 7.16 and Fig 7.17. As shown in Fig 7.16, when a Gaussian starter is used, large fluctuations in the sound field are observed—particularly in the below ground far-field regions. However, when the asymptotic solution starter field is applied, the fluctuations disappear. The results obtained agree well with the asymptotic solutions in the homogeous case. Perhaps the reason why the Gaussian starter is ineffective in predicting the sound field when the source height is very close to the ground is because it cannot fully account for the diffraction term, which becomes an important contributor to the below ground sound field. Because the asymptotic solution formulation includes the diffraction term by construction, much better accuracy is achieved.

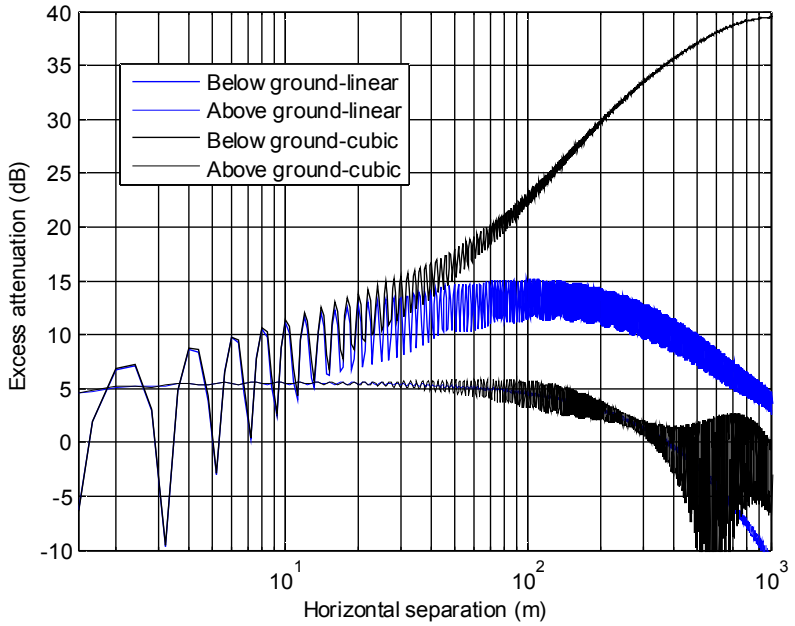

Figure 7.16: EA versus the horizontal separation using Gaussian Starter with the source height of 0.05 m above ground. The receiver height is choosen to be 1 m above ground, and 0.02 m below the ground.

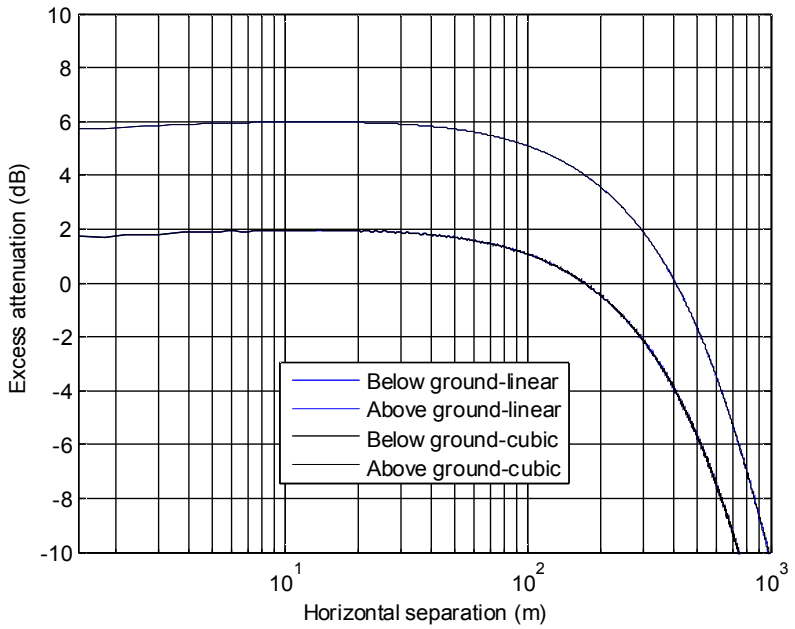

Figure 7.17: EA versus the horizontal separation using the asymptotic solution starter with the source height of 0.05 m above ground. The receiver height is choosen to be 1 m above ground, and 0.02 m below the ground.

In the previous discussion, the PE/FEM method has been applied to predict the sound fields above and below the extended reaction ground. The linear finite element basis function and cubic finite element basis function have been applied along the vertical direction to discretize the pressure. However, the comparison between the linear and the cubic basis function has not yet been considered. A comparison between these two basis functions in terms of computational time and numerical accuracy is explored.

Consider the source height at 5m and the receiver height at 1m above ground. Note that for the cubic basis functions, the asymptotic solution for a dipole source is required as an accurate starting field, which makes Chapter 6 worthwhile. As shown in Figure 7.15, using the accurate asymptotic solution as the starting field, yields results which are almost indistinguishable from the desired solution. The number of elements was chosen to be 17,004 elements for both basis funtions. Table 7.1 shows the comparison in terms of the computational time and the average error relative to the accurate asymptotic solution. As shown in Table 7.1, the computational time for the cubic basis functions is three times greater than linear basis functions, but the error is correspondingly lower. For the cubic basis function interpolation, the size of the matrix is twice the size of the linear basis function. The increased accuracy of the cubic basis function is due to the additional consideration for velocity continuity.

The relative error for the linear case is more than twice that of the cubic interpolation method. If the same 1.1% error is wanted for the linear interpolation, the number of 68,006 elements is needed, and the computation time increases to 95.6s. Another aspect is that when using the cubic interpolation, the pressure and velocity can be computed at the same time. But for linear interpolation, only pressure is obtained. In

conclusion, the cubic basis function discretization in the vertical direction has more advantages over the linear interpolation including higher accuracy and the simultaneous calculation of pressure and velocity.

Table 7.1: Comparison for the PE/FEM using cubic and linear finite elements.

the same number of elements	Cubic interpolation	linear interpolation
Computation time	58.2s	15.4s
Error	1.1%	2.7%
Results	Pressure && Velocity	Only Pressure

7.5.4 Prediction of Sound over Snow Cover

In this section, the PE/FEM method here will be applied to predict the sound propagation over snow cover. The experimental data was provided by Donald G.Albert from Cold Regions Research and Engineering Laborator and through private email communication. Attenborough's four-parameter model of ground impedance is used to describe the effect of the porous snow cover. The four parameters in the ground impedance model are the flow resistivity σ, the porosity Ω, the tortuosity q^2 and the pore shape factor s_f. The expression for the index of refraction and the density ratio are given by Eqs. (5.26) and (5.27) in Chapter 5. From the earlier publications by Donald G. Albert [116-118], the snow behaves like a hard-backed layer ground, and an initial guess of the parametric values for σ, Ω, q^2 and s_f is given. The experimental data are presented in terms of normalized Transmission Loss (TL), which is normalized by the

maximum value of TL in the frequency range from 0 Hz to 5k Hz. In the experiment, blank pistol shots were used as the source to perform the acoustic pulse measurement. An exponentially decaying source pulse form is presented in the paper [117]. Since the results here are presented with the normalized TL value, the source information will not be discussed further. In the experiment data, four sets of data are collected. The source height is set to be 1.0m. Two sets of data are for sound fields above snow, whose receiver height is set to be 0.68*m* and 0.18*m*.The other two sets of data, are for sound fields just beneath the snow. The horizontal separation between the source and the receiver is 30*m*. The thickness of the snow is 0.12*m*. The data was collected at no wind condition. Hence, The PE/FEM method in this chapter is used for the homogenous case. It is used to predict TL near the snow cover with the asymptotic solution for sound fields near hard-backed porous interfaces, and compared with the experimental data.

First, the aim is to search for a set of parametric values that result in the best agreement between the experimental data and the PE/FEM prediction for TL above a hard-backed rigid porous medium. By fitting the parameters of the ground impedance for the sound field above ground, the best fit parameters were found to be as follows: σ = 21.5 kPa s m-2, $\Omega = 0.8$, $q^2 = 1.95$ and sf = 0.8. Typical examples of the best fit data are shown in Figure. 7.18. Note that the comparison for the frequency range is from 0 Hz to 1.5 kHz because the result by PE/FEM model could not fit well with the experimental data beyond 1.5 kHz. The data at frequencies greater than 1.5 kHz may be unreliable because of poor signal-to-noise ratio. However, when the same parameters for the ground impedance of the snow are used, the predicted normalized TL for the receiver just below

the snow agree tolerably well with the experimental data, seen in Figure 7.19. It is shown that the PE/FEM method is good to predict sound propagation near a hard-backed ground.

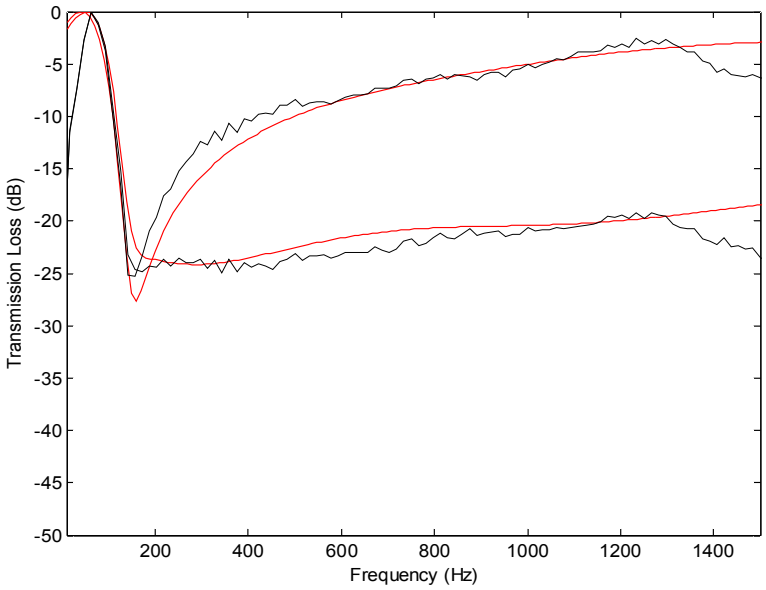

Figure 7.18: Comparison of experimental data and the PE/FEM prediction of the normalized transmission loss above the snow. From top to bottom, the receiver height is 0.68 m and 0.18 m respectively. Solid line: Experimental data by Donald G.Albert; dashed line: PE/FEM method.

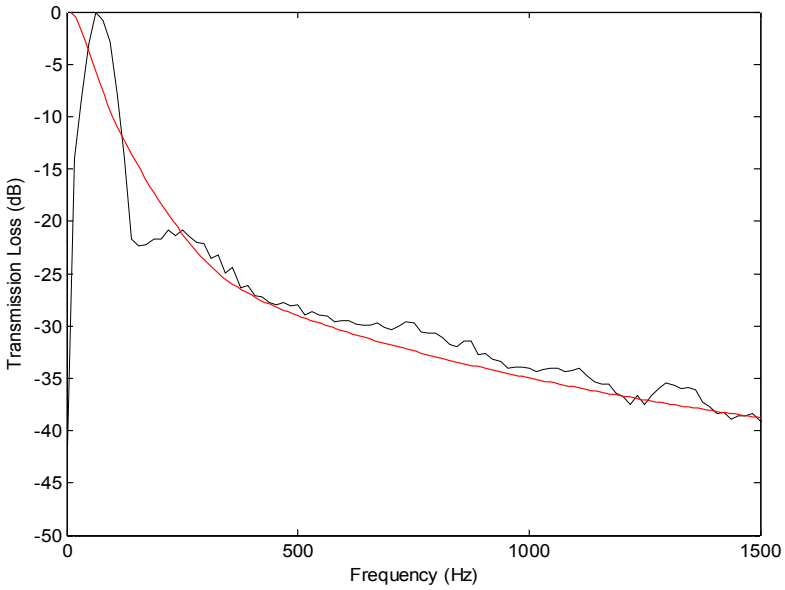

Figure 7.19: Comparison of experimental data and the PE/FEM prediction of the normalized transmission loss below the snow. The receiver height for PE/FEM model is 0.01 m. Solid line: Experimental data by Donald G.Albert; dashed line: PE/FEM method.

7.6 Summary

In this chapter, sound propagation over a porous interface is investigated using PE methods combined with the finite element discretization along the vertical direction. The PML technique is applied to model the free-radiation boundary condition, which reduces the reflection from the top layer and improves the computation efficiency substantially compared to the absorbing layer method. The analytical asymptotic solutions are used as the starting field to obtain improved predictions in the near field compared to those achieved with a Gaussian starter field under various test cases. Additional comparisons are made between the PE/FEM method described in this chapter and benchmark cases found in the literature. It has been shown that the PE/FEM method with cubic finite elements is capable of producing more accurate solutions, albeit at a greater computational expense. The PE method was also validated against experimental results for snow covered ground.

CHAPTER 8: A CUBIC PE/FEM METHOD FOR PREDICTING RANGE INDEPDENT SOUND PROPAGATION

8.1 Introduction

In the previous chapter, a PE/FEM method was presented for studying sound propagation near rigid porous interfaces. A linear FEM discretization is first applied to an arbitary function in the horizontal direction to derive the parabolic equation for the sound fields near the interfaces. Later, the linear and cubic FEM discretization was applied to a function in the vertical direction to solve the parabolic equation respectively. A uniform step-size marching scheme is obtained for the two discretizations. The only difference in the solution is the size of the matrices that march forward as seen in the F, G, J matrices in Eqs. (7.42a), (7.42b) and (7.42c). Based on the PE/FEM analysis, a cubic FEM discretization is applied to an arbitrary function in the horizontal direction. Using the cubic FEM discretization both in the horizontal and vertical direction, a cubic PE/FEM formulation is presented in this chapter. The proposed method takes into account the change in slope of a function both horizontally and vertically, which can be generalized to more rigid porous interface conditions.

Section 8.2 outlines the theory behind the cubic PE/FEM formulation. Section 8.3 presents the numerical implementation. Using the cubic discretization of a function in

the vertical direction, the vectorized function at each point is listed as four terms, which includes the pressure p, the slope of pressure horizontally $\partial p/\partial r$, the slope of pressure vertically $\partial p/\partial z$, and a cross-term $\frac{\partial^2 p}{\partial r \partial z}$. Hence, the cubic PE/FEM computes not only the pressure, but also the pressure from a dipole source as well. Validation of the cubic PE/FEM formulation is performed by comparing the analytical asymptotic solution for sound propagation near an extended reaction ground in section 8.4. A summary is given in section 8.5.

8.2 Theoretical Formulation

The current study in this section starts by solving the one-way wave equation for a forward-going wave given in Eq. (7.19). By omitting the over-bar, Eq. (7.19) can be written as

$$\partial\phi/\partial r = i(\sqrt{1+q}-1)\phi, \tag{8.1}$$

where

$$q = \frac{\partial^2}{\partial z^2} + n^2 - 1. \tag{8.2}$$

Instead of using linear finite elements in the horizontal range, we start by using the cubic finite element to express the sound pressure:

$$\phi = \upsilon_1(\xi)\phi_1 + \upsilon_2(\xi)\frac{d\phi_1}{dr} + \upsilon_3(\xi)\phi_2 + \upsilon_4(\xi)\frac{d\phi_2}{dr}, \tag{8.3}$$

where

$$\upsilon_1(\xi) = (1-\xi)^2(2\xi+1),\ \upsilon_2(\xi) = \Delta r \cdot \xi(\xi-1)^2,$$

$$\upsilon_3(\xi) = \xi^2(3-2\xi)\ ,\ \upsilon_4(\xi) = \Delta r \cdot \xi^2(\xi - 1)\ , \tag{8.4}$$

with the same definition of ξ at Eq.(7.22a,b), which is

$$\xi = \frac{r - r_1}{\Delta r},\ \Delta r = r_2 - r_1\ . \tag{8.5a, b}$$

Next, we start by writing Eq. (8.1) in its weak form. We begin by multiplying Eq. (8.1) by a test function *v(r)* and integrating to get

$$\int_r^{r+\Delta r} \partial\phi \Big/ \partial r \cdot v(r)dr = \int_r^{r+\Delta r} (\sqrt{1+q} - 1)\phi \cdot v(r)dr\ . \tag{8.6}$$

Integrating the term on the left hand side by parts,

$$\phi(r+\Delta r)v(r+\Delta r) - \phi(r)v(r) - \int_r^{r+\Delta r} dv(r) \Big/ dr \cdot \phi(r)dr = \int_r^{r+\Delta r} (\sqrt{1+q} - 1)\phi \cdot v(r)dr\ . \tag{8.7}$$

Hence, the weak formulation for the problem is to find ϕ such that

$$\phi(1)v(1) - \phi(0)v(0) - \int_0^1 dv(\xi) \Big/ d\xi \cdot \phi(\xi)d\xi = \int_0^1 (\sqrt{1+q} - 1)\phi \cdot v(\xi)\Delta r d\xi \tag{8.8}$$

holds for all v. Here, we start by choosing the four cubic basis functions as the test function, and substitution into Eq. (8.8), we get

$$\upsilon_1(1)\phi_2 - \upsilon_1(0)\phi_1 - \int_0^1 \frac{d\upsilon_1}{d\xi}\phi d\xi = i\left(\sqrt{1+q} - 1\right)\int_0^1 \phi\upsilon_1(\xi) \cdot \Delta r d\xi\ , \tag{8.9a}$$

$$\upsilon_2(1)\phi_2 - \upsilon_2(0)\phi_1 - \int_0^1 \frac{d\upsilon_2}{d\xi}\phi d\xi = i\left(\sqrt{1+q} - 1\right)\int_0^1 \phi\upsilon_2(\xi) \cdot \Delta r d\xi\ , \tag{8.9b}$$

$$\upsilon_3(1)\phi_2 - \upsilon_3(0)\phi_1 - \int_0^1 \frac{d\upsilon_3}{d\xi}\phi d\xi = i\left(\sqrt{1+q} - 1\right)\int_0^1 \phi\upsilon_3(\xi) \cdot \Delta r d\xi\ , \tag{8.9c}$$

$$\upsilon_4(1)\phi_2 - \upsilon_4(0)\phi_1 - \int_0^1 \frac{d\upsilon_4}{d\xi}\phi d\xi = i\left(\sqrt{1+q} - 1\right)\int_0^1 \phi\upsilon_4(\xi) \cdot \Delta r d\xi\ , \tag{8.9d}$$

where $\phi_1 = \phi(r)$, and $\phi_2 = \phi(r+\Delta r)$.

By substituting Eq.(8.3) into Eqs.(8.9a), (8.9b), (8.9c), and (8.9d), they are expressed as

$$\phi_1 - \int_0^1 \frac{d\upsilon_1}{d\xi}\left[\upsilon_1\phi_1 + \upsilon_2\frac{d\phi_1}{dr} + \upsilon_3\phi_2 + \upsilon_4\frac{d\phi_2}{dr}\right]d\xi = i\left(\sqrt{1+q}-1\right)\int_0^1\left[\upsilon_1\phi_1 + \upsilon_2\frac{d\phi_1}{dr} + \upsilon_3\phi_2 + \upsilon_4\frac{d\phi_2}{dr}\right]\upsilon_1\Delta r d\xi$$

$$-\int_0^1 \frac{d\upsilon_2}{d\xi}\left[\upsilon_1\phi_1 + \upsilon_2\frac{d\phi_1}{dr} + \upsilon_3\phi_2 + \upsilon_4\frac{d\phi_2}{dr}\right]d\xi = i\left(\sqrt{1+q}-1\right)\int_0^1\left[\upsilon_1\phi_1 + \upsilon_2\frac{d\phi_1}{dr} + \upsilon_3\phi_2 + \upsilon_4\frac{d\phi_2}{dr}\right]\upsilon_2\Delta r d\xi$$

$$\phi_2 - \int_0^1 \frac{d\upsilon_3}{d\xi}\left[\upsilon_1\phi_1 + \upsilon_2\frac{d\phi_1}{dr} + \upsilon_3\phi_2 + \upsilon_4\frac{d\phi_2}{dr}\right]d\xi = i\left(\sqrt{1+q}-1\right)\int_0^1\left[\upsilon_1\phi_1 + \upsilon_2\frac{d\phi_1}{dr} + \upsilon_3\phi_2 + \upsilon_4\frac{d\phi_2}{dr}\right]\upsilon_3\Delta r d\xi$$

$$-\int_0^1 \frac{d\upsilon_4}{d\xi}\left[\upsilon_1\phi_1 + \upsilon_2\frac{d\phi_1}{dr} + \upsilon_3\phi_2 + \upsilon_4\frac{d\phi_2}{dr}\right]d\xi = i\left(\sqrt{1+q}-1\right)\int_0^1\left[\upsilon_1\phi_1 + \upsilon_2\frac{d\phi_1}{dr} + \upsilon_3\phi_2 + \upsilon_4\frac{d\phi_2}{dr}\right]\upsilon_4\Delta r d\xi$$

(8.10a-d)

By averaging Eq. (8.10a) and (8.10c), we get

$$\phi_2 - \phi_1 - \left[\int_0^1\left(\frac{d\upsilon_1}{dr}+\frac{d\upsilon_3}{dr}\right)\upsilon_1 d\xi\cdot\phi_1 + \int_0^1\left(\frac{d\upsilon_1}{dr}+\frac{d\upsilon_3}{dr}\right)\upsilon_2 d\xi\cdot\frac{d\phi_1}{dr}\right.$$
$$\left.+\int_0^1\left(\frac{d\upsilon_1}{dr}+\frac{d\upsilon_3}{dr}\right)\upsilon_3 d\xi\cdot\phi_2 + \int_0^1\left(\frac{d\upsilon_1}{dr}+\frac{d\upsilon_3}{dr}\right)\upsilon_4 d\xi\cdot\frac{d\phi_2}{dr}\right]$$

$$= i\left(\sqrt{1+q}-1\right)\left[\int_0^1\left(\upsilon_1+\upsilon_3\right)\upsilon_1\Delta r d\xi\cdot\phi_1 + \int_0^1\left(\upsilon_1+\upsilon_3\right)\upsilon_2\Delta r d\xi\cdot\frac{d\phi_1}{dr}\right.$$
$$\left.+\int_0^1\left(\upsilon_1+\upsilon_3\right)\upsilon_3\Delta r d\xi\cdot\phi_2 + \int_0^1\left(\upsilon_1+\upsilon_3\right)\upsilon_4\Delta r d\xi\cdot\frac{d\phi_2}{dr}\right]. \qquad (8.11)$$

Since $\left(\frac{d\upsilon_1}{dr}+\frac{d\upsilon_3}{dr}\right)=0$, and $\left(\upsilon_1+\upsilon_3\right)=1$, Eq.(8.11) can be simplified as

$$\phi_2 - \phi_1 = i\left(\sqrt{1+q}-1\right)\left[\int_0^1\upsilon_1\Delta r d\xi\cdot\phi_1 + \int_0^1\upsilon_2\Delta r d\xi\cdot\frac{d\phi_1}{dr} + \int_0^1\upsilon_3\Delta r d\xi\cdot\phi_2 + \int_0^1\upsilon_4\Delta r d\xi\cdot\frac{d\phi_2}{dr}\right].$$

(8.12)

That is,

$$\phi_2 - \phi_1 = i\left(\sqrt{1+q}-1\right)\Delta r\left[\frac{1}{2}\cdot\phi_1 + \frac{1}{12}\Delta r\cdot\frac{d\phi_1}{dr} + \frac{1}{2}\cdot\phi_2 - \frac{1}{12}\Delta r\cdot\frac{d\phi_2}{dr}\right]. \qquad (8.13)$$

By using Claerbout's method to get the rational approximation for $\sqrt{1+q}$ in Eq. (7.29), and substituting into Eq.(8.13), Eq.(8.13) becomes

$$\left[\left(A_1-\frac{i\Delta r}{2}A_2\right)+\left(A_3-\frac{i\Delta r}{2}A_4\right)n^2+\left(A_3-\frac{i\Delta r}{2}A_4\right)\frac{\partial^2}{\partial z^2}\right]\phi_2+$$

$$\left[\frac{i(\Delta r)^2}{12}A_2+\frac{i(\Delta r)^2}{12}A_4n^2+\frac{i(\Delta r)^2}{12}A_4\frac{\partial^2}{\partial z^2}\right]\frac{d\phi_2}{dr}$$

$$=\left[\left(A_1+\frac{i\Delta r}{2}A_2\right)+\left(A_3+\frac{i\Delta r}{2}A_4\right)n^2+\left(A_3+\frac{i\Delta r}{2}A_4\right)\frac{\partial^2}{\partial z^2}\right]\phi_1+$$

$$\left[\frac{i(\Delta r)^2}{12}A_2+\frac{i(\Delta r)^2}{12}A_4n^2+\frac{i(\Delta r)^2}{12}A_4\frac{\partial^2}{\partial z^2}\right]\frac{d\phi_1}{dr}. \tag{8.14}$$

Similarly, after averaging Eq. (8.10b) and Eq. (8.10d) and reorganizing, we can obtain

$$\left[\frac{3i}{7}A_2+\frac{3i}{7}A_4n^2+\frac{3i}{7}A_4\frac{\partial^2}{\partial z^2}\right]\phi_2$$

$$+\left[\left(\frac{i\Delta r}{21}A_2-\frac{1}{3}A_1\right)+\left(\frac{i\Delta r}{21}A_4-\frac{1}{3}A_3\right)n^2+\left(\frac{i\Delta r}{21}A_4-\frac{1}{3}A_3\right)\frac{\partial^2}{\partial z^2}\right]\frac{d\phi_2}{dr}$$

$$=\left[\frac{3i}{7}A_2+\frac{3i}{7}A_4n^2+\frac{3i}{7}A_4\frac{\partial^2}{\partial z^2}\right]\phi_1$$

$$+\left[\left(-\frac{i\Delta r}{21}A_2-\frac{1}{3}A_1\right)+\left(-\frac{i\Delta r}{21}A_4-\frac{1}{3}A_3\right)n^2+\left(-\frac{i\Delta r}{21}A_4-\frac{1}{3}A_3\right)\frac{\partial^2}{\partial z^2}\right]\frac{d\phi_1}{dr}. \tag{8.15}$$

Hence, Eqs. (8.14) and (8.15) can be rewritten in matrix form as follows:

$$\begin{bmatrix} M_1^- & M_2 \\ M_3 & M_4^- \end{bmatrix}\begin{bmatrix} \phi_2 \\ \dfrac{d\phi_2}{dr} \end{bmatrix}=\begin{bmatrix} M_1^+ & M_2 \\ M_3 & M_4^+ \end{bmatrix}\begin{bmatrix} \phi_1 \\ \dfrac{d\phi_1}{dr} \end{bmatrix}, \tag{8.16}$$

where

$$M_1^- = B_1 + E_1 n^2 + E_1 \frac{\partial^2}{\partial z^2},\ M_1^+ = B_1^* + E_1^* n^2 + E_1^* \frac{\partial^2}{\partial z^2}; \tag{8.17a,b}$$

$$M_2 = B_2 + E_2 n^2 + E_2 \frac{\partial^2}{\partial z^2};\ M_3 = B_3 + E_3 n^2 + E_3 \frac{\partial^2}{\partial z^2}; \tag{8.17c,d}$$

$$M_4^- = B_4 + E_4 n^2 + E_4 \frac{\partial^2}{\partial z^2},\ M_4^+ = B_4^* + E_4^* n^2 + E_4^* \frac{\partial^2}{\partial z^2}; \tag{8.17e,f}$$

and

$$B_1 = A_1 - \frac{i\Delta r}{2} A_2,\ E_1 = A_3 - \frac{i\Delta r}{2} A_4; \tag{8.18a,b}$$

$$B_2 = \frac{i(\Delta r)^2}{12} A_2,\ E_2 = \frac{i(\Delta r)^2}{24} A_4; \tag{8.18c,d}$$

$$B_3 = \frac{3i}{7} A_2,\ E_3 = \frac{3i}{7} A_4; \tag{8.18e, f}$$

$$B_4 = \frac{i\Delta r}{21} A_2 - \frac{1}{3} A_1,\ E_4 = \frac{i\Delta r}{21} A_4 - \frac{1}{3} A_3. \tag{8.18g, h}$$

That is,

$$M_1^- \phi(r+\Delta r, z) + M_2 \frac{d\phi(r+\Delta r, z)}{dr} = M_1^+ \phi(r, z) + M_2 \frac{d\phi(r, z)}{dr}; \tag{8.19a}$$

$$M_3 \phi(r+\Delta r, z) + M_4^- \frac{d\phi(r+\Delta r, z)}{dr} = M_3 \phi(r, z) + M_4^+ \frac{d\phi(r, z)}{dr}. \tag{8.19b}$$

8.3 Numerical Implementation

Since the functions $\phi(r+\Delta r, z)$ and $\phi(r, z)$ are vertical dependent, the method in Chapter 7, i.e. cubic finite element discretization, is used to discretize them. Here, we

define $\phi_2 = \phi(r+\Delta r, z)$, and $\phi_1 = \phi(r, z)$. The function ϕ_1 and ϕ_2 can be expressed in terms of cubic finite element basis functions as

$$\phi_1(z) = \sum_{j=1}^{N-1}\left[\upsilon_1(\eta_j)\phi_1(z_j) + \upsilon_2(\eta_j)\frac{d\phi_1(z_j)}{dz} + \upsilon_3(\eta_j)\phi_1(z_{j+1}) + \upsilon_4(\eta_j)\frac{d\phi_1(z_{j+1})}{dz}\right], \tag{8.20a}$$

$$\phi_2(z) = \sum_{j=1}^{N-1}\left[\upsilon_1(\eta_j)\phi_2(z_j) + \upsilon_2(\eta_j)\frac{d\phi_2(z_j)}{dz} + \upsilon_3(\eta_j)\phi_2(z_{j+1}) + \upsilon_4(\eta_j)\frac{d\phi_2(z_{j+1})}{dz}\right] \tag{8.20b}$$

where

$$\upsilon_1(\eta_j) = (1-\eta_j)^2(2\eta_j+1),\ \upsilon_2(\eta_j) = \Delta h_j \cdot \eta_j(\eta_j-1)^2, \tag{8.21a,b}$$

$$\upsilon_3(\eta_j) = \eta_j^2(3-2\eta_j),\ \upsilon_4(\eta_j) = \Delta h_j \cdot \eta_j^2(\eta_j-1). \tag{8.21c,d}$$

and

$$\eta_j = \frac{z-z_j}{\Delta z_j},\ \Delta z_j = z_{j+1} - z_j \tag{8.22}$$

in $z_h := \{z_i : z_b = z_1 < z_2 < \cdots < z_N = z_t\}$. Here, N is the number of elements over z.

After derivation with respect to r, Eqs. (8.20a) and (8.20b) become

$$\frac{d\phi_1(z)}{dr} = \sum_{j=1}^{N-1}\left[\upsilon_1(\eta_j)\frac{d\phi_1(z_j)}{dr} + \upsilon_2(\eta_j)\frac{d^2\phi_1(z_j)}{dzdr} + \upsilon_3(\eta_j)\frac{d\phi_1(z_{j+1})}{dr} + \upsilon_4(\eta_j)\frac{d^2\phi_1(z_{j+1})}{dzdr}\right] \tag{8.23a}$$

$$\frac{d\phi_2(z)}{dr} = \sum_{j=1}^{N-1}\left[\upsilon_1(\eta_j)\frac{d\phi_2(z_j)}{dr} + \upsilon_2(\eta_j)\frac{d^2\phi_2(z_j)}{dzdr} + \upsilon_3(\eta_j)\frac{d\phi_2(z_{j+1})}{dr} + \upsilon_4(\eta_j)\frac{d^2\phi_2(z_{j+1})}{dzdr}\right] \tag{8.23b}$$

Substituting Eqs. (8.20a), (8.20b) and (8.23a), (8.23b) into Eqs. (8.19a) and (8.19b), we obtain

$$M_1^- \sum_{j=1}^{N-1}\left[\upsilon_1(\eta_j)\phi_1(z_j) + \upsilon_2(\eta_j)\frac{d\phi_1(z_j)}{dz} + \upsilon_3(\eta_j)\phi_1(z_{j+1}) + \upsilon_4(\eta_j)\frac{d\phi_1(z_{j+1})}{dz}\right] +$$

$$M_2\sum_{j=1}^{N-1}\left[\upsilon_1(\eta_j)\frac{d\phi_1(z_j)}{dr}+\upsilon_2(\eta_j)\frac{d^2\phi_1(z_j)}{dzdr}+\upsilon_3(\eta_j)\frac{d\phi_1(z_{j+1})}{dr}+\upsilon_4(\eta_j)\frac{d^2\phi_1(z_{j+1})}{dzdr}\right]$$
$$=M_1^+\sum_{j=1}^{N-1}\left[\upsilon_1(\eta_j)\phi_2(z_j)+\upsilon_2(\eta_j)\frac{d\phi_2(z_j)}{dz}+\upsilon_3(\eta_j)\phi_2(z_{j+1})+\upsilon_4(\eta_j)\frac{d\phi_2(z_{j+1})}{dz}\right]+$$

$$M_2\sum_{j=1}^{N-1}\left[\upsilon_1(\eta_j)\frac{d\phi_2(z_j)}{dr}+\upsilon_2(\eta_j)\frac{d^2\phi_2(z_j)}{dzdr}+\upsilon_3(\eta_j)\frac{d\phi_2(z_{j+1})}{dr}+\upsilon_4(\eta_j)\frac{d^2\phi_2(z_{j+1})}{dzdr}\right]$$

(8.24a)

$$M_3\sum_{j=1}^{N-1}\left[\upsilon_1(\eta_j)\phi_1(z_j)+\upsilon_2(\eta_j)\frac{d\phi_1(z_j)}{dz}+\upsilon_3(\eta_j)\phi_1(z_{j+1})+\upsilon_4(\eta_j)\frac{d\phi_1(z_{j+1})}{dz}\right]+$$

$$M_4^-\sum_{j=1}^{N-1}\left[\upsilon_1(\eta_j)\frac{d\phi_1(z_j)}{dr}+\upsilon_2(\eta_j)\frac{d^2\phi_1(z_j)}{dzdr}+\upsilon_3(\eta_j)\frac{d\phi_1(z_{j+1})}{dr}+\upsilon_4(\eta_j)\frac{d^2\phi_1(z_{j+1})}{dzdr}\right]$$
$$=M_3\sum_{j=1}^{N-1}\left[\upsilon_1(\eta_j)\phi_2(z_j)+\upsilon_2(\eta_j)\frac{d\phi_2(z_j)}{dz}+\upsilon_3(\eta_j)\phi_2(z_{j+1})+\upsilon_4(\eta_j)\frac{d\phi_2(z_{j+1})}{dz}\right]+$$

$$M_4^+\sum_{j=1}^{N-1}\left[\upsilon_1(\eta_j)\frac{d\phi_2(z_j)}{dr}+\upsilon_2(\eta_j)\frac{d^2\phi_2(z_j)}{dzdr}+\upsilon_3(\eta_j)\frac{d\phi_2(z_{j+1})}{dr}+\upsilon_4(\eta_j)\frac{d^2\phi_2(z_{j+1})}{dzdr}\right]$$

(8.24b)

Then, we multiply by $\upsilon_i(z)$ and integrate over z. When the vertical density variations is considered, $\partial^2/\partial z^2$ can be replaced by $\rho(\partial/\partial z)(1/\rho)(\partial/\partial z)$. The integration requires the computation of integrals of the form:

$$F_{ij}(f)=\int\upsilon_j(z)f(z)\upsilon_m(z)dz\,, \tag{8.25a}$$

$$G_{ij}(g)=\int\upsilon_j(z)g(z)\upsilon_m(z)dz\,, \tag{8.25b}$$

$$J_{ij}(f)=\int\frac{\partial\upsilon_i(z)}{\partial z}f(z)\frac{\partial\upsilon_j(z)}{\partial z}dz\,. \tag{8.25c}$$

The computation of the integrals in Eqs.(8.25a), (8.25b) and (8.25c) are similar to the computation of Eqs.(7.42a), (7.42b) and (7.42c). Here, the cubic finite element basis function is used, and the results are the same as in Appendix F. If a cubic interpolation is applied to the density function, the results can be found in Appendix G.

Hence, the respective structure of $M_1^{\pm}$, M_2, M_3 and $M_4^{\pm}$ are shown to be

$$M_1^{\pm} = \begin{bmatrix} [K_1]_{1,1}^{\pm} & [K_1]_{1,2}^{\pm} & 0 & 0 & \cdots \\ [K_1]_{2,1}^{\pm} & [K_1]_{2,2}^{\pm} & [K_1]_{2,3}^{\pm} & 0 & \cdots \\ 0 & [K_1]_{3,2}^{\pm} & [K_1]_{3,3}^{\pm} & [K_1]_{3,4}^{\pm} & \cdots \\ 0 & 0 & \ddots & \ddots & \ddots \end{bmatrix}_{2N\times 2N}, \tag{8.26a}$$

$$M_2 = \begin{bmatrix} [K_2]_{1,1} & [K_2]_{1,2} & 0 & 0 & \cdots \\ [K_2]_{2,1} & [K_2]_{2,2} & [K_2]_{2,3} & 0 & \cdots \\ 0 & [K_2]_{3,2} & [K_2]_{3,3} & [K_2]_{3,4} & \cdots \\ 0 & 0 & \ddots & \ddots & \ddots \end{bmatrix}_{2N\times 2N}, \tag{8.26b}$$

$$M_3 = \begin{bmatrix} [K_3]_{1,1} & [K_3]_{1,2} & 0 & 0 & \cdots \\ [K_3]_{2,1} & [K_3]_{2,2} & [K_3]_{2,3} & 0 & \cdots \\ 0 & [K_3]_{3,2} & [K_3]_{3,3} & [K_3]_{3,4} & \cdots \\ 0 & 0 & \ddots & \ddots & \ddots \end{bmatrix}_{2N\times 2N}, \tag{8.26c}$$

$$M_4^{\pm} = \begin{bmatrix} [K_4]_{1,1}^{\pm} & [K_4]_{1,2}^{\pm} & 0 & 0 & \cdots \\ [K_4]_{2,1}^{\pm} & [K_4]_{2,2}^{\pm} & [K_4]_{2,3}^{\pm} & 0 & \cdots \\ 0 & [K_4]_{3,2}^{\pm} & [K_4]_{3,3}^{\pm} & [K_4]_{3,4}^{\pm} & \cdots \\ 0 & 0 & \ddots & \ddots & \ddots \end{bmatrix}_{2N\times 2N}, \tag{8.26d}$$

where

$$[K_1]_{i,j}^{-} = B_1^* F_{ij}(f) + E_1^* \left(G_{ij}(g) + J_{ij}(f) \right) \; ; \; [K_1]_{i,j}^{+} = B_1 F_{ij}(f) + E_1 \left(G_{ij}(g) + J_{ij}(f) \right); \tag{8.27a,b}$$

$$\left[K_2\right]_{i,j} = B_2 F_{ij}(f) + E_2\left(G_{ij}(g) + J_{ij}(f)\right) \;;\; \left[K_3\right]_{i,j} = B_3 F_{ij}(f) + E_3\left(G_{ij}(g) + J_{ij}(f)\right) \text{;(8.27c,d)}$$

$$\left[K_4\right]^{-}_{i,j} = B_4^{*} F_{ij}(f) + E_4^{*}\left(G_{ij}(g) + J_{ij}(f)\right) \;;\; \left[K_4\right]^{+}_{i,j} = B_4 F_{ij}(f) + E_4\left(G_{ij}(g) + J_{ij}(f)\right) \text{.(8.27e,f)}$$

Note that all *K* matrices are sparse and symmetric. By vertical discretization, we obtain:

$$\Phi_1 = \left[\begin{array}{cccccccccc} \phi_{1,z_1} & \dfrac{d\phi_{1,z_1}}{dz} & \phi_{1,z_2} & \dfrac{d\phi_{1,z_2}}{dz} & \cdots & \cdots & \phi_{1,z_{N-1}} & \dfrac{d\phi_{1,z_{N-1}}}{dz} & \phi_{1,z_N} & \dfrac{d\phi_{1,z_N}}{dz} \end{array}\right]^T , \tag{8.28a}$$

$$\frac{d\Phi_1}{dr} = \left[\begin{array}{cccccccccc} \dfrac{d\phi_{1,z_1}}{dr} & \dfrac{d^2\phi_{1,z_1}}{dzdr} & \dfrac{d\phi_{1,z_2}}{dr} & \dfrac{d^2\phi_{1,z_2}}{dzdr} & \cdots & \cdots & \dfrac{d\phi_{1,z_{N-1}}}{dr} & \dfrac{d^2\phi_{1,z_{N-1}}}{dzdr} & \dfrac{d\phi_{1,z_N}}{dr} & \dfrac{d^2\phi_{1,z_N}}{dzdr} \end{array}\right]^T \tag{8.28b}$$

$$\Phi_2 = \left[\begin{array}{cccccccccc} \phi_{2,z_1} & \dfrac{d\phi_{2,z_1}}{dz} & \phi_{2,z_2} & \dfrac{d\phi_{2,z_2}}{dz} & \cdots & \cdots & \phi_{2,z_{N-1}} & \dfrac{d\phi_{2,z_{N-1}}}{dz} & \phi_{2,z_N} & \dfrac{d\phi_{2,z_N}}{dz} \end{array}\right]^T \tag{8.28c}$$

$$\frac{d\Phi_2}{dr} = \left[\begin{array}{cccccccccc} \dfrac{d\phi_{2,z_1}}{dr} & \dfrac{d^2\phi_{2,z_1}}{dzdr} & \dfrac{d\phi_{2,z_2}}{dr} & \dfrac{d^2\phi_{2,z_2}}{dzdr} & \cdots & \cdots & \dfrac{d\phi_{2,z_{N-1}}}{dr} & \dfrac{d^2\phi_{2,z_{N-1}}}{dzdr} & \dfrac{d\phi_{2,z_N}}{dr} & \dfrac{d^2\phi_{2,z_N}}{dzdr} \end{array}\right]^T \tag{8.28d}$$

By combining the two vectors together, we have the following information for the whole points in the vertical direction

$$\Phi(r+\Delta r) = \left[\begin{array}{cc} \Phi_2^T & \left(d\Phi_2/dr\right)^T \end{array}\right]^T , \tag{8.29a}$$

$$\Phi(r) = \left[\begin{array}{cc} \Phi_1^T & \left(d\Phi_1/dr\right)^T \end{array}\right]^T . \tag{8.29b}$$

And for each point, four terms are presented and computed, that is,

$$\left[\begin{array}{cccc} \phi & \dfrac{d\phi}{dz} & \dfrac{d\phi}{dr} & \dfrac{d^2\phi}{dzdr} \end{array}\right]^T . \tag{8.30}$$

Therefore, Eq. (8.16) can be rewritten as

$$\left[M^{-}\right]_{4N\times 4N}\left[\Phi(r+\Delta r)\right]_{4N\times 1}=\left[M^{+}\right]_{4N\times 4N}\left[\Phi(r)\right]_{4N\times 1}\ , \tag{8.31}$$

where

$$M^{-}=\begin{bmatrix}\left[K_1^{-}\right] & \left[K_2\right]\\ \left[K_3\right] & \left[K_4^{-}\right]\end{bmatrix},\ \text{and}\ M^{+}=\begin{bmatrix}\left[K_1^{+}\right] & \left[K_2\right]\\ \left[K_3\right] & \left[K_4^{+}\right]\end{bmatrix}. \tag{8.32}$$

Once the starting field is given, Eq.(8.31) can be marched horizontally. The above derivation has not yet accounted for the boundary conditions. Here, we take the impedance ground as an example to incorporate the boundary condition effects. More complicated boundary conditions can be incorporated as discussed in Chapter 7.

For the impedance ground, we have the following boundary conditions:

$$\frac{d\phi(z_b)}{dz}+i\beta\phi(z_b)=0, \tag{8.33a}$$

$$\frac{d\phi(z_t)}{dz}-i\phi(z_t)=0. \tag{8.33b}$$

Adding the boundary condition into the global matrix in the matrix form, we have

$$\left\{\left[M^{-}\right]_{4N\times 4N}+\left[C^{-}\right]_{4N\times 4N}\right\}\left[\Phi(r+\Delta r)\right]_{4N\times 1}=\left\{\left[M^{+}\right]_{4N\times 4N}+\left[C^{+}\right]_{4N\times 4N}\right\}\left[\Phi(r)\right]_{4N\times 1} \tag{8.34}$$

where the matrix C^{-} and C^{+} are both sparse matrix with only two non-zero terms:

$$C^{-}(1,1)=E_1^{*}\frac{i\beta}{\rho(z_b)},\ C^{-}(2N-1,2N-1)=E_1^{*}\frac{i}{\rho(z_t)}, \tag{8.35a,b}$$

$$C^{+}(1,1)=E_1\frac{i\beta}{\rho(z_b)},\ C^{+}(2N-1,2N-1)=E_1\frac{i}{\rho(z_t)}. \tag{8.36a,b}$$

At the same time, an abosorbing boundary layer is also needed to apply near the top of the numerical grid, to attenuate the amplitudes of waves reflecting off the top end of the

grid. For the extended reaction ground, the intermediate boundary conditions have been discussed in Chapter 7, which can be used directly.

8.4 Numerical Results

In the above discussion, the PE/FEM marching scheme has been derived based on cubic FEM discretization along both the horizontal and vertical directions. To validate its accuracy, the cubic PE/FEM method is applied to predict sound propagation above an impedance ground for the homogeneous atmosphere benchmark case. As seen in Figure 8.1, TL is plotted against the horizontal range for two different frequencies: 10 Hz and 100 Hz. Good agreements with published results for benchmark case 1 validates the accuracy of the proposed cubic PE/FEM marching scheme.

Furthermore, the cubic PE/FEM method is applied to predict the sound field above and below the extended reaction ground. Figure 8.2 displays the comparison of the excess attenuation for the source location at 5m above the ground, and the receiver location is set to be 0.1 above ground and 0.1 below the ground. The results are compared with the results by the linear PE/FEM method. Here, the Gaussian starter field is used in both methods. Good agreements between the two methods are observed. In another comparison using the same number of elements, the computation time for the linear PE/FEM method took 66.6s while the time for the cubic took 344.7s. The cubic method requires more computation time since the matrices are four times larger than those found in the linear method. However, the cubic PE/FEM method is able to compute four terms simultaneously (e.g., pressure, pressure from horizontal dipole and vertical dipole).

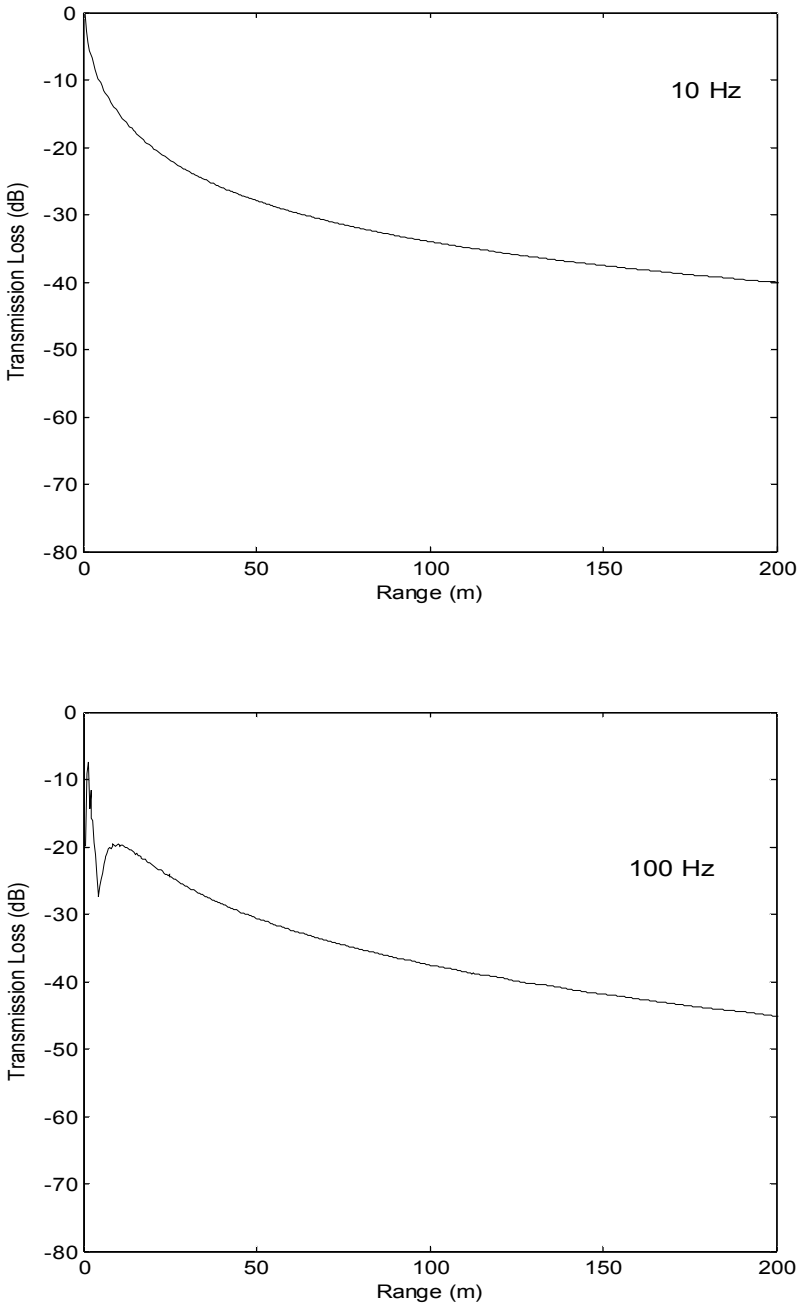

Figure 8.1: Transmission Loss (TL) versus horizontal range (m). (a) the source frequency at 10 Hz; (b)the source frequency at 100 Hz.

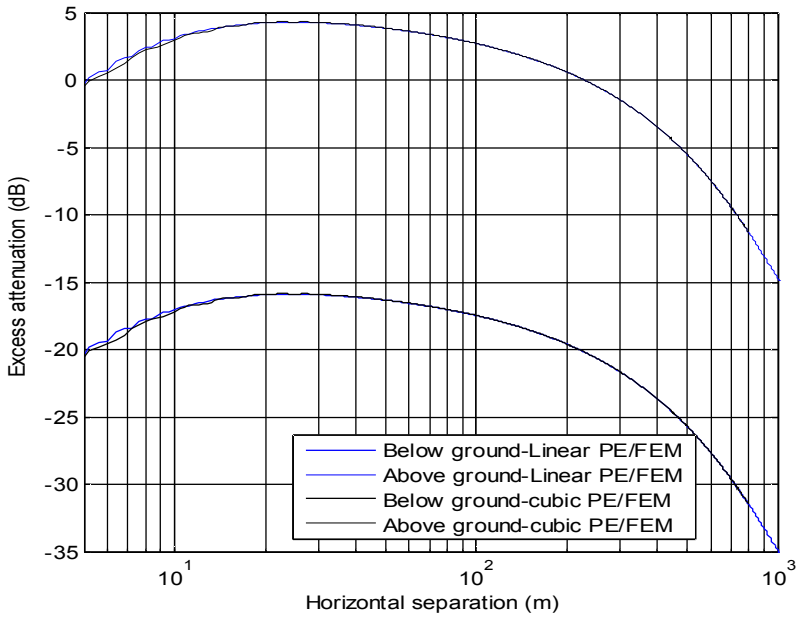

Figure 8.2: EA versus the horizontal separation using Gaussian Starter with the source height of 5 m above the ground. The receiver height is chosen to be 0.1 m above the ground, and the other receiver is at 0.1 m below the ground.

8.5 Summary

In this chapter, a cubic PE/FEM method is proposed based on the PE/FEM method described in Chapter 7. The derivation of higher ordered marching scheme is discussed in detail. The matrix representation for FEM discretization enables greater insight and facilitates efficient numerical implementation. Four terms are related at each grid point: the pressure p, the slope of pressure horizontally $\partial p/\partial r$, the slope of pressure vertically $\partial p/\partial z$, and $\dfrac{\partial^2 p}{\partial r \partial z}$. The four terms at each point with the same horizontal separation march forward simultaneously, which increases the computation time several folds. However, additional field information is obtained beyond the pressure field values.

The cubic PE/FEM implementation is validated against the benchmark cases and several numerical examples.

CHAPTER 9: SUMMARY AND FUTURE WORK

In this dissertation, the propagation of sound in the vicinity of rigid porous interfaces has been investigated systematically. Sound propagation near various rigid porous interfaces has been considered: impedance ground; semi-infinite extended reaction ground; hard-backed ground; and impedance-backed ground. The analytical solutions and the numerical solutions are compared where applicable.

Because the double saddle-point method [1-3] becomes singular when the source lies directly above (or below) the receiver or when the specific acoustic impedance of the boundary is unity, a modified saddle-point method is first exploited to study the sound field from a monopole above and below a rigid porous medium (Chapter 2 and Chapter 3). The solutions are expressed in a form comparable to the classical Weyl-Van der Pol formula, which offers a physical understanding of the problem. The validaty of the asymptotic solution is confirmed by comparison with the numerical results computed by the fast-field formulation and the direct evaluation of the integral. However, the expression of the asymptotic solution based on the modified saddle-point method becomes complicated, especially for the impedance-backed porous ground. A heuristic method based on the asymptotic solution via the double saddle-point method is then proposed to remove any singularity (Chapter 4) and a comparable analytical form as Weyl-Van der Pol formula is suggested. The improved formula offers physically

meaningful solution and allows accurate predictions of total sound fields above a locally or non-locally reacting surface for all possible geometrical configurations. Following this, the double saddle-point method is then applied to obtain a uniform asymptotic solution allowing predictions of sound fields within a hard-backed rigid porous medium due to an airborne source (Chapter 5).

It is shown that the total sound fields consist of a transmitted wave component arriving at the receiver directly through the porous interface, and a second transmitted wave component reflecting from the rigid backing plane before reaching the receiver. They can be expressed in an integral form that is amenable to analytical and numerical analysis. The validity of the asymptotic formula is verified by comparison with numerical results obtained using a more accurate wave-based numerical scheme. The accuracy of the numerical solutions has also been verified through experiments in an anechoic chamber.

The proposed model predictions suggest that when the receiver is located near the bottom of the hard-backed layer, the reflection of the refracted wave represents a significant contribution to the total sound field. Furthermore, an asymptotic analysis is conducted to examine the sound fields due to an arbitrarily oriented dipole that is placed above a rigid porous medium. In Chapter 6, the diffraction of sound owing to the effect of spherical wavefronts and the presence of the porous interface has been explored. Using a double saddle-point analysis technique supplemented by the pole subtraction method, an asymptotic solution for the dipole sound field reflected from and transmitted through the porous interface has been derived. The diffracted wave contributions in both situations can be expressed conveniently in terms of a standard complementary error function that

can be computed efficiently. These asymptotic formulas lead to accurate numerical solutions for calculating the total sound field above and below a non-locally reacting medium. So far, the analysis has been restricted to homogeneous propagation conditions in which environmental properties do not vary with range.

In Chapter 7, a hybrid PE/FEM method is proposed to study sound propagation near rigid porous interfaces. The procedure for using the linear and cubic finite element basis function to discretize an arbitrary function is reviewed. Next, the derivation of the PE method is demonstrated. The FEM method is then used to discretize the function in the vertical direction, and then solve the parabolic equation. A PML technique is applied to the PE/FEM method with great success in terms of computational time and numerical accuracy.

Issues regarding the selection of various starting fields were discussed in detail. Using the analytical asymptotic solutions derived in the previous chapters as the starting field tends to improve the near-field results compared to various Gaussian starter fields. In particular, for the extended reaction ground, the analytical starting field is able to predict the sound fields above and below the ground accurately even when the source is close to the ground surface. Since the cubic finite element discretization is used in the PE/FEM method, the analytical asymptotic solution from the dipole is necessary for the starting field. The asymptotic solution for the dipole source in Chapter 6 is a prerequisite to studying the PE/FEM method. The PE/FEM method is applied to predict the sound field near snow covered ground where good agreement is observed.

In Chapter 8, the PE/FEM method is extended to a cubic PE/FEM method where FEM cubic interpolation is applied in both the vertical and horizontal directions.

Comparison with results for the sound field above an impedance ground validates the formulation. It is shown that the cubic PE/FEM is more expensive computationally but more accurate sound predictions for the monopole and dipole sources can be achieved. The cubic PE/FEM method proposed in Chapter 8 can be applied to more complicated propagation conditions and guide future studies.

Potential future research topics into this subject area may include: (1) implementation of higher ordered finite element basis functions; (2) considerations for range-dependent geometries (*e.g.*, sloped ground interfaces, mixed impedances, *etc.*); (3) considerations for atmospheric effects (*e.g.*, wind, temperature, turbulence, *etc.*); (4) acoustical characterization of multi-layered porous materials.

LIST OF REFERENCES

LIST OF REFERENCES

[1] K. M. Li and S. Liu, "Fast asymptotic solutions for sound field above and below a rigid porous ground," J. Acoust. Soc. Am.130, 1103-1114 (2011).

[2] S. Liu and K. M. Li, "Efficient computation of the sound fields above a layered porous ground," J. Acoust. Soc. Am. 131, 4376-4388 (2012).

[3] K. M. Li and S. Liu, "Propagation of sound from a monopole source above an impedance-backed porous layer," J. Acoust. Soc. Am. 131, 4389-4398 (2012).

[4] Erik M. Salomons, Computational Atmospheric Acoustics, Kluwer Academic Publishers (2001).

[5] J. E. Piercy, T. F.W. Embleton, and L.C.Sutherland, "Preview of noise propagation in the atmosphere," J. Acoust. Soc. Am. 61(6), 1403-1418 (1977).

[6] P. H. Parkin and W. E. Scholes. "The horizontal propagation of sound from a jet noise close to the ground at Radett," J. Sound Vib. 1, 1-13 (1965).

[7] P. H. Parkin and W. E. Scholes. "The horizontal propagation of sound from a jet noise close to the ground at Hatfield," J. Sound Vib. 2, 353-374 (1965).

[8] M. E. Delaney and E. N. Bazley, "Acoustical properties of fibrous absorbent materials," Appl Acoust. 3, 105-116 (1970).

[9] C. I. Chessel, "Propagation of noise along a finite impedance boundary," J. Acoust. Soc. Am. 62(4), 825-834 (1977).

[10] T. F. W. Embleton, J. E. Piercy and G. A. Daigle, "Effective flow resistivity of ground surface determined by acoustical measurements," J. Acoust. Soc. Am. 74(4), 1239-1244 (1983).

[11] J. F. Piercy, T. F.W. Embleton and G. A. Daigle, "Atmospheric propagation of sound: process in understanding basic mechanisms," Proc. 11th ICA, Paris, 27-46 (1983)

[12] K. Attenborough, "Review of ground effects on outdoor sound propagation from continuous broadband sources" Appl Acoust. 24, 289-319 (1988).

[13] K. Attenborough, "Acoustical impedance models for outdoor ground surfaces," J. Sound Vib. 99(4), 521-544 (1985).

[14] Y. Miki, "Acoustical properties of porous materials-modification of Delany-Bazley models," J. Acoust. Soc. Jpn. E11, 19-24 (1990).

[15] Y. Miki, "Acoustical properties of porous materials-generalizations of empirical models," J. Acoust. Soc. Jpn. E11, 25-28 (1990).

[16] K. Attenborough, I. Basir, and S. Taherazadeh, "Outdoor ground impedance models," J. Acoust. Soc. Am. 129(5), 2806-2819 (2011).

[17] B. A. De Jong, A. Moerkerken and J.D. van der Toorn, "Propagation of sound over grassland and over an earth barrier," J. Sound Vib. 86(1), 23-46 (1983)
[18] P. Koers, "A note on the calculation of the sound propagation over impedance jumps and screens," in Proceedings of Inter-Noise 83, 311-314 (1983).
[19] P. Boulanger, T. Waters-Fuller, K. Attenborough, and K.M. Li, "Models and measurements of sound propagation from a point source over mixed impedance ground," J. Acoust. Soc. Am. 102(3), 1432-1442 (1997).
[20] K. Attenborough, K. M. Li and K. Horoshenkov, Predicting Outdoor Sound, Taylor & Francis, London and New York (2007).
[21] S. Taherzadeh, K. M. Li and K. Attenborough, "A hybrid BIE/FFP scheme for predicting barrier efficiency outdoors," J. Acoust. Soc. Am. 110(2), 918-924 (2001).
[22] S. Peters, "The prediction of railway noise profiles," J. Sound Vib. 32, 87-99 (1972).
[23] K. S. Bretner and F. Farassat, "Helicopter noise prediction: the current status and future directions," J. Sound Vib. 170, 79-96 (1994).
[24] U. Ingard and J. L. Lamb, "Effect of a reflecting plane on the power output of sound sources," J. Acoust. Soc. Am. 29, 743-744 (1957).
[25] M. Yildiz and O. K. Mawardi, "on the diffraction of multipole fields by a semi-infinite rigid wedge," J. Acoust. Soc. Am. 32, 743-744 (1957).
[26] D. A. Bies, "Effect of a reflecting plane on an arbitrarily oriented multipole," J. Acoust. Soc. Am. 33, 286-288 (1961).
[27] W. C. Meecham, T. D. Bui and W. R. Miller, "Diffraction of dipole sound by the edge of a rigid baffle," J. Acoust. Soc. Am. 70, 1531-1533 (1981).
[28] J. P. Shen and W. C. Meecham, "Quadrupole directivity of jet noise when impinging on a large rigid plate," J. Acoust. Soc. Am. 94, 1415-1424 (1993).
[29] Z. Hu and J. S. Bolton, "Sound proprgation from an arbitrarily oriented multipole placed near a plane, finite impedance surface," J. Sound Vib. 170(5), 637-669 (1994).
[30] K. M. Li, S. Taherzadeh and K. Attenborough, "Sound propagation from a dipole source near an impedance surface," J. Acoust. Soc. Am. 101, 3343-3352 (1997).
[31] K. M. Li, S. Taherzadeh and K. Attenborough, "The sound field of an arbitrarily oriented quadrupole near ground surfaces," J. Acoust. Soc. Am. 102, 2050-2057 (1997).
[32] K. Attenborough, S. Taherzadeh, H. E. Bass, X. Di, R. Raspet, G. R. Becker, A. Gudesen, A. Chrestman, G. A. Daigle, A. L'Esperance, Y. Gabillet, K. E. Gilbert, Y. L. Li, M. J. White, P. Naz, J. M. Noble, and H. A. J. M van Hoof, "Benchmark cases for outdoor sound propagation models," J. Acoust. Soc. Am. 97, 173-191 (1995).
[33] V. Cerveney, M. M. Popov and I. Psencik, "Computation of wave fields in inhomogeneous media-Gaussian beam approach," Geophysical Journal of the Royal Astronomical Society. 70, 109-28 (1982).
[34] L. M. Brekhovskikh, Waves in Layered Media, second edition, Academic, New York (2001).
[35] A. D. Pierce, Acoustics: An Introduction to its Physical Principles and Applications, American Institute of Physics, New York (1991).

[36] D. Broutman, J. W. Rottman and S. D. Eckermann, “Ray models for internal waves in atmosphere and ocean,” Annual Review of Fluid Mechanics. 36, 233-253 (2004).
[37] F. R. Dinapoli, “Fast field program,” J. Acoust. Soc. Am. 47, 100-100 (1970).
[38] F. R. Dinapoli and M. R. Powers, “Fast field program (FFP) and attenuation loss in hudson bay,” J. Acoust. Soc. Am. 51, 108-108 (1972).
[39] T. L. Richards and K. Attenborough, “Accurate FFT-based Hankel transform for predictions of outdoor sound propagation,” J. Sound Vib. 109(1). 157-167(1986).
[40] S. J. Franke and G. W. Swenson Jr, “A brief tutorial on the fast field program(FFP) as applied to sound propagation in the air,” J. Appl. Acoust, 27, 103-115 (1989).
[41] M. West, R. A. Sack and R. Walkden, “The Fast Field Program (FFP). A second tutorial: Application to long range sound propagation in the air,” J. Appl. Acoust. 33, 199-228 (1991).
[42] S. M. Candel, “Dual algorithms for fast calculation of the Fourier-Bessel transform,” I.E.E.E. Transactions on acoustics, speed and signal processing, ASSP-29 (1981).
[43] F. R. Dinapoli and R. L. Deavenport, “Theoretical and numerical Green's function field solution in a phase multilayered medium,” J. Acoust. Soc. Am. 67, 92-105 (1980).
[44] S. Tooms, S. Taherzadeh and K. Attenborough, “Sound propagation in a refractive fluid above a layered fluid-saturated porous elastic material,” J. Acoust. Soc. Am. 93, 173-181 (1993).
[45] M. A. Letontovich and V. A. Fock, “Solution of the problem of propagation of electromagnetic waves along the earth's surface by the method of parabolic equation,” J. Exp. Theor. Phys. 16(7), 557 (1946).
[46] F. D. Tappert, “The parabolic approximation method,” Wave propagation and underwater acoustics, Lecture Notes in Physics. 70, 224-287 (1977).
[47] J. F. Claerbout, Fundamentals of geophysical data processing, Blackwell, Oxford, 1985.
[48] K. E. Gilbert and M. J. White, “Application of the parabolic equation to sound propagation in a refractive atmosphere,” J. Acoust. Soc. Am. 85(2), 630-637 (1989).
[49] M. J. White and K. E. Gilbert, “Application of the parabolic equation to the outdoor sound propagation,” Appl Acoust. 27(3), 227-238 (1989).
[50] M. West, K. E. Gilbert and R. A. Sack, “A tutorial on the parabolic equation (PE) model used for long range sound propagation in the atmosphere,” Appl Acoust. 37, 31-49 (1992).
[51] J. S. Robertson, W. L. Siegmann, and M. J. Jacobson, “Low-frequency sound propagation modeling over a locally reacting boundary with the parabolic approximation,” J. Acoust. Soc. Am. 98(2), 1130-1137 (1995).
[52] J. S. Robertson, P. J. Schlatter, and W. L. Siegmann, “Sound propagation over impedance discontinuities with the parabolic approximation,” J. Acoust. Soc. Am. 99(2), 761-767 (1996).
[53] K. E. Gilbert and X. Di, “A fast Green's function method for one-way sound propagation in the atmosphere,” J. Acoust. Soc. Am. 94(4), 2343-2352 (1993).
[54] E. M. Salomons, “Improved Green's function parabolic equation method for atmospheric sound propagation,” J. Acoust. Soc. Am. 104(1), 100-111 (1998).

[55] V. A. Dougalis, N. A. Kampanis, "Finite element methods for the parabolic equation with interfaces," J. Comp. Acoustics. 4, 55-88 (1996).
[56] P. Malbequi, "Atmospheric sound propagation using the wide-angle parabolic equation," ONERA TP, 4, 1996-174 (1996).
[57] J. S. Robertson, "Sound propagation over a large wedge: A comparison between the geometrical theory of diffraction and the parabolic equation," J. Acoust. Soc. Am. 106(1), 113-119 (1999).
[58] N. A. Kampanis and J. A. Ekaterinaries, "Numerical prediction of far-field wind turbine noise over terrain of moderate complexity," System Analysis Modeling Simulation. 41, 107-122 (2001).
[59] N. A. Kampanis, "Numerical simulation of low frequency aeroacoustics over irregular terrain using a finite element discretization of the parabolic equation," J. Comp. Acoustics. 1, 97-112 (2002).
[60] Ph. Blanc-Benon, L. Dallois, D.Juve, "Long range sound propagation over non-flat terratin using parabolic equation," 11th International Congress on Acoustics, Rome, Italy, 2001.
[61] B. Lihoreau, B. Gauvreau, M. Berengier, P.Blanc-Benon, I. Calmet, "Outdoor sound propagation modeling in realistic environment: Application of coupled parabolic equation and atmospheric models," J. Acoust. Soc. Am. 120(1), 110-119 (2006).
[62] T.Van Renterghem, D. Bottledooren, P.Lercher, "Comparison of measurements and predictions of sound propagation in valley-slope configuration in an inhomogeneous atmosphere," J. Acoust. Soc. Am. 121(5), 2522-2533 (2007).
[63] N. A. Kampanis, A. I. Delis, D. C. Antonopoulou, G. Kozyrakis, "A finite elment discretization of the standard parabolic equation in generalized boundary fitting coordinates," Applied Numerical Mathematics (2011)
[64] Michael D. Collins, "A self-starter for the parabolic equation method," J. Acoust. Soc. Am. 92(4), 2069-2074 (1992).
[65] Robert J. Cederberg and Michael D. Collins, "Application of an improved self-starter to geoacoustic inverision," I.E.E.E J. Oceanic Engineering 22(1), 102-109 (1992).
[66] Michael D. Collins, "A split-step Pade solution for the parabolic equation method," J. Acoust. Soc. Am. 93, 1736-1742 (1993).
[67] O. Zaporozhets, V. Tokarev and K. Attenborough, "Predicting noise from aircraft operated on the ground," Appl. Acoust. 64, 941-953 (2003).
[68] P. Meounou and E. S. Papaefthymiou, "Shadowing of directional noise cources by finite noise barriers," Appl. Acoust. 71, 351-367 (2010).
[69] F. Anfoss-Ledee, P. Dangla and M. Beregier, "Sound propagation above a porous road surface with extended reaction by boundary element method," J. Acoust. Soc. Am. 122, 731-736 (2007).
[70] G. Kristensson and S. Ström, "Scattering from buried inhomogeneities – a general three-dimensional formalism," J. Acoust. Soc. Am. 64, 917-936 (1978).
[71] C. F. Chien and W. W. Soroka, "Sound propagation along an impedance plane," J. Sound Vib. 43(1), 9-20 (1975).

[72] K. Attenborough, S. I. Hayek and J. M. Lawther, "Propagation of sound over a porous half-space," J. Acoust. Soc. Am. 65, 1493-1501 (1980).
[73] M. Abramowitz and I. A. Stegun, Handbook of mathematical functions with formulas, graphs and mathematical tables Ch. 7 and Ch. 9, Dover Publications, Inc., New York (1972).
[74] K. M. Li, "An analytical formulation for predicting the attenuation of sound in a porous ground from an airborne source," J. Acoust. Soc. Am. 123, 1352-1363 (2008).
[75] M. Boue, H. Boden and I. Karasalo, "Outdoor sound propagation using an exact finite element method," AIAA Paper 2001-2261 (2001).
[76] D. L. Berry, S. N. Chandler-Wilde and K. Attenborough, "Acoustic scattering by a near surface obstacle in a rigid porous medium," J. Sound Vib. 170, 161-179 (1994).
[77] C. G. Don and A. J. Rogers, "Using acoustic impulses to identify a buried nonmetallic object," J. Acoust. Soc. Am. 95, 2837-2838 (1994).
[78] D. Velea, R. Waxler and J M Sabatier, "An effective fluid model for landmine detection using acoustic to seismic coupling," J. Acoust. Soc. Am. 115, 1993-2000 (2004).
[79] O. Doutres, Y. Salissou, N. Atalla and R. Panneton, "Evaluation of the acoustic and non-acoustic properties of sound absorbing materials using a three-microphone impedance tube," Appl Acoust. 71, 506-509 (2010).
[80] B. H. Song and J. S. Bolton, "A transfer matrix approach for estimating the characteristic impedance and wave number of limp and rigid porous materials," J. Acoust. Soc. Am.107, 1131-1152 (2000).
[81] K. M. Li and S. Liu, "Acoustical characterization of rigid porous materials," J. Acoust. Soc. Am. 127, 2038 (2010).
[82] H. Orr, "Die Sattelpunksmethode in der Umgebung eines Pols,"Annalen der Physik, 43, 393-403 (1943).
[83] W. Pauli, "On asymptotic series for functions in the theory of diffraction of light," Physical Review, 54, 924-931 (1938).
[84] P. C. Clemmow, "Some extension to the method of integration by steepest descents," Quarterly Journal of Mechanics and Applied Mathematics 3, 241-256 (1950).
[85] T. Kawai, T. Hidaka and T. Nakajima, "Sound propagation above an impedance boundary," J. Sound Vib. 83, 125-138 (1982).
[86] S. N. Chandler-Wilde and D.C. Hothersall, "Sound propagation above an inhomogeneous impedance plane," J. Sound Vib. 98, 475-491 (1985).
[87] K. M. Li, T. Waters-Fuller and K. Attenborough, "Sound propagation from a point source over extended-reaction ground", J. Acoust. Soc. Am. 104, 679-685 (1998).
[88] A. Sommerfeld, "Über die Ausbreitung der Wellen in der drahtlosen Telegraphie," Ann. Phys. 28, 665-736 (1909).
[89] J. F. Allard, M Henry, V. Gareton, G. Jansens and W. Lauriks, "Impedance measurements around grazing incidence for non-locally reacting thin porous layers," J. Acoust. Soc. Am. 113, 1210-1215 (2003).

[90] J. F. Allard, V. Gareton, M. Henry, G. Jansens and W. Lauriks, "Impedance evaluation from pressure measurements near grazing incidence for non-locally reacting porous layers," Acust. Acta Acust. 89, 595-603 (2003).
[91] J. F. Allard, M. Henry and M. Berengier, "Pole localization and impedance measurement for porous layers with a small porosity,"Acust. Acta Acust. 92289-295 (2006).
[92] J. F. Allard, G. Jansens, W. Lauriks, "Reflection of spherical waves by non-locally reacting media," Wave Motion 36, 143-155 (2002).
[93] Banos. Dipole Radiation in the Presence of a Conducting Hal-Space Ch. 3, Pergamon Press, Oxford. (1966)
[94] R. J. Donato, "Propagation of a spherical wave near a plane boundary with complex impedance," J. Acoust. Soc. Am. 60, 34-39 (1976).
[95] S-I. Thomasson, "Sound propagation above a layer with a large refractive index," J. Acoust. Soc. Am. 61, 659-674 (1977).
[96] K. Attenborough, "Predicted ground effect of highway noise," Journal of Sound and Vibration 81, 413-424 (1982).
[97] F. Goos and H. Hanchen, "Ein neuer und fundamentales Versuch zur total reflexion; (A new and fundamental test for total reflection) ," in German. Annalen der Physik 6, 333-345 (1947).
[98] A. Schoch, "Sound reflection, refraction, and bending," (in German). Ergebnisse der exakten Naturwissenschaften 23, 127-235 (1950).
[99] A. Schoch, "Sound transmission through plates," (in German). Acustica 2, 1-17 (1952).
[100] J. F. Allard and M. Henry, "Fluid-fluid interface and equivalent impedance plane,"Wave Motion 43, 232-240 (2006).
[101] G. Jansens, W. Lauriks, G Vermeir and J. F. Allard, "Free-field measurements of the absorption coefficient for nonlocally reacting absorbing porous layers," J. Acoust. Soc. Am.112, 1327-1334 (2002).
[102] J. F. Allard and W. Lauriks, "Poles and zeros of the plane wave reflection coefficient for porous surfaces,"Acta Acustica United with Acustica 83, 1045-1052 (1997).
[103] O. S. Heavens, "The propagation of lateral waves in absorbing media and thin film," Optica ACTA 21, 1-9 (1974).
[104] W. Lauriks, L Kelders, J. F. Allard, "Surface waves and leaky waves above a porous layer," Wave Motion 28, 59-67 (1998).
[105] P. J. Davis and P. Rabinowitz, Methods of numerical integration Sec. 2.1.2.4, p. 174, 2nd Ed., Academic Press, Orlando.
[106] F. X. Becot, L. Jaouen and F. Sgard, "Noise control strategies using composite porous materials–simulations and experimental validations on plate/cavity systems," Noise Control Engineering Journal 55, 464-475 (2011).
[107] E. Gourdon and M. Seppi, "On the use of porous inclusions to improve acoustic response of porous materials: Analytical and experimental verification," Appl Acoust. 71, 283-298 (2010).

[108] F. X. Becot and F. Sgard, "On the use of poroelastic materials for the control of the sound radiated by a cavity backed plate," J. Acoust. Soc. Am.120, 2055-2066 (2006).
[109] R. Panneton and N. Atalla, "Numerical prediction of sound transmission through finite multilayer systems with poroelastic materials," J. Acoust. Soc. Am.100, 346-354 (1996).
[110] M. A. Biot, "Theory of propagation of elastic waves in a fluid-saturated porous solid. I. Low-frequency range," J. Acoust. Soc. Am. 28, 168-178 (1956).
[111] M. A. Biot, "Theory of propagation of elastic waves in a fluid-saturated porous solid. I. Higher frequency range," J. Acoust. Soc. Am. 28, 179-191 (1956).
[112] Camille Perrot, Fabien Chevillotte, Minh Tan Hoang, "Microstructure, transport and acoustic properties of open-cell foam samples: Experiments and three-dimensional numerical simulations," Journal of Applied Physics 111, 014911(2012).
[113] D. L. Johnson, J. Koslik, and R. Dashen, "Theory of dynamic permeability and turtuosity in air-saturated porous media," Journal of Fluid Mechanics 176, 379-402 (1987).
[114] D. Lafarge, P. Lemarinier, J.F. Allard, and V. Tarnow, "Dynamic compressibility of air in porous structures at audible frequencies," J. Acoust. Soc. Am.102, 1995-2006 (1997).
[115] Y. Y. Lu and J. Zhu, "Perfectly matched layer for acoustic waveguide modeling-Benchmark calculations and perturbation analysis," Comp. Model. Eng. Sci., 22(3),.235-247, 2007.
[116] D. G. Albert, and Orcutt, "J. A., Acoustic pulse propagation above grassland and snow: comparison of theoretical and experimental waveforms," J. Acoust. Soc. Am. 87(l), 93-100 (1990).
[117] D. G. Albert, L. R. Hole, "Blast noise propagation above a snow cover," J. Acoust. Soc. Am. 109(6):2675–81 (2001).
[118] D. G Albert., S.N. Decato, D. L. Carbee, "Snow cover effects on acoustic sensors,"Cold Reg. Sci. Technol. 52, 132-145 (2008).

APPENDICES

Appendix A: Main Steps in the Modified Saddle-point Method

In Chapter 2, the asymptotic solution according to the modified saddle-point method has been presented. The essential steps for obtaining the solution will be offered as follows. Knowing the Taylor series for $\Gamma^{(m)}(W)$, it is found particularly useful to derive an analytical expression for $\Gamma^{(m)}(W)$ and its second derivative at $W = 0$ (i.e., at $\mu = \theta$). They will shape the structure of the asymptotic solution given in Eq. (2.35). It is tedious but straightforward to show that $\Gamma^{(m)}(0)\left[\equiv \Gamma_0^{(m)}\right]$ is furnished by

$$\Gamma_0^{(m)} = \sqrt{-1/\Phi_a''(\theta)}\left(-2[w_p^{(m)}]^2\right)\Lambda_\theta^{(m)} \quad , \tag{A1}$$

where $\Lambda_\theta^{(m)} = \Lambda^{(m)}(X)\big|_{X=0;\mu=\theta}$. Noting Eq. (15b), it can then be shown that

$$\Gamma_0^{(m)} = \sqrt{\frac{1}{ikR_2}}\left[\frac{\sin\theta}{\cos\theta + \chi_\theta^{(m)}}\right]\left(-2[w_p^{(m)}]^2\right)\left[e^{ikr\sin\theta}H_0^{(1)}(kr\sin\theta)\right]. \tag{A2}$$

The second derivative of $\Gamma^{(m)}(W)$ at $X = 0$ can be expressed in terms of $\Gamma^{(m)}(0)$ as

$$\frac{d^2}{dW^2}\Gamma^{(m)}(W)\bigg|_{W=0} = 2\Gamma_0^{(m)}\left(\frac{1}{[w^{(m)}]^2}\right)\left(b^{(m)}\left[w_p^{(m)}\Big/\sqrt{ikR_2}\right]^2 - 1\right) \quad , \tag{A3}$$

where

$$b^{(m)} = \frac{[\Lambda_\theta^{(m)}]''}{\Lambda_\theta^{(m)}} + \frac{2[\chi_\theta^{(m)}]'[\Lambda_\theta^{(m)}]'}{\chi_\theta^{(m)}\Lambda_\theta^{(m)}} + \frac{[\chi_\theta^{(m)}]''}{\chi_\theta^{(m)}} + \frac{1}{4} \quad , \tag{A4}$$

$$\frac{[\Lambda_\theta^{(m)}]''}{\Lambda_\theta^{(m)}} = 2\frac{\left([E_\theta^{(m)}]^2 - E_\theta^{(m)}\right)\sin^2\theta + E_\theta^{(m)}\left(1 + \chi_\theta^{(m)}\cos\theta\right)}{\left(\cos\theta + \chi_\theta^{(m)}\right)^2} + \frac{[E_\theta^{(m)}]'\sin\theta}{\cos\theta + \chi_\theta^{(m)}} - \tfrac{1}{4}\csc^2\theta\,, \tag{A5}$$

$$\frac{\Lambda_\theta^{(m)\prime}}{\Lambda_\theta^{(m)}} = \frac{E_\theta^{(m)} \sin\theta}{\cos\theta + \chi_\theta^{(m)}} + \tfrac{1}{2}\cot\theta \ , \tag{A6}$$

$$E_\theta^{(m)} = E^{(m)}(\theta) = 1 - [\chi_\theta^{(m)}]' \big/ \sin\theta \, , \tag{A7}$$

$$[E_\theta^{(m)}]' = [E^{(m)}(\theta)]' = -[\chi_\theta^{(m)}]'' \big/ \sin\theta + [\chi_\theta^{(m)}]' \cos\theta \big/ \sin^2\theta \, , \tag{A8}$$

and the subscript θ denotes these parameters are evaluated at $\mu = \theta$, i.e., at $X = 0$. The prime and double primes are the first and the second derivatives with respect to θ. It should be noted that Eqs. (A7) and (A8) are derived by starting from Eq. (2.19d). At the far field when $\theta \to \pi/2$, the isolated term involving $\csc^2\theta$ in Eq. (A5) and $\cot\theta$ in Eq. (25c) may be dropped without affecting the accuracy of the numerical solution. These two terms are kept in Eqs. (A5) and (A6) for preciseness and for future comparison.

Substitution of Eqs. (2.29) and (2.30a) into Eq. (2.15a) leads to

$$\Psi = \frac{-ike^{ikR_2}}{4\pi} \sum_{j=0}^{\infty} \frac{\partial_{2j}\Gamma^{(m)}}{(2j)!} \int_{C_W} \frac{W^{2j} e^{-W^2/2} dW}{\left(W^2 - [W_p^{(m)}]^2\right)} \ , \tag{A9}$$

where all the integrals for the odd terms in the series of Eq. (2.30a) vanish. It is because the kernels of these integrals are odd functions about $W = 0$ along the integration path C_W. Deforming the integration to the saddle path C_X, Eq. (A9) can be rewritten as

$$p_D = \frac{-ike^{ikR_2}}{4\pi} \sum_{j=0}^{\infty} \frac{\partial_{2j}\Gamma^{(m)}}{(2j)!} \left[\int_{-\infty}^{\infty} \frac{W^{2j} e^{-W^2/2} dW}{\left(W^2 - [W_p^{(m)}]^2\right)} + (\pi i)[W_p^{(m)}]^{2j-1} e^{-[w_p^{(m)}]^2} H\left\{-\mathrm{Im}\left([w_p^{(m)}]^2 \big/ kR_2\right)\right\} \right] \ , \tag{A10}$$

where the second term in the square bracket is the pole contribution from each term in the series of Eq. (A9) when the integration path has been transformed from C_W to C_X. These terms are often referred as the surface wave pole contributions.

The integral of Eq. (A10) can be evaluated by noting the following identities for the complementary error function, erfc(z) ,

$$\int_{-\infty}^{\infty} \frac{W^{2j} e^{-W^2/2} dW}{W - W_p^{(m)}} = W_{p,m} \int_{-\infty}^{\infty} \frac{W^{2j} e^{-W^2/2} dW}{\left(W^2 - [W_p^{(m)}]^2\right)} \quad , \quad j = 0, 1, 2, \ldots \tag{A11}$$

and

$$\int_{-\infty}^{\infty} \frac{e^{-W^2/2} dW}{W - W_p^{(m)}} = (\pi i) e^{-w_m^2} \left[I_0\left(-i w_p^{(m)}\right) - H\left\{-\mathrm{Im}\left([w_p^{(m)}]^2 / kR_2\right)\right\} \right] \ , \tag{A12}$$

where the integral series $I_j(z)$ is given by

$$I_j(z) = \frac{2}{\sqrt{\pi}} \int_z^{\infty} X^{-2j} e^{-X^2} dX \quad , \tag{A13}$$

with $I_0(z)$ = erfc(z). The integrals $I_j(z)$ satisfy the recurrent relation,

$$I_j(z) = \frac{z^{1-2j} e^{-z^2}}{2j-1} - \frac{2}{2j-1} I_{j-1}(z), \quad j = 1, 2, 3, \ldots \tag{A14}$$

By noting Eqs. (A12) and (A14) and by using mathematical induction, it is possible to show that

$$\int_{-\infty}^{\infty} \frac{W^{2j} e^{-W^2/2} dW}{W - W_p^{(m)}} = (\pi i)(W_p^{(m)})^{2j} e^{-[w^{(m)}]^2} \left[\frac{(2j)!}{j!(-4)^j} I_j(-i w_p^{(m)}) - H\left\{-\mathrm{Im}\left([w_p^{(m)}]^2 / kR_2\right)\right\} \right]. \tag{A15}$$

Hence, the diffraction integral p_D can be simplified from Eq. (A10) to the equation given in Eq. (2.31) in the main text.

Appendix B: Associated Functions for Calculating b(m) Given in Eq. (A4)

To calculate $b^{(m)}$ for different types of non-locally reacting porous media, it is sufficient to provide analytical expressions for $\chi^{(m)}$, $\chi^{(m)\prime}$, and $\chi^{(m)\prime\prime}$ as $b^{(m)}$ can be computed from Eq. (A4) – (A6) with $E^{(m)}$ given by Eq. (2.19d) in the main text. Here, the primes represent the derivatives with respect to its argument, i.e., θ in this case. The following expressions can be derived by straightforward differentiations and tedious algebraic manipulations:

(i) A locally reacting ground (*m* = -1)

$$\chi_\theta^{(-1)} = \beta_1 = \text{constant} \ , \tag{B1a}$$

$$[\chi_\theta^{(-1)}]' = [\chi_\theta^{(-1)}]'' = 0 , \tag{B1a}$$

$$E_\theta^{(-1)} = 0 \ , \tag{B1c}$$

which implies

$$b^{(-1)} = \frac{2\left(1+\beta_1\cos\theta\right)}{\left(\cos\theta+\beta_1\right)^2} - \tfrac{1}{4}\csc^2\theta \approx \frac{2\left(1+\beta_1\cos\theta\right)}{\left(\cos\theta+\beta_1\right)^2} , \tag{B1d}$$

where the subscript θ in a parameter denotes that the parameter is to be evaluated at $\mu = \theta$, i.e. at the saddle-point of $X = 0$. For instance, $\chi_\theta^{(m)} \equiv \chi^{(m)}\left(\theta\right)$, etc. The prime and double primes are the first and second derivatives with respect to θ.

(ii) a semi-infinite extended reaction porous medium (*m* = 0)

$$\chi_\theta^{(0)} = \varsigma N_\theta\,, \tag{B2a}$$

$$[\chi_\theta^{(0)}]' = \varsigma N_\theta'\,, \tag{B2b}$$

$$[\chi_\theta^{(0)}]'' = \varsigma N_\theta'' \tag{B2c}$$

where

$$N_\theta = N(\theta) = \sqrt{n^2 - \sin^2\theta}\ , \tag{B3a}$$

$$N_\theta' = N'(\theta) = \frac{-\sin\theta\cos\theta}{N_\theta}\,, \tag{B3b}$$

and

$$N_\theta'' = N''(\theta) = -\frac{\cos 2\theta}{N_\theta} - \frac{\sin^2\theta\cos^2\theta}{N_\theta^3}\quad . \tag{B3c}$$

By the use of Eqs. (B2 a–c) and (B3 a–c) in Eq. (A4) $b^{(0)}$ can be obtained and, this can be used, in term, in Eq. (A4) to obtain an asymptotic expression for computing the diffraction term p_D.

(iii) A hard-backed porous layer (*m* = 1)

$$\chi_\theta^{(1)} = -i\chi_\theta^{(0)}\tan(kN_\theta d_1)\,, \tag{B4a}$$

$$[\chi_\theta^{(1)}]' = -i[\chi_\theta^{(0)}]'\tan(kN_\theta d_1) - i\chi_\theta^{(0)}\left[\tan\left(kN_\theta d_1\right)\right]'\,, \tag{B4b}$$

$$[\chi_\theta^{(1)}]'' = -i[\chi_\theta^{(0)}]''\tan\left(kN_\theta d_1\right) - 2i[\chi_\theta^{(0)}]'\left[\tan\left(kN_\theta d_1\right)\right]' - i\chi_\theta^{(0)}\left[\tan\left(kN_\theta d_1\right)\right]'' \tag{B4c}$$

where

$$\left[\tan\left(kN_\theta d_1\right)\right]' = \frac{d\left[\tan\left(kN_\theta d_1\right)\right]}{d\theta} = kd_1N_\theta'\sec^2\left(kN_\theta d_1\right), \tag{B5a}$$

and

$$\left[\tan\left(kN_\theta d_1\right)\right]'' = kd_1 \sec^2\left(kN_\theta d_1\right)\left[N_\theta'' + 2kd_1 (N_\theta')^2 \tan\left(kN_\theta d_1\right)\right]. \tag{B5b}$$

Consequently, $b^{(1)}$ can be determined from the above equations, which can then be applied in Eqs. (A4) for computing the diffraction term p_D above a hard-backed porous layer.

(iv) An impedance-backed porous layer (m = 2)

With the knowledge of $\chi_\theta^{(0)}$, $[\chi_\theta^{(0)}]'$,$[\chi_\theta^{(0)}]''$, $\chi_\theta^{(1)}$, $[\chi_\theta^{(1)}]'$, and $[\chi_\theta^{(1)}]''$, it is possible to determine the following formulas:

$$\chi_\theta^{(2)} = \frac{\beta_2 + \chi_\theta^{(1)}}{1 + \beta_2 \chi_\theta^{(1)} / [\chi_\theta^{(0)}]^2} \quad , \tag{B6a}$$

$$[\chi_\theta^{(2)}]' = \frac{2\beta_2 \chi_\theta^{(1)} \chi_\theta^{(2)}}{[\chi_\theta^{(0)}]^2 + \beta_2 \chi_\theta^{(1)}} \frac{[\chi_\theta^{(0)}]'}{\chi_\theta^{(0)}} + \frac{\chi_\theta^{(0)} (\chi_\theta^{(2)} - \beta_2)}{[\chi_\theta^{(0)}]^2 + \beta_2 \chi_\theta^{(1)}} \frac{[\chi_\theta^{(1)}]'}{\chi_\theta^{(1)}} \quad , \tag{B6b}$$

$$[\chi_\theta^{(2)}]'' = \frac{2\beta_2 \chi_\theta^{(1)} \chi_\theta^{(2)}}{[\chi_\theta^{(0)}]^2 + \beta_2 \chi_\theta^{(1)}} \left\{ \frac{[\chi_\theta^{(0)}]''}{\chi_\theta^{(0)}} - \left(\frac{[\chi_\theta^{(0)}]'}{\chi_\theta^{(0)}} \right)^2 \right\} + \frac{\chi_\theta^{(0)} (\chi_\theta^{(2)} - \beta_2)}{[\chi_\theta^{(0)}]^2 + \beta_2 \chi_\theta^{(1)}} \left\{ \frac{[\chi_\theta^{(1)}]''}{\chi_\theta^{(1)}} - \left(\frac{\chi_\theta^{(1)\prime}}{\chi_\theta^{(1)}} \right)^2 \right\}$$

$$+ \frac{2\beta_2 [\chi_\theta^{(0)}]'}{\chi_\theta^{(0)}} \times \frac{[\chi_\theta^{(0)}]^2 [\chi_\theta^{(1)}]' \chi_\theta^{(2)} + [\chi_\theta^{(0)}]^2 \chi_\theta^{(1)} [\chi_\theta^{(2)}]' + \beta_2 [\chi_\theta^{(1)}]^2 [\chi_\theta^{(2)}]' - 2\chi_\theta^{(0)} [\chi_\theta^{(0)}]' \chi_\theta^{(1)} \chi_\theta^{(2)}}{\left\{ [\chi_\theta^{(0)}]^2 + \beta_2 \chi_\theta^{(1)} \right\}^2}$$

$$+ \frac{[\chi_\theta^{(1)}]'}{\chi_\theta^{(1)}} \left\{ \frac{\chi_\theta^{(0)} [\chi_\theta^{(2)}]'}{[\chi_\theta^{(0)}]^2 + \beta_2 \chi_\theta^{(1)}} + \frac{\left(-[\chi_\theta^{(0)}]^2 [\chi_\theta^{(1)}]' + \beta_2 [\chi_\theta^{(0)}]' \chi_\theta^{(1)} - \beta_2 \chi_\theta^{(0)} [\chi_\theta^{(1)}]' \right) \left(\chi_\theta^{(2)} - \beta_2 \right)}{\left([\chi_\theta^{(0)}]^2 + \beta_2 \chi_\theta^{(1)} \right)^2} \right\}$$

. (B6c)

Hence, $b^{(2)}$ can be computed numerically and, that can be used in Eq. (A4) to calculate the diffraction wave term for the impedance-backed porous layer.

Appendix C: The Details of the Derivation of Eqs. (3.33a) and (3.33b)

To find an approximate series solution for p_b [see Eq. (3.25)], it is useful to replace the kernel function $\Lambda_\vartheta(W_\vartheta)$ with $\Gamma_\vartheta(W_\vartheta)$, which is a Taylor series expansion about the saddle point, $W_\vartheta = 0$. These two kernel functions, $\Lambda_\vartheta(W_\vartheta)$ and $\Gamma_\vartheta(W_\vartheta)$, are related according to Eq. (3.29). The substitution of Eqs. (3.29) and (3.30) into Eq. (3.25) yields

$$p_b \approx \frac{-ike^{ikR_2}}{4\pi}\left\{\Gamma_\vartheta(0)I_0 + \frac{1}{2}\Gamma''_\vartheta(0)I_1\right\}, \tag{C1}$$

where

$$I_0 = \int_{C_W} \frac{e^{-W_\vartheta^2/2}dW_\vartheta}{\left(W_\vartheta^2 - W_{p,\vartheta}^2\right)}, \tag{C2a}$$

and

$$I_1 = \int_{C_W} \frac{W_\vartheta^2 e^{-W_\vartheta^2/2}dW_\vartheta}{\left(W_\vartheta^2 - W_{p,\vartheta}^2\right)}. \tag{C2b}$$

The integrals I_0 and I_1 can be evaluated by indenting the path from C_W to C_X to give

$$I_0 = \int_{C_X} \frac{e^{-W_\vartheta^2/2}dW_\vartheta}{\left(W_\vartheta^2 - W_{p,\vartheta}^2\right)} + \frac{(\pi i)}{\sqrt{2}w_b}e^{-w_b^2}H\left\{-\mathrm{Im}\left[w_b^2/kR_2\right]\right\}, \tag{C3a}$$

and

$$I_1 = \int_{C_X} \frac{W_\vartheta^2 e^{-W_\vartheta^2/2}dW_\vartheta}{\left(W_\vartheta^2 - W_{p,\vartheta}^2\right)} + (\pi i)\sqrt{2}w_b e^{-w_b^2}H\left\{-\mathrm{Im}\left[w_b^2/kR_2\right]\right\}, \tag{C3b}$$

where H is the Heaviside step function. The second term in either Eq. (C3a) or (C3b) is the contribution from the pole when it is crossed while the integration path is changed

from C_W to C_X. The parameters $W_{p,\vartheta}$ and w_b shown in the above equations are given in Eq. (3.34).

Since the steepest path (i.e., C_X) is chosen along the real axis, we can rewrite the integrals in Eq. (A3a,b) as

$$\int_{C_X} \frac{W_\vartheta^2 e^{-W_\vartheta^2/2} dW_\vartheta}{\left(W_\vartheta^2 - W_{p,\vartheta}^2\right)} = \int_{-\infty}^{\infty} \frac{X^2 e^{-X^2/2} dX}{X - W_{p,\vartheta}} \quad , \quad j = 0, 1, 2, \ldots \tag{C4}$$

By noting the following identities [20], the integrals can be represented in terms of the complementary error function as follows:

$$\int_{-\infty}^{\infty} \frac{X^{2j} e^{-X^2/2} dX}{X - W_{p,\vartheta}} = W_{p,\vartheta} \int_{-\infty}^{\infty} \frac{X^{2j} e^{-X^2/2} dX}{X^2 - W_{p,\vartheta}^2} \quad , \quad j = 0, 1, 2, \ldots \tag{C5a}$$

and

$$\int_{-\infty}^{\infty} \frac{e^{-X^2/2} dX}{X - W_{p,\vartheta}} = (\pi i) e^{-w_b^2} \left[\operatorname{erfc}(-iw_b) - H\left\{ -\operatorname{Im}\left(w_b^2 / kR_2 \right) \right\} \right], \tag{C5b}$$

where the complementary error function of complex argument z is defined as

$$\operatorname{erfc}(z) = \frac{2}{\sqrt{\pi}} \int_z^{\infty} e^{-X^2} dX \, . \tag{C6}$$

It is then straightforward to show that

$$\int_{C_X} \frac{e^{-W_\vartheta^2/2} dW_\vartheta}{\left(W_\vartheta^2 - W_{p,\vartheta}^2\right)} = (\pi i) \frac{e^{-w_b^2}}{\sqrt{2} w_b} \left[\operatorname{erfc}(-iw_b) - H\left\{ -\operatorname{Im}\left[w_b^2 / kR_2 \right] \right\} \right], \tag{C7a}$$

and

$$\int_{C_X} \frac{W_\vartheta^2 e^{-W_\vartheta^2/2} dW_\vartheta}{\left(W_\vartheta^2 - W_{p,\vartheta}^2\right)} = \sqrt{2\pi} F\left(w_b\right) - (\pi i) \sqrt{2} w_b e^{-w_b^2} H\left\{ -\operatorname{Im}\left[w_b^2 / kR_2 \right] \right\}, \tag{C7b}$$

where $F\left(w_b\right)$ is the boundary loss factor [see Eq. (3.35)]. The substitution of Eq. (C7a) into (C3a) leads to Eq. (3.33a) and the replacement of the integral term in Eq. (C3b) with that given in (C7b) yields Eq. (3.33b).

Appendix D: Details for Asymptotic Evaluation of the Integral in Eq. (5.8)

The main idea for its asymptotic evaluation has been provided earlier in Ref. 1 in which the penetration of sound into an extended reaction ground has been considered. Essentially, a double saddle-point method enhanced by the pole subtraction scheme is employed in the analysis. Initially, the saddle path is determined by requiring

$$\mathrm{Im}\left[ikf_b(\vartheta) - ikf_b(\mu)\right] = 0 \tag{D1}$$

where $\mu = \vartheta$ is the stationary point which can be found by solving

$$f_b'(\mu)\big|_{\mu=\vartheta} = r\cos\vartheta - z_s\sin\vartheta - nZ\sin\varphi\left.\frac{d\mu_1}{d\mu}\right|_{\mu=\vartheta} = 0\,. \tag{D2}$$

The stationary point at the lower medium, $\mu_1 = \varphi$, can be found by using Snell's law, viz Eq. (5.6a), for a known incident angle, ϑ. The saddle path, $C_{\bar{\mu}}$, in addition to the original integration path are sketched in Fig. 5.2. A new complex variable W_ϑ is then introduced to replace μ by defining

$$W_\vartheta^2/2 = ik\left[L - f_b(\mu)\right], \tag{D3b}$$

where L [$= f_b(\vartheta)$] is the acoustical path length which may be determined by Eq. (5.11a). It follows from Eq. (D3a) that the derivative of W_ϑ with respect to μ is given by

$$d\mu/dW_\vartheta = -W_\vartheta/\left[ikf_b'(\mu)\right] \tag{D3b}$$

Using W_ϑ in Eq. (5.8), the canonical integral can be rewritten as

$$I_C(Z) = I_1 + I_2 \tag{D4a}$$

where

$$I_1(Z) = -\frac{e^{ikL}}{4\pi} \int_{C_W} \sin\mu G_0^{(1)}(\mu)\gamma(\mu)\left[W_\vartheta / f_b'(\mu)\right] e^{-W_\vartheta^2} dW_\vartheta , \tag{D4b}$$

and

$$I_2(Z) = \frac{e^{ikL}}{4\pi} \int_{C_W} \frac{\chi(\mu)\gamma(\mu)G_0^{(1)}(\mu)\sin\mu}{\cos\mu + \chi(\mu)} \frac{W_\vartheta}{f_b'(\mu)} e^{-W_\vartheta^2} dW_\vartheta . \tag{D4c}$$

The kernel function of Eq. (D4b) is an entire function because there are no poles in the integrand. Hence, the asymptotic evaluation of $I_1(Z)$ can be conducted straightforwardly to yield,

$$I_1 = \gamma(\vartheta)\frac{e^{ikL}}{2\pi\Delta}, \tag{D5}$$

where the function γ is defined in Eq. (5.9a) and Δ is the physical path length determined by Eq. (5.12c) for a given depth Z. On the other hand, there are poles in the integrand of I_2 which can be located in the complex μ-plane by finding the zeros of Eq. (5.14b). Suppose that the pole locations, is determined at μ_p in the complex μ-plane and W_p in the complex W_ϑ plane. According to Eqs. (5.7c), (5.9d) and (5.14b), it can be inferred that

$$\cos\mu_p = i\zeta N(\mu_p)\tan\left[kN(\mu_p)d\right]. \tag{D6}$$

Then, making use of Eq. (D3b), the pole location in the complex W_ϑ plane is determined as

$$W_p = \sqrt{2}\,\overline{w} \tag{D7}$$

where the apparent numerical distance $\overline{w}$ [see Eq. (5.15b)] is customarily used instead of W_P in the final asymptotic solution for the sound fields given in Eq. (5.17). The approximate numerical distance, $\overline{w}_\vartheta$ [see Eq. (5.15c)] is also needed for determining $q(Z)$

[see Eq. (5.13c)] in Eq. (5.17).

When the pole is close to the saddle point, the radius of convergence of the asymptotic series will be limited. Hence, the pole subtraction scheme is needed to remove the apparent singularity of the integrand of I_2 shown in Eq. (D4c). Following the analysis detailed in Ref. [3], it is straightforward to derive a uniform asymptotic solution for I_2 to yield,

$$I_2 = \left\{ \frac{-2\beta_\vartheta \gamma(\vartheta)}{\cos\vartheta + \beta_\vartheta} + \gamma(\mu_p)\Upsilon \right\} \frac{e^{ikL}}{4\pi\Delta} \tag{D8}$$

where β_ϑ is known as the effective admittance [see Eq. (5.14a)], the function $\gamma(\mu)$ is defined by Eq. (5.9a) with N specified by Eq. (5.7c), and the parameter Υ is determined by

$$\Upsilon = 2i\sqrt{\pi}(ikR_r/2)^{1/2} \frac{\beta_p e^{-\bar{w}^2} erfc(-i\bar{w})}{E_p\sqrt{\sin\vartheta \sin\mu_p}} + \frac{2\beta_p / \sqrt{2\sin\vartheta\sin\mu_p}}{E_p\sqrt{1-\cos(\mu_p-\vartheta)}}. \tag{D9}$$

In the above equation, R_r is the energy path length defined by Eq. (5.12b), erfc( ) is the complementary error function, and, E_p is determined by Eq. (5.16d). This parameter Υ can be treated mathematically as the difference between the complementary error function term and its asymptotic approximation. Substituting Eq. (5.15b) in the second term of Eq. (D9), and noting Eqs. (5.15a), (5.15c), (5.16a), (5.16b) and (5.16c), we can obtain an expression for I_2 as follows:

$$I_2 = \left\{ -\gamma(\vartheta)\left[1 - V(\vartheta)\right] + A(\mu_p)\gamma(\mu_p)\left[1 - V(\vartheta)\right] F(\bar{w}) \right\} \frac{e^{ikL}}{4\pi\Delta}. \tag{D10}$$

Use of Eq. (D5) and (D10) in Eq. (D4a) yield the asymptotic solution for the total sound fields within the rigid porous medium. This expression is the same as that given in Eq. (5.17) in Chapter 5.

Appendix E: Diffracted Wave Fields and Total Sound Field from a Monopole

Li and Liu [1] showed that the diffracted wave term $p_a^{(m)}$ due to the monopole source can be evaluated asymptotically to yield a sum of the main term Ξ and its correction factor $\phi^{(m)}$:

$$p_a^{(d)} = \left[\Xi + \phi^{(m)}\right] \frac{e^{ikR_2}}{4\pi R_2}, \tag{E1a}$$

where Ξ is dependent on the complimentary error function term defined by Eq. (6.18) and the correction term is specified by

$$\phi^{(m)} = \phi_A - \phi_B, \tag{E1b}$$

with ϕ_A and ϕ_B given in Eqs. (6.20a) and (6.22b), respectively. By taking inspiration from the form of solutions for a diffracted wave term for the dipole source, it is possible to express the diffracted wave term of the monopole sound fields by

$$p_a^{(m)} = \left[\phi_A + \Upsilon_a\right] \frac{e^{ikR_2}}{4\pi R_2}, \tag{E2}$$

where the diffraction factor Υ_a is defined by Eq. (6.24b). The substitution of Eq. (E2) into Eq. (6.3a) leads to an asymptotic expression for the total sound field:

$$p^{(m)} = \frac{e^{ikR_1}}{4\pi R_1} + \left\{V_\theta + \Upsilon_a\right\} \frac{e^{ikR_2}}{4\pi R_2}. \tag{E3}$$

This expression provides a better physical insight of the asymptotic solution given above. The first term of Eq. (E3) is the direct wave term and the second term is the reflected wave term. There are two components for the reflected wave term: the first

component in the curly bracket of Eq. (E3) is the plane wave reflection term, and the second component is the diffraction factor. The second term vanishes when the value of w is high, i.e., a condition when the plane wave term is sufficient for representing the reflected wave term. A re-examination of Eq. (6.38a) suggests that the same interpretation holds true for the sound field due to an arbitrarily oriented dipole, although extra factors, $(\mathbf{l}\cdot\mathbf{u}_1)$, $(\mathbf{l}\cdot\mathbf{u}_2)$, and, $(\mathbf{l}\cdot\mathbf{u}_s)$, are needed to account for the source orientation relative to the receiver location. These interpretations facilitate the development of the asymptotic formula for sound penetration into the porous ground given in Chapter 6.

Appendix F: Expressions for F_{ij}, G_{ij}, and J_{ij} Matrices with Cubic Basis Functions

Here is to derive the expression for the following three integrations

$$F_{ij}(f) = \int_{z_b}^{z_t} \eta_i(z) f(z) \eta_j(z) dz , \tag{F1}$$

$$G_{ij}(g) = \int_{z_b}^{z_t} \eta_i(z) g(z) \eta_j(z) dz , \tag{F2}$$

$$J_{ij}(f) = -\int_{z_b}^{z_t} \frac{\partial \eta_i(z)}{\partial z} f(z) \frac{\partial \eta_j(z)}{\partial z} dz , \tag{F3}$$

where f is defined in Eq.(7.43). For computing each term of $J_{ij}(f)$, the derivatives of the cubic finite element basis functions is needed. By doing derivations for the cubic basis functions, it is obtained that

$$\psi'_{j,1} = -6(1-\xi)\xi / h_j \; ; \quad \psi'_{j,2} = (1-\xi)(1-3\xi) \; ; \tag{F4a,b}$$

$$\psi'_{j,3} = 6(1-\xi)\xi / h_j \; ; \quad \psi'_{j,4} = \xi(3\xi - 2) \; . \tag{F5}$$

Inserting the linear approximation for $f(z)$, seen in Eq.(7.43), into Eq. (F1) and (F3) yields expressions for each term in Eq.(F1) and Eq.(F3) as follows. Note that the F_{ij}, G_{ij} and J_{ij} matrices are symmetric, the expressions for $F_{j-1,j}$ will be calculated as the same way like $F_{j,j+1}$ by replacing the corresponding functions with the ones over the element $z \in [z_{j-1}, z_j]$.

(a) For F in Eq. (F1)

$F_{j,j}^{(1,1)} = \int (\psi_{j-1,1})^2 f_{j-1}(z) dz$	$F_{j,j}^{(1,2)} = \int (\psi_{j-1,3} \psi_{j-1,4}) f_{j-1}(z) dz$

$+\int(\psi_{j,3})^2 f_j(z)dz$	$+\int(\psi_{j,1}\psi_{j,2}) f_j(z)dz$
$F_{j,j}^{(2,1)} = \int(\psi_{j-1,3}\psi_{j-1,4}) f_{j-1}(z)dz$ $+\int(\psi_{j,1}\psi_{j,2}) f_j(z)dz$	$F_{j,j}^{(2,2)} = \int(\psi_{j-1,4})^2 f_{j-1}(z)dz$ $+\int(\psi_{j,2})^2 f_j(z)dz$
$F_{j,j+1}^{(1,1)} = \int(\psi_{j,1}\psi_{j,3}) f_j(z)dz$	$F_{j,j+1}^{(1,2)} = \int(\psi_{j,1}\psi_{j,4}) f_j(z)dz$
$F_{j,j+1}^{(2,1)} = \int(\psi_{j,2}\psi_{j,3}) f_j(z)dz$	$F_{j,j+1}^{(2,2)} = \int(\psi_{j,2}\psi_{j,4}) f_j(z)dz$

(b) For J in Eq.(F3)

$J_{j,j}^{(1,1)} = \int(\psi'_{j-1,1})^2 f_{j-1}(z)dz$ $+\int(\psi'_{j,3})^2 f_{j+1}(z)dz$	$J_{j,j}^{(1,2)} = \int(\psi'_{j-1,3}\psi'_{j-1,4}) f_{j-1}(z)dz$ $+\int(\psi'_{j,1}\psi'_{j,2}) f_j(z)dz$
$J_{j,j}^{(2,1)} = \int(\psi'_{j-1,3}\psi'_{j-1,4}) f_{j-1}(z)dz$ $+\int(\psi'_{j,1}\psi'_{j,2}) f_j(z)dz$	$J_{j,j}^{(2,2)} = \int(\psi'_{j,4})^2 f_{j-1}(z)dz$ $+\int(\psi'_{j,2})^2 f_j(z)dz$
$J_{j,j+1}^{(1,1)} = \int(\psi'_{j,1}\psi'_{j,3}) f_j(z)dz$	$J_{j,j+1}^{(1,2)} = \int(\psi'_{j,1}\psi'_{j,4}) f_j(z)dz$
$J_{j,j+1}^{(2,1)} = \int(\psi'_{j,2}\psi'_{j,3}) f_j(z)dz$	$J_{j,j+1}^{(2,2)} = \int(\psi'_{j,2}\psi'_{j,4}) f_j(z)dz$

After a set of integration, we obtain each term of the *F, J* matrices. Note that at the first node and the end node, there's only one neighbor node. The elements related to the first node and the end node have a different expression as others. They will be represented separately in the following section.

For $j = 2,3,\ldots N-1$,

$$F_{j,j}=\begin{bmatrix} F_{j,j}^{1,1} & F_{j,j}^{1,2} \\ F_{j,j}^{2,1} & F_{j,j}^{2,2} \end{bmatrix}, \text{ where}$$

$$F_{j,j}^{1,1}=\frac{1}{C}\left\{\Delta z_j\left[(2B)\overline{f}_j+(A-B)f_j\right]+\Delta z_{j-1}\left[(2B)\overline{f}_{j-1}+(A-B)f_j\right]\right\};$$

$$F_{j,j}^{1,2}=\frac{1}{C}\left\{\Delta z_j^2\left[(2B)\overline{f}_j+(A-B)f_j\right]-\Delta z_{j-1}^2\left[(2B)\overline{f}_{j-1}+(A-B)f_j\right]\right\};$$

$$F_{j,j}^{2,1}=F_{j,j}^{1,2};\ F_{j,j}^{2,2}=\frac{1}{C}\left\{\Delta z_j^3\left[(2B)\overline{f}_j+(A-B)f_j\right]+\Delta z_{j-1}^3\left[(2B)\overline{f}_{j-1}+(A-B)f_j\right]\right\}.$$

For $F_{1,1}$, the first term in the above expression is kept, while for $F_{N,N}$ the second term is kept. And

$$F_{j,j+1}=\begin{bmatrix} F_{j,j+1}^{1,1} & F_{j,j+1}^{1,2} \\ F_{j,j+1}^{2,1} & F_{j,j+1}^{2,2} \end{bmatrix}, \text{ where}$$

$$F_{j,j+1}^{1,1}=\frac{1}{C}\left\{\Delta z_j\left[(2B)\overline{f}_j+(A-B)f_j\right]\right\};\ F_{j,j+1}^{1,2}=\frac{1}{C}\left\{\Delta z_j^2\left[(2B)\overline{f}_j+(A-B)f_j\right]\right\};$$

$$F_{j,j+1}^{2,1}=F_{j,j+1}^{1,2};\ F_{j,j+1}^{2,2}=\frac{1}{C}\left\{\Delta z_j^3\left[(2B)\overline{f}_j+(A-B)f_j\right]\right\}.$$

In a similar way, the expression for *J* is listed as follows.

$$J_{j,j}=\begin{bmatrix} J_{j,j}^{1,1} & J_{j,j}^{1,2} \\ J_{j,j}^{2,1} & J_{j,j}^{2,2} \end{bmatrix}, \text{ where}$$

$$J_{j,j}^{1,1}=\frac{1}{C}\left\{\frac{1}{\Delta z_j}\left[(2B)\overline{f}_j+(A-B)f_j\right]+\frac{1}{\Delta z_{j-1}}\left[(2B)\overline{f}_{j-1}+(A-B)f_j\right]\right\};$$

$$J_{j,j}^{1,2}=\frac{1}{C}\left\{\left[(2B)\overline{f}_j+(A-B)f_j\right]-\left[(2B)\overline{f}_{j-1}+(A-B)f_j\right]\right\};$$

$$J_{j,j}^{2,1}=J_{j,j}^{1,2};J_{j,j}^{2,2}=\frac{1}{C}\left\{\Delta z_j\left[(2B)\overline{f}_j+(A-B)f_j\right]+\Delta z_{j-1}\left[(2B)\overline{f}_{j-1}+(A-B)f_j\right]\right\}.$$

And

$$J_{j,j+1} = \begin{bmatrix} J^{1,1}_{j,j+1} & J^{1,2}_{j,j+1} \\ J^{2,1}_{j,j+1} & J^{2,2}_{j,j+1} \end{bmatrix}, \text{ where}$$

$$J^{1,1}_{j,j+1} = \frac{1}{C}\left\{\frac{1}{\Delta z_j}\left[(2B)\overline{f}_j + (A-B)f_j\right]\right\}; J^{1,2}_{j,j+1} = \frac{1}{C}\left\{\left[(2B)\overline{f}_j + (A-B)f_j\right]\right\};$$

$$J^{2,1}_{j,j+1} = \frac{1}{C}\left\{\left[(2B)\overline{f}_j + (A-B)f_j\right]\right\}; J^{2,2}_{j,j+1} = \frac{1}{C}\left\{\Delta z_j\left[(2B)\overline{f}_j + (A-B)f_j\right]\right\}.$$

The value of A, B, C for each term is listed in the following table for reference.

Table F.1: Values of A, B, C with linear interpolation of $f_n(z)$.

	A	*B*	*C*		*A*	*B*	*C*
$F^{1,1}_{j,j}$	10	3	35	$F^{1,1}_{j,j+1}$	9	9	140
$F^{1,2}_{j,j}$	15	7	420	$F^{1,2}_{j,j+1}$	7	6	-420
$F^{2,1}_{j,j}$	15	7	420	$F^{2,1}_{j,j+1}$	7	6	-420
$F^{2,2}_{j,j}$	5	3	840	$F^{2,2}_{j,j+1}$	1	1	-70
$J^{1,1}_{j,j}$	3	3	5	$J^{1,1}_{j,j+1}$	3	3	5
$J^{1,2}_{j,j}$	1	1	10	$J^{1,2}_{j,j+1}$	2	0	20
$J^{2,1}_{j,j}$	1	1	10	$J^{2,1}_{j,j+1}$	0	-2	20
$J^{2,2}_{j,j}$	3	1	30	$J^{2,2}_{j,j+1}$	1	1	60

Appendix G: Expression for F_{ij}, G_{ij}, and J_{ij} Matrices with Cubic $f_n(z)$ Interpolation

When we approximate $f_n(z)$ over the element $z \in [z_j, z_{j+1}]$ as the combination of two neighbor grid points using the cubic interpolation, it is given by

$$f_n(z) = (1-\xi)^2(2\xi+1)f_n(z_j) + h_j\xi(\xi-1)^2 f_n'(z_j) + \xi^2(3-2\xi)f_n(z_{j+1}) + h_j\xi^2(\xi-1)f_n'(z_{j+1}). \tag{G1}$$

The expressions for the F_{ij} and J_{ij} matrices are calculated as follows.

For $j = 2,3,\ldots N-1$,

$$F_{j,j} = \begin{bmatrix} F_{j,j}^{1,1} & F_{j,j}^{1,2} \\ F_{j,j}^{2,1} & F_{j,j}^{2,2} \end{bmatrix}$$

$$F_{j,j}^{1,1} = \frac{1}{C}\left\{\Delta z_j\left[(2B)\bar{f}_j + (A-B)f_j\right] + \Delta z_{j-1}\left[(2B)\bar{f}_{j-1} + (A-B)f_j\right]\right\}$$

$$+\frac{1}{C'}\left\{\Delta z_j^2\left[(2B')\bar{f}_j' + (A'-B')f_j'\right] - \Delta z_{j-1}^2\left[(2B')\bar{f}_{j-1}' + (A'-B')f_j'\right]\right\};$$

$$F_{j,j}^{1,2} = \frac{1}{C}\left\{\Delta z_j^2\left[(2B)\bar{f}_j + (A-B)f_j\right] - \Delta z_{j-1}^2\left[(2B)\bar{f}_{j-1} + (A-B)f_j\right]\right\}$$

$$+\frac{1}{C'}\left\{\Delta z_j^3\left[(2B')\bar{f}_j' + (A'-B')f_j'\right] + \Delta z_{j-1}^3\left[(2B')\bar{f}_{j-1}' + (A'-B')f_j'\right]\right\};$$

$$F_{j,j}^{2,1} = F_{j,j}^{1,2};\ F_{j,j}^{2,2} = \frac{1}{C}\left\{\Delta z_j^3\left[(2B)\bar{f}_j + (A-B)f_j\right] + \Delta z_{j-1}^3\left[(2B)\bar{f}_{j-1} + (A-B)f_j\right]\right\}$$

$$+\frac{1}{C}\left\{\Delta z_j^4\left[(2B')\bar{f}_j' + (A'-B')f_j'\right] - \Delta z_{j-1}^4\left[(2B')\bar{f}_{j-1}' + (A'-B')f_j'\right]\right\}.$$

For $F_{1,1}$, the first term in the above expression is kept, while for $F_{N,N}$ the second term is kept. And

$$F_{j,j+1}=\begin{bmatrix} F_{j,j+1}^{1,1} & F_{j,j+1}^{1,2} \\ F_{j,j+1}^{2,1} & F_{j,j+1}^{2,2} \end{bmatrix}$$

$$F_{j,j+1}^{1,1}=\frac{1}{C}\left\{\Delta z_j\left[(2B)\overline{f}_j+(A-B)f_j\right]\right\}+\frac{1}{C'}\left\{\Delta z_{j+1}^2\left[(2B')\overline{f}'_j+(A'-B')f'_j\right]\right\};$$

$$F_{j,j+1}^{1,2}=\frac{1}{C}\left\{\Delta z_j^2\left[(2B)\overline{f}_j+(A-B)f_j\right]\right\}+\frac{1}{C'}\left\{\Delta z_{j+1}^3\left[(2B')\overline{f}'_j+(A'-B')f'_j\right]\right\};$$

$$F_{j,j}^{2,1}=\frac{1}{C}\left\{\Delta z_j^2\left[(2B)\overline{f}_j+(A-B)f_j\right]\right\}+\frac{1}{C'}\left\{\Delta z_{j+1}^3\left[(2B')\overline{f}'_j+(A'-B')f'_j\right]\right\};$$

$$F_{j,j+1}^{2,2}=\frac{1}{C}\left\{\Delta z_j^3\left[(2B)\overline{f}_j+(A-B)f_j\right]\right\}+\frac{1}{C'}\left\{\Delta z_{j+1}^4\left[(2B')\overline{f}'_j+(A'-B')f'_j\right]\right\}.$$

In a similar way,

$$J_{j,j}=\begin{bmatrix} J_{j,j}^{1,1} & J_{j,j}^{1,2} \\ J_{j,j}^{2,1} & J_{j,j}^{2,2} \end{bmatrix}$$

$$J_{j,j}^{1,1}=\frac{1}{C}\left\{\frac{1}{\Delta z_j}\left[(2B)\overline{f}_j+(A-B)f_j\right]+\frac{1}{\Delta z_{j-1}}\left[(2B)\overline{f}_{j-1}+(A-B)f_j\right]\right\}$$

$$+\frac{1}{C'}\left\{\left[(2B')\overline{f}'_j+(A'-B')f'_j\right]-\left[(2B')\overline{f}'_{j-1}+(A'-B')f'_j\right]\right\};$$

$$J_{j,j}^{1,2}=\frac{1}{C}\left\{\left[(2B)\overline{f}_j+(A-B)f_j\right]-\left[(2B)\overline{f}_{j-1}+(A-B)f_j\right]\right\}$$

$$+\frac{1}{C'}\left\{\Delta z_j\left[(2B')\overline{f}'_j+(A'-B')f'_j\right]+\Delta z_{j-1}\left[(2B')\overline{f}'_{j-1}+(A'-B')f'_j\right]\right\};$$

$$J_{j,j}^{2,1}=J_{j,j}^{1,2};\ J_{j,j}^{2,2}=\frac{1}{C}\left\{\Delta z_j\left[(2B)\overline{f}_j+(A-B)f_j\right]+\Delta z_{j-1}\left[(2B)\overline{f}_{j-1}+(A-B)f_j\right]\right\}$$

$$+\frac{1}{C'}\left\{\Delta z_j^2\left[(2B')\overline{f}'_j+(A'-B')f'_j\right]-\Delta z_{j-1}^2\left[(2B')\overline{f}'_{j-1}+(A'-B')f'_j\right]\right\}.$$

$$J_{j,j+1}=\begin{bmatrix} J_{j,j+1}^{1,1} & J_{j,j+1}^{1,2} \\ J_{j,j+1}^{2,1} & J_{j,j+1}^{2,2} \end{bmatrix}$$

$$J_{j,j+1}^{1,1}=\frac{1}{C}\left\{\frac{1}{\Delta z_j}\left[(2B)\overline{f}_j+(A-B)f_j\right]\right\}+\frac{1}{C'}\left\{\left[(2B')\overline{f}'_j+(A'-B')f'_j\right]\right\};$$

$$J_{j,j+1}^{1,2}=\frac{1}{C}\left\{\left[(2B)\overline{f}_j+(A-B)f_j\right]\right\}+\frac{1}{C'}\left\{\Delta z_{j+1}\left[(2B')\overline{f}'_j+(A'-B')f'_j\right]\right\};$$

$$J_{j,j+1}^{2,1}=\frac{1}{C}\left\{\left[(2B)\overline{f}_j+(A-B)f_j\right]\right\}+\frac{1}{C'}\left\{\Delta z_{j+1}\left[(2B')\overline{f}'_j+(A'-B')f'_j\right]\right\};$$

$$J_{j,j+1}^{2,2}=\frac{1}{C}\left\{\Delta z_j\left[(2B)\overline{f}_j+(A-B)f_j\right]\right\}+\frac{1}{C'}\left\{\Delta z_{j+1}^2\left[(2B')\overline{f}'_j+(A'-B')f'_j\right]\right\}.$$

The value of A, B, C for each term is listed in the following table for reference.

Table G.1: Values of A, B, C with cubic interpolation of $f_n(z)$.

	A	B	C	A'	B'	C'
$F_{j,j}^{1,1}$	774	162	2520	97	-43	2520
$F_{j,j}^{1,2}$	97	35	2520	16	-9	2520
$F_{j,j}^{2,1}$	97	35	2520	16	-9	2520
$F_{j,j}^{2,2}$	16	8	2520	3	-2	2520
$F_{j,j+1}^{1,1}$	162	162	2520	35	-35	2520
$F_{j,j+1}^{1,2}$	-43	-35	2520	-9	8	2520
$F_{j,j+1}^{2,1}$	35	43	2520	8	-9	2520
$F_{j,j+1}^{2,2}$	-9	-9	2520	-2	2	2520
$J_{j,j}^{1,1}$	504	504	840	108	-108	840
$J_{j,j}^{1,2}$	-12	96	840	6	-18	840
$J_{j,j}^{2,1}$	-12	96	840	6	-18	840

Table G.1: Continued.

$J_{j,j+1}^{1,1}$	-504	-504	840	-108	108	840
$J_{j,j+1}^{1,2}$	96	-12	840	18	-6	840
$J_{j,j+1}^{2,1}$	12	-96	840	-6	18	840
$J_{j,j+1}^{2,2}$	-14	-14	840	-1	1	840

VITA

VITA

Hongdan Tao

Email address: htao@purdue.edu

Education:

Purdue University, West Lafayette, IN, December 2013
Ph.D., Mechanical Engineering, 3.94/4.0 GPA
Dissertation: “Propagation of sound in the vicinity of rigid porous interfaces"

Northwestern Polytechnic University, Xi'an, China, July 2009
M.S., Acoustics, Environmental Engineering

Northwestern Polytechnic University, Xi'an, China, July 2007
B.S., Environmental Engineering

Publications:

1. K. M. Li, **H. Tao**," A modified saddle point method for predicting sound fields above a non-locally reacting porous medium," Wave Motion (in press).
2. K. M. Li, **H. Tao**," Reflection and transmission of sound from a dipole source near a rigid porous medium," ACTA Acustica united with Acoustica 99(5), 703-715 (2013).
3. K. M. Li, **H. Tao**," On the asymptotic solution of sound penetration into a rigid porous half-plane: A modified saddle point method," Journal of Sound and Vibration 332(19), 4584-4596 (2013).

Awards:

2013 Leo Beranek Student Medal for Excellence in Study of Noise Control
National Council of Acoustical Consultants Student Travel Awards, 2011
The Meritorious Winner of International Mathematical Contest in Modeling, 2007
Excellent Undergraduate Thesis Award of NPU, 2007

Professional Societies and Activities:

Student volunteer, Inter-Noise 2012 conference, New York
Member, Student Representative Committee, Herrick Laboratories
Mentor, OMEGA mentoring program, Purdue University, 2012
Member, Acoustical Society of America
Member, Purdue Women in Engineering Program